ADSORPTION OF PHARMACEUTICAL AND HEAVY METAL CONTAMINANTS ONTO THREE-DIMENSIONAL GRAPHENE BASED STRUCTURES

BILLIE HIEW YAN ZHANG

DOCTOR OF PHILOSPHY

UNIVERSITY OF NOTTINGHAM

JULY 2020

Abstract

Water contamination by pharmaceutical and heavy metal discharge is a serious environmental issue causing adverse effects on aquatic biota and human health. Despite showing promising pollutants decontamination efficiency, graphene oxide (GO) nanosheets are not feasible adsorbents for application in wastewater treatment. Therefore, three-dimensional (3D) graphene structures were synthesised and demonstrated to be practical adsorbents for pharmaceutical and heavy metal pollutants removal. This thesis describes the successful conversion of GO nanosheets into graphene macrostructures for the adsorption of pharmaceuticals and heavy metals from aqueous environment.

In this research, several new 3D graphene-based structures were synthesised, namely reduced graphene oxide aerogel (rGOA), reduced graphene oxide aerogel decorated with δ-MnO_2 (RGM) and zirconium functionalised graphene oxide aerogel (ZrGA). The rGOA was prepared by self-assembly of GO via chemical reduction with L-ascorbic acid while the RGM and ZrGA were assembled through ice-templating method fortified by carboxymethyl cellulose and incorporated with metal-based functionalising agents. Characterisation study revealed that the rGOA, RGM and ZrGA were amorphous and porous with hollow channels formed by interconnected graphene/binder layers. Chemical functional groups such as hydroxyl, carboxyl and epoxy groups were found in the adsorbents while Mn and Zr-based functional groups were detected in RGM and ZrGA, respectively.

The simultaneous interaction of process parameters and optimisation of batch adsorption were investigated using response surface methodology. It was determined that rGOA and RGM exhibited highest adsorption capacities of 646.5 mg/g for diclofenac and 129.4 mg/g for acetaminophen, respectively. Furthermore, ZrGA

showed highest adsorption capacities of 53.1 mg/g for Cu^{2+} and 41.6 mg/g for Ni^{2+}. The adsorption equilibrium for diclofenac-rGOA system was best described by the Freundlich model while acetaminophen-RGM, Cu^{2+}-ZrGA and Ni^{2+}-ZrGA adsorption equilibria were best described by the Langmuir model. The adsorption of diclofenac onto rGOA and Ni^{2+} onto ZrGA involved physisorption as the systems adsorption kinetics were best modelled by the pseudo-first-order kinetic model. Meanwhile, acetaminophen and Cu^{2+} uptake by RGM and ZrGA, respectively, was by chemisorption as the systems adsorption kinetics were well represented by the pseudo-second-order kinetic model. Hydrogen bonding and electrostatic interactions were the predominant mechanisms of adsorption of the pharmaceuticals and heavy metals onto the 3D graphene-based structures.

Fixed bed adsorption study demonstrated that rGOA and ZrGA could be used to remove the contaminants under continuous flow mode, however RGM was not suitable as its structure became unstable during the column operation. The study revealed that the breakthrough time was increased as the bed heights of rGOA and ZrGA increased, but decreased as the influent concentration and flowrate increased. The breakthrough curves obtained were well correlated to the Thomas and Yoon-Nelson models. The BDST model was used successfully to depict a linear relationship between column service time and bed height. Furthermore, the mass transfer analysis indicated the involvement of film mass transfer and pore diffusion.

Acknowledgements

I would like to express my appreciation to those who have supported and assisted me during my PhD study, and without their participation it would not be possible for me to accomplish the enormous task.

Firstly, I wish to extend my sincere and heartfelt thanks to my supervisor, Dr Lee Lai Yee, for providing me the opportunity to embark on this amazing PhD journey. I am truly grateful to her constant encouragement and suggestions to overcome the difficulties encountered during my PhD study, as well as the time and effort she spent on proofreading my research documents. Having discussion and brainstorming sessions with her always motivate me to try new things and explore further into the research. She has coached me to be a passionate researcher who truly enjoy discovering new ideas and trained me to think critically when searching for innovative solutions. I can never thank Dr Lee enough.

I am extremely grateful to Professor Gan Suyin and Dr Suchithra Thangalazhy Gopakumar who have provided valuable advice and tremendous guidance to me. Thank you both for sharing with me your excellent ideas, knowledge and time to enable me to carry out this research successfully.

I wish to acknowledge the financial support provided by the Ministry of Higher Education (MOHE) Malaysia, under the Fundamental Research Grant Scheme (FRGS/1/2015/SG06/UNIM/02/1).

My sincere gratitude is extended to all technical support staff for their assistance and advice on analytical equipment and chemical usage, and other laboratory matters. My earnest thanks to Ahmad Fareez Mohd Rawi, Andrew Yakin, Noor Fatihah Suhaimi,

Muhamad Asyraf Samsudin, Khairani Hasuna Jaapar and Filzah Mohd Fauzi for their willingness to help when I encountered problems in the laboratories.

To my parents and sisters, who have been very supportive of the decisions I made, I extend my utmost gratitude and love. Thank you for your continuous support and understanding, and for instilled me with the confidence and inspiration to embark on this challenging yet exciting journey of pursuing the PhD degree.

List of Publications

Selected publications

1. Hiew, B.Y.Z., Lee, L.Y., Lai, K.C., Gan, S., Thangalazhy-Gopakumar, S., Pan, G.-T. and Yang, T.C.-K., 2019. Adsorptive decontamination of diclofenac by three-dimensional graphene-based adsorbent: Response surface methodology, adsorption equilibrium, kinetic and thermodynamic studies. Environmental Research. 168, 241-253.

2. Hiew, B.Y.Z., Lee, L.Y., Lee, X.J., Thangalazhy-Gopakumar, S., Gan, S., Lim, S.S, Pan, G.-T., Yang, T.C.-K, Chiu, W.S. and Khiew, P.S., 2018. Review on synthesis of 3D graphene-based configurations and their adsorption performance for hazardous water pollutants. Process Safety and Environmental Protection. 116, 262-286.

3. Hiew, B.Y.Z., Lee, L.Y., Lee, X.J., Gan, S., Thangalazhy-Gopakumar, S., Lim, S.S., Pan, G.-T. and Yang, T.C.-K., 2019. Adsorptive removal of diclofenac by graphene oxide: Optimization, equilibrium, kinetic and thermodynamic studies. Journal of the Taiwan Institute of Chemical Engineers. 98, 150 – 162.

Other publications

1. Hiew, B.Y.Z., Lee, L.Y., Lee, X.J., Thangalazhy-Gopakumar, S. and Gan, S., 2020. Utilisation of environmentally friendly okara-based biosorbent for cadmium (II) removal. Environmental Science and Pollution Research, (*In Press*). https://doi.org/10.1007/s11356-020-09594-3

2. Lai, K.C., Hiew, B.Y.Z., Lee, L.Y., Gan, S., Thangalazhy-Gopakumar, S., Chiu, W.S. and Khiew, P.S., 2019. Ice-templated graphene oxide/chitosan aerogel as an

effective adsorbent for sequestration of metanil yellow dye. Bioresource Technology. 274, 134-144.

3. Lai, K.C., Lee, L.Y., Hiew, B.Y.Z., Thangalazhy-Gopakumar, S. and Gan, S., 2019. Environmental application of three-dimensional graphene materials as adsorbents for dyes and heavy metals: Review on ice-templating method and adsorption mechanisms. Journal of Environmental Sciences. 79, 174-199.

4. Lee, X. J., Hiew, B.Y.Z., Lai, K. C., Lee, L. Y., Gan, S., Thangalazhy-Gopakumar, S. and Rigby, S., 2018. Review on graphene and its derivatives: Synthesis methods and potential industrial implementation. Journal of the Taiwan Institute of Chemical Engineers. (In Press.)

5. Lee, X.J., Hiew, B.Y.Z., Lee, L.Y., Gan, S. and Thangalazhy-Gopakumar, S., 2017. Evaluation of the effectiveness of low cost adsorbents from oil palm wastes for wastewater treatment. Chemical Engineering Transactions. 937-942.

6. Lee, X.J., Lee, L.Y., Hiew, B.Y.Z., Gan, S., Thangalazhy-Gopakumar, S. and Ng, H.K., 2017. Multistage optimizations of slow pyrolysis synthesis of biochar from palm oil sludge for adsorption of lead. Bioresource Technology. 245, 944 – 953.

7. Ooi, J., Lee, L.Y., Hiew, B.Y.Z., Thangalazhy-Gopakumar, S., Lim, S.S. and Gan, S., 2017. Assessment of fish scales waste as a low cost and eco-friendly adsorbent for removal of an azo dye: Equilibrium, kinetic and thermodynamic studies. Bioresource Technology. 245, 656 – 664.

8. Hiew, B.Y.Z., Lee, L.Y., Thangalazhy-Gopakumar, S. and Gan, S., 2019. Biosorption. In: Bioprocess Engineering: downstream processing Taylor & Francis Group. 143-164 (Book chapter)

Conferences Attended

1. 12th Annual Conference on the Challenges in Environmental Science and Engineering (CESE), 3 – 7 November 2019, Kaohsiung, Taiwan.
   - Comparative studies on copper and nickel adsorption on zirconium-functionalised graphene aerogel: Equilibrium, kinetic and thermodynamics studies (Poster presentation)
   - Adsorption of acetaminophen onto reduced graphene oxide aerogel decorated with manganese oxide (Oral presentation)

2. 2nd Bioresource, Energy, Environment and Material Technology (BEEM) International Conference, 10 – 13 June 2018, Seoul, South Korea (Oral presentation).
   - Investigation of different three-dimensional graphene-based configurations on the adsorption of diclofenac (Material Technology)
   - Development of graphene oxide-chitosan foam for sequestration of synthetic dyes (Environment)

Awards Received

2019 - Best Young Scientist/Student Poster Presentation Award, CESE-2019

2018 - Recipient of the departmental PG Student Conference Funding

2017 - First Runner Up for PGR Research Poster Showcase

2016 - Department of Chemical and Environmental Engineering PhD Scholarship (2016 – 2019)

Table of Contents

List of Figures

List of Tables

Chapter 1: Introduction

1.1 Research background

Increasing industrial, agricultural and domestic activities arising from human population growth have caused more hazardous chemicals to be discharged into the environment within the past decades. Among these hazardous substances, pharmaceutical residues have emerged as environmental pollutants which contain therapeutically active compounds commonly found in prescribed and household drugs, such as analgesic/anti-inflammatory and antibiotics, as well as in personal care products such as sunscreen, cosmetics, shampoos and fragrances. Pharmaceuticals have been formulated to function biologically on targeted diseases in humans, plants and animals, but they could adversely affect non-targeted organisms upon exposure (Hernando et al., 2006; Jaria et al., 2020). For instance, diclofenac residue was found to cause renal failure in vulture in India and Pakistan (Sathishkumar et al., 2020). Exposure to ibuprofen and other estrogenous compounds resulted in severe genetic damage and change in gender ratio of the aquatic species (Durán-Álvarez et al., 2014). Furthermore, the presence of antibiotics in natural water resources could lead to development of antibiotic resistant bacteria posing threat to the aquatic ecosystem (Sapkota et al., 2008). Beta-blocker (β-blocker), used for heart attack prevention, not only poisoned the marine life, but exposure to humans can cause bronchoconstriction (Fent et al., 2006). Due to the detrimental effects of the pharmaceutical residues, it is essential to regulate their concentration in the environment.

The sources of pharmaceutical pollutants in the environment include industrial effluents, agricultural and livestock runoffs, direct domestic disposal of expired and unused medicines, and municipal treatment plant effluents (Karami et al., 2020; Rahman et al., 2009). Numerous pharmaceutical residues have been identified in

sewage, rivers, lakes, seas, sediments, tap water and even in drinking water in 14 countries, and the most commonly detected drugs were analgesic/anti-inflammatory compounds (Quesada et al., 2019). Traces of pharmaceutical compounds detected in drinking water suggested that conventional wastewater treatment plants (WWTP) were not effective in removing the emerging pollutants. Al-Qaim et al. (2014) detected numerous pharmaceutical residues in surface water, WWTP and hospital effluent in Malaysia, and these include caffeine, diclofenac, levonorgestrel, prazosin, hydrochlorothiazide, mefenamic acid, carbamazepine, simvastatine and enalapril. The detection of these micropollutants is a major concern as they could accumulate in the aquatic ecosystem.

Diclofenac (2-[(2,6-dichlorophenyl)amino] benzene acetic acid) is a pharmaceutical compound with analgesic and antipyretic properties, and is catogerised under the therapeutic class of non-steroidal anti-inflammatory drug (NSAID) (Hossein Beyki et al., 2017). It is widely used in pain relief treatment such as primary dysmenorrhea, mild to moderate pain and rheumatoid arthritis (Blair & Plosker, 2015; Hossein Beyki et al., 2017). Lately, diclofenac is frequently detected in natural water sources due to its high consumption and incomplete removal in municipal WWTP (Acuña et al., 2015; Antunes et al., 2012). The toxicity of diclofenac is well documented in the literature, indicating the adverse effect of this compound on the environment and terrestrial organisms (Ericson et al., 2010; Lonappan et al., 2016). For example, exposure to diclofenac was reported to cause tissue damage in mussels through lipid peroxidation and major population reduction of three *Gyps* vulture species in Indian sub-continent (Lonappan et al., 2016). Therefore, diclofenac has been labelled as a priority contaminant in the European Community Directive, 2015/495, emphasising its harmful effect (Álvarez-Torrellas et al., 2017).

Acetaminophen (N-acetyl-p-aminophenol or paracetamol) is an over-the-counter non-steroidal anti-inflammatory drug with antipyretic and analgesic properties that is widely prescribed for pain and fever relief (Zhong et al., 2019). It is considered as one of the most consumed drug globally with estimated annual production of more than 100,000 tonnes (Joncour et al., 2014). However, acetaminophen could not be completely metabolised and 20 % of the total consumed drug were excreted out as metabolites such as sulphate conjugates, paracetamol cysteinate or mercapturate to the environment (Nourmoradi et al., 2018). Generally, acetaminophen is a safe drug for ingestion under appropriate dosage, but with a narrow safety margin (Czech & Tyszczuk-Rotko, 2018). Excessive intake of acetaminophen could lead to accumulation of reactive benzoquinoneimine (N-acetyl-para-benzoquinoneimine) metabolite (Tortet et al., 2017), consequently causing acute liver failure and nephrotoxicity (Tyszczuk-Rotko et al., 2019). Therefore, an effective treatment system is necessary to regulate the pharmaceutical concentration in water body to minimise its negative impacts on human health and environment.

The routine electronic, metallurgy and chemical production have contributed to water pollution through accumulation of heavy metals such as copper (Cu^{2+}) and nickel (Ni^{2+}). The primary sources of these metals can be traced to industries such as brass manufacturing, petroleum refining, smelting and agrichemicals sectors. It has been reported that Cu^{2+} toxicity occurred when its concentration exceeded 5 mg/L in human body (Chu et al., 2020) and the associated health hazards include lethargy, DNA damage, gastrointestinal bleeding and hypertension (Mahdi et al., 2018). The prolonged exposure to Ni^{2+} could cause skin allergies, lung fibrosis and respiratory tract cancer (Kasprzak et al., 2003). Considering the severity of Cu^{2+} and Ni^{2+} toxicity, the World Health Organization (WHO) has stipulated that the concentration of Cu^{2+} and Ni^{2+}

should not exceed 2 and 0.07 mg/L, respectively, in drinking water (Oh et al., 2019). Hence, concentration of the heavy metals in water environment should be controlled using effective treatment system.

The remediation of water contaminated by pharmaceuticals and heavy metals has been investigated using methods such as membrane filtration (Schafer et al., 2011), advanced oxidation process (Rivera-Utrilla et al., 2013), electrochemical processes (Sires & Brillas, 2012) and adsorption (Rivera-Utrilla et al., 2013). Among these methods, adsorption technique appeared to be a promising alternative as it is relatively low cost, effective and simple to operate. A wide range of adsorbents have been used to remove these pollutants and the adsorption efficiency varied with the type of adsorbent, as illustrated in Table 1.1 based on the respective adsorption capacity.

Table 1.1: Adsorbent used in different pharmaceuticals and heavy metals adsorption.

Adsorbent	Pollutants	q_m (mg/g)	Reference
Biomass			
Grape stalk	Acetaminophen	89.19	(Portinho et al., 2017)
Watermelon rind	As^{3+}	4.81	(Shakoor et al., 2018)
Clay			
Aluminium pillared clay	Hg^{+}	49.75	(Eloussaief et al., 2013)
Organo bentonite	Diclofenac	188.6	(Ahmed & Hameed, 2019)
Char-based material			
Fe/Zn biochar	Tetracycline	102.00	(Zhou et al., 2017b)
Hazelnut shell biochar	Cu^{2+}	43.54	(Zhao et al., 2018)
Almond shell activated carbon	Sulphamethoxazole	344.80	(Zbair et al., 2018)
Fox nutshell activated carbon	Cr^{6+}	74.95	(Kumar & Jena, 2017)
Carbon nanomaterials			
Graphene oxide	Cd^{2+}	530	(Sitko et al., 2013)
	Ciprofloxacin	409	(Sun et al., 2018b)
	Levofloxacin	256.6	(Dong et al., 2016)
	Pb^{2+}	227.2	

Of these adsorbents, carbon nanomaterials exhibited comparatively high adsorption capacity possibly due to their high porosity, specific surface area and surface chemical functionalities. Recent research have demonstrated the potential application of low dimensional carbon nanomaterials such as graphene (Zhu et al., 2017), carbon nanotube (Patiño et al., 2015) and fullerene (Elessawy et al., 2020) as highly effective adsorbents for capturing numerous water pollutants.

Graphene oxide (GO) is the oxidised form of graphene with abundant oxygen containing functional groups such as epoxy, hydroxyl and carboxylic groups. It was widely synthesised by the modified Hummers method (Hummers & Offeman, 1958). The relatively simple method enables the synthesis of GO with decent and consistent quality enabling its widespread testing for a variety of engineering, biomedical and environmental applications. The presence of oxygeneous functional groups provided promising active sites in GO making it a possible adsorbent for removing different pollutants such as pharmaceutical pollutants and heavy metals (Al-Khateeb et al., 2014; Amalraj Appavoo et al., 2014; Chen et al., 2014a; Chen et al., 2014b; Lin et al., 2013). Other remarkable properties such as enormous surface area (~ 2630 m^2/g), better colloidal stability than other carbon materials and high aspect ratio for modification have made GO a feasible material for application in adsorption and surface reaction. Fig. 1.1 demonstrates the rising trend in research interest related to GO and its derivatives in adsorption processes. However, the application of GO in large scale wastewater processes is hindered by its nanometre-size dimension and high colloidal stability causing its recovery after adsorption very challenging. Furthermore, separation of GO from the solution after adsorption can cause agglomeration and restacking of the GO

into graphene which lead to reduction of surface area. Hence, GO suspension is not a practical adsorbent for application in wastewater treatment.

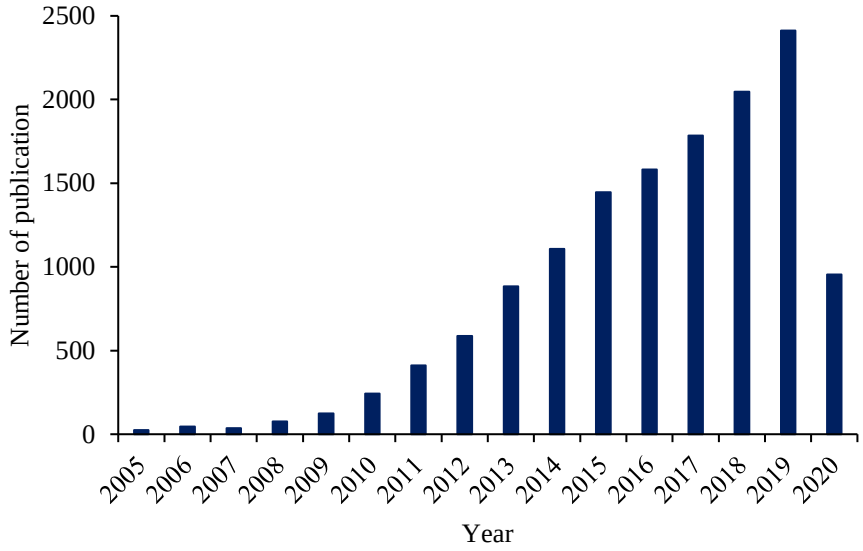

Fig. 1.1: Number of publications with terms ‘graphene adsorption’ available between 2005 and 2020 from Scopus database, extracted on 31/03/2020.

In recent years, intense research efforts have been devoted to develop GO into three dimensional (3D) structures to improve its potential application in environmental pollution control. 3D GO-based structures such as GO foams (Speyer et al., 2017), sponges (Wu et al., 2016), aerogels (Liu et al., 2017a) and hydrogels (Gan et al., 2015) have been reported in the current literature. Owing to its large specific surface area, low density, high porosity and abundant of chemical functional groups, graphene-based aerogel has been investigated for use in environmental pollution control (Jang & Lee, 2018). Aerogel adsorbents were hydrophobic with strong affinity for organic pollutants through hydrophobic interaction (Li et al., 2014b). Zhang et al. (2018) synthesised sodium bisulphite reduced GO aerogel which showed an adsorption capacity of 128.37 mg/g for tetrabromobisphenol A while Yu et al. (2017) developed a magnetic graphene

sponge which showed an adsorption capacity of 473 mg/g for tetracycline, and this was 50 % greater than that of GO. Furthermore, a new 3D graphene/polydopamine modified multiwalled carbon nanotube hybrid aerogel has been demonstrated to adsorb 350.87 mg/g of lead (Zhan et al., 2019) while a chitosan cross-linked GO aerogel showed 312.05 mg/g adsorption capacity towards chromium (Li et al., 2019). Therefore, graphene-based aerogels could be suitable adsorbents for the removal of pharmaceutical and heavy metal pollutants.

Till recently, most adsorption studies on 3D GO-based adsorbents were conducted in batch mode as the adsorption information are essential to establish the removal efficiency of a new adsorbent for specific pollutant. However, this mode of adsorption is rarely used in the wastewater industry owing to its incapability in handling large volume of wastewater. Compared to batch adsorption, the fixed bed column adsorption is capable of treating relatively large volume of contaminated water continuously. Furthermore, data obtained from the column operation can be applied for scaling up the laboratory work (Lemus et al., 2017).

In order to design an industrial adsorption system, the required kinetic data can be obtained from the breakthrough curve of fixed bed adsorption. The breakthrough curve of an adsorbate is the plot of outlet-to-inlet concentration ratio (C_t/C_o) against time. This curve describes the adsorption dynamics and behaviour related to the adsorption isotherm shape and diffusional steps within the fixed bed (Ahmed & Hameed, 2018). Furthermore, breakthrough curve provides useful column parameters such as breakthrough time, saturation time and mass transfer zone. A graphene-$MnFe_2O_4$ supported on vegetal activated carbon composite was used in the fixed bed adsorption of glyphosphate and the longest breakthrough time of 5.5 h was achieved when the column was operated at 5 mg/L glyphosphate feed concentration, 10 cm bed

height and 8 mL/min flowrate (Marin et al., 2019). From numerical simulation of breakthrough curve, it was revealed that internal diffusion step was the mass transfer limiting step. Furthermore, a sodium dodecyl sulphate modified graphene was used to remove copper (Cu^{2+}) and manganese (Mn^{2+}) in column adsorption. The study showed that the optimum adsorption capacities of Cu^{2+} and Mn^{2+} were 48.83 and 45.62 mg/g, respectively, when the column was operated at 3 cm bed height and 10 mL/min flowrate (Yusuf et al., 2020). In addition, the continuous adsorption of Cu^{2+} and Mn^{2+} onto the adsorbent was well modelled by the Thomas model and Bed-Depth Service Time (BDST) model (Yusuf et al., 2020).

1.2 Problem statement

Exposure to pharmaceutical and heavy metal pollutants can induce detrimental effects on human health and the environment. Conventional WWTP was ineffective in treating these pollutants since they were detected in the WWTP effluent, while other technologies such as membrane system, electrochemical processes and adsorption are still under investigation (Quesada et al., 2019). Adsorption is a promising technique for the treatment of water polluted by pharmaceutical residues owing to its simplicity in operation and high efficiency in treating very low concentration of pollutants. Furthermore, integration of adsorption technology into existing WWTP is relatively easy and can be carried out at comparatively low cost (Rivera-Utrilla et al., 2013).

GO has been employed to adsorb different pollutants from wastewater (Wang et al., 2013). High specific surface area, thermal and chemical stability are the major properties supporting GO as a potential adsorbent for pharmaceuticals and heavy metals removal. In comparison to other carbon nanomaterials such as fullerenes and carbon nanotubes, GO is more cost effective (Kuila et al., 2012). The surface properties of GO

can be modified to enhance its removal efficiencies by treatment with different chemicals such as acid, base, surfactant and polymeric materials (Wang et al., 2019).

The free standing two-dimensional (2D) GO is not a practical form for utilisation in the wastewater industry. Due to its extremely small size and high dispersibility in aqueous system, the recovery of GO from solution requires the use of energy intensive and costly separation techniques (Liu et al., 2012). To overcome the challenge, it is desired to configure the GO sheets into a 3D structure while preventing re-stacking of the individual GO sheets. The construction of 3D GO networks should enable the graphene intrinsic properties to be embedded into the bulk volume and hence, improve the use of GO in wastewater treatment. Therefore, it would be of great interest to develop GO into 3D structures and to determine their potential in adsorbing pharmaceuticals and heavy metals.

1.3 Aims and objectives

This research was aimed to develop novel 3D graphene-based structures as effective adsorbents for the removal of pharmaceutical and heavy metal contaminants in aqueous solutions. The specific objectives of this research were as follows:

- to synthesise new 3D graphene-based structures and determine their physiochemical properties.
- to determine the batch adsorption performance of the as-synthesised adsorbents in removing pharmaceuticals (diclofenac and paracetamol) and heavy metals (Cu^{2+} and Ni^{2+}) and fit the experimental data to various adsorption models (Langmuir, Freundlich, Temkin, Dubinin-Radushkevich, pseudo-first-order, pseudo-second-order and Elovich models) as well as optimise the adsorption systems by RSM.

- to evaluate the fixed bed adsorption performance of the 3D graphene-based adsorbents in sequestrating the pharmaceuticals (diclofenac and paracetamol) and heavy metals (Cu^{2+} and Ni^{2+}) as well as to correlate the breakthrough data to different kinetic models (Thomas, Yoon-Nelson and Adam-Bohart and Bed-Depth Service Time).
- to determine suitable the regeneration reagent and efficiency as well as the adsorption-desorption cycle number of the 3D graphene-based adsorbents.

Chapter 2: Literature Review

The literature review firstly describes the overall properties and synthesis methods of graphene-based materials such as graphene, graphene oxide (GO) and reduced graphene oxide (rGO). The synthesis routes of 3D graphene-based structures were next reviewed for selection of appropriate method for this research. The adsorption capacities and mechanisms for pharmaceuticals and heavy metals removal by different graphene-based derivatives were compiled for identification of potential starting materials to synthesise 3D graphene-based structures. Lastly, the operation modes of adsorption and effects of different process parameters on the adsorbates removal were reviewed.

2.1 Overview of graphene-based materials

Graphene is a sheet of sp^2 hybridised carbon atoms arranged in a honeycomb manner with a thickness equivalent to the diameter of an atom. The carbon atoms are covalently bonded together in the same planar and the monolayer graphene sheets are linked by van der Walls forces. Graphene was estimated to possess exceptionally high surface area indicating its potential application in adsorption and surface reaction processes. It is the basic building block of carbon nanocomposites such as graphene sheets, GO and rGO, and their properties are shown in Table 2.1.

Table 2.1: Main properties and chemical structures of graphene materials (Gómez-Navarro et al., 2008; Lee et al., 2008; Park & Ruoff, 2009; Sreeprasad & Berry, 2013; Suk et al., 2010).

Material	**Graphene**	**GO**	**rGO**
Chemical structure	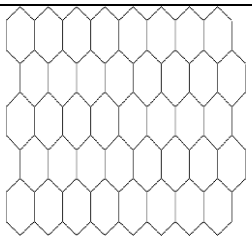	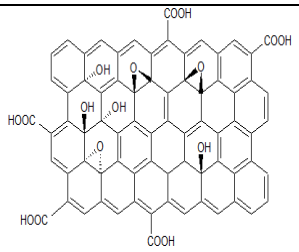	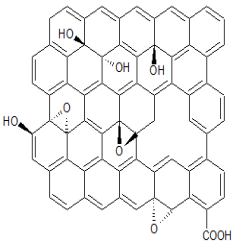
C:O ratio	No oxygen	2 - 4	8 - 246
Young's modulus (GPa)	1000	200	250
Electron mobility ($cm^2/V s$)	10000 – 50000	Insulator	0.05 – 200
Synthesis pathway	- Chemical vapour deposition (CVD) - SiC thermal decomposition - Graphite exfoliation	- Oxidation and exfoliation of graphite	- Chemical or thermal reduction of GO - Photo-assisted - Microwave-assisted
Production cost	High	Low	Low

GO is the product of the oxidation of graphene sheets and the oxidation process significantly alters its physiochemical properties. The introduction of oxygen-containing functional groups to the carbon structure lowers the electronic and mechanical properties of GO as compared to graphene (Gómez-Navarro et al., 2008; Sreeprasad & Berry, 2013; Suk et al., 2010). The incorporated oxygen functionalities increase the hydrophilicity of GO such that it is readily dispersed and forms stable colloidal suspension in aqueous media.

GO is a cost effective starting material for the synthesis of rGO through reduction processes such as chemical reduction by reducing reagents, thermal annealing,

microwave-assisted reduction and photo-reduction process (Singh et al., 2016). The reduction processes could eliminate a large fraction of the oxygen content, yielding C:O ratio between 2:1 to 246:1. However, a complete reduction of GO was still impossible. The reduction could also alter the chemical structure of GO. During reduction, the GO sheets underwent changes in carbon vacancies and residual oxygen content which resulted in the deformation of hexagonal carbon chains into pentagonal or heptagonal carbon structures (Gómez-Navarro et al., 2010). Hence, the reduction process could only produce GO derivatives with mechanical and electronic properties which were a fraction of those of pristine graphene (Table 2.1). The insights and data gathered on the characteristics and synthesis pathways of the graphene materials could contribute to the development of graphene-based composites for wastewater treatment (Peng et al., 2017b).

2.2 Synthesis of GO

The preparation of GO generally involved chemical oxidation and exfoliation of graphite which can be extended to produce rGO through reduction processes, as illustrated in Fig. 2.1.

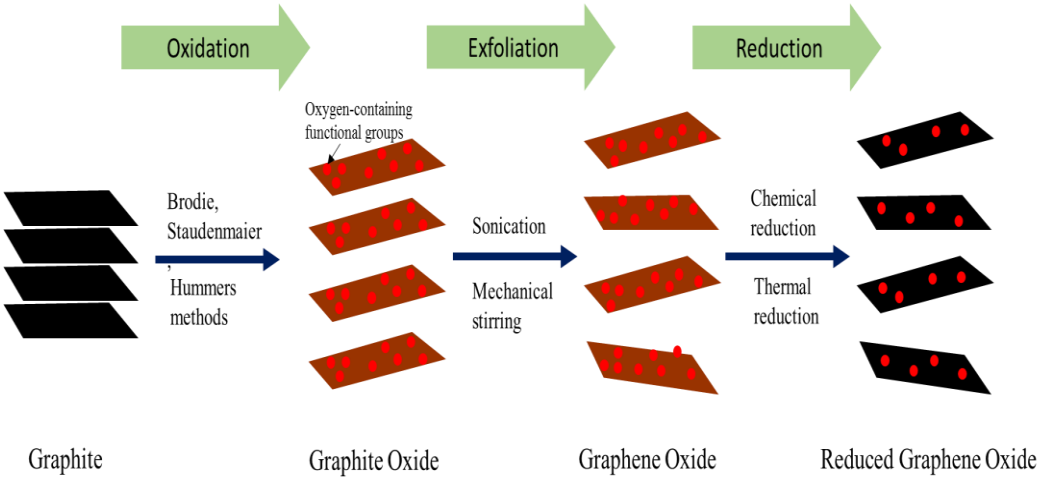

Fig. 2.1: Typical processes in synthesis of GO and rGO from pristine graphite.

A number of synthesis routes of GO have been developed between the years 1859 and 1958, and these included Brodie method (Brodie, 1859), Staudenmaier method (Staudenmaier, 1898), Hoffmann method (Hofmann & König, 1937) and Hummers method (Hummers & Offeman, 1958) as well as their modified and improved versions (Fig. 2.2). The major issues with Brodie method were its long reaction time which ranged from 72 to 96 h, and the release of toxic gaseous by-products. Staudenmaier improved the Brodie method by increasing the acidity level of the reaction using concentrated sulphuric acid (H_2SO_4) which resulted in a single reaction vessel system. Nonetheless, Staudenmaier method was also time consuming and produced explosive chlorine dioxide. Over the years, Hoffmann reduced the risk level of the synthesis process by using non-fuming nitric acid (HNO_3).

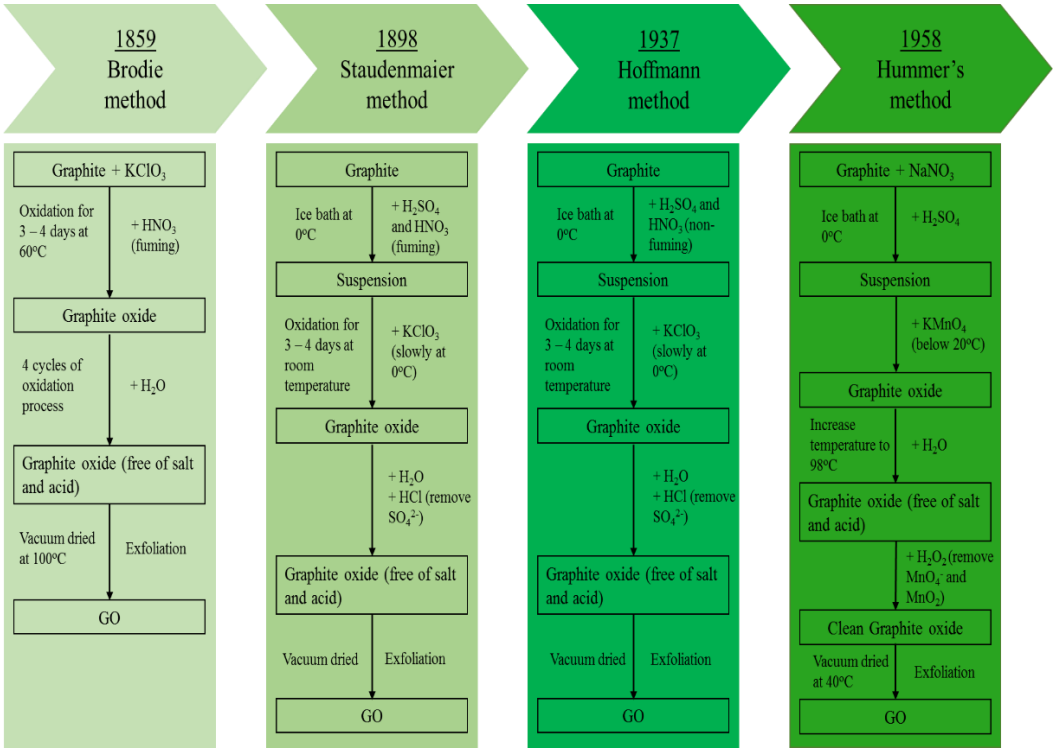

Fig. 2.2: General graphite oxide synthesis routes.

In 1958, an alternative approach was introduced by Hummers and Offeman for the oxidation of graphite which is known widely as Hummers method (Hummers & Offeman, 1958). This method involved reacting graphite oxide with acids (HNO_3 and H_2SO_4), followed by intercalating with alkali metals ($KClO_3$, $KMnO_4$ and $NaNO_3$) into the graphitic layers in graphite, dissembling of the graphitic layer into smaller pieces (Singh et al., 2016). The intercalation of oxygen-containing functional groups could increase the lattice distance of the graphite from 0.34 to 0.8 – 1.0 nm (Peng et al., 2016a). The increase in interlayer distance in graphite oxide could be beneficial for exfoliation of graphite oxide to obtain GO through sonication or mechanical stirring due to the weakening of van der Waals forces between the adjacent graphitic layers (Cai & Song, 2007; Zhu et al., 2010). Hummers and its modified methods are the most preferred approaches for the synthesis of GO nowadays (Wu et al., 2016; Zhao et al., 2015b).

2.3 Synthesis of 3D graphene-based structures

Generally, 3D graphene structures are graphene sheets assembled on top of each other to form a three-dimensional macro-size shape (Bianco et al., 2013). In literature, many terminologies have been used to describe the 3D graphene-based structures such as foam, network, hydrogel, aerogel, monolith, bead and sponge (Adhikari et al., 2012; Branca et al., 2015; Chen et al., 2017b; Zhang et al., 2014c; Zhuang et al., 2016).

The synthesis methods of the 3D configurations can be largely classified into (1) direct synthesis from carbon sources and (2) solution-based synthesis. The overview on the synthesis of 3D graphene-based structures is illustrated in Fig. 2.3. For each of the synthesis classes, two different approaches including template-assisted and template-free methods are available for fabrication of 3D graphene-based structures. The direct synthesis approach offers better control in pore size, pore density and pore size

distribution development in the 3D structures. However, it is associated with relatively high manufacturing cost.

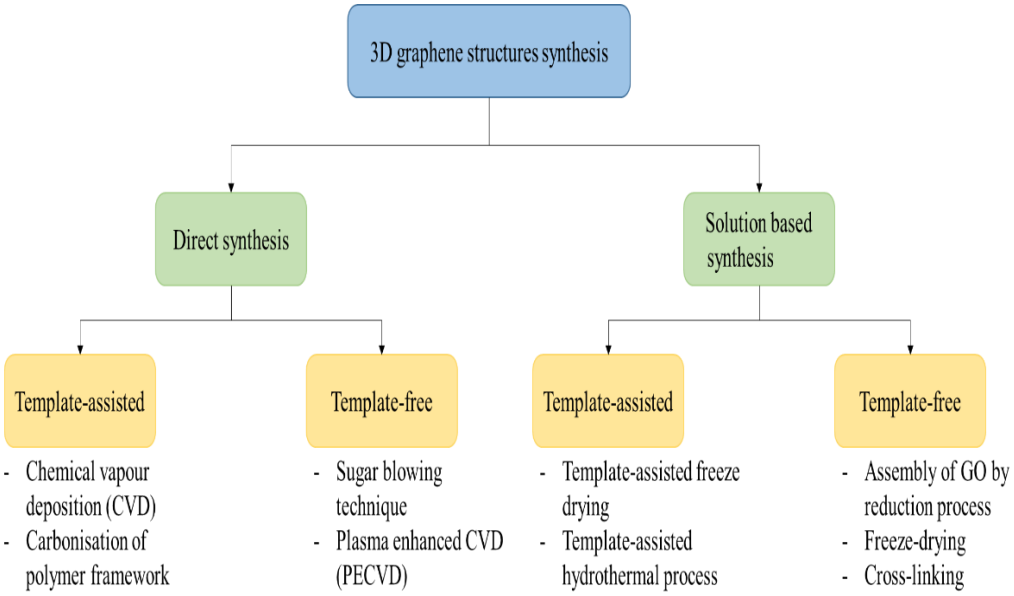

Fig. 2.3: Overview on 3D graphene-based structures synthesis.

In contrast, the solution-based synthesis method provides benefits such as elemental functionalisation, potential scalability, higher production yield and lower production cost albeit the random distribution of pore structure. In the following sections, the solution-based synthesis approaches will be reviewed.

2.3.1 Template-assisted freeze drying

Template-assisted freeze drying or ice-template is the process which utilises the rapid freezing of aqueous dispersion containing amphiphilic polymers to construct a porous 3D structure. This process is also termed as the ice-segregation-induced-self-assembly (ISISA) (Shehzad et al., 2016). GO was first incorporated into the aqueous media either with or without additional chemical binders before freeze drying (He et al., 2013b; Hong et al., 2015; Jayanthi et al., 2016; Li et al., 2015; Ma et al., 2016). In this process,

the formation of ice crystals provided the structural support for the 3D graphene structure, and the morphological properties and porosity of the structure were dependent on the freezing temperature and temperature gradient (Abarrategi et al., 2008; He et al., 2013b). During freeze drying, the GO sheets were ejected and entrapped between the neighbouring ice crystals, yielding highly oriented inter-connected GO-composite layers that formed a solid 3D graphene-based structure (Shehzad et al., 2016). However, the pore structure of the graphene configuration fabricated by ISISA was inconsistent throughout the structure which was attributed to the local differences in freezing time and the temperature gradient applied onto the template during the synthesis process.

In literature, many chemical additives were used to fabricate 3D graphene-based structures by ISISA, and these included chitosan (He et al., 2011; Yu et al., 2013), polyvinyl alcohol (PVA) (Dai et al., 2016; Fu et al., 2017; Tan et al., 2016), carboxylmethyl cellulose (Liu et al., 2016b; Zhang et al., 2014c) and gum (Sahraei & Ghaemy, 2017; Yu et al., 2015). Typically, the process involved mixing of GO suspension with the chemical additive solution. The homogeneous mixture of GO-composite solution was frozen overnight prior to freeze drying or drying by super critical CO_2 to form 3D graphene aerogel. For instance, Liu et al. (2017b) have successfully demonstrated the green development of xanthan gum-GO hybrid aerogel by mixing 5 mL GO dispersion (0.002 g/mL) with 5 mL of xanthan gum solution (0.01 g/mL). The resultant mixture was subjected to freezing at −40 °C for 1 h before freeze drying for 8 h as illustrated in Fig. 2.4 (Liu et al., 2017b). From their findings, the freezing temperature played an important role in the formation of porous structure. The aerogel which was frozen at lower temperature (~40 °C) displayed an oriented hierarchical thin sheet structure and the formation of networks connecting the co-

aligned and pores channel was also observed. Conversely, for the sample which was frozen at higher temperature (~10 °C), the thickness of the GO composite sheets increased and the aerogel had a disoriented structure. The orientation of the aerogel also affected the adsorption performance as the reported adsorption efficiency for rhodamine B and methylene blue dyes of the aerogel frozen at −40 °C were higher than that at −10 °C. The volume per unit mass of the developed aerogel was reported to range from 52.7 to 63.2 cm^3/g, indicating the xanthan gum /GO aerogel had a tunable porosity (Liu et al., 2017b). The ISISA or template-assisted freeze drying is one of the most commonly used techniques for synthesis of 3D graphene structure as the process has relatively straightforward steps.

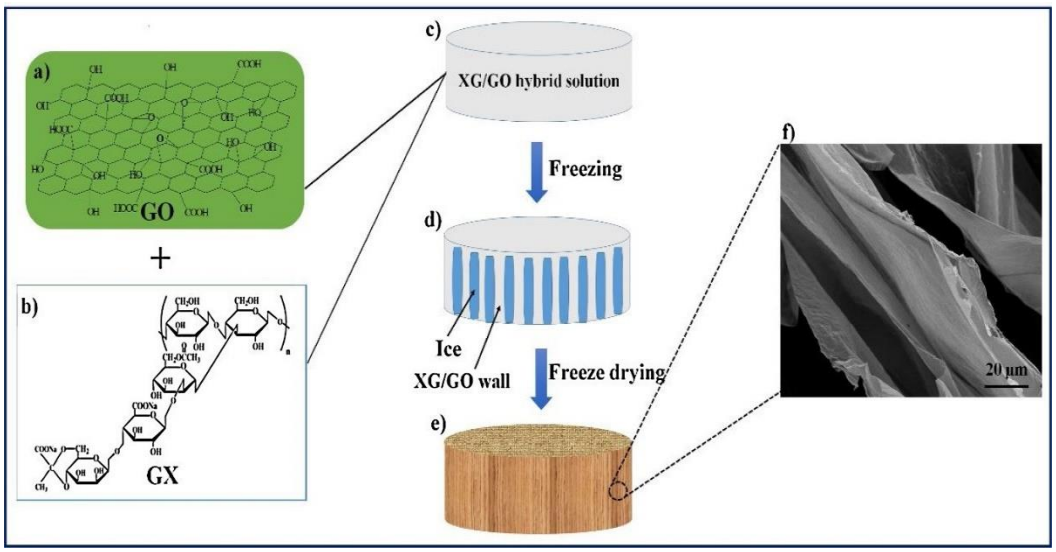

Fig. 2.4: Green synthesis of xanthan gum/GO hybrid aerogel (Liu et al., 2017b).

2.3.2 Template-assisted hydrothermal process

Template-assisted hydrothermal synthesis involves the use of porous foam-like template and the 3D graphene structure is obtained through hydrothermal process (Yin et al., 2014). The foam template used can be either metallic or polymeric foam. In the fabrication process, the templates were soaked in GO dispersion and the soaked

template was subjected to hydrothermal process for deposition of GO sheets on the template wall. After chemically reducing the GO, the template skeleton was removed to obtain the graphene-based structure. Typically, the removal of metallic template was achieved by chemical etching whereas polymeric template was eliminated by solvent dissolution or thermal decomposition. In this synthesis method, the quality of 3D graphene foam is poorer than that fabricated by chemical vapour deposition (CVD) due to stacking of multi-layered GO sheets. Furthermore, this method is associated with higher manufacturing cost due to the sacrifice of the template support at the end of the process, and the higher difficulty in controlling the morphological properties of the final product. Yin et al. (2014) has developed a rGO/ZnO foam by immersing nickel foam into GO suspension before transferring into autoclave for hydrothermal treatment at 90 °C for 16 h. The rGO foam was then etched with 2 M HCl and dialysed with deionised water to remove excess acid residue and metal ions. The ZnO nanorods was then deposited on the rGO foam by contacting the rGO foam with aqueous solution containing 25 mM zinc nitrate hydrate and 25 mM hexamethyleneteramine (HMTA) at 90 °C for 6 h. It was reported that the rGO/ZnO foam was densely packed with ZnO nanorods with diameters between 40 and 60 nm and lengths within 1–2 μm. Several works on synthesis of 3D graphene structures by this method have been reported in literature (Ghosh & Das, 2015; Huang et al., 2012; Xie & Zhan, 2015).

2.3.3 Assembly of GO by reduction process

The assembly of 2D GO sheets into 3D graphene-based structures is initiated from dispersion of GO in aqueous media. Due to strong electrostatic repulsion force in GO dispersion, the 2D GO sheets form a stable colloidal system hindering the self-assembly of GO into 3D structure. Several methods have been proposed to overcome this problem,

and one of them is the reduction of GO either by chemical or thermal treatment (He et al., 2013a; Yang et al., 2013). In-situ reduction of GO by chemical additives is a potential approach for fabrication of 3D graphene structure. The mechanism for chemical reduction of GO is governed by sol-gel chemistry. The process involved elimination of the oxygenated functional groups from the GO, triggering gelation of the GO sheets into a 3D form known as rGO hydrogel. A large variety of reducing agents have been tested and these include acids (Wang et al., 2017a; Zhang et al., 2010), hydrazine (Gao et al., 2010; Park et al., 2011), metal or metal oxides (Chua & Pumera, 2014; Pei & Cheng, 2012), reducing salts (Bo et al., 2014) and plant extracts (Firdhouse & Lalitha, 2014; Lee & Kim, 2014). In typical chemical reduction process, the reducing agent was introduced to the GO dispersion and subsequently heated to complete the reduction process. During reduction, the reaction vessel was left to stand without stirring to enable stacking of graphene layers in an orderly arrangement. The properties of the developed 3D graphene structure were dependent on the type of reducing agent used. It was reported that mild reducing agent such as L-ascorbic acid, could assist in the construction of more uniform and stable graphene structure in water (Abdolhosseinzadeh et al., 2015; De Silva et al., 2017; Zhang et al., 2010). The stability of the rGO hydrogel could be attributed to the formation of hydrogen bonds between the oxidised ascorbic acid and residual oxygen functional groups, as well as the disruption of π-π stacking between the rGO hydrogel which prevented agglomeration (De Silva et al., 2017). Recently, green reducing agents such as plant extracts (tea leaves, spinach leaves and Roselle flower) were investigated as alternative reagents for GO reduction. It was reported that the plant extracts could effectively reduce GO (Chu et al., 2014; Suresh et al., 2015; Wang et al., 2011).

Hydrothermal reduction process is commonly used to reduce GO to initiate the self-assembly of GO under high temperature and pressure environment. In this method, a fixed concentration of GO dispersion was heated in a Teflon-lined hydrothermal reactor to form the hydrogel. During hydrothermal process, the reduction of GO was achieved through elimination of carboxylic groups which significantly reduced the electrostatic repulsion in the GO dispersion. This phenomena triggered the self-assembly of graphene-based hydrogel through the π-π deposition of GO sheets at the graphene basal planar (Shehzad et al., 2016). The feasibility of adjusting the pores morphology of hydrogel through hydrothermal process was demonstrated by altering GO concentration, hydrothermal reaction time or addition of metallic catalyst (Zhu et al., 2016). The hydrothermal reduction also offers a possibility for elemental functionalisation onto the graphene lattice through doping. Du et al. (2014) have successfully synthesised nitrogen-doped rGO structures for high performance lithium ion battery anode by hydrothermal process. In their work, the nitrogen-doped rGO was formed by hydrothermal treatment of a mixture of melamine and GO suspension in a Teflon-lined autoclave at 180 °C for 6 h (Du et al., 2014). From their work, the nitrogen-doped rGO exhibited Type IV adsorption isotherm indicating the existence of mesopores within the structure with a Brunauer-Emmett-Teller (BET) specific surface area of 146 m^2/g. In addition, the hydrothermal process can be extended to solvothermal process by replacing the water with organic solvents (Dubin et al., 2010; Liu et al., 2016e; Wang et al., 2009). This method enables the use of chemicals which are soluble in organic solvents for functionalisation of the 3D graphene structures.

2.3.4 Freeze drying

Freeze drying is commonly practised to eliminate the water molecules trapped inside the structure of rGO hydrogel to produce an orderly configured aerogel (He et al., 2016;

Worsley et al., 2012; Wu et al., 2012). The preparation of rGO aerogel from GO sheets involved three key steps as illustrated in Fig. 2.5. Generally, the GO sheets are transformed into rGO hydrogel through reduction process, followed by freezing of the hydrogel to crystallise the water molecules. The water crystals act as the pore forming agent. Finally, the solidified water molecules are sublimated under vacuum condition to form a 3D porous rGO aerogel.

The porous microstructure of the 3D graphene-based aerogel is highly dependent on the nature of hydrogel, freezing conditions and temperature gradient. Zhang et al. (2011c) have prepared a mechanically strong and highly conductive graphene-based aerogel for electrochemical application. The 3D graphene aerogel was produced by adding L-ascorbic acid into aqueous GO suspension. Upon stirring and heating, the mixture was allowed to stand for at least 16 h for construction of rGO hydrogel. The hydrogel was then purified and subjected to freezing and freeze drying to form the graphene-based aerogel. In their research, Zhang et al. (2011c) investigated two types of sublimation system which included freeze drying and super-critical CO_2 drying. They reported that the graphene aerogel made by super-critical CO_2 drying exhibited remarkable mechanical properties as it could withstand 14000 times its own weight than that prepared by freeze drying (3300 times its own weight). The aerogel prepared by super-critical CO_2 showed a BET surface of 512 m^2/g which was higher than that of aerogel prepared by freeze drying (11.8 m^2/g) (Zhang et al., 2011c). Wan et al. (2016) have also investigated the influence of reducing agents (vitamin C (VC), ethanediamine (EDA) and ammonia) on the formation of graphene aerogel by hydrothermal technique. The specific surface areas for graphene aerogels reduced by VC, EDA and ammonia were reported to be 661, 440 and 1089 m^2/g, respectively (Wan et al., 2016). However, the highest mechanical strength was demonstrated by the VC-

reduced graphene aerogel. The researchers further reported that the surface roughness could be governed by the pH values which were determined by the functional groups of reducing agents. The pH of the mixed solutions of VC-GO, EDA-GO and ammonia-GO before hydrothermal reduction were 3.4, 11 and 10.4, respectively. The acidic condition promoted agglomeration and fragmentation of graphene sheets during reduction process whereas the basic condition favoured the production of larger graphene sheets with thin morphology (Fan et al., 2008; Wan et al., 2016; Xu et al., 2015).

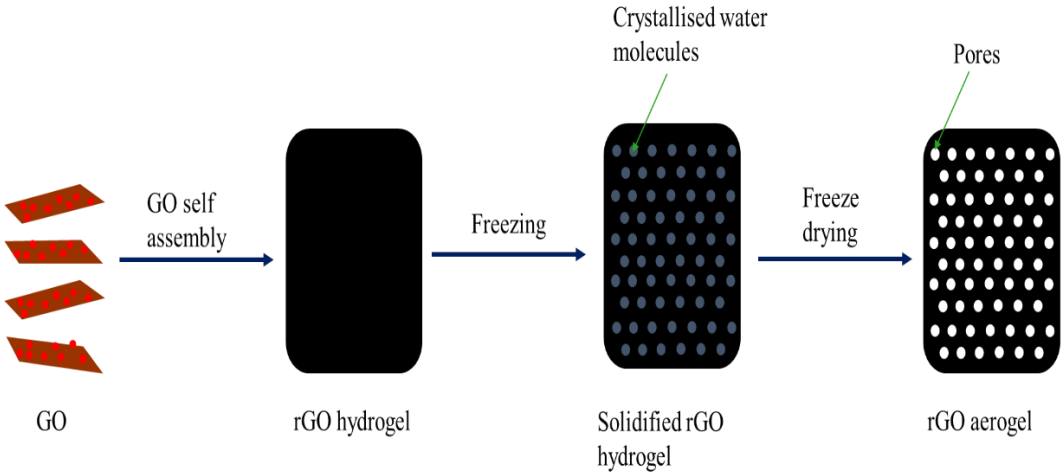

Fig. 2.5: Synthesis of rGO aerogel by freeze drying.

2.3.5 Cross-linking assembly

Cross-linking induced assembly is based on the addition of different chemicals to promote gelation of the GO dispersion, construction and strengthening of the 3D structures through chemical or physical cross-linking. In this approach, the chemical additives act as pore forming agent and introduce new functional groups to the 3D graphene structure.

The first cross-linking agent reported in literature was polyvinyl alcohol (PVA) by Bai et al. (2010). It was found that the gelation between GO and PVA was governed

by hydrogen bonding between the functional groups (hydroxyl, epoxy and carboxyl groups) on the GO surface and the hydroxyl-rich PVA chains. One notable finding from their work was that gelation of GO-PVA hydrogel was a reversible process made possible by tuning the pH of the system. In their research, the hydrogel was formed at pH < 7, but remained in aqueous form at pH > 7. This sol-gel transition of GO-PVA hydrogel occurred due to insufficient binding force between the molecules under high pH condition. The hydrogel produced under acidic condition was found to be much stronger than that prepared under elevated pH condition. This was attributed to reduction of GO sheets through acidification which facilitated the π-π stacking of graphene sheets (Bai et al., 2010). The development of GO-PVA hydrogel was also reported by other researchers for applications such as adsorbent, material reinforcement and wound dressing (Fan et al., 2016; Huang et al., 2014; Li et al., 2014a; Zhang et al., 2011a).

Apart from PVA, various chemicals were reported to be effective cross-linkers for the construction of 3D graphene-based structures such as polymers (poly(N-isopropylacrylamide), polypyrrole and polyaniline), polysaccharide-based materials (chitosan, sodium alginate, carboxylmethyl cellulose and cyclodextrin), bivalent and trivalent metal ions (Ni^{2+}, Mg^{2+} and Fe^{3+}) (Bai et al., 2011; Chen et al., 2017a; Chen et al., 2013b; Khodaverdi et al., 2014; Li et al., 2013b; Lin et al., 2016; Luan et al., 2015; Moussa et al., 2015; Park et al., 2008; Zhang et al., 2014a; Zhao et al., 2015a). The type of cross-linking mechanisms formed between the GO and cross-linker depends on the cross-linking chemical used (Sui et al., 2013). For example, the cross-linking mechanism between chitosan and GO was reported to be nucleophilic addition mechanism as the epoxy groups in GO were cross-linked with the amino groups of chitosan (Han et al., 2011; Shao et al., 2013). Huang et al. (2015b) hypothesised that

the GO sheets and polyethyleneimine (PEI) film were cross-linked through electrostatic interaction and covalent bonding between the epoxy groups of GO and the primary amine groups of PEI. The cross-linked GO-PEI film was more mechanically stable in water as no brownish yellow colouration leached out from the film after 6 h of oscillation at 120 rpm (Huang et al., 2015b).

Additionally, cross-linking assembly offers the flexibility in making different 3D graphene structures such as beads. The development of 3D graphene beads has received worldwide attention as an alternative practical structure for fixed bed packing and drug carriers (Bao et al., 2016; Ouyang et al., 2015; Platero et al., 2017; Rasoulzadeh & Namazi, 2017). Generally, the GO beads were synthesised by injecting droplets of GO dispersion and chemical additives (such as chitosan, sodium alginate or carboxylmethyl cellulose) mixture into a cross-linking agent (such as CaCl2, NaOH, boric acid or cetyltrimethylammonium bromide). The formed beads were then washed to remove excess cross-linker molecules. Sahraei et al. (2017) developed a novel magnetic PVA-modified gum tragacanth-GO hydrogel beads for the removal of heavy metals (lead and copper) and dyes (crystal violet and congo red). The Fe^{3+} functionalised beads displayed high regeneration efficiency, bio-compatibility and chemical stability. Additionally, they could be easily separated from the liquid phase. The functionalisation of beads with Fe^{3+} introduced magnetism property and additional chemical functional groups to the beads, and these features assisted in the solid-liquid separation as well as enhanced the removal of pollutants through electrostatic interactions between the adsorbent and adsorbates. The magnetic beads of spherical shape reportedly had an average diameter of 3.0 mm, a specific surface area of 283.84 m^2/g and an average pore diameter of 0.42767 nm (Sahraei et al., 2017).

2.4 Adsorption performance of 3D graphene structures

2.4.1 Pharmaceutical adsorbates

2.4.1.1 Characteristics and classification of pharmaceuticals

Pharmaceutical residues are emerging anthropogenic pollutants which contain different groups of biological active compounds. The extensive application of pharmaceuticals in disease control and personal care products, coupled with poor removal efficiency by conventional wastewater treatment plant have caused significant amount of the compounds to be released into the environment. The escaped pharmaceuticals entered the surface water or ground water around the industrial and residential area directly (Kyzas et al., 2015a). Despite the presence of very low concentration in the environment, pharmaceutical compounds can pose potential long term risk for the aquatic and terrestrial organisms due to their bioaccumulation and resistance to biodegradation (Al-Khateeb et al., 2014). The classification of pharmaceuticals is based on their respective therapeutic functions (Daughton & Ternes, 1999). The classes and main properties of pharmaceuticals are summarised in Table 2.2. The pharmaceutical residues frequently found in wastewater include antibiotics, anticonvulsants, antidepressants, antineoplastic, beta blocker, hormones (steroids), lipid regulator and nonsteroidal anti-inflammatory drugs (NSAIDs).

Antibiotics are commonly used to protect humans and animals against diseases and infection caused by bacteria (Yang et al., 2017b). The most important antibiotics are tetracyclines, penicillins, sulfonamides, macrolides, and quinolones. Prolong presence of the antibiotics in aquatic systems can lead to the growth of drug resistant bacteria which are harmful to the environment (Acosta et al., 2016). Analgesics and non-steroidal anti-inflammatory drugs (NSAIDs) are utilised to relieve pain and impede inflammation. The most known analgesics are acetaminophen and aspirin (Feng et al.,

2013). Ibuprofen, ketoprofen, diclofenac and naproxen are examples of NSAIDs are hazardous contaminants because of their high resistance to degradation and tendency to accumulate in sediment of the aquatic system (Tiwari et al., 2017). Hormones are important pharmaceuticals due to their extensive applications in human and veterinary medicines. Estrogens, such as estriol, are common natural hormone, whereas 17α-ethynylestradiol is a synthetic hormone (Li et al., 2014b; Yang et al., 2017b). Estrogens have been identifed as abundant micropollutants and their presence in wastewater poses significant hazard to the ecosystem. β-blockers, such as metoprolol, propranolol and atenolol, are extensively utilised pharmaceuticals for the treatment of cardiovascular diseases, such as angina and hypertension. Metoprolol is a widely consumed β-blocker, and it metabolises in human body to produce metoprolol acid and other derivatives which comprise nearly 85 % of the urinary content (Evgenidou et al., 2015). Lipid regulators represent important pharmaceuticals which impede cardiovascular disease progression and reduce cholesterol concentration to prevent heart diseases. These drugs contain mainly statins and fibrates. The first group of lipid regulators is rarely present in the environment as metabolites are the main source of statins (Gracia-Lor et al., 2012). By contrast, the second group decreases the amount of cholesterol by impeding lipoprotein formation. Clofibric acid and its derivatives are among the fibrates most frequently detected in waters (Patrolecco et al., 2013).

Table 2.2: Classification and main properties of pharmaceuticals (Wang & Wang, 2016).

Classification	**Functions**	**Examples**	**Molecular weight (g/mol)**	pK_a
Antibiotics	Eliminate bacteria	Sulfamethoxazole	253.3	5.70
		Trimethoprim	290.3	7.12
		Ofloxacin	261.4	5.97
		Ciprofloxacin	331.3	6.09
		Sulfadiazine	250.3	6.36
		Tetracycline	444.4	3.30
		Oxytetracycline	460.4	3.27
Anticonvulsants	Mood stabiliser and treat mood	Carbamazepine	236.3	2.30
	disorder	Primidone	218.3	-
		Mephobarbital	246.3	7.80
Antidepressants	Corrects chemical imbalances of	Diazepam	284.7	3.40
	neurotransmitter in brain and treat	Doxepin	279.4	-
	depression	Oxazepam	286.7	10.9
Antineoplastic	Control or kill neoplastic cells	Epirubicin	543.5	9.17
		Methotrexate	454.4	4.70
		Tamoxifen	371.5	8.87
Beta (β) blocker	Inhibits hormone adrenaline and the	Atenolol	266.3	9.60
	neurotransmitter noradrenalin	Metoprolol	267.4	9.60
		Propranolol	259.3	9.42
		Sotalol	272.4	-
Diagnostic	Enhancement of vascular on magnetic	Iopromide	791.1	-
contrast media	resonance (MR)	Iomeprol	777.1	-
		Diatrizoate acid	613.9	1.13
Hormones	Regulate rate of metabolism, control of	Estrone	270.4	10.91
	sexual development, keep homeostasis	Testosterone	288.2	19.09

		17-β Estradiol	272.4	10.08
Lipid regulators	Regulate triglycerides and cholesterol	Clorfibric acid	214.6	3.15
	in blood	Gemfibrozil	250.3	4.50
		Clofibrate	242.7	-4.90
Nonsteroidal	Reduce pain and inflammation	Diclofenac	296.1	4.15
anti-inflammatory		Naproxen	230.3	4.15
drugs (NSAIDs)		Ibuprofen	206.3	4.91
		Ketoprofen	254.3	4.45
		Salicylic acid	138.1	2.97
		Paracetamol	151.2	9.38

In general, pharmaceutical residues entered the aquatic environment through discharge from pharmaceutical industries, livestock activities, hospital effluent and municipal treatment plant effluent (Kyzas et al., 2015a). Conventional treatment processes for pharmaceutical residues include activated sludge treatment, photocatalytic oxidation, catalytic ozonation and membrane bioreactor (Al-Khateeb et al., 2014). These technologies however are ineffective due to the pharmaceuticals having high resistance to biodegradation and ability to retain their chemical structures after treatment processes (Santos et al., 2007). Adsorption technique is the most effective method for the removal of pharmaceuticals due to its simple operation, cost effectiveness and feasibility in regeneration. Furthermore, one of the most frequently detected pharmaceutical groups in the aquatic environment was the NSAIDs (Sun et al., 2015). Hence, acetaminophen and diclofenac were selected as the target pollutants in this research.

2.4.1.2 Adsorption of pharmaceuticals onto GO and 3D graphene structures

Various studies have indicated that GO and its derivatives are effective adsorbents for sequestrating pharmaceuticals in aqueous media. Table 2.3 summarises the maximum

adsorption capacities of different pharmaceuticals on GO and the 3D graphene-based structures. The tabulated data showed that several adsorption mechanisms were involved in the pharmaceuticals uptake, with the main mechanisms being hydrogen bonding, π-π, hydrophobic and electrostatic interactions (Fei et al., 2016; Liu et al., 2014b; Liu et al., 2016a; Wang et al., 2017b). As observed in Table 2.3, the adsorption equilibrium and kinetic of the different pharmaceuticals onto GO and its 3D derivatives were well correlated mostly to the Langmuir and pseudo-second-order kinetic models. The adsorption of pharmaceutical residues such as antibiotics and nonsteroidal anti-inflammatory drugs (NSAIDs) using GO and its 3D structures have been investigated by other researchers. Nevertheless, there are limited reports on the adsorption of antidepressants, anticonvulsants, antineoplastic and diagnostic contrast media onto GO and its 3D derivatives to date.

Table 2.3: Adsorption capacity and mechanism of pharmaceuticals onto GO and 3D graphene-based structures.

Adsorbate	Adsorbent	C_o (mg/L)	T (°C)	m (mg)	pH	t (min)	q_m (mg/g)	Isotherm model	Kinetic model	Mechanism	Reference
Antibiotics											
Sulfamethoxazole	3D cellulose nanofibril/GO hybrid aerogel	20-160	25-45	0.25-2 .0 g/L	2-12	0-180	302.7	Langmuir	Pseudo-second-order	Electrostatic attraction, p-π, π-π interactions, hydrogen bonding, physical adsorption	(Yao et al., 2017)
	GO nanosheets	-	25-45	10	3-11	0-240	122	Redlich-Peterson and Koble-Corrigan	Pseudo-second-order	π-π interaction, electrostatic interaction	(Rostamian & Behnejad, 2016)
Tetracycline	Magnetic GO sponge	50-1000	0-55	5	2-12	60-2880	473	Langmuir	Pseudo-second-order	π-π interaction, hydrogen bonding, electrostatic interaction	(Yu et al., 2017)
	GO	8.33-333.33	4-45	-	3-11	15-150	313.5	Langmuir	Pseudo-second-order	π-π interaction, cation-π bonding, electrostatic interaction	(Gao et al., 2012)
	Magnetic GO doped with strontium titanium trioxide nanoparticle	10-100	20-40	5-100	2-10	1-180	65.78	Langmuir	Pseudo-second-order	Electrostatic and π-π interaction, hydrogen bonding	(Rashidi Nodeh & Sereshti, 2016)
Ofloxacin	3D graphene hydrogel	100	25	-	7	0-1400	134	-	Pseudo-second-order	π-π interaction, hydrogen bonding and hydrophobic interaction	(Ehtesabi et al., 2019)
Ciprofloxacin	Sodium alginate/GO hydrogel beads	10-150	25	20	2-12	0-170 hours	86.12	Langmuir	Pseudo-second-order	π-π interaction	(Fei et al., 2016)
	GO/calcium alginate bio-	-	RTP	0.25-2.0 g/L	3-9.3	0-1440	66.25	Langmuir	Pseudo-second-order	Ionic exchange, surface complexation,	(Wu et al., 2013)

	composite fibres									electrostatic interaction	
	Long TiO_2 nanotube/GO hydrogel	1-200	25	10	7	1440	181.8	Langmuir	-	π-π interaction, hydrogen bonding and electron transfer	(Zhuang et al., 2015)
Doxycycline	Graphene hydrogel GO/cellulose nanofibril hybrid aerogel	-	25	8	-	-	469.7	Langmuir	Pseudo-second-order	π-π interaction, hydrogen bonding, electrostatic interaction	(Wang et al., 2017c)
Anticonvulsants									Pseudo-second-order		
Carbamazepine	rGO	6-100	25	-	2-12	7 day	115	Dubinin-Ashtakhov	Pseudo-second-order	Hydrogen bonding, electrostatic interaction, π-π interaction	(Liu et al., 2014b)
	GO-C	5-220	RTP	0.5-2.0 g/L	3-11	0-1440	110	Freundlich	Pseudo-second-order	π-π interaction, electrostatic interaction	(Cai & Larese-Casanova, 2014)
Beta blocker									Pseudo-second-order		
Atenolol	GO	10-150	25-65	10	2-10	0-1440	116	Langmuir	Pseudo-second-order	Electrostatic and π-π interaction, hydrogen bonding	(Kyzas et al., 2015b)
Propranolol	GO	10-150	25-65	10	2-10	0-1440	67	Langmuir	Pseudo-second-order	Electrostatic and π-π interaction, hydrogen bonding	(Kyzas et al., 2015b)
Dorzolamide	GO and acrylic acid grafted chitosan	0-500	25-65	20	3-9	0-1440	334	Langmuir-Freundlich	Pseudo-second-order	Electrostatic and polar interaction, hydrogen bonding, Lewis acid-base, amide formation	(Kyzas et al., 2014)

Hormones											
17-β Estradiol	Few-layered GO nanosheets	1-16	25-65	3	3-12	15-720	149.4	Langmuir	Pseudo-second-order	Hydrogen bonding, π-π interaction	(Jiang et al., 2016)
	β-cyclodextrin/ poly (l-glutamic acid) supported magnetic GO	-	25-50	5	4.2-10.1	0-1440	85.80	Langmuir	Pseudo-second-order	Hydrogen bonding, π-π interaction, hydrophobic effect, electrostatic interaction	(Jiang et al., 2017)
	Superparamagnetic amino-functionalised GO nanocomposite*	1-10	-	0.5 g/L	3-11	20-720	106.38	Langmuir	Pseudo-second-order	Hydrogen bonding, π-π interaction, electrostatic interaction	(Bai et al., 2017)
Lipid regulators									Pseudo-second-order		
Clorfibric acid	GO	1-2000	25	5	3-11	5-120	994	Langmuir	Pseudo-second-order	Hydrogen bonding, π-π interaction, electrostatic interaction	(Zhang et al., 2014b)
NSAIDs									Pseudo-second-order		
Diclofenac	GO	10-100	20	0.1 g/L	3-11	0-1440	500	Langmuir	Pseudo-second-order	Hydrophobic, π-π interaction, electrostatic interaction	(Nam et al., 2015)
	rGO	20-200	25	30	8-10	0-480	59.67	Liu*	Pseudo-second-order	π-π interaction, electrostatic interaction	(Jauris et al., 2016)
	High surface area graphene nanoplatelets	20	8-50	40	2-11	0-60	19.3**	-	Pseudo-second-order	π-π interaction, electrostatic interaction	(Al-Khateeb et al., 2017)
Naproxen	High surface area graphene nanoplatelets	20	8-50	40	2-11	0-60	17.8**	-	Pseudo-second-order	π-π interaction, electrostatic interaction	(Al-Khateeb et al., 2017)
	Self-assembled 3D rGO-based hydrogel	100-1000	2-10	40 - 60	2-8	10-100	357	Langmuir	Pseudo-second-order	π-π, π-n interaction, hydrogen bonding, n-	(Umbreen et al., 2018)

										hydrogen bonding, electrostatic forces and hydrophobic interactiion	
Paracetamol	Porous GO/ decafluorobiphenyl (DFB) composite	0.03.0.41 mmol/L	25	5	4-10	0-72 hours	350.6 µmol/g	Freundlich	Pseudo-second-order	π-π interaction, electrostatic interaction, hydrophobic interaction	(Shan et al., 2017)
Ketoprofen	rGO	6-100	25	-	2-12	7 day	62.5	Dubinin-Ashtakhov	-	Hydrogen bonding, electrostatic interaction, π-π interaction	(Liu et al., 2014b)
Ibuprofen	GO nanoplatelets	2-10	25-40	0.50 – 1.25 g/L	2-10	180	3.24	Langmuir	Pseudo-second-order	Electrostatic interaction	(Banerjee et al., 2016)
	Magnetic adsorbent genipin-crosslinked chitosan/GO-SO_3H (GC/MGO-SO_3H)	1- 10	25-40	0.005	2-12	180	160.83	Freundlich	Pseudo-second-order	Physical bond, electrostatic interaction	(Liu et al., 2019b)

Note: C_o is the initial concentration of adsorbate, *T* is the temperature, *m* is the adsorbent dosage, *t* is the contact time, q_m is the maximum adsorption capacity, *RTP* is the room temperature.

'–' denotes unavailable/not applicable

The morphological and internal properties of adsorbents contribute significantly to the pharmaceuticals adsorption as different chemical functional groups in the adsorbents can result in different adsorption mechanisms (Khan et al., 2017). This was evident from adsorption of tetracycline on magnetic GO sponge as reported by Yu et al. (2017). The developed magnetic GO sponge was able to achieve a maximum adsorption capacity of 473 mg/g, about 50 % greater than that of the GO material developed by Gao et al. (2012). The incorporation of Fe_3O_4 nanoparticles into the GO matrix introduced superparamagnetic property to the GO sponge enabling solid-liquid separation by magnetism. The magnetic GO sponge was prepared by lyophilising the mixture of GO and Fe_3O_4 nanoparticles through co-precipitation. According to Yu et al. (2017), the Fe_3O_4 nanoparticles were responsible for the increase in adsorption capacity of tetracycline as the nanoparticles prevented restacking of GO sheets during lyophilisation and adsorption process. The performance of the magnetic GO sponge was compared with other magnetic graphene derivatives (Lin et al., 2013; Rashidi Nodeh & Sereshti, 2016). It was found that the larger the Fe_3O_4 nanoparticle, the more Fe_3O_4 nanoparticles of the same size were required to avoid GO re-stacking during functionalisation. Yu et al. (2017) also compared the surface functionalities of their magnetic GO sponge (modified by citric acid) with GO-Fe_3O_4nanoparticles (modified by NH_2) prepared by Lin et al. (2013). The positively charged -NH_2 caused the Fe_3O_4 nanoparticles to be attached tightly to the existing oxygenated groups on the GO surface, hindering the formation of hydrogen bonds between the tetracycline and the sorption sites, and hence a reduction in adsorption capacity was observed. The drying method applied during the synthesis stage could also affect the adsorption performance of the GO composite. As a comparison, Lin et al. (2013) prepared a GO composite through hydrothermal process while Yu et al. (2017) utilised lyophilisation to prepare

a magnetic GO sponge. The hydrothermal process resulted in the reduction of GO which caused serious stacking of the GO sheets and subsequently lowered the adsorption capacity.

A 3D cellulose nanofiber (CNF)-GO hybrid aerogel developed by Yao et al. (2017) demonstrated a remarkably high adsorption capacity (302.7 mg/g) for sulfamethoxazole in comparison with other adsorbents such as GO nanosheets (122 mg/g) (Rostamian & Behnejad, 2016), functionalised multi-walled carbon nanotube (118.58 mg/g) (Song et al., 2016a) and activated carbon (42.5 mg/g) (Akhtar et al., 2011). The CNF-GO aerogel had a porous microstructure network of pore sizes varying from nano- to macro-scale, enhancing the adsorption capacity. The BET surface area and pore volume of the aerogel were 97.5 m^2/g and 0.4 cm^3/g, respectively. The BJH analysis suggested that the CNF-GO aerogel had uniformly distributed mesopores of 0.2 nm (Yao et al., 2017). These morphological properties indicated the CNF-GO aerogel possessed high surface area. The 3D aerogel also exhibited removal efficiency greater than 69 % for six different antibiotics. The adsorption efficiency of the antibiotics increased in the following order: quinolones (128.3 mg/g) < sulphonamides (227.3 mg/g) < β-lactams (230.7 mg/g) < macrolides (291.8 mg/g) < chloramphenicol (418.7 mg/g) < tetracyclines (454.6 mg/g) (Yao et al., 2017). Additionally, the CNF-GO matrix contained numerous hydroxyl groups which facilitated the pharmaceuticals uptake through hydrogen bonding. The π-π stacking of CNF-GO enabled π-π electron donor-acceptor (EDA) interaction to attract unsaturated double bond or conjugate structure of the antibiotics molecules (Yao et al., 2017).

2.4.2 Heavy metal ions

2.4.2.1 Characteristics of heavy metal ions

Heavy metals exist as natural constituents of the earth's crust which can be found in rocks and soils. They are generally referred to as any dense metal or metalloid with atomic weight of 63.5 – 200.6 Dalton and specific gravity greater than 5 g/mL (Järup, 2003; Vunain et al., 2016). Industrial activities such as smelting, mining, electroplating, painting processing and fertiliser manufacturer have resulted in severe heavy metal pollution in water resources (Vunain et al., 2016).

Toxic metals such as cadmium (Cd), lead (Pb), chromium (Cr), arsenic (As), nickel (Ni), manganese (Mn), zinc (Zn), tin (Sn), mercury (Hg)), copper (Cu) and iron (Fe) are often discharged from metal processing industries. These heavy metals can cause adverse health effects such as mutagenic, toxicity and carcinogenic to humans (Volesky & Holan, 1995; Wang & Chen, 2006). Due to its rarity in nature, precious metals have high commercial value and the recovery of these metals are the utmost priority before any removal treatment, and these precious metals include palladium (Pd), platinum (Pt), silver (Ag), gold (Au) and ruthenium (Ru) (Das, 2010). Uranium (U), thorium (Th), radium (Ra) and americium (Am) are some of the examples of radionuclides which can be presented in metal form, beta emitter and gross alpha particle which emit radiation. Radioactive effects from such metals are lethally dangerous and toxic to all life forms. Hence, there is a need to regulate the discharge of heavy metals by the industries.

To regulate the discharge of heavy metals, various discharge limits for different heavy metals have been formulated, such as the Malaysia effluent discharge standard (Standard A and B), China integrated wastewater discharge standards, USEPA maximum contaminant level and WHO guideline standard (Table 2.4). The discharge

standards varied according to governing bodies and geographical location of the industrial sites. For example, the maximum discharge of limits of copper in Malaysia are much lower (Standard A: 0.2 mg/L, Standard B: 1 mg/L) as compared to that of USEPA (1.3 mg/L) and WHO (2 mg/L). Nonetheless, these standards set a framework for the industry to install appropriate wastewater treatment systems to limit the discharge of heavy metals into the environment.

Table 2.4: Discharge limits and health hazards of heavy metals (Carolin et al., 2017; DOE, 1979; Drake & Hazelwood, 2005; MEP, 1998; USEPA, 2009; WHO, 2011).

Heavy metal	Health hazard	Threshold limit (mg/L)				
		Malaysia effluent discharge Standard A[(a)]	**Malaysia effluent discharge Standard B[(b)]**	**U.S. EPA Maximum Contaminant Level (MCL)**	**WHO Guideline Standard**	**China integrated wastewater discharge standard**
Cd	Renal failure, itai-itai disease, birth defects, anaemia, carcinogenic	0.01	0.02	0.005	0.003	0.1
Pb	Kidney failure, loss of voluntary muscle function	0.1	0.5	0.015	0.01[(P)]	1.
Cr (III)	Genotoxic, alopecia	0.2	1	-	-	1.5[(T)]
Cr (VI)	Genotoxic, alopecia	0.05	0.05	0.1[(T)]	0.05[(T)(P)]	0.5
As	Gastrointestinal symptoms, death, melanosis, hepatomegaly	0.05	0.1	0.01	0.01[(P)]	0.5
Ni	Anaphylaxis, lung cancer, red blood cells loss, nephrotoxic	0.2	1	-	0.07	1
Mn	Neurotoxic, sleep dysfunctions	0.2	1	0.05[(S)]	0.4[(H)]	-

Zn	Dizziness	1	1	5[(S)]	3[(N)]	-
Sn	Metabolism disruption, carcinogenic	0.2	1	-	-	-
Hg	Kidney disease, death, muscle movement impairment, gum inflammation	0.005	0.05	0.002	0.006	0.05
Cu	Liver and kidney disease, cancer, stomach irritation	0.2	1	1.3	2	-
Fe	Blood creatinine, kidney damage	1	5	0.3[(S)]	0.3[(N)]	-
Ag	Argyria, argyrosis, respiratory damage	-	-	0.1[(S)]	-	0.5
α photon emitter	Carcinogenic, genetic damage, infertility	-	-	15 pCi/L	0.5 Bq/L	1 Bq/L
β photon emitter	Carcinogenic, genetic damage, infertility	-	-	4 mrems/year	1.0 Bq/L	10 Bq/L
^{226}Ra	Carcinogenic, genetic damage, infertility	-	-	5 pCi/L[(R)]	1.0 Bq/L	-
^{228}Ra	Carcinogenic, genetic damage, infertility	-	-	-	0.1 Bq/L	-
U	Change in bone structure, carcinogenic, nephritis	-	-	0.03	0.03[(P)]	-

[a] = Effluent discharged of upstream water intake, [b] = downstream effluent discharge, [T] = Total chromium, [S] = Secondary MCL, [R] = Combined total of ^{226}Ra and ^{228}Ra, [P] = Provisional guideline, [H] = Health-based guideline, [N] = non-formal guideline, Bq = Becquerel, Ci = Curie, rems = Roentgen equivalent in mammals, U.S. EPA = United States Environmental Protection Agency, WHO = World Health Organization

2.4.2.2 Adsorption performance of heavy metals on GO and 3D graphene structures

GO and its derivatives have showed promising results as effective adsorbents for heavy metal removal. The maximum adsorption capacities of different heavy metals on GO and 3D graphene networks are summarised in Table 2.5. The uptake of the heavy metals varied with the GO composite type, pH condition, process temperature and concentration of the heavy metals. As evident from Table 2.5, the mechanisms of heavy metals adsorption onto GO and its 3D configurations were mainly surface complexation, ionic exchange and electrostatic interaction. Data modelling suggested that the adsorption systems generally involved monolayer deposition of the heavy metals on the adsorbents which were controlled by chemisorption, as proven from the best-fit of data to the Langmuir isotherm and pseudo-second-order kinetic model.

Generally, GO has a strong adsorption affinity towards various heavy metals due to the existence of reactive oxide functional groups such as hydroxyl and carboxyl groups. The affinities of GO for divalent metals such as Cu^{2+}, Zn^{2+}, Cd^{2+} and Pb^{2+} increased from $Zn^{2+} < Cd^{2+} < Cu^{2+} < Pb^{2+}$ (Sitko et al., 2013). The affinity order was in good agreement with the electronegativity and the stability constant of the resulted metal hydroxide (Dastgheib & Rockstraw, 2002; Peng et al., 2017b). The higher the electronegativity of the metal ions, the stronger the attraction force of the positively charged metal ions on the negatively charges GO surface. The standard reduction potential (electronegativity) for Pb^{2+}, Cu^{2+}, Cd^{2+} and Zn^{2+} were reported to be -0.1262, -0.3419, -0.4030 and -0.7618 V, respectively, which supported the above affinity sequence (Haynes & Handbook, 2010).

The formation of metal complexes through the surface complexation between the positively charged metal ions and the negatively charged functional groups on GO surface (e.g. -OH and -COOH) is one of the adsorption mechanisms, and the speciation

of heavy metal complexes is determined by the stability constant. The general equations of the formation of metal hydroxide and metal acetate are represented by Eqs. (2.1) and (2.2), respectively.

$$M^{n+} + OH^{-} \leftrightarrow M(OH)_n \quad (2.1)$$

$$M^{n+} + CH_3COOH^{-} \leftrightarrow M(CH_3COOH)_n \quad (2.2)$$

where *M* is the metal species, *n* is the valency of the metal ions

Table 2.5: Adsorption capacity and mechanism of different heavy metals on GO and 3D graphene structures.

Adsorbate	Adsorbent	C_o (mg/L)	T (°C)	m (mg)	pH	t (min)	q_m (mg/g)	Isotherm model	Kinetic model	Mechanism	Reference
As^{3+}	Iron oxide/GO nanocomposite	0.1-1200	23	2.4	2 - 10	15-1440	147	Langmuir	Pseudo-second-order	Complexation, electrostatic interaction	(Su et al., 2017)
	Magnetite-GO composite	-	25	3	4-10	0-1440	42.9	Langmuir	Pseudo-second-order	Complexation, electrostatic interaction	(Yoon et al., 2016)
	Magnetite-rGO composite	-	25	3	4-10	0-1440	29.8	Langmuir	Pseudo-second-order	Complexation, electrostatic interaction	(Yoon et al., 2016)
As^{5+}	Iron oxide/GO nanocomposite	0.1-1200	23	2.4	2 - 10	15-1440	113	Langmuir	Pseudo-second-order	Complexation, electrostatic interaction	(Su et al., 2017)
	3D Fe_3O_4/ graphene aerogels	0.5 - 30	25	2	7	720	40.05	Langmuir	Pseudo-second-order	-	(Ye et al., 2015)
	Magnetite GO encapsulated in alginate beads	10-200	20	5 g/L	3-10	0-1440	6.859	Langmuir	Pseudo-second-order	Electrostatic interaction, chemical interaction	(Vu et al., 2017)
Cd^{2+}	GO	-	-	10	2-8	0-120	30.8	Langmuir	Pseudo-second-order	Electrostatic interaction, ionic exchange	(Bian et al., 2015)
	3D sulfonated rGO aerogel	-	25	1	2-9	0 - 1440	234.8	Langmuir	Pseudo-second-order	Cation exchange, electrostatic interaction	(Wu et al., 2015)
	Modified gum tragacanth/	20 - 100	25	5-30	2-6	0-3600	112.5	Langmuir	Pseudo-second-order	Electrostatic interaction, chelation,	(Sahraei &

	GO composite hydrogel									ionic exchange	Ghaemy, 2017)
Cr^{6+}	Nanoscale zerovalent iron decorated graphene nanosheets (NZVI/GNS)	15-35	RTP	20	3 - 13	0 -180	21.72	Langmuir	Pseudo-first-order	Electrostatic interaction	(Zhu et al., 2016)
	3-aminopropyltriethoxysilane-functionalized GO (AS-GO)	50-200	10 - 55	20	2 - 8	5-480	215.2	Langmuir	Pseudo-second-order	Electrostatic interaction, hydrogen bonding, electron transfer, chelation	(Jiang et al., 2017)
	Magnetic cyclodextrin-chitosan/GO composite	5-50	30-50	100	1 -7	-	67.66	Langmuir	Pseudo-second-order	Electrostatic interaction, complexion, electron transfer, physisorption	(Li et al., 2013a)
	Magnetite GO encapsulated in alginate beads	10-200	20	5 g/L	3-10	0-1440	14.90	Langmuir	Pseudo-second-order	Electrostatic interaction, chemical interaction	(Vu et al., 2017)
	Poly(m-phenylenediamine) /rGO/nickel ferrite magnetic adsorbent	50-250	RTP	10	2-9	0-90	502.5	Langmuir	Pseudo-second-order	Electrostatic interaction, reduction of Cr^{6+} to Cr^{3+}	(Wang et al., 2017d)

	Amino functionalised GO decorated with Fe_3O_4 nanoparticle	-	25-45	0.2 g/L	1-8	0-300	123.4	Langmuir	Pseudo-second-order	Electrostatic interaction, chemical reduction by electron transfer	(Zhao et al., 2016)
	Multithiol functionalised graphene bio-sponge	10-110	21	1 g/L	4-9	0 – 300	102.99	Langmuir	Pseudo-second-order	Electrostatic interaction, electron sharing, hydrogen bonding, chelation and physical bond	(Yap et al., 2020)
Cu^{2+}	GO/chitosan aerogel	1.92 - 32	30	5	2-7	720	25.4	Langmuir	Pseudo-second-order	Physisorption,	(Yu et al., 2013)
	GO/zirconium phosphate (GO-Zr-P) nanocomposite	5-400	-	100	1-8	0-400	328.6	Freundlich	Pseudo-second-order	Chemical interaction, electrostatic interaction	(Pourbeyram, 2016)
	GO	-	25	2	2-8	0-120	294 mmol/g	Langmuir	Pseudo-second-order	Electrostatic interaction	(Sitko et al., 2013)
	Poly-allylamide hydrochloride/GO composite (PAH/GO)	10 - 210	20	10	1 - 6	0 - 350	349	Langmuir	Pseudo-second-order	Surface complexation, metal coordination, electrostatic interaction	(Xing et al., 2015)
	Amino-functionalised carbon nanotube-graphene	50-400	RTP	25	2-7	5-600	318.47	Langmuir	Pseudo-second-order	Complexation and chelation	(Zhan et al., 2019)

	hybrid aerogel										
Hg^{2+}	Magnetic polypyrrole-GO nanocomposite (PPy-GO)	20-100	27-47	0.01-0.09 g/L	2-10	20-720	400	Langmuir	Pseudo-second-order	Ionic exchange, hydrogen bonding, electrostatic contact	(Zhou et al., 2017a)
	Thymine-grafted rGO complexes	-	25-45	-	2-6	0-180	128	Langmuir	Pseudo-second-order	Coordination of -NH with Hg^{2+}, chelation.	(Liu et al., 2016d)
	GO foam	50 µg/L	21	1-20 mg/L	3-9	0-2880	35	Langmuir	Pseudo-second-order	Chemical interaction, ionic exchange	(Henriques et al., 2016)
	Graphene-diatom silica aerogel	50-400	21	10	2-10	0-90	>500	Langmuir	Pseudo-second-order	Physical trapping, electrostatic interaction, chemical bonding by functional group	(Kabiri et al., 2015)
Ni^{2+}	Porous GO/carboxymethyl cellulose/sawdust	40-300	20-50	100	7	1-60	-	Freundlich	Pseudo-second-order	Chelation	(Wu et al., 2014)
	Glycerine-functionalised GO	10-25	10-35	20	-	10-70	36.63	Langmuir	Pseudo-second-order	-	(Najafi et al., 2015)
	GO/cellulose membrane	1-20	25	-	1-8	15-180	14.3	Langmuir	Pseudo-second-order	Electrostatic interaction, chelation, complexation	(Sitko et al., 2016)
	Fe_3O_4/rGO nanocomposite	20-100	25	100	2.-7	0-240	76.34	Langmuir	Pseudo-second-order	Electrostatic interaction,	(Vuong Hoan et al., 2016)

										protonation and ionisation	
Pb^{2+}	Carboxymethyl cellulose sodium/GO hydrogel microparticles	100	20	30	2-12	0-240	19.19	Langmuir	Pseudo-second-order	Electrostatic interactions, surface complexation, ionic exchange	(Liu et al., 2016b)
	EDTA/GO	5-300	25	10-25	2-8.2	3-120	479	Langmuir	Pseudo-second-order	Electrostatic interaction, ionic exchange, surface complexation	(Madadrang et al., 2012)
	GO	10.37-259.25	30	-	5	5-180	766.8	Langmuir	Pseudo-second-order	Surface complexation	(Peng et al., 2016b)
	GO/zirconium phosphate (GO-Zr-P) nanocomposite	5-400	-	100	1-8	0-400	363.4	Freundlich	Pseudo-second-order	Chemical interaction, electrostatic interaction	(Pourbeyram, 2016)
	3D graphene/δ-MnO_2 aerogel	1-200	25	65	2-6	0-200	643.3	Langmuir	Pseudo-second-order	Ionic exchange, Interlayer trapping, complexation, interaction	(Liu et al., 2016b)
	GO-wrapped magnetic composite	50-400	30	-	2-7	0-1400	255.6	Langmuir	Pseudo-second-order	Chelation, electrostatic interaction, covalent bonding	(Vu et al., 2017)
U^{6+}	GO/amidoxime hydrogel	-	RTP	10	2-12	0-360	398.4	Langmuir	Pseudo-second-order	Chelation, hydrogen bonding,	(Wang et al., 2016)

									electrostatic interaction	
GO	0.04 - .6 mM	RTP	0.1 g/L	1-10	0-1440	299	Langmuir	Pseudo-second-order	Surface complexation, electrostatic interaction	(Li et al., 2012)
rGO	0.04 - .6 mM	RTP	0.1 g/L	1-10	0-1440	47	Langmuir	Pseudo-second-order	Surface complexation, electrostatic interaction	(Li et al., 2012)
GO-activated carbon felt composite	0-50	RTP	10	1-11	0-60	298	Langmuir	Pseudo-second-order	Electrostatic interaction, surface complexation	(Chen et al., 2013a)
Bovine Serum Albumin-coated GO (BVA-GO)	50-600	25	10	3-10	0-300	389	Langmuir	Pseudo-second-order	Coordination, electrostatic interaction, intraparticle diffusion	(Yang et al., 2017a)

where C_o is the initial concentration of adsorbate, T is the temperature, m is the adsorbent dosage, t is the contact time, q_m is the maximum adsorption capacity, *RTP* is the room temperature.
'–' denotes unavailable/not applicable

The first stability constant of the above metal hydroxide (log K_1 = 7.82, 7.0, 4.17, 4.4 for Pb, Cu, Cd and Zn, respectively) and metal acetate (log K_1 = 2.52, 2.16, 1.5, 1.5 for Pb, Cu, Cd and Zn, respectively) complexes are in good agreement with the aforementioned heavy metal ions affinity (Dean, 1990). Similar finding was reported by Gu and Fein (2015). In addition, Sitko, et al. (2016) studied the selectivity of different divalent heavy metal pollutants by GO/cellulose membrane and found that the adsorption capacity increased in the following order: $Co^{2+} < Zn^{2+} < Ni^{2+} < Cu^{2+} < Cd^{2+} < Pb^{2+}$. GO/zirconium phosphate (GO-Zr-P) nanocomposite and 3D graphene/δ-MnO2 aerogel showed different heavy metal affinity order as follows: $Cd^{2+} < Zn^{2+} < Cu^{2+} < Pb^{2+}$ and $Cu^{2+} < Cd^{2+} < Pb^{2+}$, respectively (Liu et al., 2016b; Pourbeyram, 2016). Generally, GO and its derivatives have strong affinity towards Pb^{2+}. The overall adsorption capacity of the 3D graphene structure has been significant improved as compared to the pristine GO. However, there is no apparent trend to predict the order of heavy metal affinity by GO and its derivatives because the functionalities available on their structures are dependent on the functionalisation process and the type of chemical additives used. Nonetheless, it is important to understand the selectivity of adsorbent to synthesise a suitable nano-adsorbent for wastewater treatment.

The adsorption performance of U^{6+} by GO (299 mg/g) was better than by rGO (47 mg/g) (Li et al., 2012). From the studies, the functional groups of the adsorbents played an important role in removing U^{6+} from aqueous solution. It was reported that GO contained functional groups such as hydroxyl, carbonyl and carboxyl groups, while rGO contains mainly non-oxygenated carbon (Li et al., 2012). The functional groups of GO contributed to the negatively charged surface to attract the cationic U^{6+} through electrostatic interaction. The same trend was observed in adsorption of Pb^{2+} onto GO and rGO, and the reported maximum adsorption capacities were 766.8 and 413.22 mg/g,

respectively (Peng et al., 2016b; Wang et al., 2014). However, through chemical functionalisation and construction of 2D GO sheets into 3D structure, the heavy metals adsorption performance could be significantly improved. For instance, the 3D sulfonated rGO aerogel constructed by Wu et al. (2015) exhibited remarkable Cd^{2+} adsorption capacity (234.8 mg/g) as compared to GO (139.9 mg/g) and activated carbon (23.5 mg/g). The aerogel was synthesised through freeze drying of a mixture of rGO aqueous dispersion and diazonium salt solution from sulphanilic acid. The sulphonation process introduced extra -SO_3H functional groups into the rGO surface. The findings of zeta potential suggested that the 3D aerogel was negatively charged over pH ranging from 2 to 10, favouring the adsorption of positively charged heavy metals (Wu et al., 2015).

The incorporation of metal oxide into GO has been carried out to produce effective adsorbents for heavy metal decontamination (Hoan et al., 2016; Liu et al., 2016c). Liu et al. (2016c) reported a highly efficient 3D graphene-δ-MnO_2 aerogel for Pb^{2+}, Cd^{2+} and Cu^{2+} removal. Manganese, oxygen and carbon were determined to be uniformly distributed in the 3D graphene-based structure, and K^+ was successfully incorporated into the structure. The unique layer of δ-MnO_2 offered additional uptake capability from surface to bulk adsorption through ionic exchange with the pre-inserted K^+ (Liu et al., 2016c). It was also reported that adsorption of Pb^{2+} resulted in the disappearance of Mn-O lattice vibration bands. The maximum adsorption capacities of Pb^{2+}, Cd^{2+} and Cu^{2+} onto the 3D graphene-δ-MnO_2 aerogel were 643.62, 250.31 and 228.46 mg/g, respectively. The results indicated that incorporation of metal oxide to the 3D graphene-based structure was an effective functionalisation approach to enhance the adsorption performance (Liu et al., 2016c).

2.5 Regeneration of GO and 3D graphene-based structures

An effective adsorbent should not only exhibit high adsorption capability, but also display high desorption efficiency. Regeneration of exhausted adsorbents for further use in adsorption could assist in reducing overall operating cost and eliminating secondary solid waste formation. Regeneration performance of an adsorbent is hence crucial to support the feasibility of GO and its derivatives in large scale wastewater treatment. Several regeneration methods such as steam treatment, electrochemical, temperature change, pressure swing and chemical eluting agents have been applied to regenerate spent adsorbents (Lata et al., 2015). The majority of the studies reported that the regeneration of graphene based adsorbents by chemical eluting agents (acid, base and organic solvent) was effective. Table 2.6 summarises the regeneration parameters for several graphene based structures used to remove heavy metals and pharmaceuticals.

Table 2.6: Regeneration of heavy metals and pharmaceuticals loaded graphene composites.

Adsorbate	**Adsorbent**	**Eluting agent**	**Desorption cycle**	**Desorption efficiency (%)**	**Reference**
Heavy metals					
Cu^{2+}	Porous chitosan-gelatin/GO monoliths	HNO_3	6	81	(Zhang et al., 2011b)
Pb^{2+}	GO/zirconium phosphate (GO-Zr-P) nanocomposite	3M HCl	5	90	(Pourbeyram, 2016)
As^{3+}	Graphene modified by iron-manganese binary oxide ($FeMnO_x$/rGO)	0.1M NaOH and 0.1 M NaClO	4	> 90	(Zhu et al., 2015)
Pharmaceuticals					
Tetracycline	3D cellulose nanofiber (CNF)/GO hybrid aerogel	5 wt. % NaOH	10	78.9	(Yao et al., 2017)
17-β Estradiol	Few-layered GO nanosheets	4 wt. % NaOH and acetone	5	94.14	(Jiang et al., 2016)
Dorzolamide	GO and acrylic acid grafted chitosan (GO/CSA)	Deionised water at acidic condition (pH = 3)	10	90	(Kyzas et al., 2014)

2.6 Fixed bed adsorption

Although batch adsorption study provides useful information and parameters on the application of specific adsorbent for pharmaceutical and heavy metal decontamination, there is a necessity to design a practical operation to evaluate the operational parameters for continuous adsorption of large volume of contaminated water. Generally, there are 5 common adsorption processes for wastewater treatment, namely batch adsorption, fixed bed adsorption, moving bed adsorption, fluidised bed adsorption and pulsed bed adsorption. The general features, advantages and disadvantages of these processes are listed in Table 2.7. Among the listed adsorption processes, fixed bed adsorption is the most preferred process for wastewater treatment due to its straightforward operation, relative low cost and capability in treating large volume of wastewater continuously (Ahmed & Hameed, 2018). Laboratory tests can be conducted to simulate the potential performance of adsorbent in fixed bed structure and the collected data can be used to design industrial adsorbers.

Table 2.7: Advantages and disadvantages of different adsorption systems.

Process	Batch	Fixed bed	Moving bed	Fluidised bed	Pulsed bed
Description	Adsorbent and adsorbate are present in aqueous solution at constant volume in well-mixed system	A packing of adsorbent bed is in contact with adsorbate that is continuously flow through the bed at constant flowrate	Steady-state system where both adsorbent and adsorbate are in motion and fresh adsorbent is constantly in contact with adsorbate while exhausted adsorbent is replaced	The adsorbate is in contact with adsorbent bed in fluidised motion (sufficient or insufficient flow)	Adsorbate is in contact with adsorbent bed until undesired process response is achieved
Advantages	- Easy operation and cheap	- Straightforward operation and cheap - Able to treat large volume of wastewater treatment continuously	- Efficient in treating great volume of wastewater	- Able to treat high quantity of wastewater with high pollutant load - More adsorbent surface is exposed for pollutant uptake	- Straightforward operation and cheap - Easy control system - Low dosage of adsorbent is required
Disadvantages	- Used to treat small volume of wastewater with minimum pollutant load - Hardly applied in industrial scale	- Performance is affected by adsorbent attrition, feed channelling and non-uniform flow of pollutant through adsorbent bed	- Complicated design and expensive - Large amount of adsorbent is required	- Complicated design and expensive - Inconsistent adsorbate flow which may cause column channelling and bubbling - Non-uniform residence time	- Used to treat small volume of wastewater with minimum pollutant load
Remarks	- Filtration is required to remove exhausted adsorbent - Often used to analyse feasibility of adsorbent in adsorption process	- Widely used in industries due to simple design	- Continuous regeneration of adsorbent is required during operation	- Potential application in industrial scale due to rapid mixing between adsorbent and adsorbate - Adsorbate is continuously flow through the column with controlled operation	- Regeneration of adsorbent can be performed as soon as the adsorbent is exhausted

2.6.1 Process parameters for fixed bed adsorption

As mentioned earlier, the shape of breakthrough curve is highly depended on the process parameters such as bed height, influent concentration, flowrate, flow direction, particle size and solution pH. Therefore, it is crucial to study the effect of each parameters to understand the dynamic adsorption behaviour of the fixed bed.

2.6.1.1 Effect of bed height

Bed height is often regarded as one of the most influential parameters in affecting the column performance. The bed height is linked to the amount of adsorbent used in the process and the availability of binding sites provided by the adsorbent within column will impact the total uptake of adsorbate species. Various studies demonstrated that the column operation time is dependent on the bed height.

Generally, the column operation times (t_b and t_s) are extended as bed height is increased. The binding sites of adsorbent increased proportionally with the bed height and this also improve the residence time of adsorbate across the adsorbent bed. Consequently, the adsorbate species will have sufficient contact time with the adsorbent, allowing more adsorbate species to diffuse into the inner pores of adsorbent and subsequently, elongate the column operation time. Hence, the breakthrough curve is expected to shift towards the right as the bed height is increased.

2.6.1.2 Effect of influent concentration

During the initial column operation, the adsorption is rapid due to abundant fresh binding sites for adsorbate uptake. The binding sites are gradually occupied causing greater mass transfer resistance between the liquid-adsorbent phases as time elapsed. To overcome the mass transfer resistance, an appropriate driving force for adsorbate transportation is required. The driving force is related to the influent concentration of

solution fed into the fixed bed. Generally, the mass transfer driving force increases with increasing influent concentration which in turn accelerates the moving rate of adsorbate across the fixed bed. This leads to fast saturation of column and shorten the t_b and t_s, showing influent concentration exhibited a negative impact onto the column operation operation time.

2.6.1.3 Effect of flowrate

The superficial velocity of adsorbate moving across the adsorbent bed is associated with the flowrate. At higher flowrate, the adsorbate species moves through the bed in quick succession which results in poor or insufficient contact time for adsorption. Therefore, the column is rapidly saturated and the adsorbate exited the column before attaining equilibrium. Moreover, undesired flow pattern such as axial dispersion and column channelling may occur due to high degree of turbulence at high flowrates, thus the column performance may decrease at high flowrates. The selection of appropriate flowrate is critical to design an effective fixed bed operation as too high flowrate can result in shortening of column operation time and poor adsorption efficiency whereas too low flowrate may extend the column operation time but may not be desirable when taking account on the separation efficiency and operation cost.

2.6.1.4 Effect of solution pH

Adsorption process is a surface phenomenon and the surface properties of adsorbent can affect the column operation. The surface charge of adsorbent is related to the solution pH which can be determined from tests such as point of zero charge (PZC) and isoelectric point. To facilitate the adsorption process through electrostatic interaction, it is important to ensure attraction between positively charged and negatively charged species occurs throughout the process. The ionisable form of a pharmaceutical pollutant depends on its acid dissociation constant (pKa) value. The pharmaceutical exists as a

neutral charged molecule when the pH < pKa while dissociated into either cationic or anionic form when pH > pKa. On the other hand, most heavy metal presented as cationic species in aqueous media, but certain metals such as MnO_4^- and $Cr_2O_7^{2-}$ presented as oxyanionic metal ions, forming negatively charged metal species in water body. Hence, the column efficiency can be improved by operating the column at appropriate solution pH to trigger electrostatic interaction between the adsorbate and adsorbent bed.

2.6.1.5 Effect of particle size

An adsorption column usually is a vertical and cylindrical vessel in which the solid adsorbent is packed at certain height and adsorbate fluid is passed through. Undesired flow pattern such as channelling and axial dispersion may result in the domination of convective flow over diffusion causing premature leakage of unadsorbed adsorbate from the adsorber and decrease the column efficiency. This can be avoided by increasing the ratio of bed height to particle diameter (H/D). Higher H/D can be achieved by using smaller particle sizes at constant bed height and this can minimise the large mass transfer zone and improve the breakthrough time of adsorber. Furthermore, smaller particle diameter could increase the total surface area exposed for adsorbate uptake, thus increase the adsorption efficiency (Gupta & Garg, 2019). Using higher H/D could increase the column effectiveness, however high pressure drop across the adsorption bed could occur if H/D is too large (Michel et al., 2018). As such, H/D > 1.5 is desirable for column operation (Song et al., 2016b) and H/D >7 is preferred for laboratory scale column adsorption experiments (Ang et al., 2020).

2.6.1.6 Fixed bed adsorption of 3D graphene-based adsorbents

Currently, the published work of column adsorption, particularly on pharmaceutical removal using 3D graphene-based adsorbent fixed bed are scarce compared to batch

study. Most literature data revealed that the breakthrough curves are significantly affected by the process parameters.

Li et al. (2020a) fabricated magnetic porous reduced graphene oxide (MPrGO) for fixed bed adsorption of triclosan. From their work, the breakthrough time of 2.3 mm bed, which was 50 days, was significantly improved by 4 and 60 times as compared to 1 and 0.3 mm bed heights, at influent concentrations of 100 μg/L and 2 mL/min flowrate, respectively. This was due to the longer contact time between triclosan and MPrGO bed at higher bed height, thus improving the diffusivity of triclosan into binding sites of MPrGO (Li et al., 2020a). Furthermore, the Thomas rate constant (K_{Th}) was observed to decrease from 0.80 to 0.15 mL/min mg as the bed height was increased. This was due to the increase of mass transfer resistance at higher bed heights (Li et al., 2020a). Moreover, the column performance of MPrGO was observed to be more efficient than powdered activated carbon by 6.5 times, further supporting the effectiveness of using 3D graphene-based adsorbent in wastewater treatment.

A PVA-alginate encapsulated Prussian blue-GO hydrogel beads was synthesised and reported to exhibit enhanced adsorption of cesium (Cs) in fixed bed column by Jang & Lee (2016). They investigated the effects of parameters such as pH, influent concentration, flowrate, bed height and adsorbent size on the column adsorption performance. Low pH condition showed poor adsorption of Cs due to structural destruction of adsorbent occurred in acidic condition (pH 1, 3 and 5). The column saturated at the fastest when operated at pH 9 and this was due to leaching of ferric ions at alkali condition had caused the cleavage of Fe-CN-Fe bond between the ferric functional group on Prussian blue and hydroxyl ions in bulk liquid. This finally resulted in the poor structural stability of the adsorbent in highly alkaline solution (Jang & Lee, 2016). Therefore, the column was best operated at pH 7. The longest column service

time was reported (t_b = 2 h and t_s =15 h) when operated at 1 mM influent Cs concentration, 0.83 mL/min, 2 mm adsorbent size and 20 cm bed height, achieving 161.1 mg/g adsorption capacity and 99 % removal percentage. From their findings, influent Cs concentration, adsorbent size and flowrate demonstrated negative synergy with column service time, while bed height showed positive synergy.

An increase in flowrate commonly results in quick saturation of column and reduction of adsorption capacity as the adsorbate leaves the column before reaching equilibrium. However, several studies indicated that adsorption capacity was increased at higher flowrate. For instance, MgO nanocubes decorated GO demonstrated a depletion in adsorption capacity from 187.9 to 142.8 mg/g for Pb^{2+} when flowrate increased from 1.66 to 4.98 mL/min (Mohan et al., 2017) while fixed bed adsorption of glyphosate using $MnFe_2O_4$ functionalised GO on activated carbon support showed an increase in adsorption capacity (3.90 – 5.49 mg/g) at elevated flowrates (4 – 8 mL/min). Since flowrate controls the contact time between adsorbent and adsorbate, it exerted influence on the mass transfer mechanisms in the bulk liquid film surrounding the solid surface (Ruthven, 1984). If the adsorption was favoured at higher flowrate, it indicated that external boundary diffusion was the rate-limiting steps due to thinning of the liquid film resistance at higher flowrate. The process was dominated by intraparticle diffusion if the flowrate showed negative impact onto adsorption capacity (Marin et al., 2019).

Several studies suggested that both the Thomas and Yoon-Nelson models were the best model to describe the fixed bed adsorption. Zhang et al. (2019c) developed a phosphorylated carbon aerogel via sol-cryo method for U^{4+} fixed bed adsorption. The Thomas model was best fitted by the breakthrough data for the effects of bed height and flowrate. The values of K_{Th} (1.6 – 1.4 mL/min mg) and K_{YN} (0.016 – 0.007/min) decreases with increasing bed height (1.6 – 3.2 cm) and K_{Th} (0.3 – 12.7 mL/min mg),

and K_{YN} (0.003 – 0.131/min) increases with increasing flowrate (0.5 – 10 mL/min). Meanwhile, the $q_{Th,m}$ (52.1 – 61.4 mg/g) and τ (260.9 – 819.3 min) increased as the bed height was increased, but $q_{Th,m}$ (64.5 – 37.3 mg/g) and τ (1291.8 – 37.7 min) were reduced at higher flowrate. This could be attributed to the greater sorption sites and longer residence time at higher bed height and lower flowrate, allowing more U^{4+} to be adsorbed onto the adsorbent bed (Zhang et al., 2019c).

GO-terminated hyperbranched amino polymer-carboxymethyl cellulose ternary composite (GO-HBP-NH_2-CMC) was utilised to remove Pb^{2+} and Cu^{2+} in fixed bed operation. The data obtained were fitted with the Adams-Bohart, Thomas and Yoon-Nelson models. It was reported that the Thomas model was the best fitting model. An increase in bed height and influent concentration had decreased the K_{Th}, but it increased with an increase in flowrate. This was due to the higher mass transfer resistance at higher bed height and influent concentration, but lower mass transfer resistance at higher flowrate (Kong et al., 2020a). Notably, the $q_{Th,m}$ was increased at higher influent concentration and this was due to the enhanced driving force at higher concentration.

2.7 Conclusions

3D graphene-based structures have attracted much research interest in wastewater treatment application, particularly in adsorptive removal of pollutants. These structures displayed superior adsorption capacity towards a variety of contaminants which included pharmaceutical and heavy metal residues. The synthesis of 3D graphene network offers additional functionalities resulting from the chemical additives which are favourable for adsorption of the pollutants through hydrogen bonding, π-π and hydrophobic interactions. Various 3D graphene composites have been investigated in term of their adsorption efficiencies for different heavy metals, nevertheless,

investigation on adsorption of pharmaceuticals such as antidepressants, anticonvulsants, beta-blockers and lipid regulators is still scarce.

Currently, large scale production of 3D graphene structures is hindered by several challenges. The graphene networks discussed in this review were mostly prepared at laboratory scale and the structures were fragile and easily destroyed during handling. The mechanical properties of the 3D structures can be improved by optimising the cross-linking conditions, surface modification with fibrous or nanomaterials, and incorporation of polymeric matrix such as polyvinyl alcohol. A further challenge involved the difficulty in manufacturing cost effective and size controllable 3D graphene structure at large scale. Therefore, it is vital to gain indepth understanding of surface growth and self-assembly mechanism to develop sturdy, scalable and low-cost 3D graphene networks in the future.

Progressive research innovation and development on 3D graphene structures are critical to overcome the major challenges in the commercialisation of nanomaterials for practical applications. Overall, the laboratory investigations highlighted the great potential of utilising 3D graphene-based networks as a practical adsorbent for wastewater treatment. The key challenge lies in understanding the synthesis mechanism in order to produce a vigorous and cost efficient nanosorbent of consistent quality. Furthermore, adsorption of multi-components, continuous adsorption through fixed bed column and pilot plant studies of the 3D graphene structures are still lacking in the literature. These studies are highly recommended to provide essential information for the commercial application of graphene networks.

Chapter 3: Research Materials and Methodology

This chapter describes the materials and methodology applied in this research. Firstly, graphene oxide (GO) and new 3D graphene-based structures were synthesised. Thereafter, the materials were characterised and tested on their efficiency in removing the representative pharmaceuticals (diclofenac and acetaminophen) and heavy metals (Cu^{2+} and Ni^{2+}) using batch adsorption mode. Optimisation study was performed by response surface methodology (RSM) and continuous adsorption of the pharmaceuticals and heavy metals was investigated by fixed bed operation. The experimental breakthrough curves were used to identify the mass transfer phenomena in the fixed bed operation. The details of these studies are described in the following sections.

3.1 Synthesis of graphene oxide

GO was prepared based on the modified Hummers method (Hummers & Offeman, 1958). A mixture of 23 mL sulphuric acid (H_2SO_4, 96 %, Fischer Scientific, USA) containing graphite powder (1 g, Bendosen, China) and sodium nitrate ($NaNO_3$, 0.5 g, Sigma Aldrich, Germany) was stirred in an icebath for 2 h. Next, potassium permanganate ($KMnO_4$, 3 g, Sigma Aldrich, Germany) was added slowly into the mixture and stirred for 1 h. The temperature of waterbath shaker (Protech, Malaysia) was then increased to 35 °C and the mixture was stirred for another 30 min. Then, 46 mL of deionised water was added into the mixture and heated to 95 °C for 1 h. Approximately 140 mL deionised water was added and stirred for 30 min and the mixture cooled down to room temperature. The reaction was terminated by adding 10 mL H_2O_2 (30 %, Fischer Scientific, USA). Finally, the precipitated graphene was washed thoroughly with deionised water and diluted HCl (0.1 M, Fischer Scientific, USA) before dried overnight in a vacuum oven (Memmert, Germany) at 60 °C.

3.2 Synthesis of 3D reduced graphene oxide aerogel

The 3D reduced graphene oxide aerogel (rGOA) was prepared using GO as the precursor and L- ascorbic acid (> 99 %, Sigma Aldrich, USA) as the reducing agent. The schematic illustration of the synthesis process is illustrated in Fig.3.1.

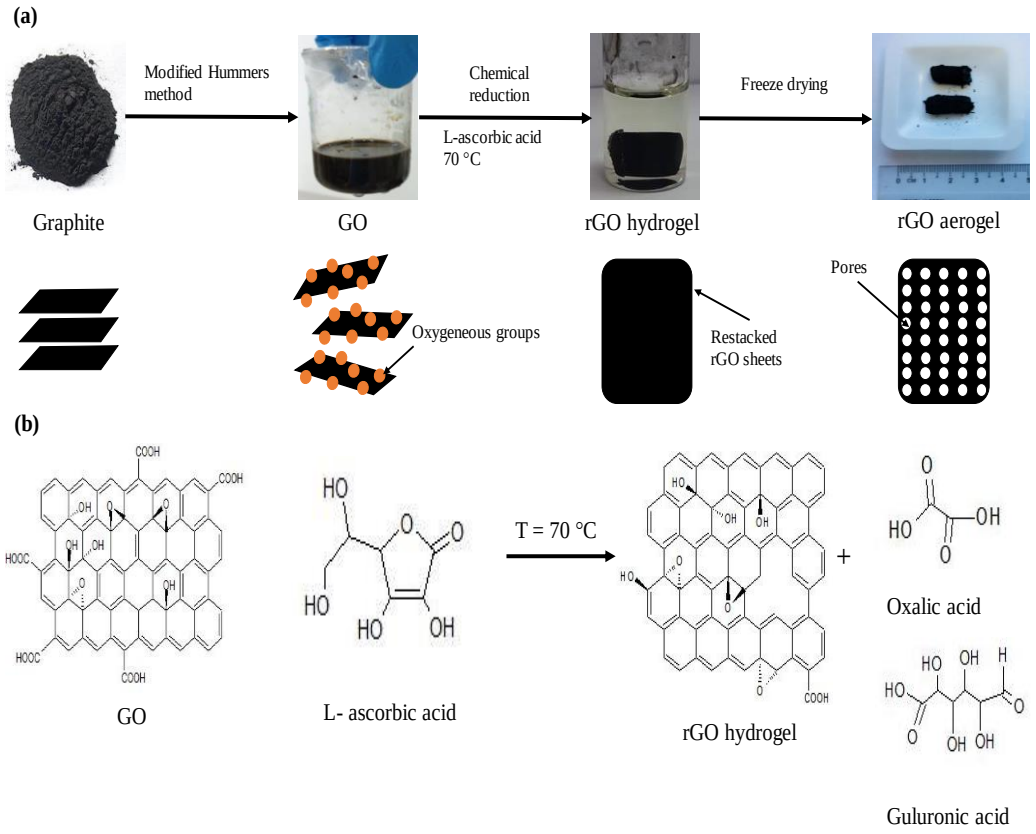

Fig. 3.1: Schematic flowchart of (a) rGOA synthesis and (b) chemical reduction of GO.

L-ascorbic acid was added to GO dispersion at a fixed mass ratio (GO:L-ascorbic acid = 1:3) and the mixture was stirred for 5 min to obtain homogeneous mixture. Approximately 4 mL of GO/L-ascorbic acid mixture was aspirated into a centrifuge tube which was subsequently placed in the oven at 70 °C for 12 h to initiate GO self-assembly via chemical reduction. The 3D rGO hydrogel formed was washed thoroughly to remove the by-products (oxalic acid and guluronic acid). The 3D rGOA was obtained by freeze drying (Christ Alpha 1-2 LDplus, Germany) the hydrogel for 24 h. The

resulted rGOA was then stored in sealed container for subsequent adsorption experiment.

3.3 Synthesis of 3D manganese oxide functionalised reduced GO

Fig. 3.2 illustrated the schematic diagram for the synthesis of 3D reduced GO aerogel functionalised with manganese oxide (RGM). The RGM was prepared by mixing GO suspension (6 mg/mL) with carboxymethyl cellulose (CMC, 2 g, Sigma Aldrich, Germany). The mixture was stirred overnight to achieve homogeneous suspension. Then, it was transferred into a mould and frozen at -20 °C for 24 h, before undergoing lyophilisation at -55 °C and vacuum condition in the freeze dryer.

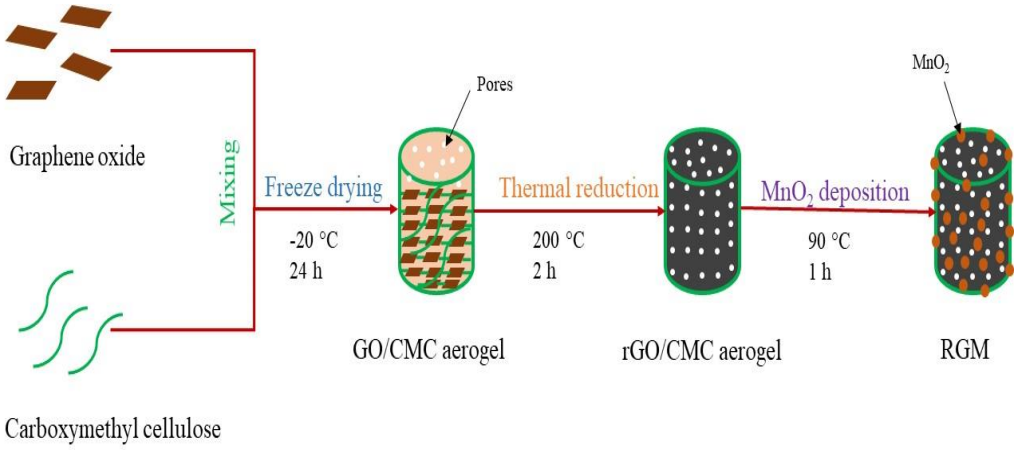

Fig. 3.2: Schematic flowchart of RGM synthesis.

The resulted graphene aerogel was subjected to thermal reduction at 200 °C to improve the water stability of the structure. The MnO_2 nanoparticles was decorated onto the reduced GO aerogel through co-precipitation method. 0.8 g of $KMnO_4$ was added into 100 mL of deionised water and the solution pH was adjusted to 2 by adding an appropriate amount of 0.1 M HCl. Then, 0.3 g of the graphene aerogel was immersed in the acidic $KMnO_4$ solution for 1 h and the temperature of the reacting vessel was maintained at 90 °C. The reaction was terminated by pouring 10 mL 30 % H_2O_2 into

the reaction vessel. The final product (RGM) was collected and washed thoroughly to remove any impurities before storing in the desiccator.

3.4 Synthesis of 3D zirconium functionalised graphene aerogel

Zirconyl chloride octahydrate ($ZrOCl_2 \cdot 8H_2O$, 98 %, reagent grade, Sigma Aldrich, USA) was added into 100 mL of 2 mg/mL of GO suspension at a weight ratio of 3:1. The mixture was then agitated for 30 min before the addition of 2 g CMC. The mixture was agitated for 8 h to obtain homogeneous suspension. Thereafter, the mixture was casted into 96 wellplate and frozen in a vertical freezer at -20 °C for 12 h. The final product, namely zirconium functionalised graphene aerogel (ZrGA), was synthesised by freeze drying the frozen mixture in the freeze dryer for 24 h in vacuum condition, followed by drying in the oven at 100 °C, overnight. The synthesis steps of ZrGA is illustrated in Fig. 3.3.

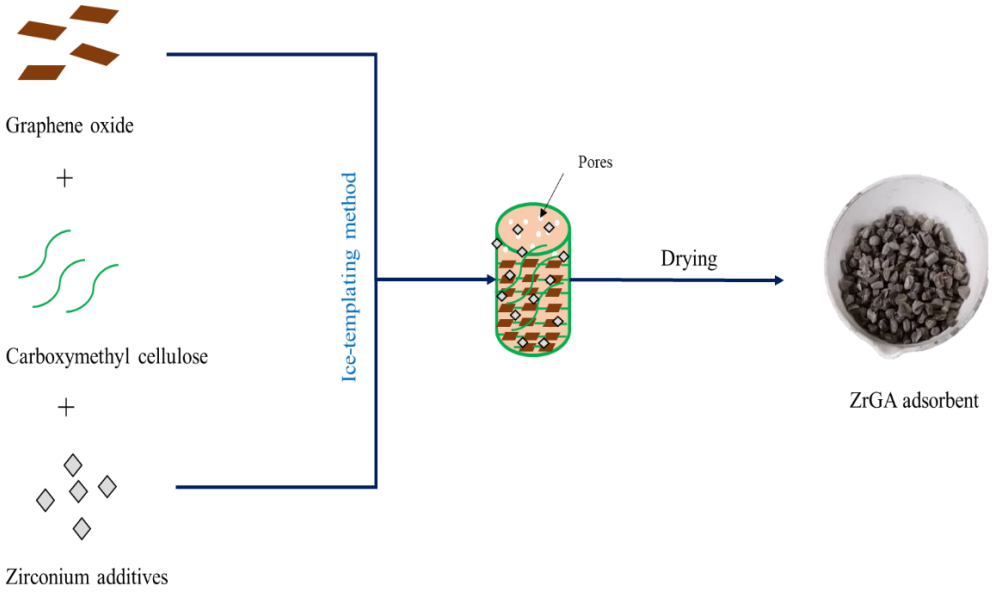

Fig. 3.3: Schematic flowchart of ZrGA synthesis.

3.5 Characterisation study

Fourier transform infrared spectroscopy (FTIR, Spectrum RXI Perkin-Elmer, USA) equipped with attenuated total reflection (ATR) detector was used to determine the chemical functional groups present in the adsorbent. The morphological structure of adsorbent was characterised by scanning electron microscope (SEM, Quanta 400F, USA, 20 kV). The elemental composition of the sample was analysed by energy dispersive X-ray (EDX) and X-max detector (Oxford-Instruments INCA 400, UK) attached to the SEM. The specific surface area, pore volume and pore size distribution of rGOA were measured using nitrogen adsorption-desorption isotherm at liquid nitrogen temperature (77 K) by surface area and porosity analyser (ASAP 2020, Micromeritics, USA). The specific surface area and pore size distribution of rGOA were evaluated by Brunauer-Emmett-Teller (BET) and Barrett-Joyner-Halenda (BJH) algorithms, respectively. The sample was degassed at 200 °C with a holding time of 120 min. The crystal structure of the materials was determined by X-ray diffraction (XRD, PANalytical, USA) operated at 40 kV and 30 mA with CuK radiation ($\lambda = 0.15418$ nm) over $7° \leq 2\theta \leq 80°$. The point of zero charge (PZC) of rGOA was identified by contacting 20 mg of adsorbent with 50 mL of 0.1 M potassium nitrate (KNO_3, Sigma Aldrich, Germany) solutions of different pH (2–11). The mixtures were agitated in the waterbath shaker at 200 rpm and 30 °C, for 24 h. Finally, the pH of the mixtures was recorded.

3.6 Batch adsorption study

The stock solutions of 500 mg/L of diclofenac, acetaminophen, Cu^{2+} and Ni^{2+} were prepared separately by dissolving 0.51 g sodium salt of diclofenac ($C_{14}H_{10}C_{l2}NNaO_2$, 318.1 g/mol, purity > 98 %, analytical grade, Sigma Aldrich, Germany), 0.51 g of acetaminophen salt ($C_8H_9NO_2$, 151.165 g/mol, purity > 98 %, analytical grade, Sigma

Aldrich, Germany), 1.965 g copper (II) sulphate pentahydrate ($CuSO_4 \cdot 5H_2O$, 249.69 g/mol, Acros Chemical, Belgium) and 2.025 g nickel (II) chloride hexahydrate ($NiCl_2 \cdot 6H_2O$, 237.69 g/mol, Acros Chemical, Belgium) in 1 L deionised water, respectively. The stock solution was then diluted into desired concentration for the adsorption experiments. Batch adsorption studies were conducted by contacting a specific mass of adsorbent in fixed volume of adsorbate (50 mL) of known concentration. The mixtures were agitated the waterbath shaker (Protech, Malaysia) at fixed temperature for 4 h. The adsorption efficiency was examined based on different process parameters which included dosage, initial solution pH, temperature, initial concentration and ionic strength.

The adsorption kinetic experiment was conducted by contacting fixed adsorbent dosage in specific concentration solution. The mixtures were agitated at 200 rpm and 30 °C, followed by collection of sample solution at different time intervals. The experiment procedures were repeated at different initial concentrations.

The adsorption efficiency of adsorbent was evaluated by removal efficiency (R, %) and adsorption capacity (q_e, mg/g) represented by Eqs. (3.1) and (3.2), respectively.

$$R = \left(1 - \frac{C_e}{C_o}\right) \times 100\ \% \tag{3.1}$$

$$q_e = \frac{(C_o - C_e)V}{m} \tag{3.2}$$

where C_o and C_e are the initial and equilibrium concentration of adsorbate (mg/L), respectively, V is the volume of concentration (L), m is the mass of adsorbent (g).

3.7 Regeneration study

The assessment of adsorbent regenerability was determined by conducting five successive adsorption – desorption cycles. The adsorbate loaded adsorbent was first

separated from liquid using filter paper and was washed with deionised water to remove any unadsorbed adsorbate. Thereafter, the adsorbate loaded adsorbent was regenerated using different eluents and rinsed with deionised water to remove excess eluent residue before reutilised in subsequent adsorption test. The regeneration efficiency (η, %) was determined by Eq. (3.3):

$$\eta = \frac{q_{ei+1}}{q_{eo}} \times 100\ \% \tag{3.3}$$

where q_{ei+1} is the adsorption capacity at i^{th} cycle (mg/g) and q_{eo} is the initial adsorption capacity (mg/g).

3.8 Fixed bed adsorption study

The fixed bed column adsorption experiments were conducted in a borosilicate glass column with an internal diameter of 1.5 cm and height of 65 cm. A fixed mass of adsorbent was packed in the column supported by a layer of glass beads (1 cm) at the bottom of the bed. A layer of the glass beads (1 cm) was gently placed on top of the bed to hold down the adsorbent. The adsorbate solution was introduced into the column in a downflow manner at a constant flowrate. The effects of column parameters which included bed height, influent concentration and flowrate were investigated, and the effluent samples were collected at specific time intervals until the bed reached saturation. The breakthrough concentration (C_b, mg/L) and saturation concentration (C_s, mg/L) were defined as 5 and 99.5 % of influent concentration, respectively.

3.9 Column parameters

3.9.1 Breakthrough curve

During the initial stage of fixed bed adsorption, mass transfer occurs mostly near the inlet of adsorbent bed where the adsorbate first in contact with the adsorbent surface. At this stage, the adsorbate is adsorbed rapidly onto the upper few layers of the fresh

adsorbent and no adsorbate escape from the column. The normalised concentration (C_t/C_o) is zero during the initial stage as the concentration of adsorbate is zero. Furthermore, the mass transfer zone (MTZ) is obtained near the top of adsorbent bed.

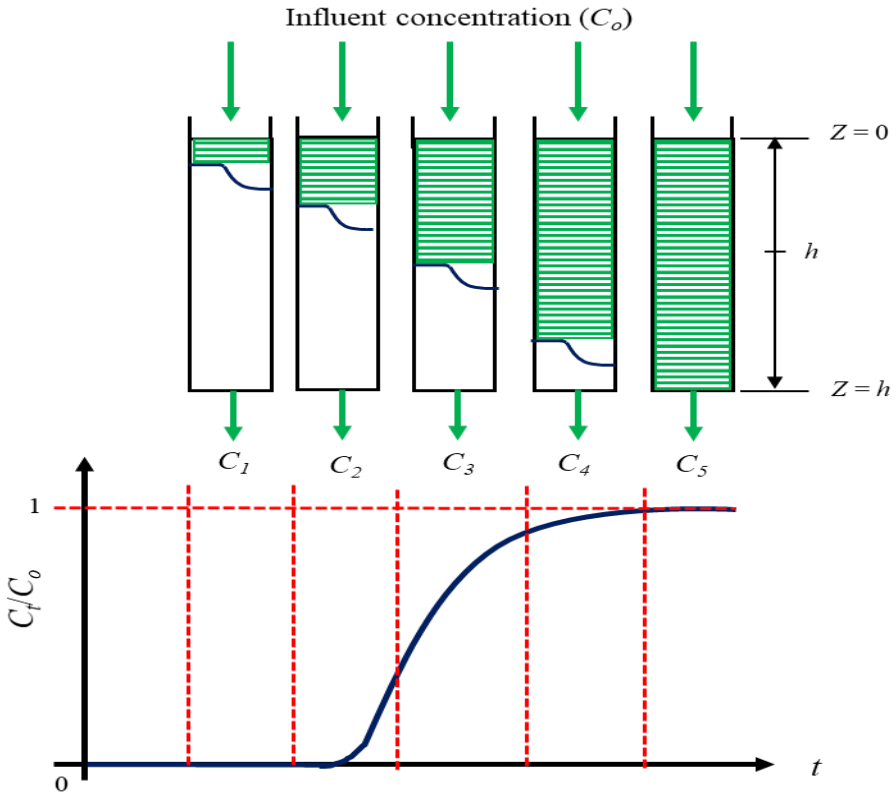

Fig. 3.4: Fixed bed adsorption profile.

Thereafter, the upper layer of the bed is progressively saturated by the continuous addition of adsorbate into the column, thus making it less efficient as the operation time increases. As shown in Fig. 3.4, the C_t/C_o plot gradually increased as the column MTZ descended to the unsaturated part in the bed when the column operation time elapsed. Adsorption process is terminated when the column is fully exhausted as indicated by C_t/C_o = 1. In most cases, the profile of C_t/C_o plot exhibits a characteristic S-shaped curve with different slope based on process parameters and this curve is known as breakthrough curve.

3.9.2 Breakthrough curve characteristics

From the breakthrough curve shown in Fig. 3.5, the breakthrough point is located at the lower end of the curve and the breakthrough concentration (C_b) is the specific concentration set by authority body or 5 % of influent concentration. Additionally, saturation concentration (C_s) is the concentration that is close to influent concentration (95 – 99 % influent concentration). Therefore, the breakthrough time (t_b) and saturation time (t_s) of the column are the times at which the effluent concentration attained C_b and C_s, respectively.

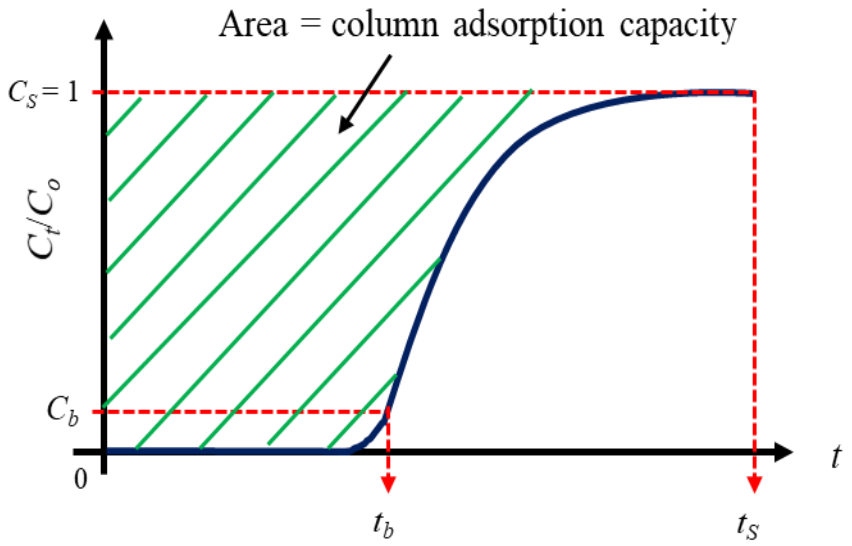

Fig. 3.5: Breakthrough curve for fixed bed adsorption.

When the entire bed reaches equilibrium with the influent adsorbate, the total column adsorption capacity is proportional to the area between the breakthrough curve and a horizontal line at C_t/C_o =1. The equivalent times for total column adsorption capacity (t_t) and usable column capacity up to breakthrough point (t_u) are represented by the total shaded area in Fig. 3.5, and they can be expressed as by Eqs. (3.4) and (3.5):

$$t_t = \int_0^{\infty} \left(1 - \frac{C_t}{C_o}\right) dt \tag{3.4}$$

$$t_u = \int_0^{t_b} \left(1 - \frac{C_t}{C_o}\right) dt \tag{3.5}$$

The ratio of t_u/t_t usually is the length of bed utilised up to breakthrough point. Therefore, the length of used bed (h_u) and length of unused bed (h_{unb}) for a given bed height (h) can be represented by Eqs. (3.6) and (3.7):

$$h_u = h\left(\frac{t_u}{t_t}\right) \tag{3.6}$$

$$h_{unb} = h\left(1 - \frac{t_u}{t_t}\right) \tag{3.7}$$

The value of h_{unb} represents the mass transfer zone (*MTZ*) of the column which is assumed to be constant and important parameter for process scale up. Generally, a small *MTZ* indicates the breakthrough curve is close to an ideal step with negligible mass transfer resistance. In ideal case, no axial dispersion occurs in the process and the superficial velocity profile would be identical to an ideal breakthrough curve and the *MTZ* = 0. However, this case is not achievable in real adsorption application. As such, column operation with 0 < *MTZ* < *h* can be considered whereas the adsorption process is highly inefficient when *MTZ* > *h*. The mathematical expression for *MTZ* based on column operation time is given by Eq. (3.8):

$$MTZ = h\left(1 - \frac{t_b}{t_s}\right) \tag{3.8}$$

Based on breakthrough curves obtained from the fixed bed adsorption study, the total amount of adsorbate adsorbed (q_{total}, mg) and column adsorption capacity (q_c, mg/g) were evaluated by numerical integration with computational software MATLAB 2013a (MathWorks, USA) as expressed by Eqs. (3.9) and (3.10), respectively:

$$q_{total} = \frac{Q}{1000}\int_{t=0}^{t=t_n} C_{ad}\ dt = \frac{Q}{1000}\int_{t=0}^{t=t_n} (C_o - C_t)\ dt \tag{3.9}$$

$$q_c = \frac{q_{total}}{m} \tag{3.10}$$

where Q is the volumetric flowrate (mL/min), C_{ad} is the adsorbed heavy metal concentration (mg/L), C_o is the influent concentration (mg/L), C_t is the effluent concentration (mg/L), t_n is the operational time (min) and m is the mass of adsorbent (g).

The breakthrough time (t_b, min) and saturation time (t_s, min) were defined as the time where the effluent achieved C_b and C_s, respectively. Other design data of the adsorption column such as fractional bed utilisation (*FBU*), empty bed contact time (*EBCT*, min), initiation time of adsorption process (t_f, min) and moving rate of adsorption zone (U_z, cm/min) were calculated by Eqs. (3.11) – (3.14), respectively.

$$FBU = \frac{q_b}{q_s} \tag{3.11}$$

$$EBCT = \frac{V_b}{Q} \tag{3.12}$$

$$t_f = t_z\left(1 - \frac{q_z}{q_{total}}\right) \tag{3.13}$$

$$U_Z = \frac{MTZ}{t_s - t_b} \tag{3.14}$$

where q_b is the adsorption capacity at breakthrough point (mg/g), q_s is the adsorption capacity at saturation point (mg/g), t_z is time during mass transfer ($t_z = t_s$-t_b, min), V_b is the volume of packed bed (m^3), h is the bed height (cm), q_z is the adsorption capacity during mass transfer (mg/g).

3.10 Adsorption modelling

The experimental data were fitted to several theoretical adsorption models to evaluate the model parameters to describe the batch adsorption equilibrium, kinetic and mechanisms as well as dynamic adsorption behaviour of the developed adsorbent-

adsorbate systems. The non-linear mathematical expressions and assumptions for the models are summarised in Table 3.1. The model fitting was performed using non-linear regression method with the best fitting model determined by coefficient of determination (R^2), whereby R^2 closest to unity indicated that the experimental data agreed well with the specific model.

The Gibbs free energy change (ΔG, kJ/mol), entropy change (ΔS, kJ/mol K), and enthalpy change (ΔH, kJ/mol) for the adsorption systems were evaluated by Eqs. (3.15) – (3.17):

$$\Delta G = \Delta H - T\Delta S \tag{3.15}$$

$$\ln K = \frac{\Delta S}{R} - \frac{\Delta H}{RT} \tag{3.16}$$

$$K = \frac{q_e}{C_e} \tag{3.17}$$

where K is the equilibrium constant, R (8.314 J/mol K) is the universal gas constant, T (K) is the absolute temperature, q_e is the equilibrium adsorption capacity (mg/g) and C_e is the equilibrium concentration (mg/L). The values of ΔS and ΔH were determined from the intercept and slope of the plot of ΔG against T, respectively.

Table 3.1: Adsorption models and assumptions.

Model	Equation	Assumption	Reference
Batch adsorption			
Equilibrium			
Langmuir	$q_e = \frac{q_m K_L C_e}{1 + K_L C_e}$	Assumes finite number of occupancy sites are present on uniform solid surface where no further adsorption occurs at the occupied sites and no interaction between the adsorbed species of neighbouring sites.	(Langmuir, 1918)
Hall's separation factor	$R_L = \frac{1}{1 + K_L C_o{}'}$	Evaluates the process desirability (Unfavourable if $R_L > 1$, linear if $R_L = 1$, irreversible if $R_L = 0$ and favourable if $0 < R_L < 1$)	(Hall et al., 1966)
Freundlich	$q_e = K_F C_e{}^{1/n}$	Considers reversible sorption process occurred on heterogeneous surface with uneven binding sites. It also describes the exponential decrease of adsorption efficiency with increase in surface coverage.	(Freundlich, 1906)
Temkin	$q_e = \frac{RT}{b_T} \ln(A_T C_e)$	Takes into account that heat of adsorption decreases linearly as surface occupation on adsorbent increases with consideration on the influences of other indirect interactions between adsorbate and adsorbent.	(Temkin & Pyzhev, 1940)
Dubinin-Radushkevich (D-R)	$q_e = q_{DR} e^{-K_{DR}\varepsilon^2}$	Assumes the adsorbent is porous and the isotherm has high degree of rectangularity.	(Dubinin, 1947)
Mean free sorption energy (*E*)	$E = \frac{1}{\sqrt{2K_{DR}}}$	Describes the free energy when 1 mole of adsorbate is transported from bulk solution to adsorbent surface.	(Dubinin, 1947)
Kinetic			

Pseudo-first-order	$q_t = q_e(1 - e^{-k_1 t})$	Assumes the adsorption process is a physisorption and adsorption rate is proportional to available binding sites.	(Lagergren et al., 1898)
Pseudo-second-order	$q_t = \frac{t k_2 {q_e}^2}{1 + t k_2 q_e}$	Considers the adsorption rate is proportional to the squared number of unsaturated sites.	(Ho & McKay, 1998)
Elovich	$q_t = \frac{1}{\beta}\ln(\alpha\beta) + \frac{1}{\beta}\ln(t)$	Describes a chemisorption process on highly heterogeneous solid surface.	(Low, 1960)
Intraparticle diffusion	$q_t = K_p t^{0.5} + C$	Determines the rate controlling steps (pore, film or surface diffusion) of the adsorption process.	(Weber & Morris, 1963)
Column adsorption			
Thomas	$C_t/C_o = \frac{1}{1 + \exp\left[\frac{K_{Th} q_{Th,m} m}{Q} - K_{Th} C_o t\right]}$	Assumes adsorption behaved according to the Langmuir isotherm with no occurrence of axial dispersion in the column. The driving force for adsorption is driven by the pseudo-second-order kinetic model of a reversible system.	(Thomas, 1944)
Yoon – Nelson	$C_t/C_o - C_t = \exp(K_{YN} t - K_{YN}\tau_{YN})$	Considers the adsorbate depletion rate during adsorption is corresponded to the probability of its adsorption breakthrough. This model is also used to estimate the time for the column to achieve 50 % breakthrough.	(Yoon & Nelson, 1984)
Adams – Bohart	$C_t/C_o = \exp(K_{AB} C_o t - \frac{K_{AB} N_o h}{U})$	Assumes adsorption equilibrium does not achieved instantly and the adsorption rate is controlled by external mass transfer.	(Bohart & Adams, 1920)

where q_m is the Langmuir maximum adsorption capacity (mg/g), C_o' is the highest initial concentration (mg/L), K_L is the Langmuir adsorption constant (L/mg), K_F is the Freundlich constant ((mg/g)(L/mg)$^{1/n}$), n is the Freundlich exponent, A_T (L/mg) is the Temkin isotherm equilibrium binding constant, b_T (J/mol) is the Temkin isotherm constant q_{DR} is the D-R maximum sorption capacity (mg/g), K_{DR} is the D-R constant related to sorption energy, k_1 is the pseudo-first order rate constant (1/min), k_2 is the pseudo-second

order rate constant (g/(mg.min)), β is the Elovich constant (mg/g), α is the initial adsorption rate (mg/ g min), K_p is the intraparticle diffusion rate constant (mg/g $min^{0.5}$), C is the y-intercept of intraparticle diffusion plot (mg/g), K_{Th} is the Thomas model rate constant (1/min), $q_{Th,m}$ is the Thomas model maximum adsorption capacity (mg/g), t is the column operation time (min), K_{YN} is the Yoon-Nelson model rate constant (1/min), τ_{YN} is the time required to achieve 50 % breakthrough (min), k_{AB} is the Adams-Bohart model rate constant (1/min), U is the superficial velocity of the adsorption column (cm/min) and N_o is the saturation concentration (mg/L).

3.11 Response surface methodology

The mathematical expression for the batch adsorption systems was modelled based on the interaction between the independent process parameters and expressed by a second-order polynomial equation as shown by Eq. (3.18):

$$q_{pred} = \beta_o + \sum_{i=1}^{k} \beta_i X_i + \sum_{i=1}^{k} \beta_{ii} {X_i}^2 + \sum_{i=1}^{k-1} \sum_{j=1}^{k} \beta_{ij} X_i X_j + \varepsilon \quad (3.18)$$

where q_{pred} is the predicted adsorption capacity (mg/g), X_i, X_i, …, X_k are the invididual factors, X_i^2, X_j^2, …, X_k^2 are the quadratic effects, X_iX_j, X_iX_k , and X_jX_k are the interaction relationship between each individual factor, β_i, β_{ii} and β_{ij} (i=1,2,…,k; j=1,2,…,k) are the linear, quadratic and interactive effects coefficients, respectively, and ε is the random error.

The range of the selected parameters was predetermined from preliminary study. The experimental set-up was designed by RSM which generated the parametric study randomly using the Design Expert® version 7. The experimental work was carried out according to the RSM designed experimental runs. The established model was evaluated by analysis of variance (ANOVA) to examine the significance of model and each term based on probability value (p-value) and Fischer's test value (F- value) at 95 % confidence level. Additional diagnostic analysis such as R^2, adjusted R^2, predicted R^2, normalised residue plots and adequate precision can be utilised to assure the accuracy and predictability of the developed model.

3.12 Adsorbate concentration analysis

After the adsorption experiment, the sample solution was collected for final concentration determination. For pharmaceutical adsorption study, the sample solution was filtered through polytetrafluoroethylene (PTFE) membrane syringe filter (pore size 0.45 μm, CHROMAFIL. Germany). The filtrate was then injected into 2 mL screw-

neck vial. A high-performance liquid chromatography (HPLC, Agilent Technologies, HPLC 1260, USA) coupled with ultra-violet detector was used to determine the equilibrium concentration of diclofenac. The HPLC analysis was conducted with a 4.6 x 100 mm and 3.5 μm pore size C18 column (ZORBAX Eclipse Plus C18, Agilent Technologies, USA) and the column temperature was set at 40 °C. The mobile phases for diclofenac detection consisted of 60 % acetonitrile (C_2H_3N, HPLC grade, R&M, Malaysia) and 40 % of 0.1 % formic acid buffer (CH_2O_2, Fischer Scientific, USA) running at 1 mL/min flowrate while the detection wavelength was set at 230 nm. For acetaminophen concentration measurement by the HPLC, the mobile phases used were 25 % methanol (CH_3OH, HPLC grade, Fischer Scientific, USA) and 75 % ultrapure water, under the flowrate of 0.8 mL/min. The wavelength detection of acetaminophen was 243 nm. The diclofenac and acetaminophen calibration curves are presented in Fig. 3.6 (a) and (b), respectively.

(a)

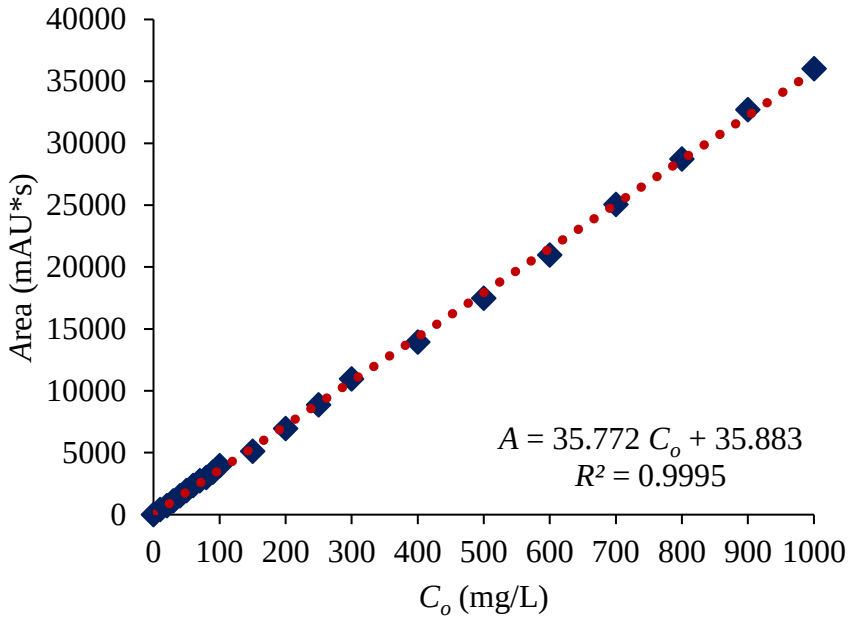

(b)

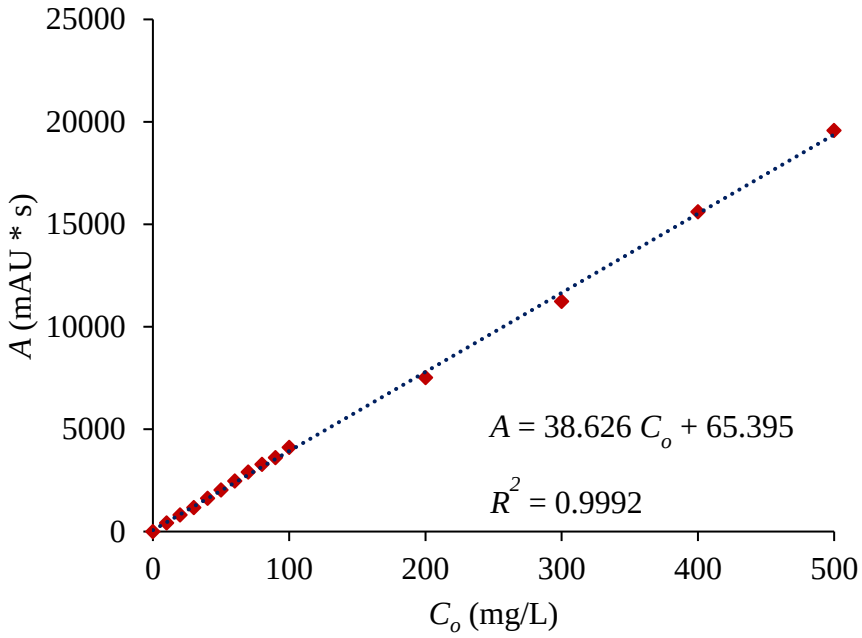

Fig. 3.6: Calibration curves for (a) diclofenac and (b) acetaminophen concentration detection by HPLC.

For heavy metal concentration detection, approximately 10 mL of the sample solution were extracted and the concentration of Cu^{2+} and Ni^{2+} in the soluions were determined by atomic absorption spectrophotometer (AAS, AAnalyst 400, Perkin Elmer, USA). The AAS calibration curves for Cu^{2+} and Ni^{2+} are depicted in Fig. 3.7 (a) and (b), respectively.

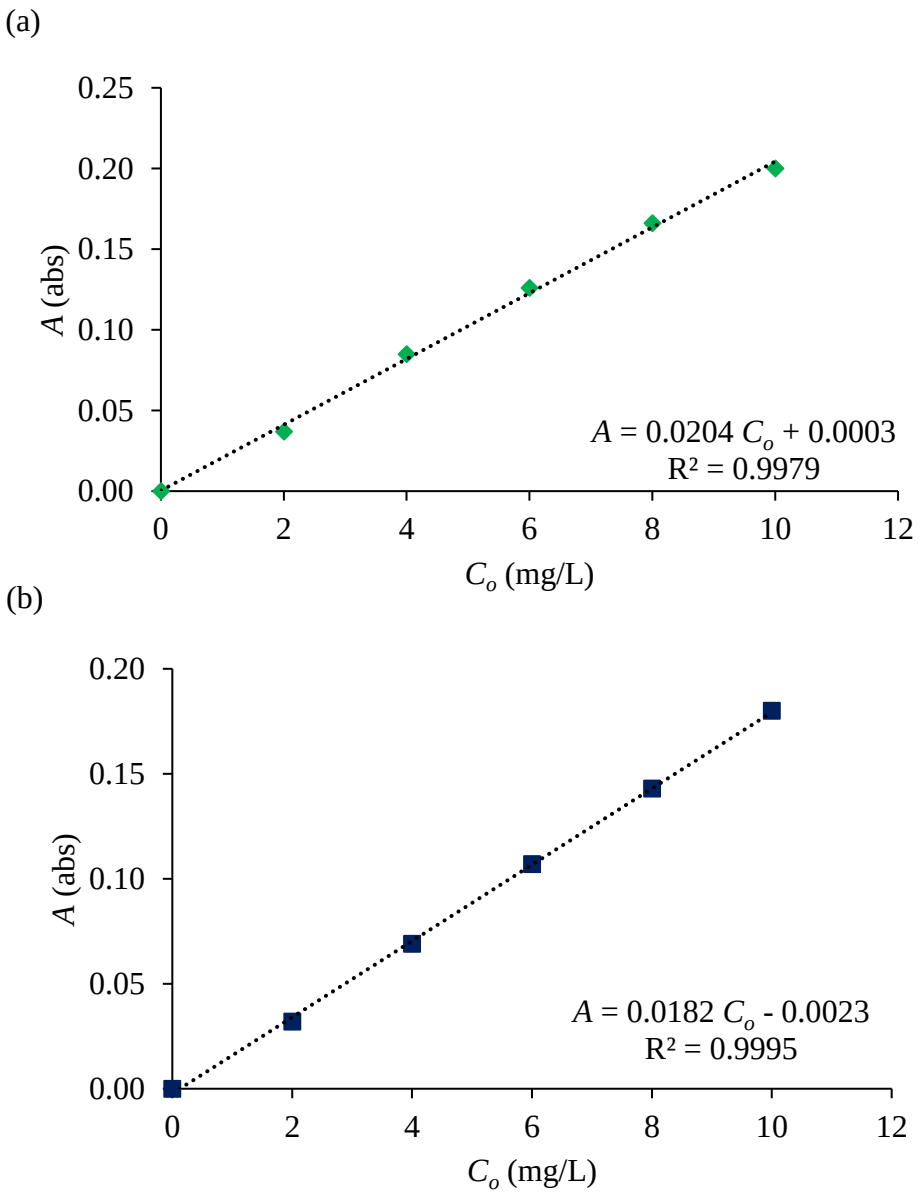

Fig. 3.7: Calibration curves for (a) Cu^{2+} and (b) Ni^{2+} concentration measurement by AAS.

3.13 Mass transfer factor analysis

The adsorption of adsorbate onto adsorbent involved several consecutive mass transfer steps: (1) film mass transfer where adsorbate transfers from bulk liquid to external surface of adsorbent, (2) pore or intraparticle diffusion where adsorbate transfers from external surface to internal pores of adsorbent and (3) fixation of adsorbate on the adsorbent surface. Fig. 3.8 illustrates the mass transfer mechanisms involved in the solid-liquid adsorption system.

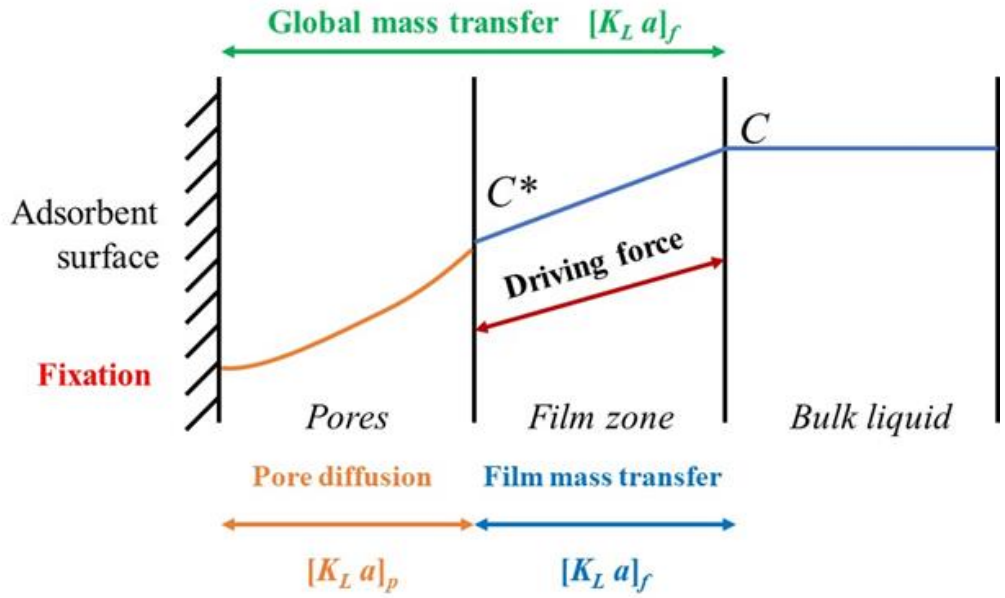

Fig. 3.8: Mass transfer steps in adsorption.

The fixation step is usually rapid and hence, the overall mass transfer resistance is considered due to either film mass transfer or pore diffusion, or both. To study the mass transfer coefficients, Fulazzaky (2011) proposed the following mathematical models to evaluate the global mass transfer and individual film and pore diffusion mass transfer coefficients.

The mass balance at the solid-liquid interface in fixed bed adsorption was developed by combining the hydraulic flow model and chemical reaction kinetic, and the general equation is expressed by Eq. (3.19):

$$N_A = -[K_L]_f \times A \times (C - C^*) \tag{3.19}$$

where N_A is the quantity of adsorbate transferred per unit time (mg/min), $[K_L]_f$ is the film mass transfer coefficient (min^{-1}), A is the surface area (m^2) and (C - C*) is the driving force (mg/L). The fixed bed adsorption was assumed to operate in a plug flow manner, as depicted in Fig. 3.9.

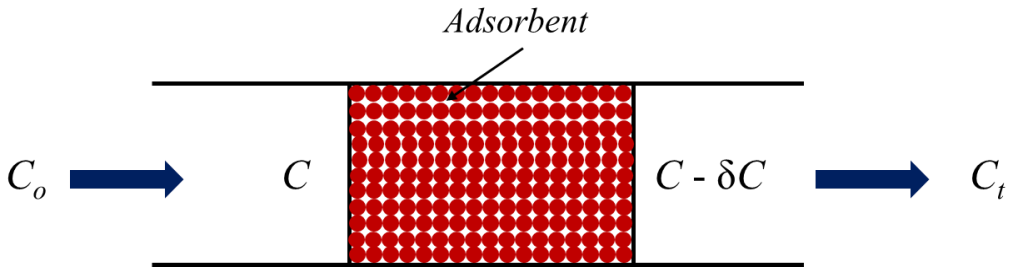

Fig. 3.9: Schematic diagram of plug flow continuous adsorption.

Since surface area remain constant during adsorption, the film mass transfer coefficient $[K_L]_f$ is assumed to be constant. Therefore, the mass balance for the plug adsorption system at a fixed flowrate (Q) (Fig. 3.9) is represented by Eq. (3.20):

$$QC = Q \times (C - \delta C) - [K_L]_f \times A \times (C - C^*) \tag{3.20}$$

where Q is the flowrate (mL/min) and C is the adsorbate concentration (mg/L). Taking the form of differential equation, Eq. (3.21) is modified to Eq. (3.22):

$$-\frac{\delta C}{\delta t} = [K_L]_f \times \frac{A}{\delta V} \times (C - C^*) \tag{3.22}$$

where V is the volume of effluent treated (L). Thereafter, Eq. (3.22) was solved numerically by integration based on the following boundary conditions:

$C_1 = C_o$, $C_2 = C_t$ $\quad\quad$ $t_1 = 0$, $t_2 = t$

$V_1 = 0$, $V_2 = V$ $\quad\quad$ $C^* << C$

Hence, a continuous equation for mass transfer at the liquid film is expressed by Eq. (3.23):

$$\ln\left(\frac{C_o}{C_t}\right) = [K_L a]_f \times t \tag{3.23}$$

where C_o is the influent concentration (mg/L), C_t is the concentration of adsorbate exiting the column (mg/L), a is the interfacial solid-liquid surface (S/V, m^{-1}), $[K_L a]_f$ is the film mass transfer coefficient (min^{-1}) and t is the accumulative time across the column (min).

The relationship between film mass transfer and global mass transfer coefficients is given by Eq. (3.24):

$$[K_L a]_f = [K_L a]_g \times e^{-\beta q} \tag{3.24}$$

where $[K_L a]_g$ is the global mass transfer coefficient (min^{-1}), β is the adsorbate-adsorbent affinity parameter (g min/mg) and q is the adsorption capacity of adsorbate (mg/g).

By substituting Eq. (3.25) into (3.19), Eq. (3.20) is formed representing the variation of global mass transfer coefficient in accordance to percentage of breakthrough concentration, and the linear expression is described by Eq. (3.25)

$$\ln\left(\frac{C_o}{C_t}\right) = [K_L a]_g \times e^{-\beta q} \times t \tag{3.25}$$

$$q = B + \frac{1}{\beta} \times \ln(t) \tag{3.26}$$

where B ($= \frac{\ln([K_L\ a]_g) - \ln(\ln(\frac{C_o}{C_t}))}{\beta}$) is the potential mass transfer index relating to driving force (mg/g).

Based on Fig. 3.9, the relationship between global, external and internal mass transfer is given by Eq. (3.27):

$$[K_L\ a]_g = [K_L\ a]_f + [K_L\ a]_p \tag{3.27}$$

Using Eq. (3.27), the numerical values of $[K_La]_p$ can be computed in accordance with the breakthrough concentration as $[K_La]_g$ and $[K_La]_p$ can be calculated using Eqs. (3.25) and (3.27), respectively. Furthermore, this study also revealed the mass transfer resistance for the adsorption process onto 3D graphene-based adsorbents.

3.14 Bed depth service time model (BDST)

BDST model was commonly used to describe the relationship between the service time of adsorption column as a function of bed height. This study can derive a predictive equation based on the experimental breakthrough curve which can be used for process scale up without further experiments. The mathematical expression of BDST model is shown by Eq. (3.28):

$$t = \left(\frac{N_o{}'}{C_o\ U}\right) h - \frac{1}{k_\alpha C_o} \ln\left[\frac{C_o}{C_t} - 1\right] \tag{3.28}$$

where $N_o{}'$ is the saturation concentration predicted by the BDST model (mg/L) and k_α is the BDST rate constant (L/ min mg).

The assumptions made by this model are the bed height (h) and service time (t) presented a linear relationship under 50 % breakthrough, the moving rate in adsorption zone is constant across the column and surface adsorption is the rate controlling step (Hutchins, 1973). The k_α and $N_o{}'$ values can be evaluated from the intercept and slope

of *t* vs. *h* plot, respectively, and subsequently be used to calculate the minimum bed height required to prevent breakthrough (h_o) through Eq. (3.29):

$$h_o = \frac{U}{k_\alpha N_o'} \ln\left(\frac{C_o}{C_b} - 1\right) \tag{3.29}$$

This information is useful for preliminary setting of the minimum bed height required for the fixed-bed operation.

Chapter 4: Batch Adsorption of Pharmaceuticals and Heavy Metals onto 3D Graphene Aerogels

4.1 Introduction

Chemical functionalisation of graphene aerogel may improve its adsorption performance with additional functional groups being incorporated into its structure. A simple and efficient way to achieve this is by introducing metal oxide such as titanium dioxide (TiO_2) (Xiang et al., 2018), manganese dioxide (MnO_2) (Liu et al., 2016b) and iron (III) oxide (Fe_2O_3) (Xu et al., 2018) nanoparticles. Yu et al. (2019) reported that the addition of TiO_2 into 3D graphene composite demonstrated an outstanding adsorption capacity of 441.3 mg/g towards uranium, which was significantly higher than those of GO (280 mg/g), rGO (140.9 mg/g) and TiO_2 (98.5 mg/g). The remarkable adsorption performance was contributed by the uniform deposition of Ti rod on the graphene skeleton and synergistic effect between the oxygeneous functional of GO and free metal groups of TiO_2 (Song et al., 2019a).

Functionalisation by MnO_2 offered remarkable benefits such as unique layered nanostructures in the crystal lattices (Zeng et al., 2019), high specific surface area (Song et al., 2019a) and environmental friendliness (Saharan et al., 2019). Furthermore, the interlayer gaps of MnO_2 on graphene aerogel provided abundant nano-size channels to facilitate the transportation of adsorbate with sizes smaller than the interlayer gaps into the inner pores of graphene aerogel (Bian et al., 2015). A MnO_2/graphene nanocomposite has achieved a tetracycline removal up to 99.4 % due to complexation of Mn^{4+} and π-π interactions between the benzene ring of MnO_2/graphene nanocomposite and tetracycline (Song et al., 2019c). Jiang et al. (2019) synthesised

GO/δ-MnO_2 nanosheets for methylene blue dye adsorption. The large specific surface area (125 m^2/g) and layered structure embedded with K^+ functionality has significantly improved the dye adsorption capacity of GO/δ-MnO_2 nanosheets (1432 mg/g) by 5 times as compared to pristine δ-MnO_2 (267.6 mg/g) (Jiang et al., 2019). Therefore, the incorporation of MnO_2 on 3D graphene aerogel offers great opportunity in tailoring microstructures within the adsorbent as well as addition of new chemical functional groups.

The selection of binding and functionalising agents used in the graphene aerogel synthesis plays an important role in determining the adsorption capability of the assembled graphene aerogel. The formation of microstructure and surface functionalities are dependent of the choice binder and functionaliser, respectively (Lai et al., 2019; Xu et al., 2018). Carboxylmethyl cellulose (CMC) is widely used in the assembly of aerogels as it is biodegradable, low cost and environmental friendly (Varaprasad et al., 2017). Additionally, the hydroxyl groups of CMC could successfully bind with oxygenated functional groups on GO through hydrogen bonding, forming a mechanically strong graphene aerogel for use in wastewater treatment (Ge et al., 2018; Luo et al., 2019). Among the transition metals used in functionalisation, zirconium (Zr) showed promising improvement on non-functionalised graphene aerogel. It was reported to be biologically inert with relatively low toxicity, good resistance against oxidising chemicals, acids and bases and high thermal stability (Elanchezhiyan et al., 2016). Furthermore, Zr could bind with CMC functional groups through chelation which prevented its leakage into the environment (Liu et al., 2016d).

In the present research, three different 3D graphene-based adsorbents were synthesised and applied for the removal of pharmaceuticals (diclofenac and acetaminophen) and heavy metals (copper and nickel) in aqueous media. This chapter

presents the characterisation results of the developed adsorbents along with the results of batch adsorption equilibrium, kinetic and thermodynamics. Lastly, the batch adsorption mechanisms were discussed.

4.2 Batch adsorption of diclofenac onto rGOA

4.2.1 Adsorbent characteristics

The density of rGOA was determined by dividing the aerogel mass by its volume (Liang et al., 2018). The measured density of rGOA was 20.39 ± 5.28 mg/cm^3 which included the air within the aerogel pores. As observed in Fig. 4.1(a), the rGOA was supported on a grass (mass = 63.5 mg) without any noticeable bending of the grass. The low density of rGOA was attributed to the porous network interpenetrating the skeleton of graphene sheets (Liang et al., 2018).

The surface morphology of rGOA was investigated by SEM as presented in Fig. 4.1(b) – (c). It manifested a 3D porous structure with interconnected thin layers of graphene sheets as observed in Fig. 4.1(b). Upon inspection at higher magnifications (Fig. 4.1(c)), the aerogel pores showed wrinkle features. The pore sizes ranged from hundred nanometres to several micrometres, formed by the coalescing and overlapping of graphene sheets. Hence, the morphological study revealed that rGOA consisted of various pore sizes which might facilitate the migration of diclofenac molecules within the adsorbent.

(a)

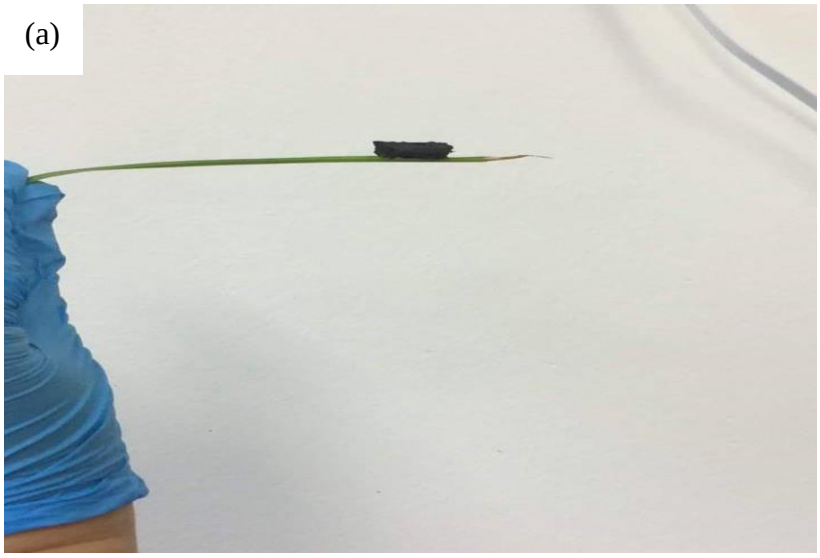

(b)

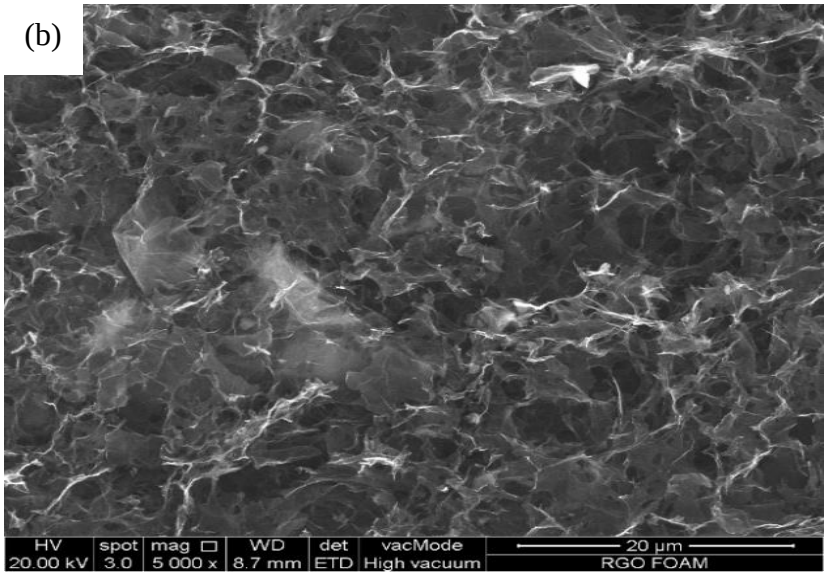
HV
20.00 kV
spot
3.0
mag
5 000 x
WD
8.7 mm
det
ETD
vacMode
High vacuum
20 µm
RGO FOAM

(c)

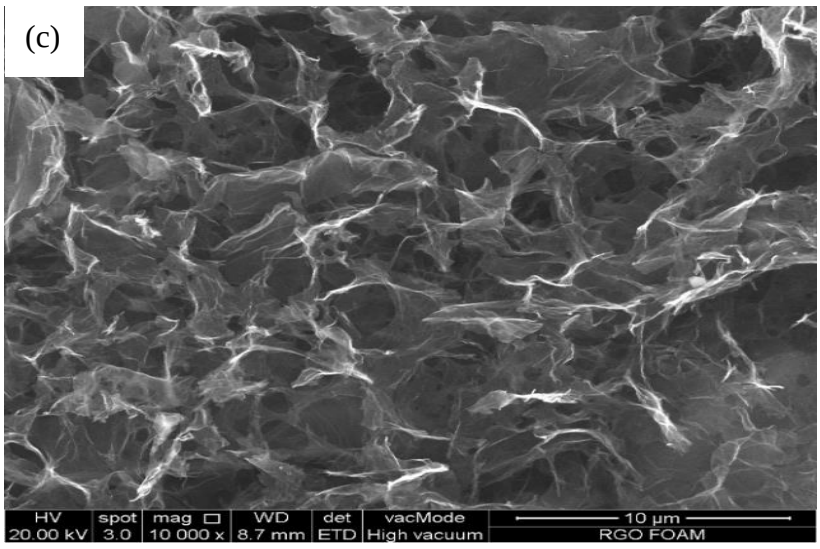
HV
20.00 kV
spot
3.0
mag
10 000 x
WD
8.7 mm
det
ETD
vacMode
High vacuum
10 µm
RGO FOAM

(d)

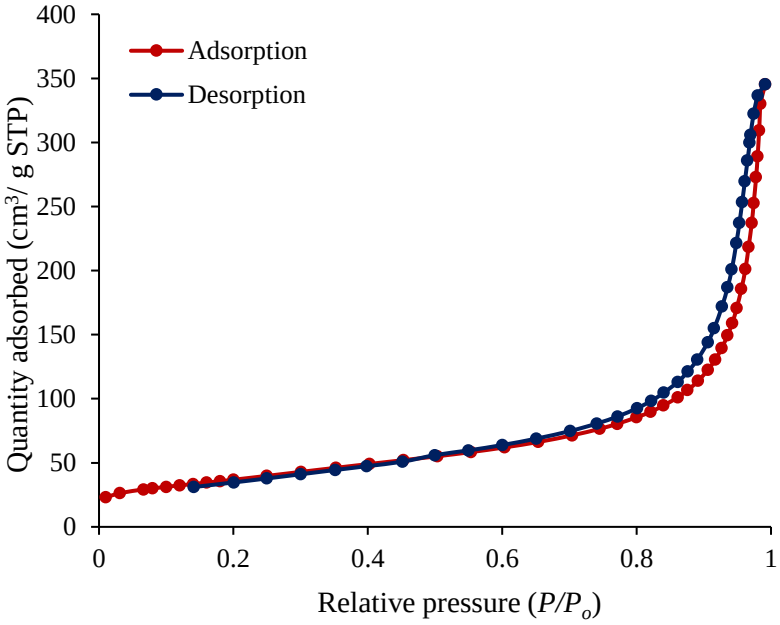
Adsorption
Desorption
Quantity adsorbed (cm³/ g STP)
Relative pressure (P/P_o)
0
50
100
150
200
250
300
350
400
0
0.2
0.4
0.6
0.8
1

(e)

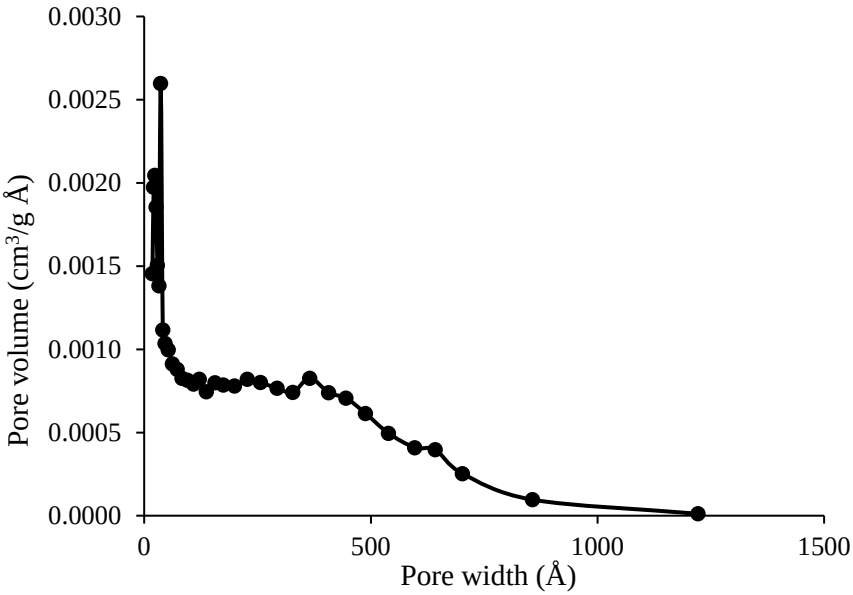
Pore volume (cm³/g Å)
Pore width (Å)
0.0000
0.0005
0.0010
0.0015
0.0020
0.0025
0.0030
0
500
1000
1500

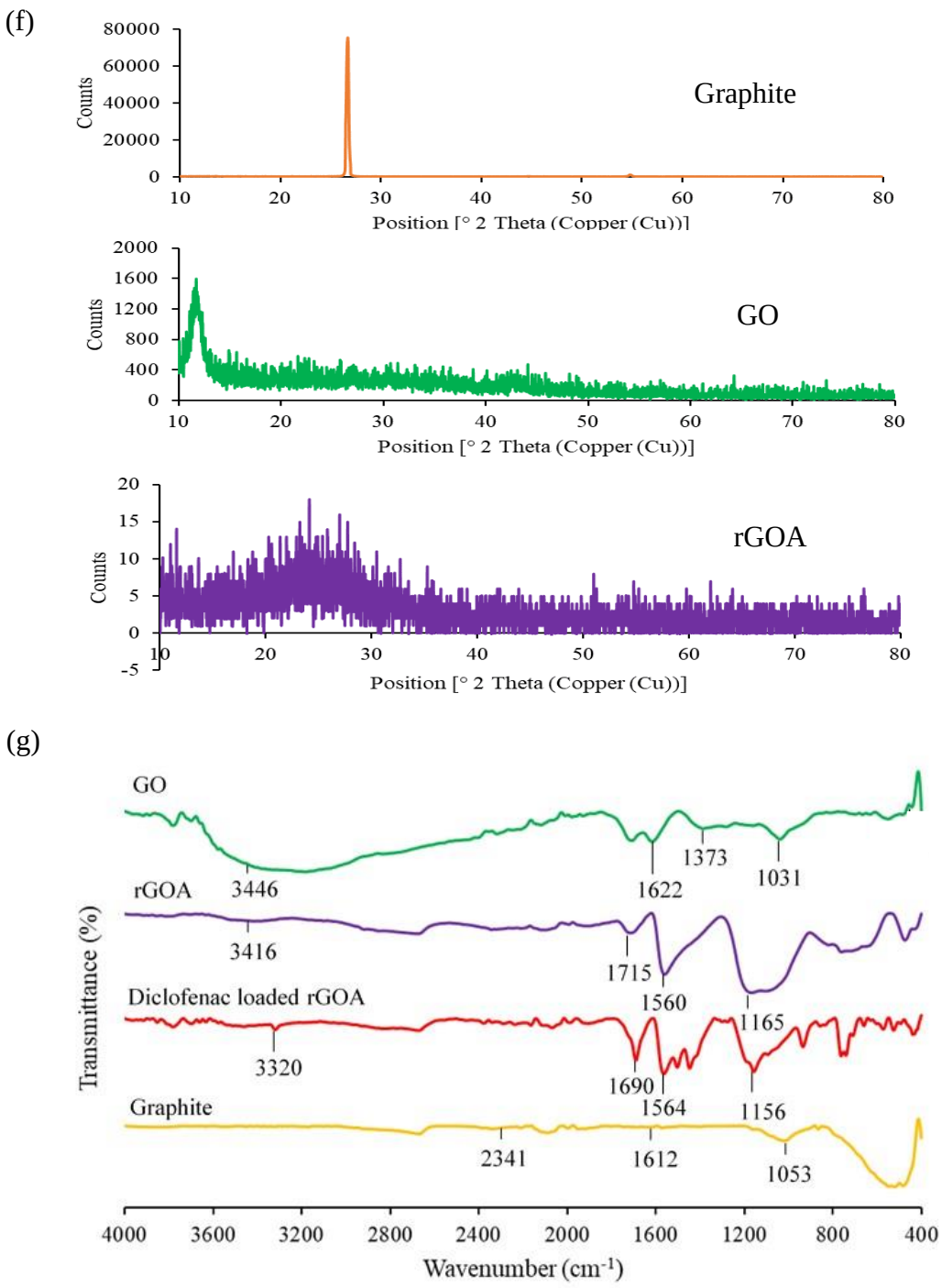

Fig. 4.1 Characterisation of rGOA (a) on a grass photo, SEM images (b) x5000 and (c) x10000 magnifications, (d) N_2 adsorption-desorption isotherm, (e) pore size distribution, (f) XRD scans and (g) FTIR spectra comparison.

The specific surface area and pore size distribution of rGOA were measured by N_2 adsorption-desorption isotherms and the results are illustrated in Fig. 4.1(d) and (e), respectively. As shown, the rGOA exhibited a Type IV isotherm profile indicating the presence of mesopores in the adsorbent (Rahmani et al., 2018). Furthermore, the isotherm profile showed the H_3-type hysteresis loop over a relative pressure range of 0.45 – 1.00, associated with the aggregation of plate-like particles and open large pores in the rGOA (Cheng et al., 2017). According to Brunauer-Emmett-Teller (BET) model, the specific surface area (S_{BET}) was reported to be 132.19 m^2/g. Moreover, the pore size distribution of rGOA (Fig. 4.1(e)) calculated by Barret-Joyner-Halenda (BJH) method showed the majority of the pores were distributed within the range of 2 to 90 nm, with average pore width of 14 nm. Notably, large proportion of mesopores were identified over a narrow distribution from 2 to 4 nm with a distinctive peak pore width centred at approximately 3.6 nm. The cumulative pore volume of rGOA was 0.5388 cm^3/g. The BET analysis coupled with SEM and TEM findings revealed that the rGOA was a mesoporous material.

The crystal structures of pristine graphite, GO and rGOA were analysed using XRD and the results are shown in Fig. 4.1(f). For pristine graphite, the characteristic diffraction peak of graphite at (0 0 2) crystal plane was detected at $2\theta=26.69°$ and the d-spacing was 0.3340 nm. In comparison, a broad peak at $2\theta=11.77°$ was observed in GO and the corresponding d-spacing was 0.7519 nm. The increase in d-spacing between GO and graphite suggested the successful incorporation of oxygen-containing functional groups into graphite crystal structure from the modified Hummers method. However, the GO dominant peak ($2\theta=11.77°$) disappeared and a new broad peak was determined at $2\theta=24.11°$ in rGOA. Upon chemical reduction, the oxygen-containing groups and the interlayer of GO greatly released, resulting in the decreased in d-spacing

of rGOA (0.3691 nm) (Shan et al., 2016). Notably, rGOA exhibited the broadest diffraction peak as compared to GO and pristine graphite, indicating rGOA was an amorphous material with the highest disorder in crystallinity, followed by GO and graphite.

The chemical functional groups existed in graphite, GO and rGOA before and after adsorption of diclofenac were determined by FTIR. Fig. 4.1(g) shows that the graphite spectrum has peaks at 2341 (sp^2 and sp^3 hybridized C-H stretch), 1612 (sp^2 hybridized C=C stretch) and 1053 cm^{-1} (C-O stretch), whereas the GO spectrum contains peaks at 3446 (O-H stretch), 1622 (O-H stretch), 1373 (C-O stretch) and 1031 cm^{-1} (C-O stretch) (Aleksandrzak et al., 2017; Hadi et al., 2018; White et al., 2018). The chemical functional groups in GO which interacted with diclofenac were hydroxyl, carboxyl and alkoxy groups. These functional groups were eliminated and reduced during the reduction of GO to rGOA, as indicated by the comparatively lower peak intensity and relocation of peaks (1715, 1560 and 1165 cm^{-1}) in the rGOA spectrum (Fernández-Merino et al., 2010). The resultant rGOA comprised of oxygen-rich functional groups such as hydroxyl group (3416 cm^{-1}), carbonyl or carboxyl group (1715 cm^{-1}), deformed C-C bond from existing epoxy group (1560 cm^{-1}) and carboxylic group (1165 cm^{-1}) (Liu et al., 2014a; Oh et al., 2014). This finding implied that the reduction process has not completely removed the oxygen-rich functional groups, and the remaining groups in rGOA had facilitated the adsorption of diclofenac. This statement is supported by the FTIR spectrum of rGOA-diclofenac which displays the shift of peaks to 3320, 1690, 1564 and 1156 cm^{-1} after diclofenac adsorption.

PZC is the pH at which the adsorbent surface acquired a net zero charge. The PZC of rGOA was found to be 6.3 indicating that the surface of the aerogel was

positively charged at pH < 6.3. Deprotonation occurred at pH > 6.3 causing the surface of rGOA to become negatively charged.

4.2.2 Effect of dosage

The dependence of diclofenac removal efficiency and adsorption capacity onto rGOA dosage (0.1 – 0.6 g/L) is illustrated in Fig. 4.2. An increase in removal efficiency (32 to 89 %) was observed as the rGOA dosage was increased from 0.1 – 0.4 g/L, followed by a plateau pattern as the dosage exceeded 0.4 g/L. This trend was due to the greater amount of sorption sites available at higher rGOA dosage enabling more diclofenac to be adsorbed onto the aerogel. However, the removal efficiency showed minimum improvement beyond 0.4 g/L because the effective surface area for diclofenac adsorption was reduced owing to aggregation of particles at excessive dosage (Darweesh & Ahmed, 2017b).

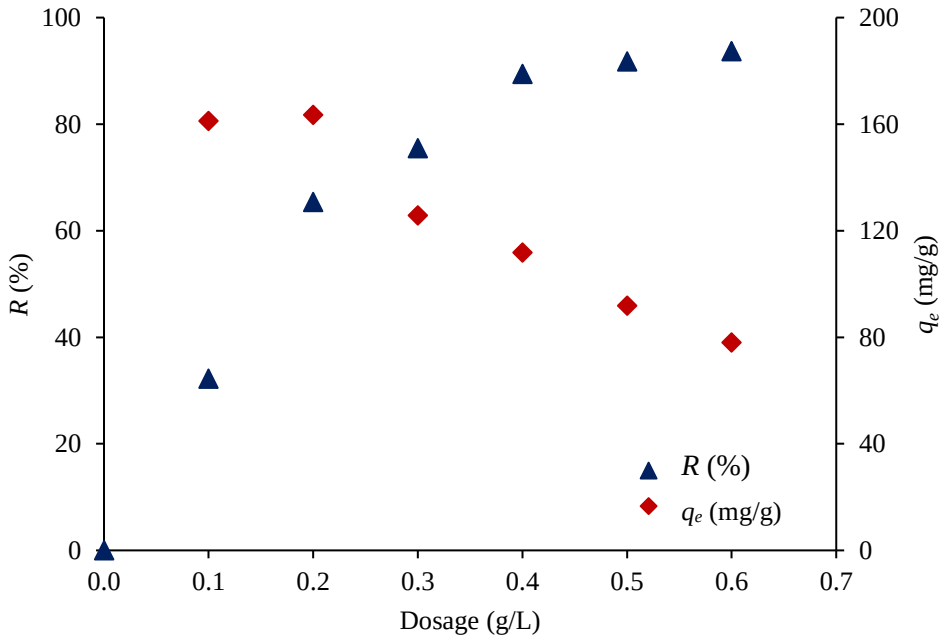

Fig. 4.2: Effect of rGOA dosage on diclofenac removal and adsorption capacity.

In contrast, the adsorption capacity (q_e) exhibited a decreasing pattern with increasing rGOA dosage. This implied that large number of adsorption sites were not fully utilised at excess dosage which possibly caused by particle agglomeration that hindered the diffusion of diclofenac in the rGOA (Abo El Naga et al., 2019). As such, a dosage of 0.4 g/L was selected to be used in subsequent experiments as the removal efficiency was relatively high at this dosage.

4.2.3 Effect of pH

The adsorption of an ionisable micropollutant onto the adsorbent surfaces could be contributed by electrostatic interactions, depending on the acid dissociation constant (pKa) of the compound (Nam et al., 2015). In this study, the effect of pH was investigated over a wide pH range of 2 – 11. Fig. 4.3 shows the removal efficiency of diclofenac by the rGOA at different pH.

The pKa of diclofenac is 4.2 suggesting that the pharmaceutical is a neutral ion species under acidic environment (pH < pKa). The control plot obtained from the experiment without the use of rGOA showed that the removal efficiency of diclofenac was highest between pH 2 – 4 (pH < pKa), but it decreased at pH > 4.2 (pKa) and no diclofenac removal was observed between pH 6 – 11. In contrast, the effect of solution pH with the presence of rGOA showed that the removal efficiency of diclofenac was relatively high (81 < R < 99 %) between pH 2 – 9 and drastically decreased at pH 10-11. The results implied that the solution pH had a significant effect on the adsorption of diclofenac onto rGOA.

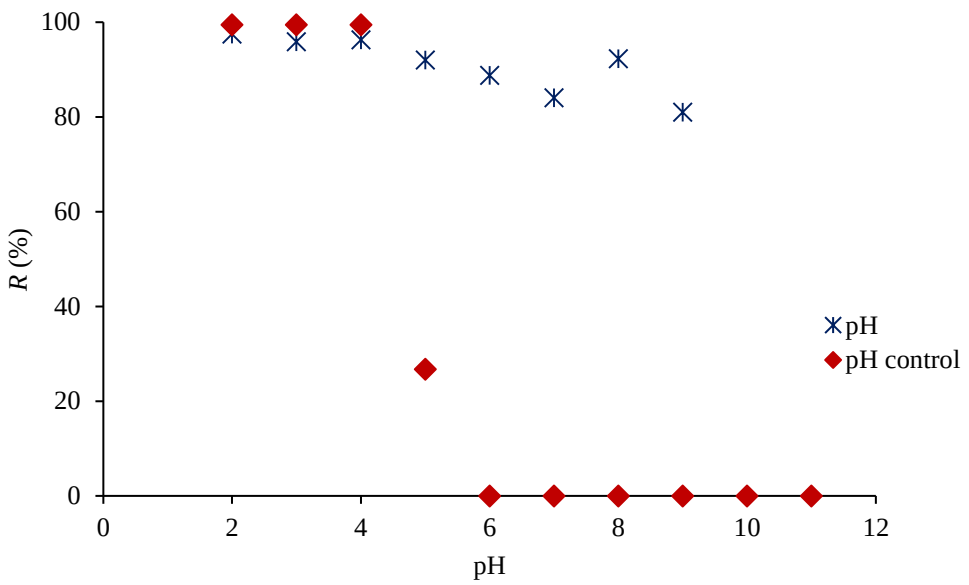

Fig. 4.3: Effect of pH on diclofenac removal efficiency.

At pH > pKa, the diclofenac compound was deprotonated which caused electrostatic repulsion between the dissociated diclofenac and negatively charged rGOA over wide range of pH (pH 4.2 – 11). Therefore, electrostatic interaction is not appropriate to describe the adsorption mechanism at pH > 6.3 (PZC = 6.3). Due to the electrostatic repulsion between the negatively charged diclofenac and rGOA, the removal of diclofenac was slightly lowered at pH > 6.3. Between pH 6.3 and 9, the adsorption of diclofenac on rGOA could be due to hydrogen bonding between the phenolic/carboxylic acid protons from diclofenac and the oxygeneous functional groups of rGOA such as carboxyl, hydroxyl and epoxy groups (Bhadra et al., 2016; Saucier et al., 2015). At pH > 10, more functional groups on rGOA were deprotonated resulting in an electrostatic repulsive environment and the hydrogen bonds formation was hindered.

4.2.4 Effect of shaking speed

Fig. 4.4 illustrates the effect of shaking speed on diclofenac removal by rGOA. The removal percentage was increased from 18.99 to 77.89 % as the shaking speed was increased from 50 to 200 ppm before dropping to 55.89 % at 250 rpm.

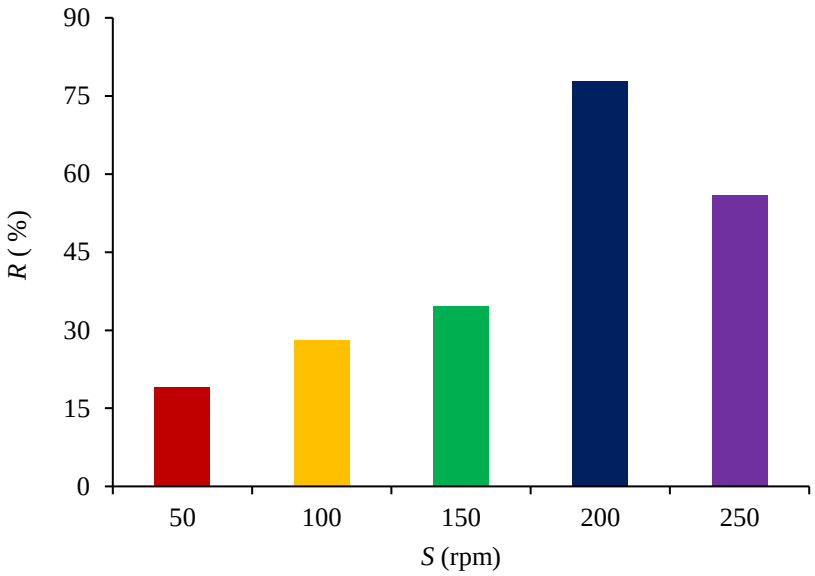

Fig. 4.4: Effect of shaking speed on diclofenac adsorption onto rGOA.

The high shaking speed improved the kinetic energy gained by the adsorbate and adsorbent, causing rapid collision between the two species and reduction of external diffusional layer, thus improving the diclofenac adsorption (Mohammed & Kareem, 2019). However, the structure of rGOA was collapsed at 250 rpm and the loss of sorption sites resulted in lower diclofenac removal.

4.2.5 Adsorption equilibrium

For determination of the adsorption equilibrium parameters, the experimental data were fitted to the Langmuir, Freundlich, Temkin and Dubinin- Radushkevich (D-R) models. The isotherm plots are shown in Fig. 4.5 while the parameters are presented in Table 4.1. Based on R^2 values, the adsorption equilibrium was best described by the Freundlich model ($0.9500 < R^2 < 0.9802$), followed by the Langmuir ($0.9432 < R^2 <$

0.9685), Temkin (0.9053< R^2 < 0.9413) and D-R (0.8589 < R^2 < 0.8872). Accordingly, multi-layer of diclofenac molecules were adsorbed onto heterogeneous surface of rGOA which was associated with different adsorption energy (Jiryaei Sharahi & Shahbazi, 2017). The Freundlich model further assumed that the stronger sorption sites of rGOA were first occupied and adsorption affinity depleted as surface coverage increased (Tan et al., 2014). The process favourability was related to the Freundlich exponent (*n*). According to the model, adsorption would be favourable if n was between 1 and 10. As observed from Table 4.1, diclofenac was favourably adsorbed onto rGOA as *n* varied from 1.99 to 2.59 at the range of temperatures studied (Jiryaei Sharahi & Shahbazi, 2017).

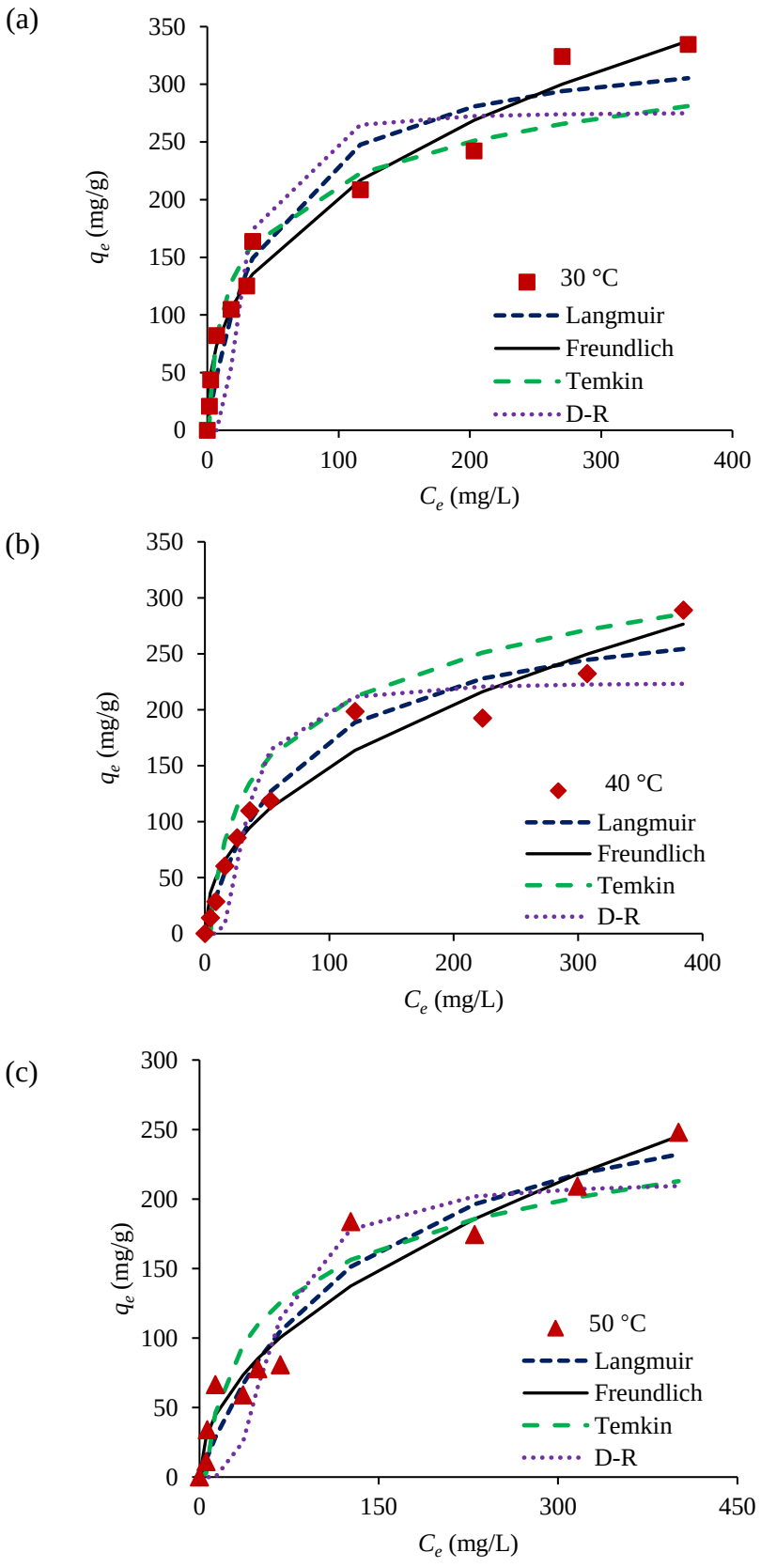

Fig. 4.5: Adsorption equilibrium isotherms (a) 30 °C, (b) 40 °C and (c) 50 °C for diclofenac-rGOA system.

4.2.6 Adsorption kinetic

Adsorption kinetic study is an important aspect in the design of an adsorption system as it determines the rate and mechanism of the process. The variation of adsorption capacity of diclofenac with contact time is illustrated in Fig. 4.6(a). It can be observed that the adsorption capacity increased rapidly from 0 to 20 min due to the availability of abundant sorption sites at the initial period of the process. Thereafter, the adsorption of diclofenac progressed slower from 20 to 40 min, and eventually reached equilibrium at contact time > 40 min. The plots further revealed that the adsorption capacity of diclofenac at equilibrium was increased as the initial concentration increased. Liu et al. (2017a) explained that this phenomenon was due to the increased in driving force for mass transfer of adsorbate from the liquid to the adsorbent.

The experimental data were fitted to the pseudo-first order, pseudo-second order and Elovich kinetic models. The plots of the kinetic models are depicted in Fig. 4.6(a) whereas the kinetic parameters are summarised in Table 4.1. The best fit model was the pseudo-first-order kinetic model as shown by the highest R^2 (0.8467 – 0.9621). Furthermore, the predicted adsorption capacities were closer to the experimental values for the range of initial concentrations investigated. This implied that the adsorption of diclofenac onto rGOA was due to physisorption and the rate of adsorption was proportional to the availability of free sorption sites (Lagergren, 1898).

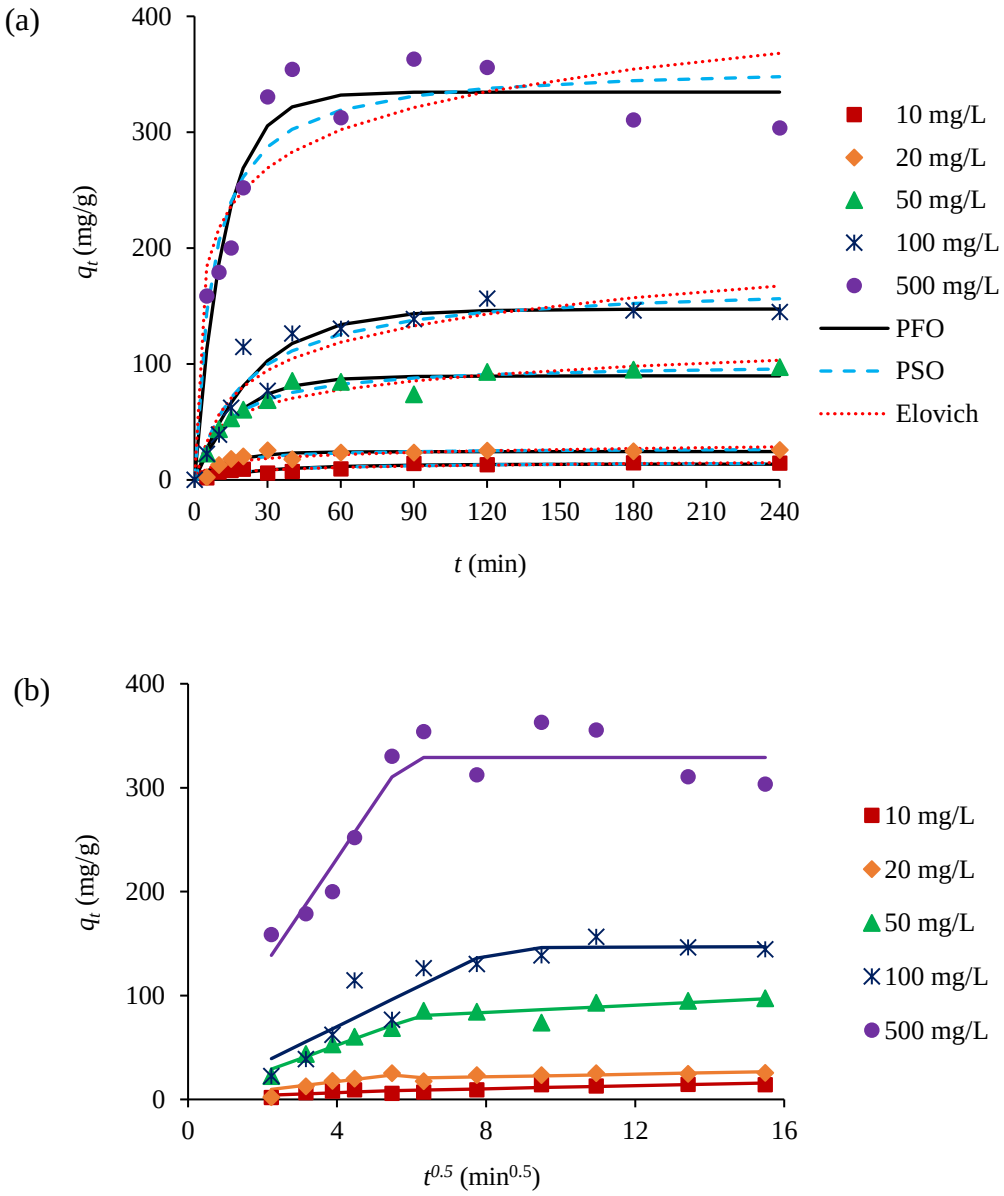

Fig. 4.6: (a) Adsorption kinetic and (b) intraparticle diffusion plots at different initial concentrations for diclofenac-rGOA system.

Table 4.1: Adsorption equilibrium, kinetic and thermodynamic parameters for diclofenac adsorption onto rGOA.

Equilibirum	**Temperature (°C)**		
	30	**40**	**50**
Langmuir			
q_m (mg/g)	342.55	302.28	308.09
K_L	0.0224	0.0138	0.0076
R_L	0.0820	0.1268	0.2077
R^2	0.9498	0.9685	0.9432
Freundlich			
K_F	34.45	18.66	12.08
n	2.59	2.21	1.99
R^2	0.9802	0.9634	0.9500
Temkin			
A_T	0.6874	0.2292	0.1903
b	49.56	40.82	54.71
R^2	0.9413	0.9136	0.9053
Dubinin-Radushkevich			
K_{DR}	8.87E-05	1.30E-04	4.01E-04
q_{DR} (mg/g)	276.08	224.49	213.18
R^2	0.8589	0.8872	0.8768

Kinetic	C_o **(mg/L)**				
	10	**20**	**50**	**100**	**500**
Pseudo-first order					
$q_{e,\,exp}$	14.27	25.67	97.36	144.71	303.53
$q_{e,\,calc}$	13.58	24.47	89.73	147.46	334.63
k_1	0.0327	0.0727	0.0581	0.0399	0.0815
R^2	0.8467	0.9188	0.9621	0.9374	0.9369
Pseudo-second order					
$q_{e,\,calc}$	15.48	27.36	101.03	170.13	358.71
k_2	0.0028	0.0034	0.0007	0.0003	0.0004
R^2	0.8781	0.9017	0.9692	0.9275	0.9174
Elovich					
α	1.71	7.27	21.49	17.44	452.67
β	0.3291	0.2061	0.0546	0.0286	0.0210
R^2	0.8951	0.8551	0.9479	0.9050	0.8623

Thermodynamic	**Δ*G* (kJ/mol)**			**Δ*H***	**Δ*S***
C_o **(mg/L)**	**30 °C**	**40 °C**	**50 °C**	**(kJ/mol)**	**(kJ/mol K)**
10	-6.40	-3.05	-1.88	-12.82	-0.2261
20	-7.19	-3.11	-4.47	-10.38	-0.1363
40	-6.14	-3.47	-4.30	-8.32	-0.0921
60	-4.42	-3.12	-1.30	-9.20	-0.1562
80	-3.60	-2.90	-1.25	-7.28	-0.1174
100	-3.93	-2.12	-0.48	-9.07	-0.1725
200	-1.46	-1.29	-1.00	-2.17	-0.0230

4.2.7 Thermodynamic analysis

The process spontaneity and feasibility were evaluated based on thermodynamic parameters such as the Gibbs free energy change (ΔG), entropy change (ΔS) and enthalpy change (ΔH). Table 4.1 shows that the ΔG were negative for all temperatures and initial concentrations assayed. This finding confirmed that removal of diclofenac by rGOA was thermodynamically feasible and spontaneous (Liang et al., 2018). Nevertheless, ΔG was higher at higher initial concentration and higher temperature, indicating that the process was more spontaneous at low concentration and temperature conditions (Ooi et al., 2017). Furthermore, diclofenac was physically adsorbed onto rGOA as the ΔG (-7.19 to -0.48 kJ/mol) were within the range of $-20 < \Delta G < 0$ kJ/mol. The adsorption process was exothermic as supported by the negative ΔH shown in Table 4.1. The ΔH varied from -12.82 to -2.17 kJ/mol indicating the process to be physisorption (Zhang et al., 2018). The negative ΔS values corresponded to a decrease in randomness at the solid-liquid interface when diclofenac was adsorbed onto rGOA.

4.2.8 Regeneration study

Fig. 4.7 demonstrates the regeneration efficiency of rGOA versus adsorption-desorption cycle number. It can be seen that the regeneration efficiency of rGOA was relatively high (> 73 %) after 5 successive adsorption-desorption cycles. The declining trend was due to structural collapse and also incomplete regeneration of diclofenac at the previous adsorption cycle causing reduction in vacant sites for diclofenac adsorption in subsequent cycles.

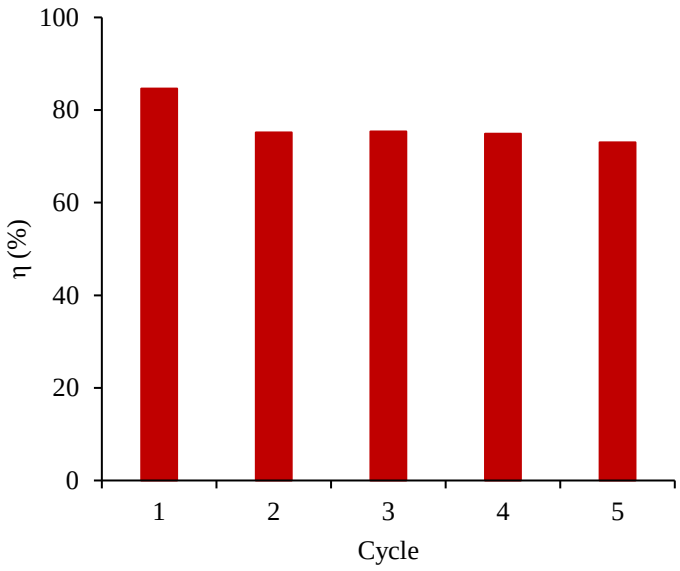

Fig. 4.7: Regeneration efficiency versus adsorption-desorption cycle for diclofenac-rGOA system.

4.2.9 Adsorption mechanisms

The intraparticle diffusion model is commonly used to identify the rate controlling step of adsorption process. In general, the adsorption system is controlled solely by intraparticle diffusion if the intraparticle diffusion plot showed a straight line passing through the origin. However, the adsorption of diclofenac onto rGOA portrayed intraparticle diffusion plots with multi-linearity. Moreover, the plots did not pass through the origin (Fig. 4.6(b)). The results suggested that the adsorption of diclofenac onto rGOA was controlled by several steps such as boundary layer and intraparticle diffusion (Leone et al., 2018; Liu et al., 2017a).

Diclofenac is a weak acid with a pKa of 4.2 (Feng et al., 2018). Hence, the mechanisms involved in the adsorption of diclofenac was influenced by its surrounding pH. From the initial single-factor study, the percentage removal of diclofenac was approximately 96 % at pH < pKa, and decreased slightly (to ~81 %) as pH was increased to 9. The high removal of diclofenac at pH < pKa was not due to electrostatic

attraction as diclofenac existed in neutral form, while rGOA adsorbent was positively charged (PZC = 6.3). Therefore, the large removal of diclofenac at the acidic condition could be attributed to other adsorption mechanisms such as precipitation (Nam et al., 2015; Samah et al., 2018). At pH > pKa, dissociation of diclofenac occurred, making it negatively charged. Hence, between pH 4.2 (pKa of diclofenac) and 6.3 (PZC of rGOA), electrostatic attraction could play a major role in attaching diclofenac anions to the positively charged surface of rGOA. At pH > 6.3, rGOA became negatively charged, and this caused the decrease in diclofenac removal as electrostatic repulsion became dominant. Nevertheless, the removal of diclofenac was still significant between pH 6.3 and 9 (decreased from ~89 to 81 %). This observation suggested that non-electrostatic mechanisms such as hydrogen bonding, hydrophobic attraction and π−π electron donor-acceptor (EDA) interaction between the rGOA and aromatic rings of diclofenac metabolites contributed to the removal of diclofenac under the basic condition (Awad et al., 2020; Dai et al., 2011; Lonappan et al., 2016).

The adsorption mechanisms between diclofenac and rGOA could also be explained based on the FTIR results (Fig. 4.2(g)). As previously discussed, the rGOA spectrum showed peaks which were consistent with hydroxyl, carbonyl/carboxyl and epoxy groups, and these oxygen-rich sites had strong affinity for diclofenac via hydrogen bonding (Fang et al., 2014). The FTIR spectrum for rGOA-diclofenac (Fig. 4.2(g)) showed that the original peaks of rGOA (3416, 1560 and 1165 cm^{-1}) were shifted to 3320, 1564 and 1156 cm^{-1}, respectively, after adsorption of diclofenac. This result suggested the possible occurrence of hydrogen bonding between the functional groups of rGOA and diclofenac. Notably, the peaks at 1564 and 1156 cm^{-1} corresponded to the NH bend and CN stretch from secondary amine, respectively, confirming the attachment of the electronegative sites of diclofenac (nitrogen atom) to

the hydrogen atoms of the functional groups in rGOA through hydrogen bonding (Lonappan et al., 2018).

4.3 Batch adsorption of acetaminophen onto RGM

4.3.1 Adsorbent characteristics

The morphological characteristics of RGM was examined by SEM as presented in Fig. 4.8(a) – (c). The surface of the aerogel was interconnected by smooth wrinkled lamellar layers, forming a porous structure (Fig. 4.8(a)). Furthermore, there was no agglomeration observed on the RGM surface, indicating the carboxymehyl cellulose has bonded with the active groups on the GO surface without damaging the internal structure of GO (Rao et al., 2018). The pore diameter was estimated to range from 138.4 to 235.3µm. The atomic percentage for carbon (C), oxygen (O), potassium (K) and Mn elements are 35.16, 49.31, 0.81 and 14.73 %, respectively, according to the EDX results. This finding confirmed the presence of Mn element in RGM which was originated from MnO_2 during the aerogel synthesis. Upon inspection at higher magnification (Fig. 4.8(b), the RGM surface was deposited with clusters of MnO_2 nanoparticles. The diameter of MnO_2 particles were approximately 344.8 – 493.8 nm as shown in Fig. 4.8(c). The as-synthesised MnO_2 exhibited spherical structure and hence the MnO_2 could be in δ-phase (Huang et al., 2015a; Liu et al., 2019a). Furthermore, the aggregated δ-MnO_2 nanoparticles formed a platelet-like structure across the surface of graphene aerogel. The results revealed that RGM consisted various pores size and its surface was decorated with δ-MnO_2 which could facilitate the transportation of acetaminophen within the RGM.

N_2 adsorption-desorption isotherms were employed to evaluate the specific surface area and pore size distribution of RGM as illustrated in Fig. 4.8(d) and (e), respectively. The isotherm curve of RGM follows the Type IV isotherm accompanied

by a H_3-hysteresis loop over relative pressures of 0.45 – 1. This implied that RGM structure consisted of mesopores associated with the aggregation of non-rigid plate-like particles and open large pores (Liu et al., 2019a). The specific surface area of RGM was determined to be 6.2825 m^2/g according to the BET model. The pores characteristics of RGM was calculated by the BJH method and the pore size distribution is illustrated in Fig. 4.8(e). The RGM aerogel exhibited an average pore width of 2.02 nm and majority of the pores were distributed within 2 – 2.08 nm. The RGM adsorbent also possessed a large proportion of mesopores over the pore width of 1.98 – 2.07 nm as indicated by the narrow peak in the pore size distribution curve. The cumulative pore volume of RGM was 0.017842 cm^3/g. The BET, BJH and SEM results concluded that RGM was a mesoporous adsorbent which could offer abundant sorption sites for acetaminophen adsorption.

The surface charge of RGM was determined by the PZC test. PZC is the pH at which the adsorbent surface acquired a neutral or net zero charge. The PZC of RGM was identified to be 6.5 as shown in Fig. 4.8(f). This result implied that the aerogel surface was positively charged at pH < 6.3 and deprotonation occurred at pH > 6.5 forming a negatively charged surface.

The surface functional groups on GO, RGM and acetaminophen loaded RGM were identified by FTIR and the results are illustrated in Fig. 4.8(g). The GO spectrum manifested characteristic peaks located at 3446 (O-H stretch), 1622 (O-H stretch), 1373 (C-O stretch) and 1031 cm^{-1} (C-O stretch), indicating the presence of hydroxyl, carboxyl and alkoxyl functional groups on GO surface. By comparing the GO and RGM spectra, the intensities of the peaks at 3446, 1622 and 1031 cm^{-1} were significantly reduced. This was due to the removal of oxygen functional groups of GO by thermal reduction (Saleem et al., 2018). Fig. 4.8(g) shows the RGM spectrum has peaks at 3203,

2880, 1572, 1415 and 1325 cm^{-1} which were due to O-H bonds stretching (Darvishi et al., 2018), C-H bonds stretching (Zhang et al., 2019a), -COO^- groups stretching (Liang et al., 2019), C=O stretching vibration (Akpotu & Moodley, 2018b) and O-H groups vibration bending (Dai & Huang, 2017), respectively. The detection of remaining O-H and C-H groups in RGM after thermal reduction could be due to the CMC binder (Liu et al., 2019a). Furthermore, the characteristic peaks at 716 and 499 cm^{-1} represented the Mn-O stretching vibration and the identification of δ-MnO_2 birnessite structure on RGM (Al-Ghouti et al., 2009; Baruah & Kumar, 2018). Notably, the FTIR spectrum of acetaminophen-loaded RGM displayed the shift of peaks to 3176, 2881, 1571, 1414, 1326, 1030, 720 and 496 cm^{-1} with lower peak intensities as compared to RGM spectrum. The FTIR results suggested the successful incorporation of δ-MnO_2 onto RGM aerogel which increased its surface functionality and the interaction of acetaminophen with the functional groups in RGM.

The XRD patterns of graphite, GO and RGM are illustrated in Fig. 4.8(h). The diffraction peaks of graphite, GO and RGM located at 26.69, 11.77 and 12.57°, corresponded to the interlayer spacing (d-spacing) of 0.3340, 0.7519 and 0.7042 nm, respectively. The insertion of oxygen-containing functional groups into graphite structure was proven by the larger interlayer spacing of GO than graphite (0.7519 > 0.3340 nm). Additionally, the presence of birnessite MnO_2 on graphene aerogel was confirmed by the peak at 12.57° in the XRD pattern for RGM (Song et al., 2019b). Furthermore, the RGM was amorphous as indicated by the relatively broad diffraction peak and low intensity counts.

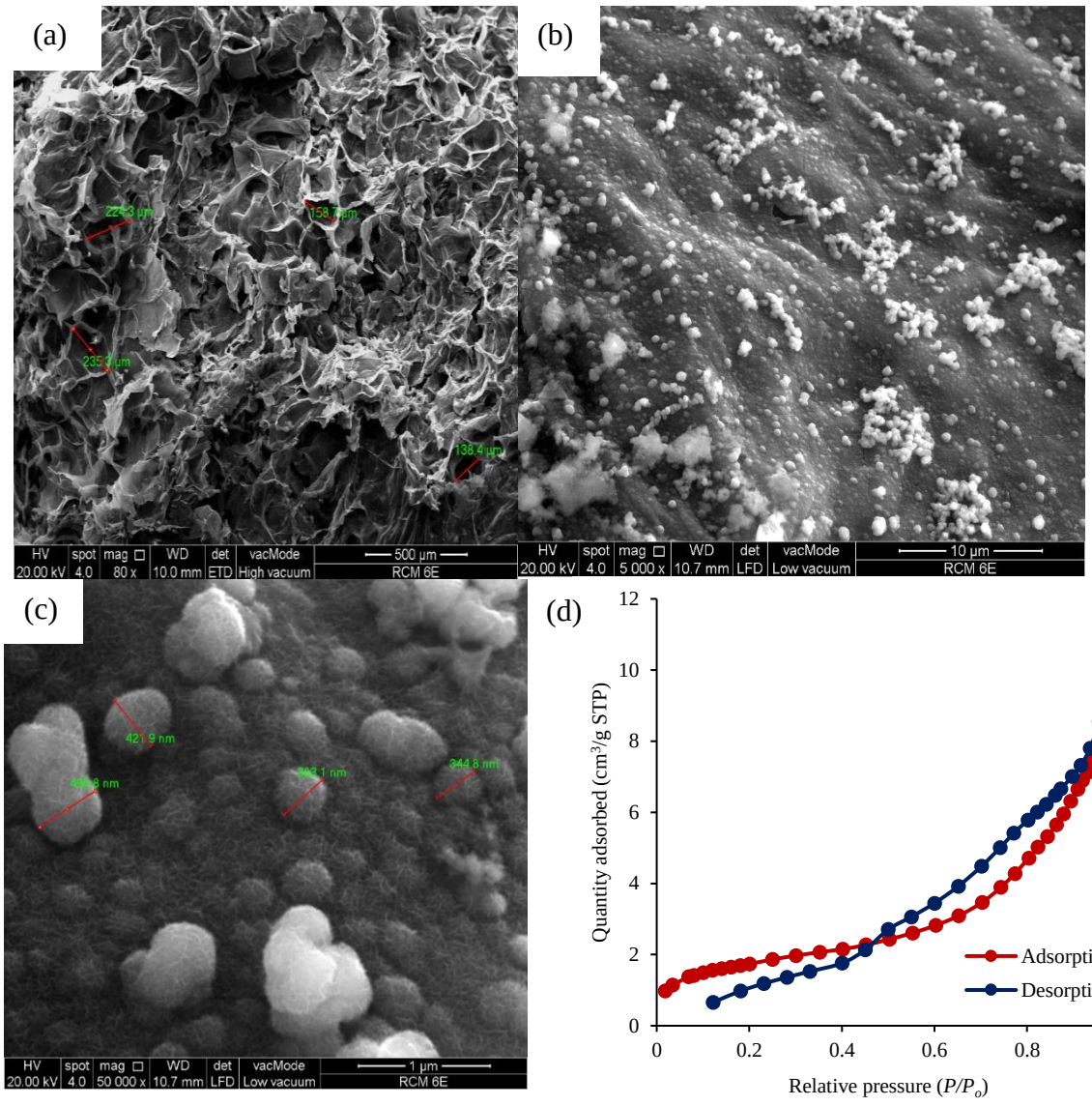
(a)
(b)
(c)
(d)
(e)
(f)
Quantity adsorbed (cm³/g STP)
Relative pressure (P/Po)
Adsorption
Desorption
Pore Volume (10⁻³ cm³/g Å)
Pore width (Å)
ΔpH
pH

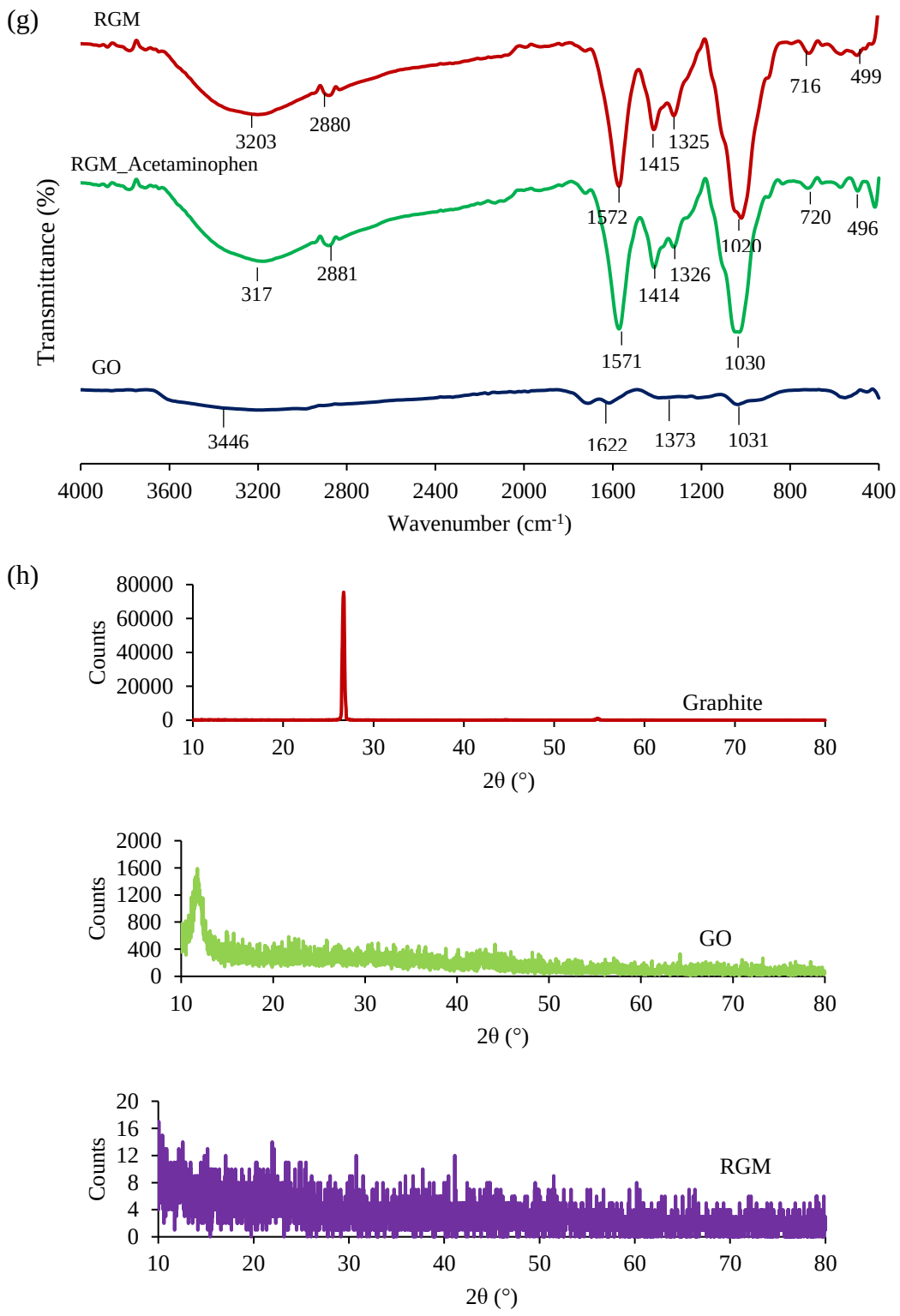

Fig. 4.8. Characterisation of RGM: SEM images at (a) x50, (b) x5000 and (c) x50000 magnifications, (d) BET isotherm, (e) pore size distribution and (f) PZC; for RGM; (g) FTIR spectra and (h) XRD patterns comparison.

4.3.2 Effect of dosage

Fig. 4.9 illustrates that the acetaminophen removal efficiency increased from 34.7 – 96.1 % as the RGM dosage was increased from 0.2 to 0.6 g/L and it reached 100 % between dosages of 0.8 – 1.2 g/L before dropping to 95 % as the dosage was further increased to 2 g/L. On the other hand, the adsorption capacity exhibited a decreasing trend with the increased in RGM dosage. The result was due to the availability of larger amount of sorption sites at higher dosage, allowing more acetaminophen to be adsorbed from the aqueous body. However, particle agglomeration occurred at excessively large dosages which extended the diffusional pathway in the RGM, thus causing the decrease in removal efficiency (Wong et al., 2018). As such, 0.6 g/L dosage was selected for further batch adsorption study as relatively high removal efficiency (96.13 %) and adsorption capacity (80.11 mg/g) were attained at this dosage.

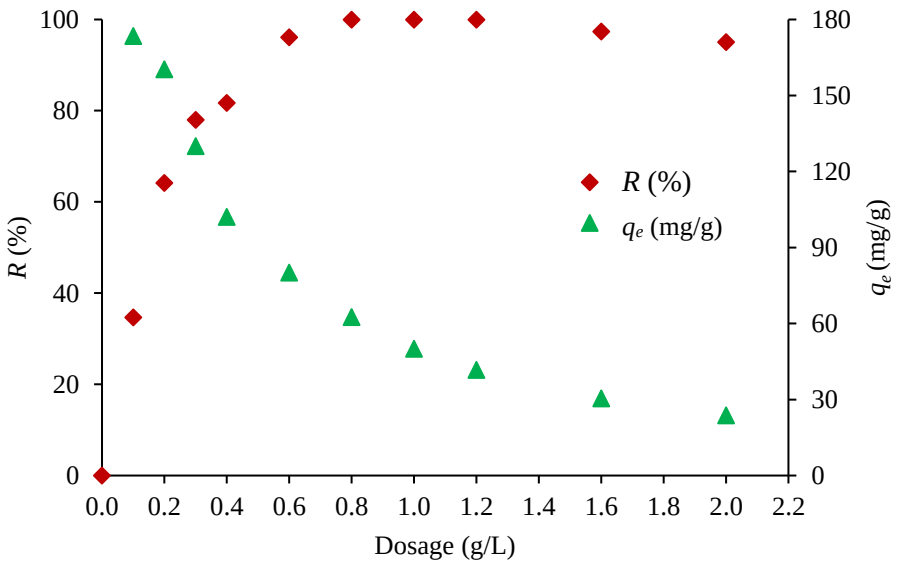

Fig. 4.9: Effect of dosage on removal efficiency and adsorption capacity of RGM.

4.3.3 Effect of pH

The form of an ionisable pollutant in solution depends on its acid dissociation constant (pKa) and working solution pH. Moreover, the solution pH alters the surface charge of adsorbent, hence affecting the adsorption system. The pKa of acetaminophen is 9.38 indicating that the pharmaceutical existed as a neutral molecule at pH < 9.38, whereas at pH > 9.38, it dissociated into negatively charged ions. The effect of pH onto acetaminophen removal by the RGM aerogel is depicted in Fig. 4.10.

The control plot revealed that the removal efficiency of acetaminophen was unaffected by altering the solution pH 2 to 11. However, its removal efficiency varied significantly with pH as RGM was introduced into the solution. Fig. 4.10 shows that the removal efficiency was drastically increased (> 90 %) as the pH was increased from 2 to 7. The high removal of acetaminophen was likely due non-electrostatic interactions such as hydrophobic and π-π electron donor acceptor acceptor (EDA) interactions (Sumalinog et al., 2018). However, electrostatic interaction might play a role in the removal process at pH < 9.38, as reported by several researchers (Peng et al., 2017a; Sumalinog et al., 2018). Accordingly, the acetaminophen was partially ionised in the presence of different adsorbents at pH < 9.38, making it able to induce electrostatic interaction with positively charged adsorbent surface. Hence, the electrostatic interaction between the positively charged RGM (PZC = 6.5) and the partially dissociated acetaminophen anion might synergised the removal efficiency of acetaminophen (Sumalinog et al., 2018). When the pH was further increased to 11, the high concentration of hydroxyl ions (OH^-) and deprotonation of acetaminophen had caused electrostatic repulsion between the similar charged adsorbate and RGM,

reducing the removal efficiency. Hence, the solution pH selected for subsequent experiments were the natural pH of acetaminophen solution (pH ~ 6).

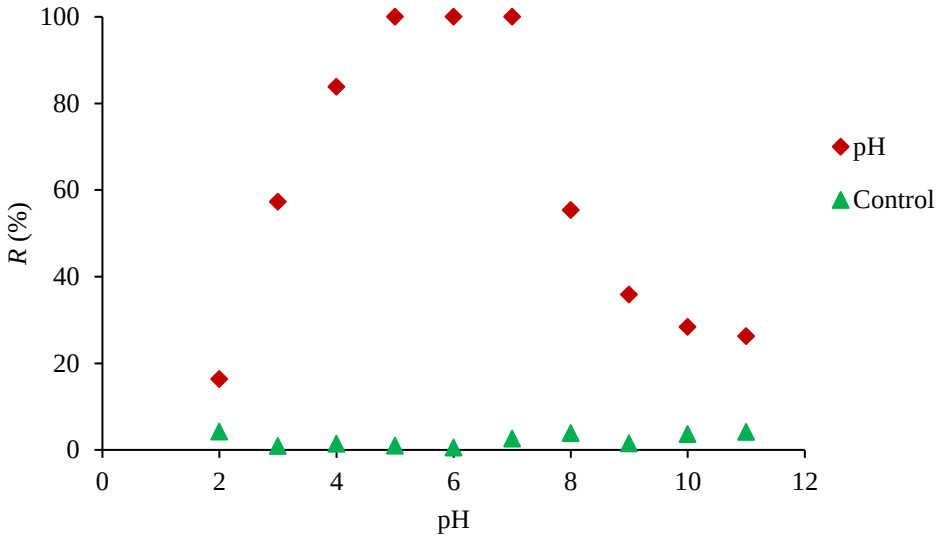

Fig. 4.10: Effect of pH on removal efficiency of RGM.

4.3.4 Adsorption equilibrium

The adsorption equilibrium between acetaminophen and RGM was investigated to determine the maximum adsorption capacity of the aerogel. The experimental data were fitted to the Langmuir, Freundlich, Temkin and D-R models. The isotherm plots are displayed in Fig. 4.11 and the equilibrium parameters are listed in Table 4.2. The results clearly showed that the Langmuir model was the best model to describe the adsorption equilibrium with R^2 closest to unity (0.9769 – 0.9880), followed by the Temkin (0.9659 – 0.9854), Freundlich (0.9656 – 0.9688) and D-R (0.8630 – 0.8916) models. The good fit of data to the Langmuir model implied that the sorption sites were uniformly distributed on RGM surface and monolayer adsorption of acetaminophen occurred on homogeneous sites (Langmuir, 1918). The maximum adsorption capacity (q_m) predicted by the Langmuir model varied from 203.12 to 252.87 mg/g while the

Langmuir constant (K_L) varied between 0.0162 and 0.0292 L/mg over the temperatures ranging from 30 to 40 °C. Furthermore, adsorption favourability was gauged by the Hall's separation factor (R_L). The calculated R_L for acetaminophen adsorption onto RGM fell within 0 – 1 ($0.0641 \leq R_L \leq 0.1097$), indicating that the adsorption process was favourable at the investigated temperatures (Hall et al., 1966).

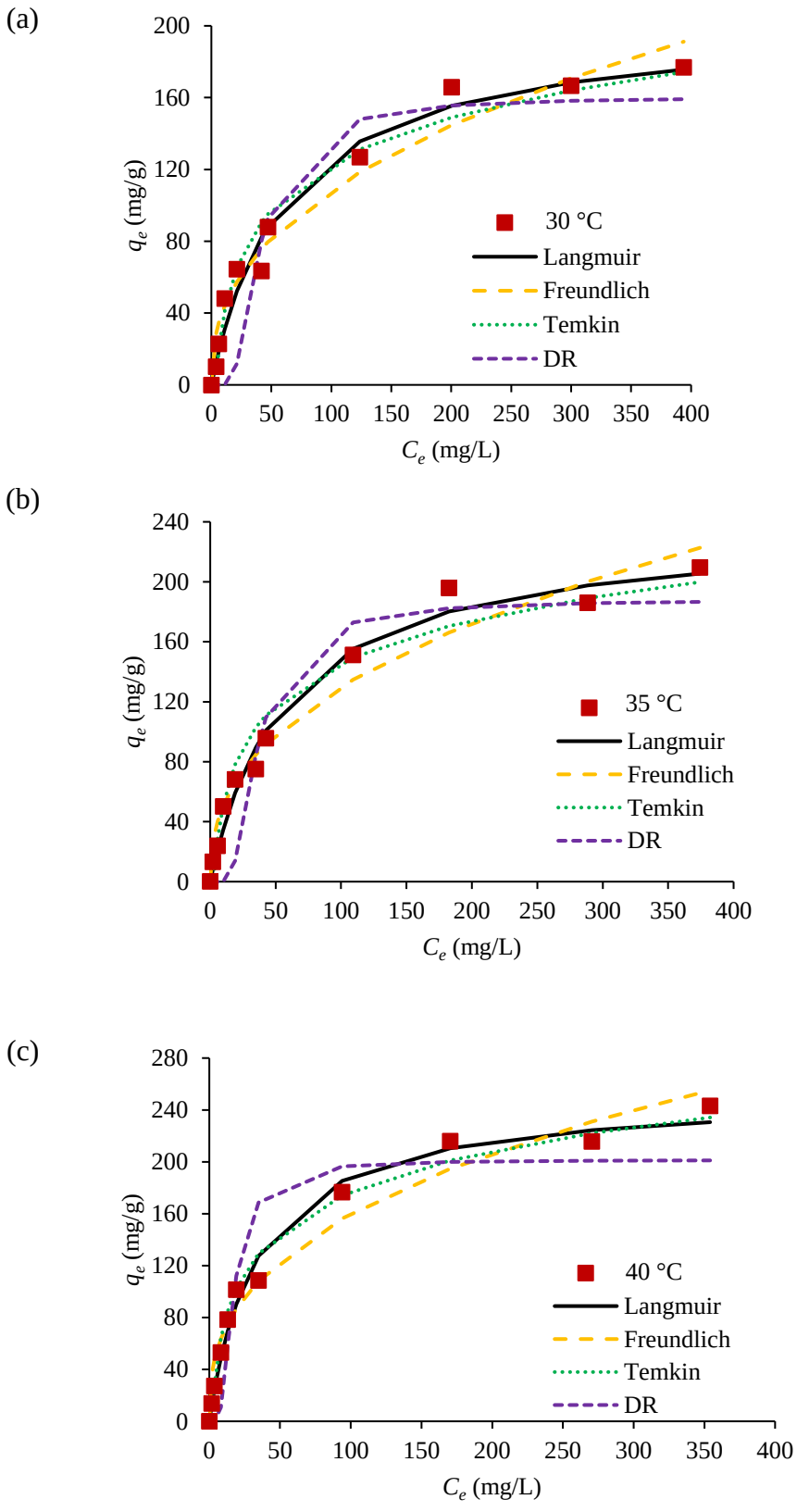

Fig. 4.11. Adsorption equilibrium isotherms at (a) 30 °C, (b) 35 °C and (c) 40 °C for acetaminophen-RGM system.

Table 4.2 Adsorption equilibrium isotherm, kinetic and thermodynamic parameters for acetaminophen adsorption onto RGM.

Equilibrium	**Temperature (°C)**		
	30	**35**	**40**
Langmuir			
q_m (mg/g)	203.12	237.15	252.87
K_L	0.0162	0.0173	0.0292
R_L	0.1097	0.1034	0.0641
R^2	0.9769	0.9832	0.9880
Freundlich			
K_F	16.28	19.86	29.15
n	2.43	2.45	2.71
R^2	0.9656	0.9656	0.9688
Temkin			
A_T	0.2710	0.3541	0.5022
b	67.55	62.65	57.60
R^2	0.9721	0.9659	0.9854
Dubinin-Radushkevich			
K_{DR}	4.4700	3.5000	0.7520
q_{DR} (mg/g)	160.40	187.94	201.45
R^2	0.8630	0.8870	0.8916

Kinetic	C_o **(mg/L)**				
	10	**20**	**50**	**100**	**500**
Pseudo- first-order					
$q_{e,\,exp}$	16.62	32.48	56.37	109.87	176.93
$q_{e,\,calc}$	16.29	31.25	52.96	106.76	168.57
k_1	0.0867	0.1149	0.0428	0.0173	0.0282
R^2	0.9841	0.9841	0.9439	0.9579	0.9601
Pseudo- second-order					
$q_{e,\,calc}$	17.02	32.38	57.28	122.20	187.71
k_2	0.0101	0.0079	0.0012	0.0002	0.0002
R^2	0.9549	0.9899	0.9900	0.9780	0.9775
Elovich					
α	4.416E+3	6.868E+5	32.375	5.8707	22.710
β	0.8274	0.5778	0.1282	0.0403	0.0306
R^2	0.9022	0.9624	0.9877	0.9765	0.9527

Thermodynamic	**Δ*G* (kJ/mol)**			**Δ*H***	**Δ*S***
C_o **(mg/L)**	**30 °C**	**35 °C**	**40 °C**	**(kJ/mol)**	**(kJ/mol K)**
10	-19.79	-22.44	-23.36	88.03	0.3568
20	-20.65	-21.38	-23.18	56.09	0.2527
40	-21.10	-21.86	-22.83	31.32	0.1729
60	-20.20	-20.95	-22.67	54.84	0.2471
80	-18.46	-19.65	-22.34	99.36	0.3880
100	-18.98	-19.76	-20.94	40.51	0.1961
200	-17.47	-18.53	-19.63	47.99	0.2160

4.3.5 Adsorption kinetic

The effect of contact time and adsorption kinetic model fittings are depicted in Fig. 4.12 (a). At low initial concentration (10 – 20 mg/L), the adsorption capacity was observed to be increased rapidly from t = 0 – 30 min and attained equilibrium at t > 30 min. Meanwhile, at high initial concentrations (50 – 500 mg/L), a rapid increase in adsorption capacity was observed from t = 0 – 60 min due to the availability of abundant binding sites during the initial adsorption stage. As time progressed, the binding sites of RGM were gradually saturated as depicted by the slower adsorption rate at t = 60 – 240 min, and eventually reached equilibrium at t > 240 min. Notably, the adsorption capacity at equilibrium was increased with the increased in initial concentration. This can be explained by the increase in mass transfer driving force for acetaminophen molecules from bulk liquid to the surface of RGM.

The adsorption kinetic modelling provides insights related to the rate of acetaminophen adsorption and plausible rate limiting step. The kinetic models (pseudo-first-order, pseudo-second-order and Elovich) parameters are tabulated in Table 4.2. At C_o = 10 mg/L, the pseudo-first-order kinetic model was the best model (R^2 = 0.9841) to describe the adsorption kinetic, while the pseudo-second-order kinetic model was the best model to describe the adsorption kinetic at C_o = 20 – 500 mg/L as evident by the highest R^2 (0.9775 – 0.9900). Therefore, the kinetic modelling suggested that the acetaminophen adsorption onto RGM was controlled by physisorption and chemisorption at low and high concentration conditions, respectively.

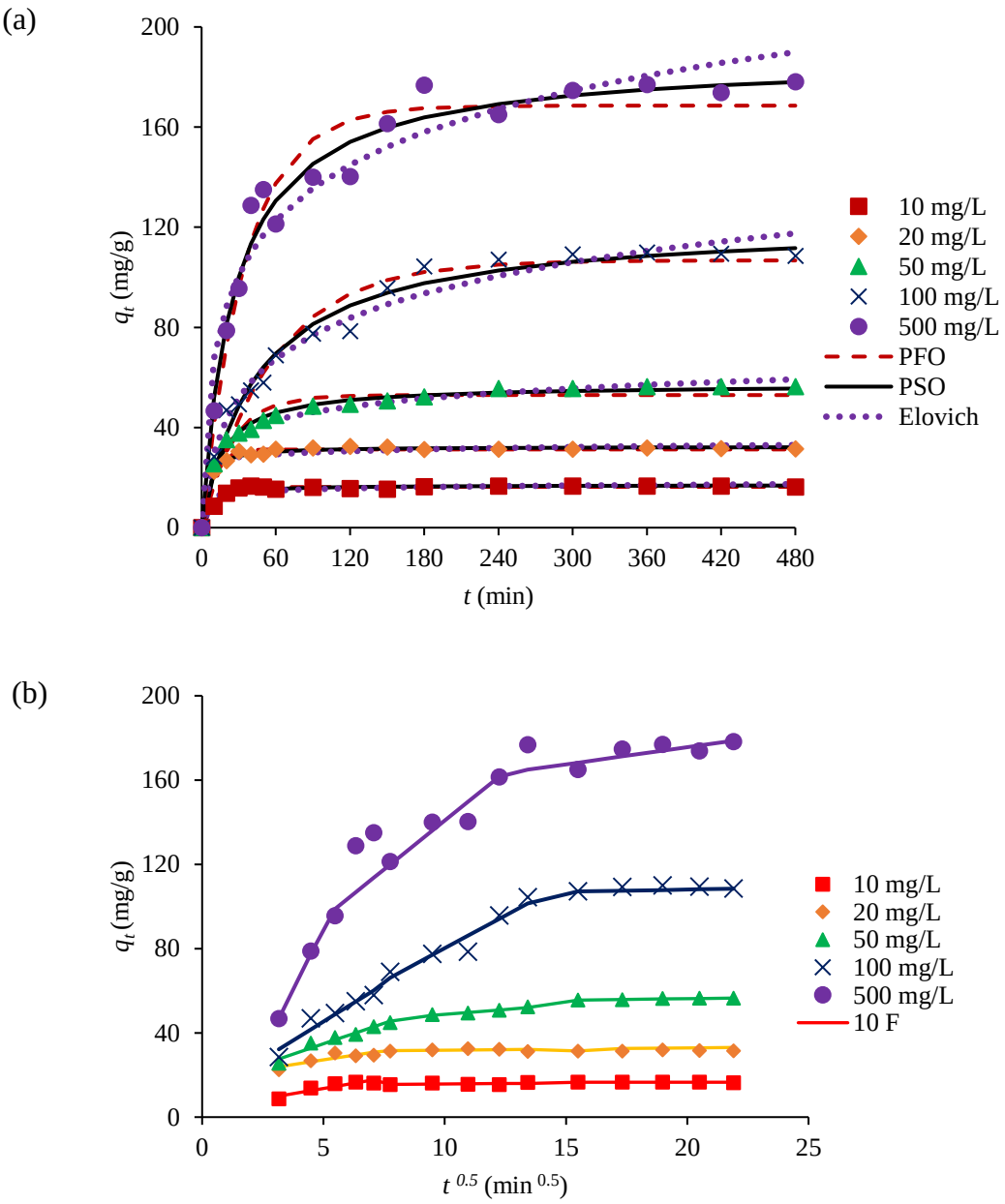

Fig. 4.12 (a) Adsorption kinetics and (b) intraparticle diffusion plots at different initial concentrations for acetaminophen-RGM system.

The rate limiting step of the adsorption of acetaminophen was identified by fitting the experimental kinetic data with the intraparticle diffusion model. As shown in Fig. 4.12 (b), the intraparticle diffusion plots of this study demonstrated multi-linearity and did not pass through the origin, implying that the adsorption of acetaminophen onto RGM was based on several rate limiting steps such as film diffusion and intraparticle diffusion.

4.3.6 Thermodynamic analysis

Thermodynamic parameters such as the Gibbs free energy (ΔG), enthalpy change (ΔH) and entropy change (ΔS) were evaluated for the acetaminophen-RGM system. Table 4.2 shows that the ΔG (-23.36 to -15.39 kJ/mol) were negative for all temperatures and concentrations assayed. The results indicated that the adsorption was thermodynamically spontaneous and feasible. As the temperature increased, the ΔG was decreased. However, ΔG increases with initial concentration. These findings suggested that the acetaminophen uptake was more spontaneous at high temperature and low concentration conditions. The positive ΔH (28.51 – 99.36 kJ/mol) and ΔS (0.1466 – 0.3880 kJ/mol K) implied that acetaminophen adsorption was endothermic and the degree of randomness increased at the solid-liquid interface during the adsorption process.

4.3.7 Regeneration study

Several chemicals were investigated to identify the potential eluting agent for regenerating used RGM. As shown in Fig. 4.13(a), acetone exhibited the highest regeneration efficiency (η = 99.47 %) after the first regeneration cycle, followed by 0.1 M NaCl (87.64 %), acidified acetone (81.43 %), acidified ethanol (81.31 %), 50 % methanol solution (55.19 %), ethanol (52.26 %), 0.1 M H_2SO_4 (26.55 %), H_2O_2

(14.40 %) and acidified H_2O_2 (9.30 %). Therefore, acetone was selected as the most suitable eluting agent for cyclic regeneration experiment.

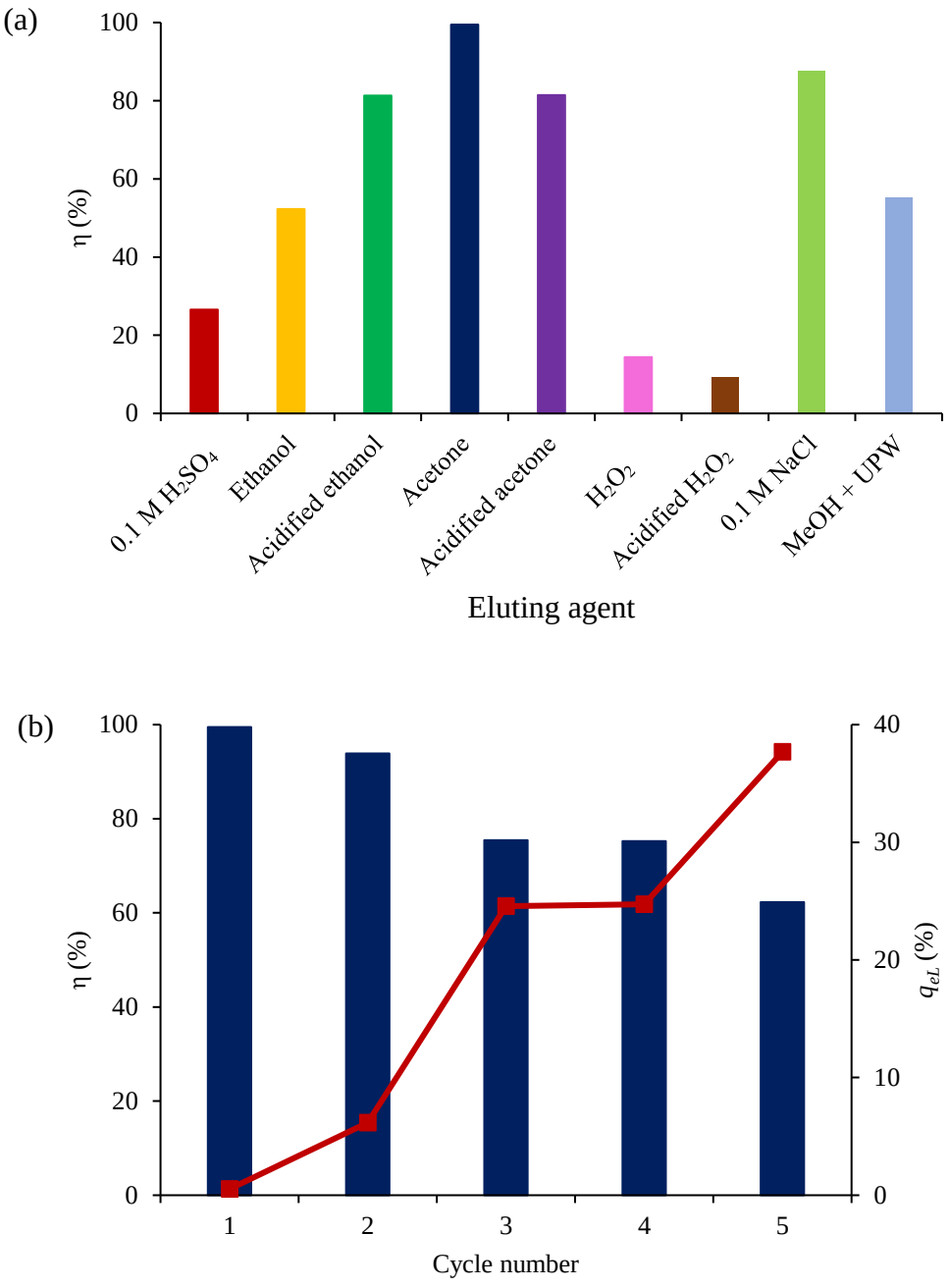

Fig. 4.13. Regeneration efficiency versus (a) eluting agent and (b) adsorption-desorption cycle for acetaminophen-RGM system.

The regeneration of used RGM by using acetone as the eluting agent was performed for 5 cycles of adsorption-desorption and the results are illustrated in Fig. 4.13(b). The regeneration efficiency (η) was observed to decrease with an increase in adsorption capacity loss (q_{eL}) and cycle number. The η exhibited promising efficiency (93.85 – 99.47 %) during the first two cycles, then it decreased and was maintained around 75 % during the 3rd and 4th cycle, and finally decreased to 62.32 % at the 5th cycle. Furthermore, the q_{eL} was progressively increased from 0.53 to 37.68 % as more adsorption-desorption cycles were conducted. This could be explained by the structural damage of RGM and accumulation of chemically adsorbed acetaminophen on the RGM surface, leading to incomplete elution (Boudrahem et al., 2017). The present study revealed that acetaminophen-loaded RGM adsorbent was regenerated using acetone and the regeneration efficiency was maintained above 60 % after 5 cycles of adsorption-regeneration, despite a degree of loss in adsorption performance.

4.3.8 Adsorption mechanisms

The adsorption mechanism for pharmaceutical residues could be governed by governed by different factors. Ionisable acetaminophen could interact with the adsorbent through several mechanisms. Acetaminophen has a pKa of 9.38, indicating that it dissociates to anions at pH > 9.38 and at pH < 9.38 it is a neutral compound. The removal efficiency of acetaminophen was increased gradually from pH 2 to 4 (16.34 to 83.81 %) and maintained at high removal level (> 90 %) between pH 5 and 7, before decreasing gradually with further increase in pH to 11 (55.39 to 26.23 %). The low removal efficiency of acetaminophen at pH 2 was caused by the destruction of the RGM structure under the extreme acidic condition. The adsorption mechanism at pH < 9.38 could be attributed to non-electrostatic interactions such as hydrophobic (Sumalinog et al., 2018) and π-π EDA interactions (Akpotu & Moodley, 2018a). However, the

ionisation of acetaminophen could be affected by the presence of adsorbent in the solutions. Several researchers have reported that the oxygens in amide and hydroxyl groups of acetaminophen were induced to become partial negatively charged at pH < 9.38 in the presence of adsorbents such as activated biochar (Peng et al., 2017a; Sumalinog et al., 2018) and Fe^{3+}-saturated montmorillonite (Peng et al., 2017a). Therefore, electrostatic attraction might occur between the negatively charged functional groups of acetaminophen and the positively charged RGM (PZC = 6.5), facilitating the adsorption process at pH < 6.5. As the pH was increased from 8 to 11, acetaminophen gradually dissociated to form anion due to deprotonation of the functional groups. Hence, the removal efficiency decreased due to the electrostatic repulsion between the anionic acetaminophen and negatively charged RGM between pH 8 and 11. Furthermore, the decreasing trend at pH > 10 was due to structural destruction of RGM.

The FTIR results were applied to support the adsorption mechanisms in this study. The FTIR spectrum revealed that RGM possessed various functional groups which might interact with acetaminophen via hydrogen bonding. Based on Fig. 4.8 (g), the original FTIR peaks for the functional groups in RGM at 3203, 1572, 1415, 1325, 1020, 716 and 499 cm^{-1} were shifted to 3176, 1571, 1414, 1326, 1030, 720 and 496, respectively, after adsorption of acetaminophen. These shifts indicated the participation of RGM oxygenated functional groups in adsorbing acetaminophen via hydrogen bonding (Akpotu & Moodley, 2018a; Sumalinog et al., 2018).

4.4 Batch adsorption of copper and nickel onto ZrGA

4.4.1 Adsorbent characteristics

As depicted in Fig. 4.14(a) – (c), the SEM images of ZrGA presented the 3D porous structure with interconnected rough layers of GO/Zr/CMC sheets in random lateral

direction. The formation of this structure could be due to multi-layered assembly of GO and Zr-CMC functional groups, as well as π-π stacking of Zr and GO forming coalesces on the adsorbent surface as indicated by the presence of clump-liked particles in Fig. 4.14 (c) (Wu et al., 2020). It is worth mentioning that the raw materials used in the synthesis of ZrGA were hydrophilic and had high tendency in isolating water molecules within the GO/Zr/CMC matrix during synthesis stage. Upon freezing, the water molecules were turned into ice crystals which were subsequently volatilised via freeze drying, leading to the construction of porous ZrGA adsorbent. The unique structure of ZrGA might promote the diffusion of heavy metals through inner structure of adsorbent, thus enhancing its adsorption performance.

Five primary elements were found on the ZrGA surface by EDX analysis and these included carbon (C, 45.72 %), oxygen (O, 40.55 %), sodium (Na, 4.61 %), chloride (Cl, 3.41 %) and zirconium (Zr, 5.71 %) (Table 4.3). Hence, these elements played a crucial role in controlling the adsorption mechanisms.

Table 4.3: EDX analysis for pristine, Cu^{2+}- and Ni^{2+}-loaded ZrGA.

Element	**Weight percentage (%)**		
	ZrGA	**Cu^{2+}-loaded ZrGA**	**Ni^{2+} loaded ZrGA**
Carbon (C)	45.72	41.96	42.02
Oxygen (O)	40.55	47.08	50.18
Sodium (Na)	4.61	-	-
Chlorine (Cl)	3.41	-	-
Zirconium (Zr)	5.71	4.81	4.18
Copper (Cu)	-	6.15	-
Nickel (Ni)	-	-	3.62

The FTIR spectra of pristine ZrGA, Cu^{2+}-loaded and Ni-loaded ZrGA are illustrated in Fig. 4.14(d). The characteristic peaks of pristine ZrGA located at 3735, 3365, 2181 and 1975 cm^{-1} were corresponded to the vibration of C-OH band (Aydın, 2019), O-H group stretching (Bhargava et al., 2020), C≡C vibration (Huang et al.,

2019) and C≡O stretching of carboxyl groups (Li et al., 2018). The chemical functional groups contributed by GO such as C-OH stretching vibration (Pazani & Aroujalian, 2020), asymmetrical COO- stretching of carboxylate group (Kong et al., 2020b), carboxyl group stretching vibrations (Ocsoy et al., 2017) and C-O bonds from alkoxyl groups (You et al., 2019) were represented by the peaks at 1729, 1416, 1318 and 1020 cm^{-1}, respectively. The involvement of Zr-based functional groups was determined at the fingerprint zone of the FTIR spectrum. The peaks at 687, 583, 490 and 458 cm^{-1} were assigned to stretching vibration of C-Cl_2 stretching (Arfin & Tarannum, 2019), Zr-O bond, Zr-O-Zr vibration (Puangjan & Chaiyasith, 2016) and Zr-O stretching vibration (Yin et al., 2019), respectively. Therefore, the FTIR results confirmed the contribution of GO and $ZrOCl_2 \cdot 8H_2O$ in embedding functionalities such as carboxylate, carboxylic, alkoxy and Zr-based functional groups in the ZrGA adsorbent.

The PZC of ZrGA was identified to be 4.8, indicating ZrGA surface would be positively charged at pH < PZC, neutral at pH = PZC and negatively charged at pH > PZC.

(a)

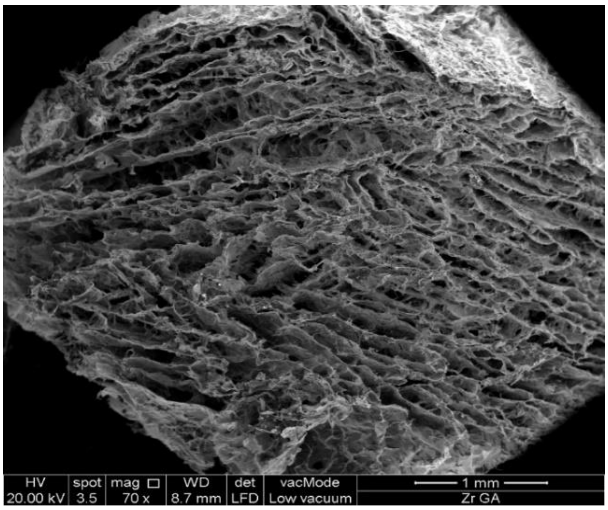
HV spot mag WD det vacMode 1 mm
20.00 kV 3.5 70 x 8.7 mm LFD Low vacuum Zr GA

(b)

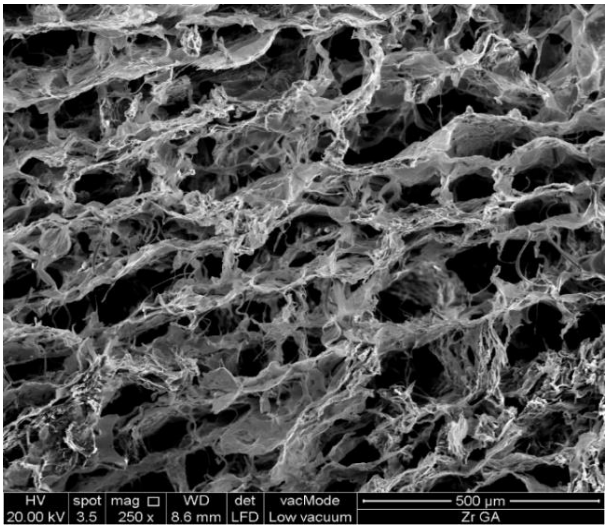
HV spot mag WD det vacMode 500 µm
20.00 kV 3.5 250 x 8.6 mm LFD Low vacuum Zr GA

(c)

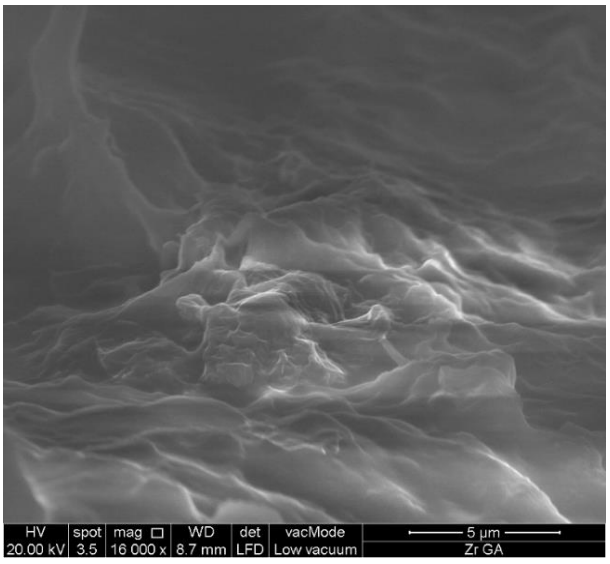
HV spot mag WD det vacMode 5 µm
20.00 kV 3.5 16 000 x 8.7 mm LFD Low vacuum Zr GA

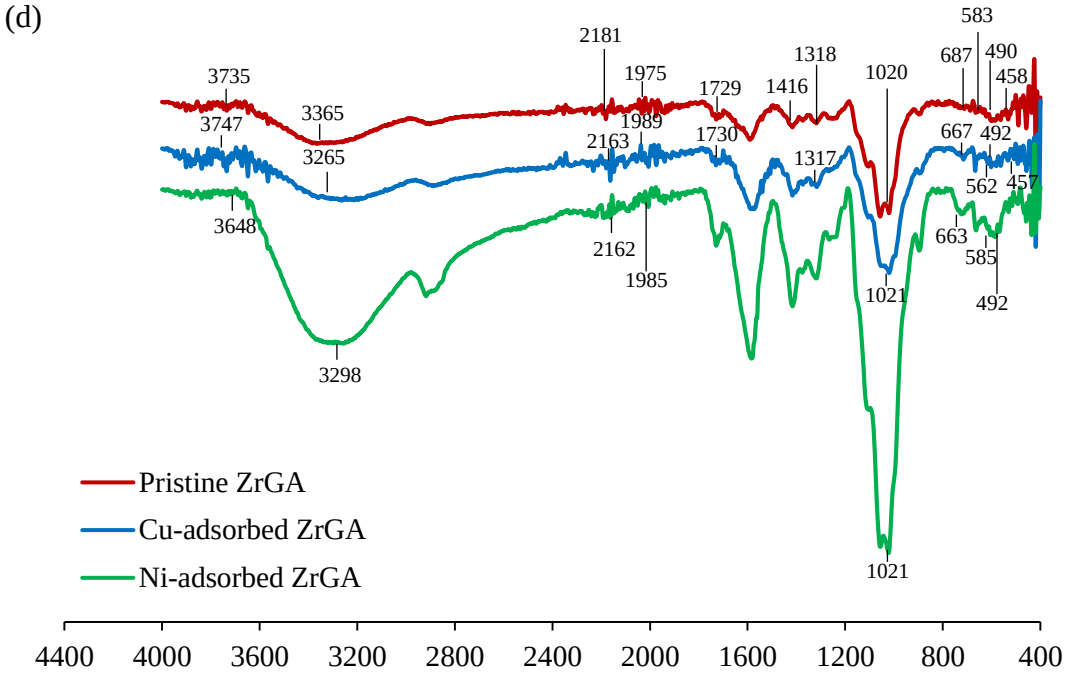

Fig. 4.14: Characterisation of ZrGA: SEM images (a) x70, (b) x250 and (c) x16000 magnifications, and (d) FTIR spectra comparison.

4.4.2 Effect of dosage

The effect of ZrGA dosage on the removal of Cu^{2+} and Ni^{2+} is illustrated in Fig. 4.15. As observed, the Cu^{2+} removal efficiency increased from 16.35 to 95.05 % when ZrGA dosage was increased from 0.2 g/L to 1.6 g/L, and the removal efficiency did not vary significantly beyond 1.6 g/L. The removal of Ni^{2+} by ZrGA also showed an increase in removal percentage (16.29 to 90.65 %) with the increase in dosage (0.2 to 2 g/L), but it remained constant at dosage greater than 2 g/L. This phenomenon could be explained by the high availability of binding sites at higher ZrGA dosage, allowing more Cu^{2+} and Ni^{2+} to be adsorbed onto ZrGA surface (Zhang et al., 2020). However, particle agglomeration could occur at excessive dosage which reduced the avaibility of sorption sites (Mahmoud et al., 2020). In contrast, the adsorption capacities for Cu^{2+} and Ni^{2+} decreased with the increase in ZrGA dosage. The decreasing trend indicated the

unsaturation of sorption sites in ZrGA and the aggregation of particles at high dosages had extended the diffusional pathway for the heavy metals. Hence, the best ZrGA dosage for adsorption of Cu^{2+} and Ni^{2+} in this study are 1.6 and 2 g/L, respectively.

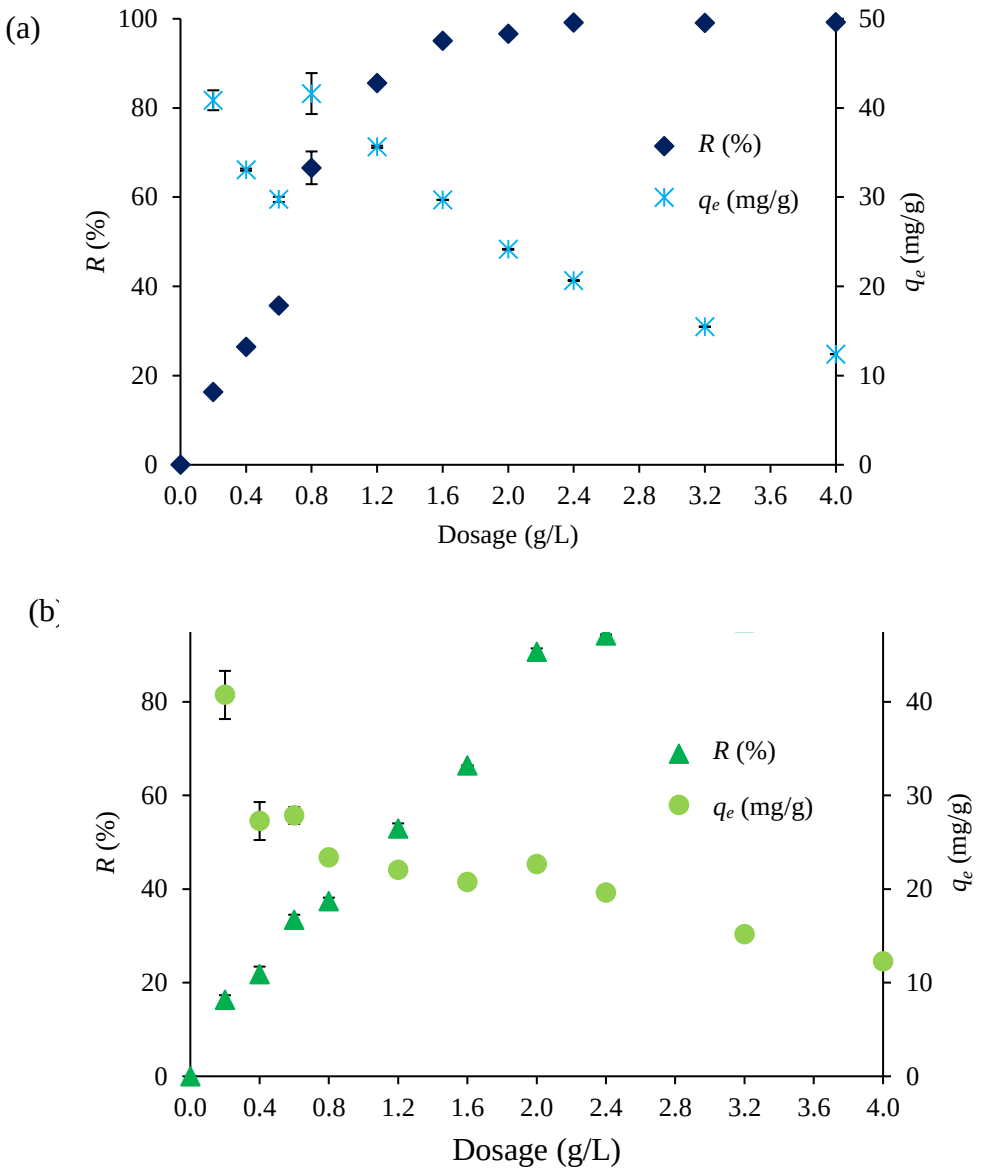

Fig. 4.15: Effect of dosage on (a) Cu^{2+} and (b) Ni^{2+} removal by ZrGA.

4.4.3 Effect of pH

The effect of pH on Cu^{2+} and Ni^{2+} adsorption along with the respective control plot (without using adsorbent) are depicted in Fig. 4.16. The removal percentage for Cu^{2+}

(R < 48 %) and Ni^{2+} (R < 12 %) was low at acidic condition (pH <4), but it increased and then remained constant (88 < R < 99 %) as the pH was increased from 5 to 11. Between pH 2 and 4.8, the surface of ZrGA (PZC = 4.8) was protonated, creating a positive surface which was unfavourable for adsorbing the like-charged heavy metals due to electrostatic repulsion (Kong et al., 2020a). The surface become negatively charged when pH > 4.8, facilitating the adsorption of Cu^{2+} and Ni^{2+} through electrostatic attraction (Vicente-Martínez et al., 2020).

According to the control plot and speciation curves for the heavy metals (Cu^{2+} and Ni^{2+}), the predominant species of copper was Cu^{2+} and $Cu(OH)^{+}$ at pH < 7 (Qiao et al., 2020) while the predominant species of nickel was Ni^{2+} at pH < 8 (Ji & Cooper, 1996). As pH was further increased, the concentration of OH^{-} increased which led to the formation of metal hydroxide precipitates. The formation of $Cu(OH)_2$ occurred when Cu^{2+} was exposed to pH > 7 while $Ni(OH)_2$ formed at pH > 8. The Cu^{2+} control plot showed that in the absence of ZrGA, the removal of Cu^{2+} was very low (< 3 %) at pH < 6, but its removal was significantly increased (> 88 %) as the pH was increased from 7 to 11. The Ni^{2+} control plot illustrates low removal efficiency at pH < 8, but it increased sharply (> 75 %) at pH > 8. The notable increase was associated with the formation of $Cu(OH)_2$ and $Ni(OH)_2$ at pH > 7 and > 8, respectively. Therefore, the pH study suggested that the removal of Cu^{2+} and Ni^{2+} by ZrGA was due to adsorption phenomena at pH < 7 and < 8, respectively, while precipitation occurred at pH > 6.5 and > 8, respectively. As such, subsequent experiments were carried out at the natural pH of Cu^{2+} and Ni^{2+} solutions which were pH 6 and 6.1, respectively.

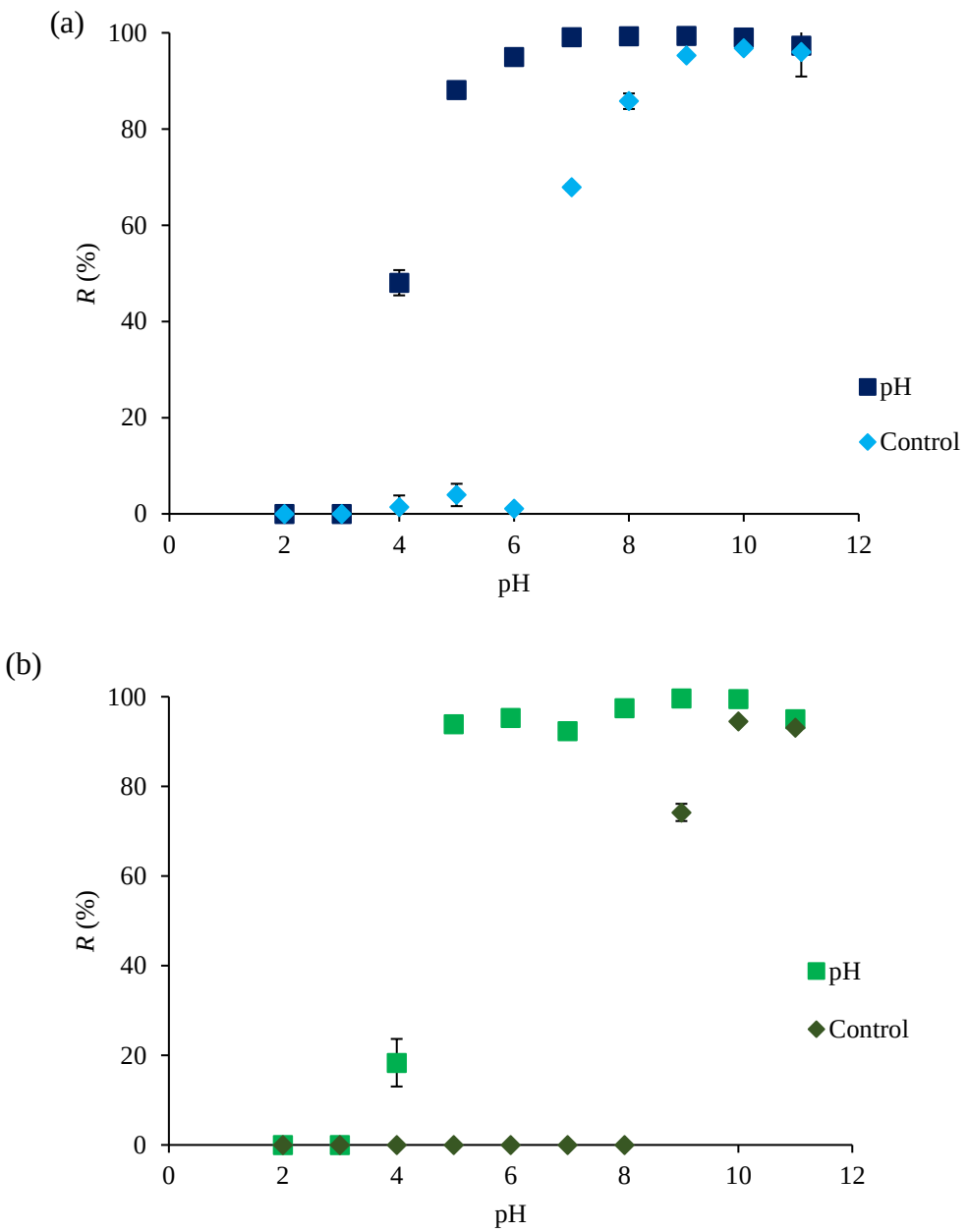

Fig. 4.16: Effect of pH on (a) Cu^{2+} and (b) Ni^{2+} removal by ZrGA.

4.4.4 Effect of ionic strength

The influence of ionic strength is important to identify the possible adsorption mechanisms of Cu^{2+} and Ni^{2+} onto ZrGA (Jun et al., 2019). As illustrated in Fig. 4.17, the removal of Cu^{2+} (R > 90 %) and Ni^{2+} (R > 80 %) was not affected significantly by the interference of Na^{+} at the concentration range studied (0 – 0.1 M). Both Cu^{2+} and Ni^{2+} are divalent metal ions and have twice the positive charge than the monovalent Na^{+}, hence they have higher affinity to be adsorbed by ZrGA via electrostatic attraction (Zhao et al., 2019). Furthermore, the ionic radii for Cu^{2+} and Ni^{2+} are 0.72 Å (Pinalli et al., 2018) and 0.69 Å (Cristine de Sousa Santos et al., 2020), respectively, which are smaller than that of Na^{+} (0.95 Å). The metal ions with smaller radius had higher tendency to be adsorbed onto the inner pores of ZrGA (Zhao et al., 2019).

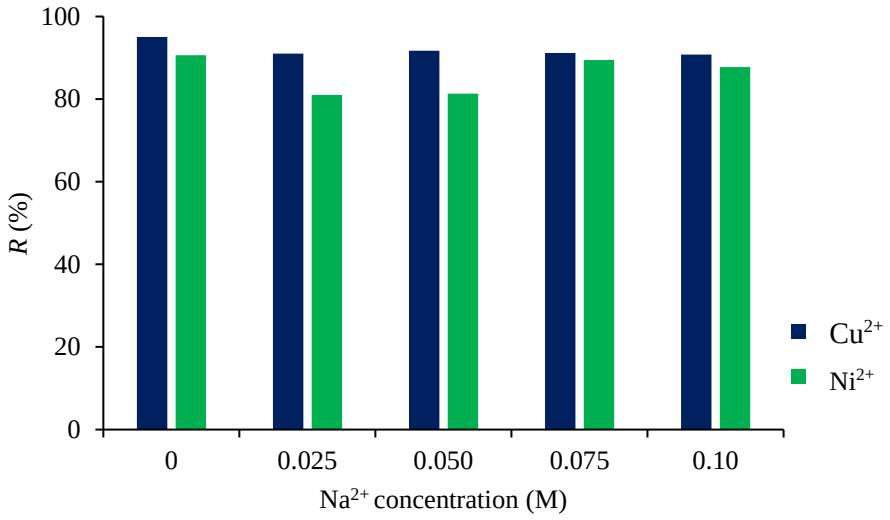

Fig. 4.17: Effect of ionic strength Cu^{2+} and Ni^{2+} removal by ZrGA.

4.4.5 Adsorption equilibrium

The Cu^{2+} and Ni^{2+} adsorption equilibrium isotherms are presented in Fig. 4.18. For both heavy metals, the adsorption capacity was increased with the metal concentration, and it eventually reached a plateau. This can be explained by the enhancement of mass transfer driving force at higher concentrations overcoming the mass transfer barrier between the liquid phase and solid phase, thus leading to a greater adsorption capacity of the metals until saturation of the sorption sites was reached (Jun et al., 2019). Notably, the isotherms on Cu^{2+} adsorption shared similar trend with those of Ni^{2+} adsorption, where adsorption capacity decreased as temperature was increased, indicating the adsorption was exothermic. The decreasing trend could be due to the weak interaction between the heavy metals and the functional groups of ZrGA, such as Van der Waals force, at higher temperatures (White et al., 2018).

The adsorption isotherm data were fitted to different equilibrium models such as the Langmuir, Freundlich, Temkin and D-R. The evaluated model parameters are tabulated in Table 4.4. Accordingly, the adsorption of Cu^{2+} and Ni^{2+} onto ZrGA was best described by the Langmuir model as evident from the highest R^2 (Cu^{2+}: R^2 = 0.9631 – 0.9787; Ni^{2+}: R^2 = 0.9769 – 0.9923), followed by the Temkin (Cu^{2+}: R^2 = 0.9418 – 0.9743; Ni^{2+}: R^2 = 0.9762 – 0.9849), Freundlich (Cu^{2+}: R^2 = 0.9410 – 0.9657; Ni^{2+}: R^2 = 0.9634 – 0.9849) and D-R (Cu^{2+}: R^2 = 0.8956 – 0.9515; Ni^{2+}: R^2 = 0.9846 – 0.9863) models. This implied that a monolayer of Cu^{2+} and Ni^{2+} was deposited on homogeneous surface of ZrGA. The adsorption favourability was determined by gauging the Hall's separation factor (R_L) in Table 4.4. The adsorption of Cu^{2+} and Ni^{2+} onto ZrGA was found to be favourable as the R_L values were in range of $0 < R_L < 1$ (Cu^{2+}: R_L = 0.004 – 0.0083; Ni^{2+}: R_L = 0.0024 – 0.0037). Furthermore, the Langmuir maximum adsorption capacity (q_m) for Cu^{2+} decreased from 45.07 to 34.80 mg/g as the temperature was

elevated from 30 to 50 °C. The q_m for Ni^{2+} adsorption also showed similar decreasing pattern from 26.44 to 20.69 mg/g over the investigated temperatures. This trend further validated the exothermic nature of Cu^{2+} and Ni^{2+} adsorption onto ZrGA as previously reported (Kaur et al., 2019).

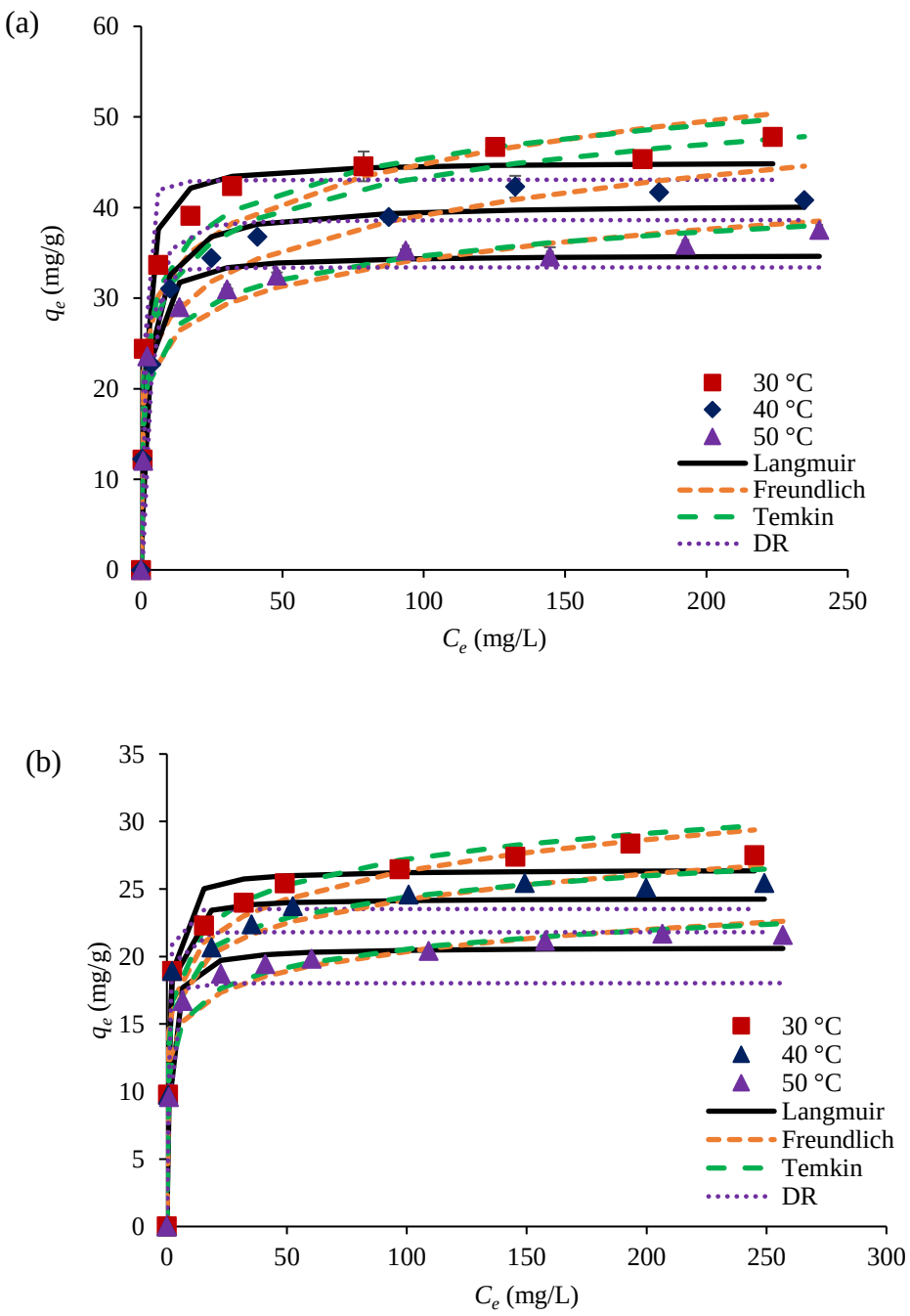

Fig. 4.18: Adsorption equilibrium isotherms for (a) Cu^{2+}- and (b) Ni^{2+}-ZrGA systems.

4.4.6 Adsorption kinetic

The information on the adsorption rate and mechanisms were identified from the kinetic experimental data as illustrated in Fig. 4.19 (a) and (b). As observed, both Cu^{2+} and Ni^{2+} adsorption kinetic profiles demonstrated three distinctive steps: (1) rapid heavy metal uptakes at t = 0 – 15 min, (2) slow adsorption rate at t = 15 – 45 min and (3) adsorption equilibrium at t > 45 min. The rapid uptake of the heavy metals during the initial adsorption stage was attributed to the high amount of vacant sorption sites available for the adsorbates uptake. As time progressed, the adsorption rate was slowed down as the sorption sites were gradually occupied by Cu^{2+} and Ni^{2+}, before reaching equilibrium. Overall, the adsorption of Cu^{2+} and Ni^{2+} onto ZrGA was comparatively fast, reaching equilibrium at relatively short contact time (45 min) and the adsorption capacities increased as the initial concentration was increased. This trend was ascribed to the greater mass transfer driving force to overcome the resistance at the solid-liquid interface at higher concentration.

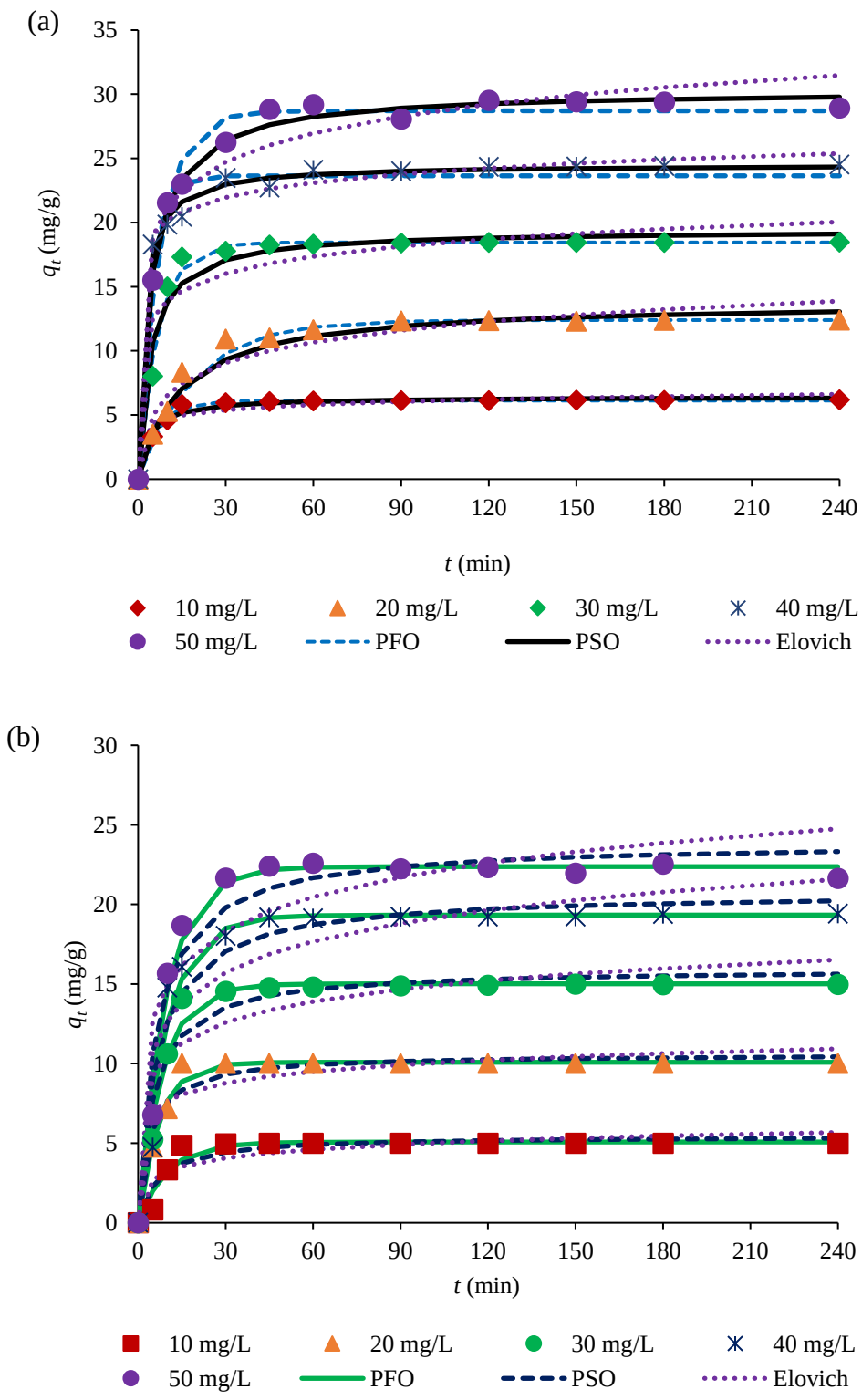

Fig. 4.19: Adsorption kinetic plots for (a) Cu^{2+}- and (b) Ni^{2+}-ZrGA systems.

The pseudo-first-order, pseudo-second-order and Elovich models were used to identify the kinetic behaviour and rate-controlling steps of present study, and the evaluated model parameters are listed in Table 4.4. By comparing the R^2 values, the pseudo-first-order was the best model to describe Cu^{2+} uptake at low concentration zone (10 – 30 mg/L) while at high concentrations (40 – 50 mg/L), Cu^{2+} adsorption kinetic was best fitted to the pseudo-second-order model. For Ni^{2+} adsorption, the kinetic profile obeyed the pseudo-first-order model at all concentrations assayed, based on the highest R^2 (0.9382 – 0.9941). The results indicated that Cu^{2+} adsorption onto ZrGA was governed by both physisorption and chemisorption subjected to the metal concentration, whereas Ni^{2+} adsorption onto ZrGA was a physisorption process.

4.4.7 Thermodynamic analysis

The isotherm obtained from experimental study was further used to determine the thermodynamic parameters such as the Gibbs free energy (ΔG), enthalpy change (ΔH) and entropy change (ΔS) (Table 4.4). The results revealed that the adsorption of Cu^{2+} and Ni^{2+} onto ZrGA were spontaneous and feasible as shown by the negative ΔG values. Additionally, the negative ΔH values indicated that both Cu^{2+} and Ni^{2+} adsorption were exothermic, further reaffirming the previous findings obtained in adsorption equilibrium study. The positive values in ΔS implied that the uptake of both heavy metals by ZrGA led to a decreased disorder at the solid-liquid interface during adsorption process.

Table 4.4: Adsorption equilibrium, kinetic and thermodynamic parameters for Cu^{2+} and Ni^{2+} adsorption onto ZrGA.

Adsorbate	**Cu^{2+}**			**Ni^{2+}**		
			Equilibrium			
***T* (°C)**	**30**	**40**	**50**	**30**	**40**	**50**
Langmuir						
K_L	0.8216	0.3991	0.7618	1.1568	1.3839	0.8906
q_m	45.07	40.47	34.80	26.44	24.32	20.69
R_L	4.03E-03	8.28E-03	4.36E-03	2.87E-03	2.40E-03	3.73E-03
R^2	0.9750	0.9631	0.9787	0.9769	0.9923	0.9868
Freundlich						
K_F	4.56E+09	4.32E+08	5.23E+09	6.52E+09	6.24E+10	1.14E+10
n	7.06	6.67	7.63	8.31	9.24	9.20
R^2	0.9410	0.9657	0.9569	0.9634	0.9849	0.9707
Temkin						
A_T	63.11	41.68	93.51	199.82	528.37	339.64
b	484.38	500.14	707.64	916.71	1159.31	1362.09
R^2	0.9669	0.9418	0.9743	0.9762	0.9849	0.9835
Dubinin-Radushkevich						
K_{DR}	0.0115	0.0958	0.0133	0.0071	0.0065	0.0096
q_{DR}	43.06	38.62	33.39	23.52	21.80	18.03
R^2	0.9500	0.8956	0.9515	0.9857	0.9863	0.9846
				Kinetics				
C_o (mg/L)	**10**	**20**	**30**	**40**	**50**	**10**	**20**	**30**	**40**	**50**
Pseudo-first-order										
$q_{e,\,exp}$	6.19	12.41	18.48	24.52	28.95	5.00	10.00	14.98	19.42	21.63
k_1	0.1550	0.0521	0.1446	0.2421	0.1342	0.1011	0.1417	0.1200	0.1051	0.1054

$q_{e,\ calc}$	6.12	12.40	18.45	23.64	28.71	5.07	10.08	15.01	19.33	22.38
R^2	0.9960	0.9781	0.9887	0.9817	0.9931	0.9382	0.9941	0.9814	0.9740	0.9914
Pseudo-second-order										
k_2	0.0433	0.0050	0.0125	0.0200	0.0074	0.0263	0.0232	0.0117	0.0074	0.0067
$q_{e,\ calc}$	6.42	13.84	19.43	24.54	30.34	5.47	10.60	15.97	20.78	23.93
R^2	0.9809	0.9718	0.9618	0.9960	0.9973	0.8964	0.9821	0.9492	0.9521	0.9711
Elovich										
α	193.53	3.89	254.32	34992.29	220.23	5.00	171.59	48.78	25.17	38.57
β	1.71	0.43	0.52	0.61	0.31	1.30	0.97	0.53	0.36	0.32
R^2	0.9341	0.9361	0.9036	0.9940	0.9800	0.8261	0.9572	0.8835	0.8999	0.9258

Thermodynamics

C_o (mg/L)	**ΔG (kJ)**			**ΔH**	**ΔS**	**ΔG (kJ)**			**ΔH**	**ΔS**
	30 °C	**40 °C**	**50 °C**	**(kJ/mol)**	**(kJ/mol K)**	**30 °C**	**40 °C**	**50 °C**	**(kJ/mol)**	**(kJ/mol K)**
20	-7.85	-8.74	-7.11	-19.37	-0.0366	-7.71	-7.51	-6.14	-31.81	-0.0789
40	-8.12	-4.57	-5.91	-40.88	-0.1107	-5.51	-5.49	-2.33	-54.19	-0.1589
60	-4.29	-2.77	-1.91	-40.28	-0.1191	-0.93	-0.26	-0.47	-22.16	-0.0700

4.4.8 Regeneration study

In practical engineering application, regeneration of adsorbent is important to ensure low operating cost. Hydrochloric acid (HCl) was used as the eluting agent in this study because the adsorbed metal ions would be replaced by hydrogen ion (H^+) via ionic exchange mechanism (Da'na & Awad, 2017). The regeneration results for this study are illustrated in Fig. 4.20. As shown, the ZrGA demonstrated relatively high regeneration efficiency for Cu^{2+} ($\eta > 70$ %) and Ni^{2+} ($\eta > 68$ %) over five successive adsorption – desorption cycles. The lost in regeneration efficiency could be caused by chemically adsorbed heavy metals on ZrGA surface and partial destruction of inner structure of ZrGA. These factors might resulted in the depletion of sorption sites availability for the heavy metals adsorption and hence, a decreased in the performance of ZrGA in subsequent adsorption cycles (Khazaei et al., 2018).

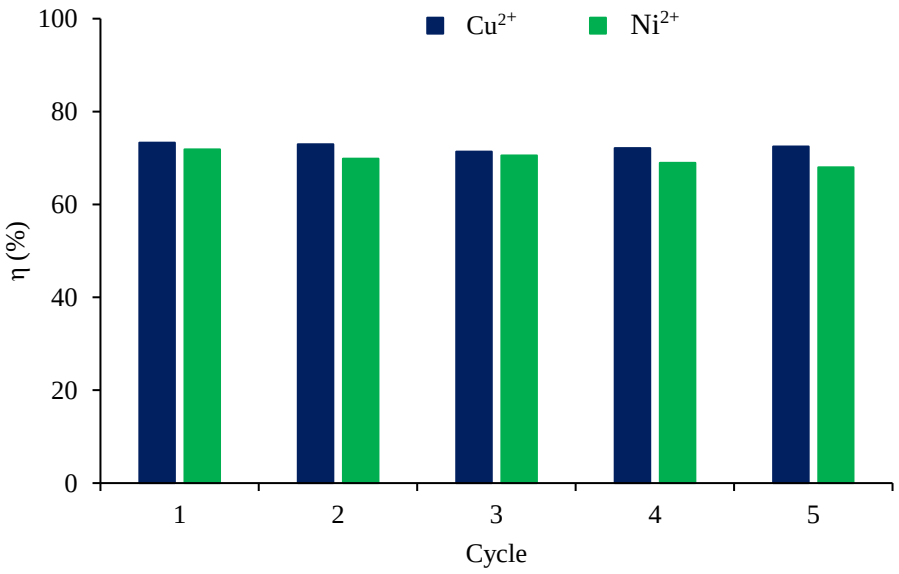

Fig. 4.20: Regeneration efficiency versus adsorption-desorption cycle for Cu^{2+}- and Ni^{2+}-ZrGA systems.

4.4.9 Adsorption mechanisms

The experimental kinetic data were fitted to the intraparticle diffusion model to identify the rate controlling steps for adsorption of Cu^{2+} and Ni^{2+} onto ZrGA. Based on the model, the adsorption is governed by intraparticle diffusion if the q_t vs. $t^{0.5}$ plot is a straight line passing through the origin, whereas a non-linear trend indicates the involvement of multiple mechanisms in controlling the adsorption rate. In Fig. 4.21, the intraparticle diffusion plots for Cu^{2+} and Ni^{2+} adsorption onto ZrGA displayed a multi-linearity with three distinctive segments. This finding suggested that the adsorption systems were controlled by several steps such as boundary layer diffusion and pore diffusion.

From SEM characterisation, a shiny surface was observed on the SEM image for heavy metals loaded ZrGA and the presence of Cu^{2+} and Ni^{2+} was confirmed by EDX analysis. According to Table 4.3, the elemental composition of pristine ZrGA was altered after adsorption of the heavy metals. The changes include the elimination of Na and Cl, slight change in C, O and Zr weight percentages and addition of Cu and Ni after adsorption. These results confirmed the successful attachment of Cu^{2+} and Ni^{2+} onto ZrGA through various mechanisms that involved C, O, Na, Cl and Zr-based functional groups. The appearance of Cu and Ni and disappearance of Na and Cl after adsorption (Table 4.3) further implied that Cu^{2+} and Ni^{2+} were not only adsorbed through surface diffusion on ZrGA, but also went through ionic exchange with Na and Cl on the ZrGA surface (Liu et al., 2016b).

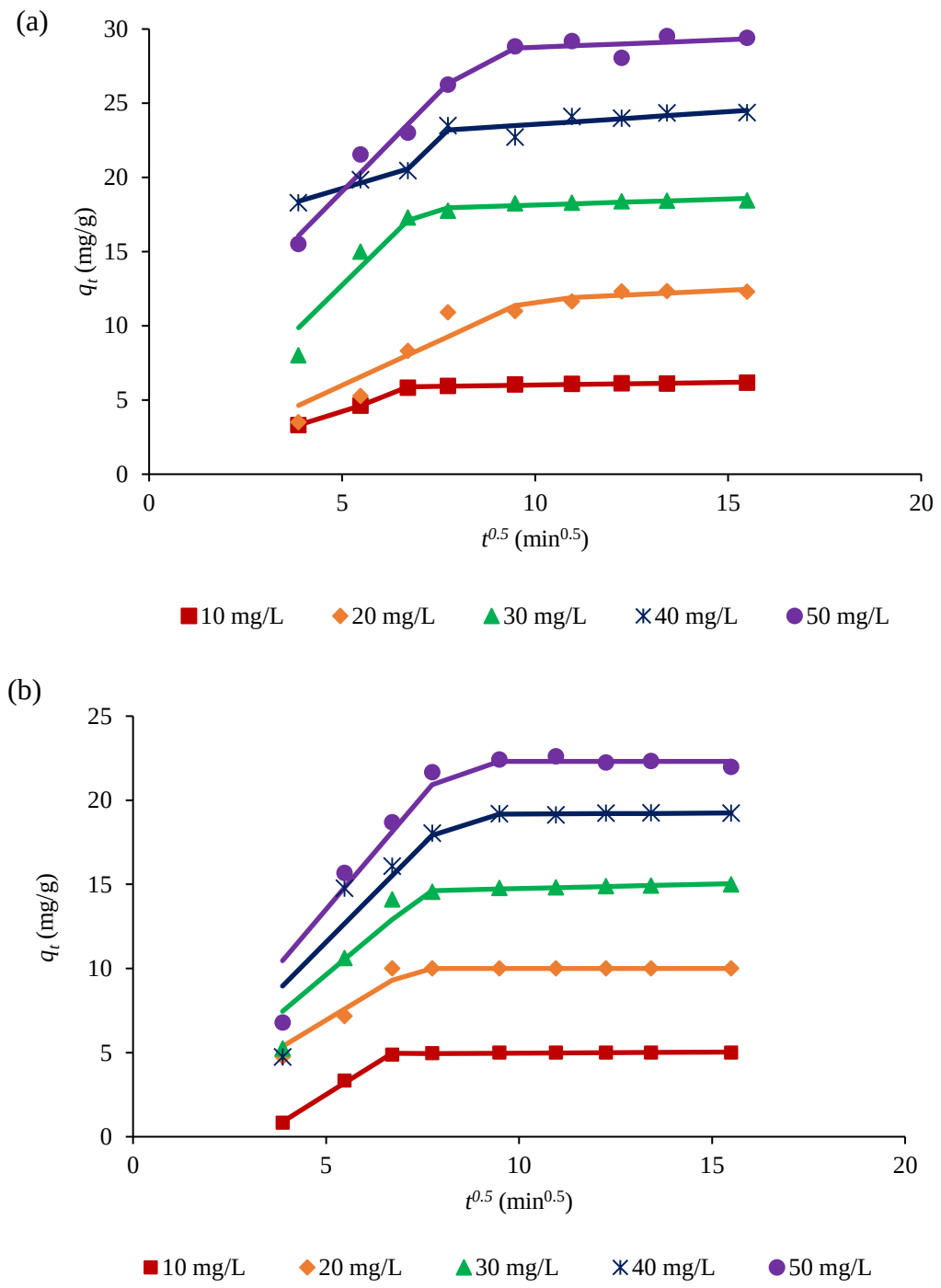

Fig. 4.21: Intraparticle diffusion plots for (a) Cu^{2+} and (b) Ni^{2+} adsorption onto ZrGA.

Additionally, CMC and GO contained heavy metal chelating active sites such as carboxylic and hydroxyl functional groups as shown in the FTIR spectrum. These sites could bind with zirconium ions through electrostatic interaction, forming a metal-ligand complex that would adsorb Cu^{2+} and Ni^{2+} through chelation (Abdullah et al., 2019). Moreover, the involvement of hydrogen bonding was identified by the shift in FTIR peaks. Based on Fig. 14(d), peak shifts was observed at 3747, 3264, 2163, 1989, 1730, 1317, 667, 562, 492 and 457 cm^{-1} for Cu^{2+} loaded ZrGA, while Ni^{2+} loaded ZrGA, the FTIR peak shifts occurred at 3648, 3298, 2162, 1985, 1021, 663, 585 and 492 cm^{-1}. This indicated that the attachment of the metal ions to the hydroxyl, carbonyl and Zr-based functional groups via hydrogen bonding, forming part of the adsorption mechanisms.

Since Cu^{2+} and Ni^{2+} are positively charged ions in aqueous media, the surface charge on ZrGA has an impact on the heavy metals adsorption. As shown in the effect of pH study, the removal of Cu^{2+} and Ni^{2+} was low at pH < 4 and increased greatly at pH 5 – 11. The PZC of ZrGA was 4.8 and hence, the low removal of the heavy metals was due to electrostatic repulsion between the liked-charged ZrGA surface and Cu^{2+} and Ni^{2+} at pH < 4.8. At the low pH condition, the adsorption mechanisms could be due to hydrogen bonding and chelation. The surface of ZrGA became negatively charged from deprotonation at pH > 4.8, leading to adsorption of the cationic metal ions onto the negatively charged ZrGA surface through electrostatic attraction.

4.5 Conclusions

3D graphene-based structures have received worldwide attention as new generation of adsorbents for wastewater treatment owing to their high porosity, large specific surface area and availability of various functional groups. The research work describes the development of rGOA through self-assembly of GO coupled with reduction by L-ascorbic acid. The characterisation of rGOA was performed by FTIR, SEM and XRD. The diclofenac adsorption equilibrium and kinetics were best described by the Freundlich and pseudo-first-order kinetic models, respectively. Thermodynamically, adsorption of diclofenac was spontaneous, feasible and exothermic. The possible adsorption mechanisms were hydrogen bonding, electrostatic and hydrophobic interactions. This study concluded that rGOA was a promising adsorbent for the remediation of water polluted by diclofenac residue.

RGM was developed for the removal of acetaminophen contaminant. It was a mesoporous structure with an average pore width of 2.02 nm. RGM possessed multiple oxygeneous surface functional groups. The adsorption equilibrium data were best fitted to the Langmuir model with R^2 ranging from 0.9769 – 0.9880. The kinetic data were best fitted to the pseudo-first-order kinetic model (R^2 = 0.9841) at low acetaminophen concentration (10 mg/L), and to the pseudo-second-order kinetic model ($0.9775 \leq R^2 \leq 0.9900$) at high concentrations (20 – 500 mg/L). The thermodynamic results suggested that the process was spontaneous and endothermic with an increased randomness at the solid-liquid interface. Furthermore, RGM was regenerated using acetone maintaining reasonably high regeneration efficiency (> 60 %) after 5 cycles of adsorption-desorption operation.

Adsorption of Cu^{2+} and Ni^{2+} onto the as-synthesised ZrGA was investigated. Characterisation test revealed that ZrGA possessed porous structure covered with

numerous oxygen- and Zr-based functional groups. The Cu^{2+} and Ni^{2+} adsorption equilibria were best described by the Langmuir model demonstrating maximum Cu^{2+} and Ni^{2+} adsorption capacities of 45.07 and 26.44 mg/g at 30 °C, respectively. The kinetic study showed that Cu^{2+} adsorption rate followed the pseudo-first-order and pseudo-second-order models at low and high concentration regions, respectively. The adsorption kinetics of Ni^{2+} onto ZrGA were best represented by the pseudo-first-order model. Thermodynamically, the adsorption process was spontaneous, feasible and exothermic, with a decrease in randomness at the solid-liquid interface. The adsorption of Cu^{2+} and Ni^{2+} onto ZrGA was controlled by multiple rate limiting steps and the plausible adsorption mechanisms were ionic exchange, chelation, hydrogen bonding and electrostatic interaction. This research concluded that ZrGA was a promising and recyclable adsorbent for treatment of heavy metals contaminated water.

This chapter describes the characterisation results of the synthesised 3D graphene-based structures (rGOA, RGM and ZrGA) and the single-factor study on batch adsorption of diclofenac, acetaminophen, Cu^{2+} and Ni^{2+}. The adsorption studies revealed the influence of process parameters on removal efficiency based on variation of one parameter at a time. Hence, there was a need to explore simultaneous interaction of multiple parameters on the adsorption performance for determination of complex relationship among the parameters to achieve highest possible removal efficiency. Therefore, the next chapter discusses on the batch adsorption modelling.

Chapter 5: Response Surface Methodology Optimisation of Batch Adsorption of Pharmaceuticals and Heavy Metals

5.1 Introduction

Laboratory batch adsorption studies are commonly carried out using the one-factor-at-a-time (OFAT) approach. In this method, one factor is varied while other factors are kept constant during the experiment. The OFAT method which is time consuming, requires a large number of experiments. Hence, it is associated with high experimental cost and manpower requirement. Furthermore, OFAT is not able to study the interactive effects between the process factors. In this study, response surface methodology (RSM) was applied to plan and conduct experiments to determine maximum information on the adsorption process based on data collected from minimum experimental runs.

RSM is a collection of mathematical and statistical tools that can be applied to design experiments and develop empirical models by considering the interactions between multiple independent factors and their effect on the process response. It can also be used for process optimisation whereby the optimum operational conditions to attain highest response are identified. The modelling and optimisation of batch adsorption process by RSM comprise of six consecutive steps (Karimifard & Alavi Moghaddam, 2018):

I. Screening of independent factors and selection of desired response.
II. Selection of experimental design model.
III. Execution of planned experiments and data collection.
IV. Fitting of experimental data to the mathematical model.
V. Model validation using diagnostic plot and analysis of variance (ANOVA).
VI. Determination of optimum conditions from the response surface plots.

The selection of appropriate design strategy is important to create the response surfaces for process modelling and optimisation. Typically, central composite design (CCD) and Box-Behnken design (BBD) are widely used in the modelling of batch adsorption study. CCD model yields useful prediction of linear and quadratic effect of parameters with less experimental runs. Furthermore, CCD consists of centre points, axial points and factorial points which allows it to predict the trend of process responses at wider range of process parameters (Sadhukhan et al., 2016). BBD is can also be used to study the interactive effects of process parameters towards the response. In this method, the number of experimental runs is reduced and the interactive effects (linear or quadratic) can be accurately be analysed using second-order polynomial equation (Box & Behnken, 1960; Witek-Krowiak et al., 2014). The main advantage of BBD is that the process extreme conditions is avoided because the experimental runs of BBD strategy does not include the extreme values. Furthermore, it is more labour efficient than CCD model. However, BBD model is not applicable to study a system with less than three process factors and it is restricted solely for quadratic model (Karimifard & Alavi Moghaddam, 2018). As such, it is important to select the appropriate design model to analyse the batch adsorption process.

Various studies have demonstrated the successful application of RSM in optimising batch adsorption systems. A magnetic chitosan-functionalised 3D graphene decorated with $NiFe_2O_4$ nanoparticles for Pb^{2+} removal was optimised by RSM-CCD. From the study, a Pb^{2+} removal efficiency of 100 % was achieved under the optimum conditions of pH = 8.5, adsorbent dosage = 36 mg, Pb^{2+} concentration = 26 mg/L and volume = 200 mL (Nasiri et al., 2018). Sun et al. (2019) applied RSM-BBD to optimise the synthesis conditions for graphene hydrogel through one-step hydrothermal reduction. The as-synthesised graphene aerogel achieved 348 mg/g ciprofloxacin

adsorption capacity under the optimum synthesis conditions of 1 mg/mL GO, 1:2 (GO:reducer) ratio, 75 °C and 6 h reaction time. The experimentally obtained adsorption capacity showed 3 % deviation from the predicted value (360 mg/g). Hence, RSM is a potential tool for modelling batch adsorption systems as well as for optimising the systems based on response surface plots.

In this chapter, RSM was applied to develop empirical models to describe the simultaneous interactive effects of adsorption parameters for diclofenac-rGOA, acetaminophen-RGM, Cu^{2+}-ZrGA and Ni^{2+}-ZrGA systems discussed in Chapter 4. CCD was used to study the diclofenac-rGOA and acetaminophen-RGM batch systems, whereas, the Cu^{2+}-ZrGA and Ni^{2+}-ZrGA systems utilised BBD model as ZrGA experienced structural instability at high temperature (> 50 °C), hence 50 °C will be considered as the maximum tolerance to study the adsorption process. Thereafter, process optimisation was performed to optimise the adsorption capacity for each adsorbate-adsorbent system.

5.2 RSM study on diclofenac adsorption onto rGOA

5.2.1 Model validaton and diagnostic analysis

By fitting of the experimental data shown in Table 5.1 to Eq. (3.18), a second order polynomial model representing the relationship between the independent variables and process response was established. This model is expressed by Eq. (5.1) in actual unit:

$$q = +13608.56 - 3822.22\,A - 24.099\,B - 2.06\,C - 620.04 - 5.60\,AB - 5.62\,AC + 20.45\,AD - 6.35 \times 10^{-3}BC + 0.11\,BD + 0.06\,CD + 7917.22\,A^2 + 0.07\,B^2 + 0.01\,C^2 + 8.37\,D^2 \quad (5.1)$$

The predicted response (q_{pred}) calculated by Eq. (5.1) are tabulated in Table 5.1. The established model demonstrated a good representation to the experimental data

with residue values varying from 0.49 to 106.50 mg/g. The q_{pred} provided satisfactory approximation to the actual response (q_{exp}) with high correlation, as demonstrated in Fig. 5.1(a). The R^2 of the developed model was 0.9613, implying that 96.13 % of the total variations in the results could be due to the factors which were studied. Additionally, the R^2 was very close to the adjusted R^2 (0.9251). Generally, R^2 would increase with addition of terms to the model, but adjusted R^2 would decrease if the term added was insignificant (increase if the included term is significant). Therefore, these two values should be close to each other to ensure that only significant terms were included in the model. Furthermore, the difference between the adjusted R^2 (0.9251) and predicted R^2 (0.8023) was less than 0.2, signifying each model terms over the design space. The 'lack-of-fit' (p-value = 0.1336, F-value = 2.80) of this model was found to be statistically insignificant, supporting the good fitting of the model and was relatively negligible compared to pure error. Therefore, the adsorption of diclofenac onto rGOA could be represented by Eq. (5.1) without any model reduction.

Table 5.1: RSM-CCD design matrix with experimental and predicted response for diclofenac adsorption onto rGOA.

Independent variables			**Level**				
			- 2	**-1**	**0**	**+1**	***+2***
A: rGOA dosage (g/L)			0.1	0.2	0.3	0.4	0.5
B: Shaking speed (rpm)			125	150	175	200	225
C: Initial concentration (mg/L)			100	175	250	325	400
D: Temperature (°C)			30.0	32.5	35.0	37.5	40.0
Run	***A***	***B***	***C***	***D***	q_{exp} **(mg/g)**	q_{pred} **(mg/g)**	**Residue**
1	0.3	175	250	35.00	123.95	147.45	-23.50
2	0.2	200	325	32.50	686.09	649.89	36.20
3	0.4	200	175	37.50	191.25	194.02	-2.77
4	0.2	150	325	37.50	728.69	677.13	51.56
5	0.2	150	175	37.50	177.98	194.18	-16.20
6	0.4	200	175	32.50	157.53	158.02	-0.49
7	0.4	150	325	37.50	463.25	482.61	-19.36
8	0.3	125	250	35.00	288.54	301.08	-12.54
9	0.2	200	175	37.50	268.90	275.75	-6.85
10	0.2	200	325	37.50	748.96	711.07	37.90
11	0.4	150	175	37.50	183.28	168.41	14.87
12	0.3	175	100	35.00	53.29	24.01	29.28
13	0.4	200	325	32.50	421.32	378.97	42.34
14	0.2	200	175	32.50	305.70	260.20	45.50
15	0.3	225	250	35.00	267.41	332.08	-64.67
16	0.2	150	175	32.50	203.52	207.18	-3.66
17	0.3	175	250	35.00	146.64	147.45	-0.81
18	0.4	200	325	37.50	515.32	460.59	54.73
19	0.2	150	325	32.50	673.42	644.50	28.92
20	0.1	175	250	35.00	564.40	612.48	-48.08
21	0.4	150	175	32.50	149.21	160.96	-11.75
22	0.3	175	250	35.00	223.55	147.45	76.11
23	0.3	175	250	35.00	132.36	147.45	-15.09
24	0.3	175	400	35.00	621.41	727.91	-106.50
25	0.3	175	250	40.00	372.56	390.89	-18.33
26	0.3	175	250	30.00	263.38	322.27	-58.89
27	0.3	175	250	35.00	122.81	147.45	-24.63
28	0.4	150	325	32.50	487.46	429.54	57.92
29	0.3	175	250	35.00	135.36	147.45	-12.08
30	0.5	175	250	35.00	286.65	315.79	-29.14

Table 5.2: ANOVA for the RSM model of diclofenac adsorption onto rGOA.

Source	**Sum of squares**	**Mean square**	**F- value**	**p-value Prob > F**	**Remark**
Model	1.200E+006	85720.58	26.59	< 0.0001	Significant
A	1.320E+005	1.320E+005	40.96	< 0.0001	Significant
B	1441.43	1441.43	0.45	0.5138	Insignificant
C	7.432E+005	7.432E+005	230.57	< 0.0001	Significant
D	7063.82	7063.82	2.19	0.1595	Insignificant
AB	3131.42	3131.42	0.97	0.3399	Insignificant
AC	28475.52	28475.52	8.83	0.0095	Significant
AD	418.11	418.11	0.13	0.7238	Insignificant
BC	2268.71	2268.71	0.70	0.4147	Insignificant
BD	815.08	815.08	0.25	0.6224	Insignificant
CD	2081.29	2081.29	0.65	0.4342	Insignificant
A^2	1.719E+005	1.719E+005	53.34	< 0.0001	Significant
B^2	49038.37	49038.37	15.21	0.0014	Significant
C^2	89512.96	89512.96	27.77	< 0.0001	Significant
D^2	74977.25	74977.25	23.26	0.0002	Significant
Residual	48349.97	3223.33			
Lack of Fit	41024.54	4102.45	2.80	0.1336	Insignificant
Pure Error	7325.43	1465.09			
Std. dev.	56.77		R^2	0.9613	
Mean	332.14		Adjusted R^2	0.9251	
			Predicted R^2	0.8023	
			Adequate Precision	17.534	

ANOVA such as p-value, Fisher value (F-value) and adequate precision was used to assess the model validity, and the ANOVA results for the developed model are shown in Table 5.2. The statistical significance of each term in Table 5.2 was set at 95 % confidence level as indexed by its p-value ($p < 0.05$). Also, the lower the p-value, the more significant is the model term. As observed in Table 5.2, the developed model with $p < 0.0001$ and model terms of *A*, *C*, *AC*, A^2, B^2, C^2 and D^2 with $p < 0.05$, were statistically significant. The adequate precision which represents the signal to noise ratio, is preferably to be greater than 4. In this study, the adequate precision of the model

was 17.534, indicating an adequate response signal and its suitably in navigating the design space (Jiryaei Sharahi & Shahbazi, 2017).

The model adequacy and predictability were confirmed by the diagnostic plots, as shown in Fig. 5.1. Fig. 5.1(b) represents the normal distribution of internally studentised residuals for the process response. This plot demonstrated a linear profile with no occurrence of large variation of the variance, suggesting the high degree of fitness of the predicted model and confirming the assumption on the error terms are normally distributed (Karri & Sahu, 2018). The plot of internally studentised residuals versus experimental runs contributes information on the model accuracy. Fig. 5.1(c) was used to determine any outlier from all 30 experimental runs for diclofenac adsorption onto rGOA. The outlier plot indicates the residual magnitude of each experimental run to determine potential outlier if the magnitude exceeded the general threshold of ± 3 % standard deviation (Mallaiah & Reddy, 2016). In Fig. 5.1(c), the internally studentised residuals were randomly distributed across all experimental run and the magnitude was within the limits. Notably, most of experimental data were in range of -2 to +2, representing a 95 % confidence level. Hence, there is no outliers detected and the model prediction is considered accurate (Mallaiah & Reddy, 2016; Sun et al., 2018a).

The residual versus predicted response plot (Fig. 5.1(d)) provides indication on the independency of residuals to the response value, and it is expected to be randomly scattered (Sharifi et al., 2018). If the plot displayed in funnel shape, it is assumed that the residual is related to the mean value of response (Mallaiah & Reddy, 2016). Fig. 5.1(d) exhibits random scattering pattern, implying that Equation (5.1) is a good model. Based on the ANOVA results and diagnostic plots, the developed model could be used to describe the adsorption of diclofenac onto rGOA at 95 % confidence level.

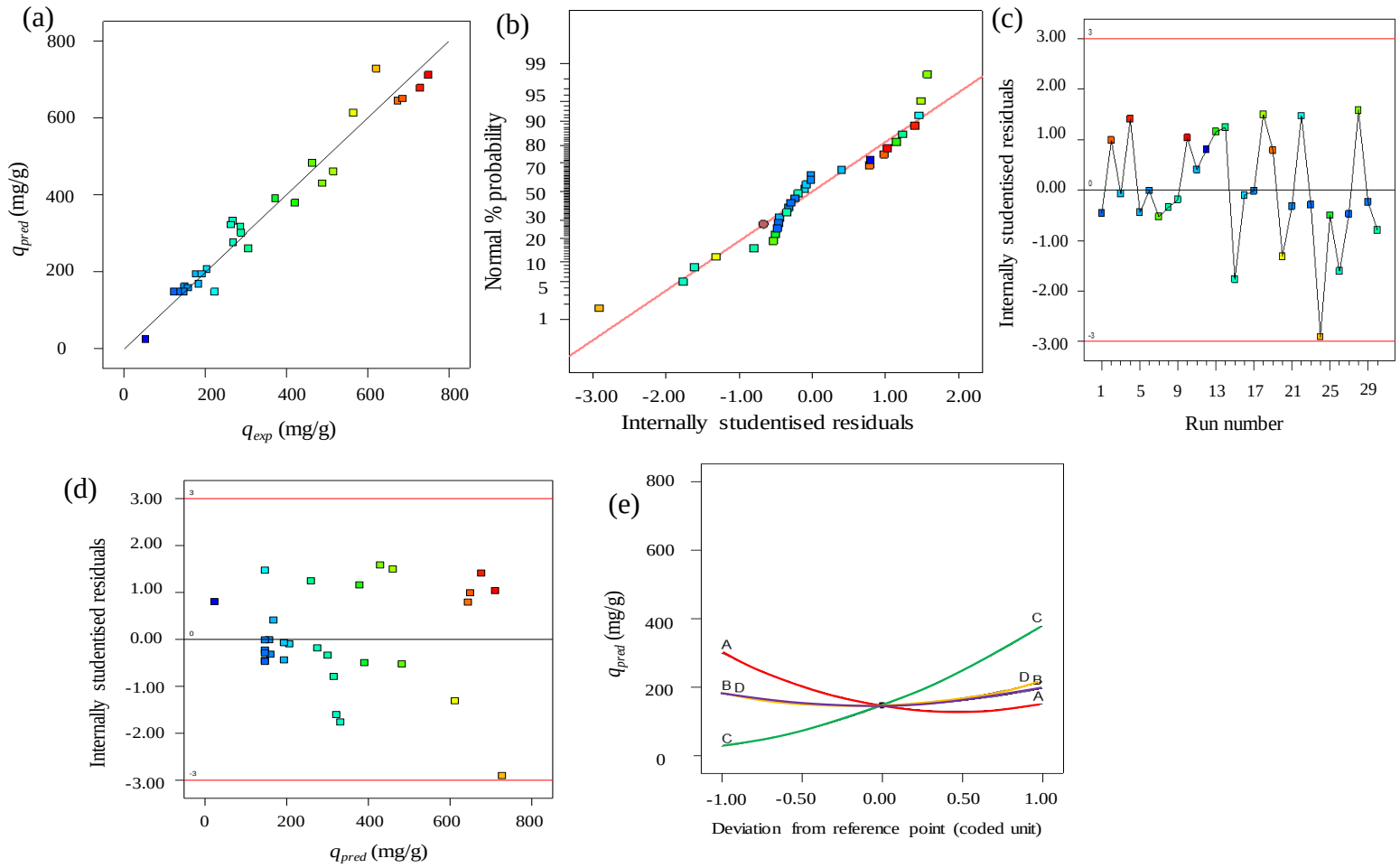

Fig. 5.1: Diagnostic and perturbation plots: (a) predicted versus actual plot, (b) internally studentised plot, (c) internally studentised plot vs. run plot, (d) internally studentised plot vs predicted value plot and (e) perturbation plot.

5.2.2 Perturbation study

The relative impact of each factor on the process response (q) was explained by the mathematical expression derived from the design matrix in coded unit, as shown by Eq. (5.2):

$$q = +147.45 - 74.17\,A + 7.75\,B + 175.97\,C + 17.16\,D - 13.99\,AB - 42.19\,AC + 5.11\,AD - 11.91\,BC + 7.14\,BD + 11.41\,CD + 79.17\,A^2 + 42.28\,B^2 + 57.13\,C^2 + 52.28\,D^2 \quad (5.2)$$

The degree of influence and associated effect were determined based on the numerical value and sign of each model terms in Eq. (5.2), respectively. The negative sign of dosage (*A*) indicated that this factor has a negative impact on the response *q*, whereas the positive sign associated with factors such as shaking speed (*B*), initial concentration (*C*) and temperature (*D*) suggested the synergistic effects on the response *q*. In addition, the effects of A and C were more influential over other terms based on the higher numerical magnitude (Eq. (5.2)). The perturbation plot (Fig. 5.1(e)) shows the relative impact of each factor towards *q*. As observed in the plot, factors *A* and *C* exhibited a sharp curvature, implying higher sensitivity towards *q* while the flatter curvature for *B* and *D* indicated that these factors had less impact on *q*. Therefore, the results revealed that diclofenac uptake by rGOA was highly affected by initial concentration (*C*), followed by dosage (*A*), temperature (*D*) and shaking speed (*B*).

5.2.3 3D response surface and process optimisation

The 3D response surface plots shown in Fig. 5.2 were used to examine the simultaneous interactions of two factors on *q* while the other two factors were maintained at the optimum conditions. In this study, the dosage of rGOA (*A*: *W*, g/L) was investigated within 0.1 – 0.5 g/L, and the surface response plots on the interaction with shaking speed (*B: S*, rpm), initial concentration (*C: C_o*, mg/L) and temperature (*D*: *T*, °C) are

depicted in Fig. 5.2 (a), (b) and (c). An increase in *W* had caused a decrease in q in all cases. This decreasing trend could be due to the increase in diffusional pathway for diclofenac molecules which resulted from the agglomeration of particles at higher dosage (Sheikhmohammadi et al., 2017). Therefore, the highest *q* was achieved when $W < 0.3$ g/L, $125 < S < 200$ rpm, $C_o > 250$ mg/L and $T > 35$ °C.

The initial concentration (*C*: C_o, mg/L) demonstrated a dominant synergistic influence on the adsorption of diclofenac and the interactive plots of C_o with other parameters are illustrated in Fig. 5.2 (b), (e) and (f). The increase in C_o provided a larger concentration driving force to overcome the mass transfer resistance at the solid-liquid interface and hence, increased the adsorption capacity of diclofenac (Mousavi et al., 2018). The response surface plots also revealed that the highest *q* occurred at $W < 0.3$ g/L, $S > 175$ rpm and $T > 35$ °C.

Fig. 5.2 (a), (d) and (e) present the interactions of *S* and *W*, *S* and C_o, and *S* and *T*, respectively. Overall, the effect of shaking speed showed flatter increment in *q* when the shaking speed was increased and the maximum *q* was achieved when $W < 0.3$ g/L, $C_o > 250$ mg/L and $T > 35$ °C. Under higher shaking speed, the external diffusional layer was eliminated, facilitating the uptake of diclofenac (Kuśmierek & Świątkowski, 2015; Yang et al., 2014). The effect of temperatures with other parameters are represented in Fig. 5.2(c), (e) and (f). The rise in temperature has accelerated the transportation of diclofenac molecules to adsorbent surface, thus leading to the increase in *q* (El Essawy et al., 2017). Therefore, the desirable conditions for achieving the highest *q* were $W < 0.3$ g/L, $S > 150$ rpm and $C_o > 250$ mg/L.

The adsorption of diclofenac onto rGOA was optimised by the Derringer's desirability function (d_i) based on *q* as the response. It was determined that at these conditions: $W = 0.25$ g/L, $S = 200$ rpm, $C_o = 325$ mg/L and $T = 35$ °C, the highest d_i

(0.969) was obtained along with q = 596.71 mg/g. The model predicted results were validated by performing experiments in triplicates at the optimised conditions. The experimental validation showed a low deviation (7.7 %) from the predicted q (646.49 mg/g) at the optimum conditions, signifying the accuracy of the developed model.

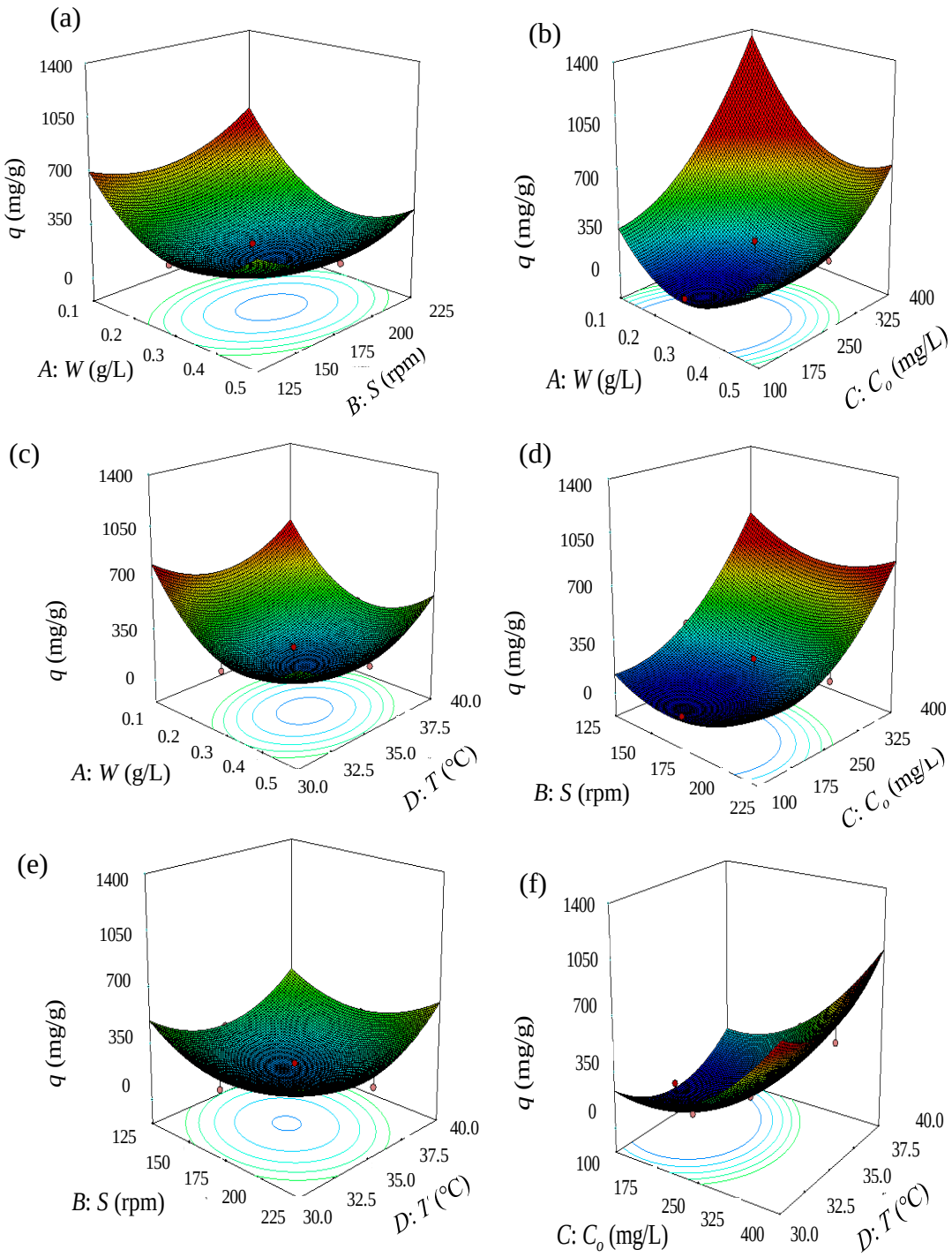

Fig. 5.2: Effects of (a) dosage and shaking speed, (b) dosage and initial concentration, (c) dosage and temperature, (d) shaking speed and initial concentration (e) temperature and shaking speed, and (f) temperature and initial concentration on *q*.

5.3 RSM study on acetaminophen uptake by RGM

5.3.1 Model validation and diagnostic analysis

The experimental data obtained from RSM – CCD design matrix in Table 5.3 was fitted into a quadratic model to correlate the interactions between the independent factors and process response (q), and the empirical model in actual unit of this study is expressed by Eq. (5.3):

$$q = -319.84 + 598.38\,A + 0.9065\,B + 78.64\,C - 13.25\,D - 0.7079\,AB - 43.44\,AC - 7.0337\,AD - 0.0474\,BC + 0.0298\,BD + 0.7486\,CD - 39.97\,A^2 - 3.3.14 \times 10^{-3}\,B^2 - 5.122\,C^2 + 0.2069\,D^2 \quad (5.3)$$

The model validity was assessed based on the ANOVA results (Table 5.4). The established model was statistically significant as evident by the sufficiently high *F*-value (23.43), *p*-value < 0.0001 and insignificant lack-of-fit error (*p*-value = 0.4326). The ANOVA result also revealed that the terms *A*, *B*, *C*, *D*, *AB*, *AC*, B^2 and C^2 were significant with *p*-value < 0.05 for each term. Furthermore, the R^2 of the developed model was 0.9563, indicating that 95.63 % of the total variation in q_{pred} could be explained based on the studied parameters with Eq. (5.3). The adjusted R^2 (R^2_{adj} = 0.9155) matched closely with the R^2 value as well. Notably, the difference between the R^2_{adj} and predicted R^2 (R^2_{pred} = 0.8027) was less than 0.2, implying the significance of each model terms over the design matrix. Additionally, adequate precision measures the signal to noise ratio and an adequate precision greater than 4 is preferred in model validation. The adequate precision of the model was 20.901 based on ANOVA and the developed model could provide adequate signal in predicting the acetaminophen adsorption capacity by RGM under the investigated factors.

Diagnostic plots such as predicted vs. actual, normal residuals distribution and residual vs. run, provided another statistical approach to justify the model predictability and adequacy. The diagnostic plots are presented in Fig. 5.3. The predicted vs. actual plot (Fig. 5.3(a)) shows that the q of Eq. (5.3) provided close approximation to the actual response (q_{exp}), with the residual errors varied between 0.31 – 13.46. The residue errors were distributed around a linear line with slight variation in the variance as depicted from the normal distribution plot (Fig. 5.3(b)). This suggested that the residuals were normally distributed, and the model has a satisfactory degree of fitness. Moreover, the outlier plot for all the 30 experimental runs (Fig. 5.3(c)) showed that the externally studentised residuals were randomly scattered across all experimental runs and the magnitude of each residuals were keep within the general outlier threshold of ±3 % standard deviation. It is worth mentioned that most experimental runs were distributed over 95 % confidence level as represented by the range of -2 to +2. Thus, the diagnostic plots revealed that no outliers were detected, and the model could provide adequate prediction onto the response.

Table 5.3 RSM-CCD design matrix with experimental and predicted response for acetaminophen adsorption onto RGM.

Independent variables			**Level**				
			- 2	**-1**	**0**	**+1**	***+2***
A: RGM dosage (g/L)			0.2	0.4	0.6	0.8	1.0
B: Initial concentration (mg/L)			50	100	150	200	250
C: pH			4	5	6	7	8
D: Temperature (°C)			30.0	32.5	35.0	37.5	40.0
Run	***A***	***B***	***C***	***D***	q_{exp} **(mg/g)**	q_{pred} **(mg/g)**	**Residue**
1	0.6	150	4	35.0	26.93	25.96	0.97
2	0.4	100	5	32.5	16.22	12.10	4.12
3	0.8	200	7	37.5	57.33	62.06	-4.72
4	0.6	150	6	35.0	73.06	66.85	6.21
5	0.6	150	6	35.0	70.79	66.85	3.94
6	0.8	100	5	32.5	18.59	25.63	-7.03
7	0.4	200	7	37.5	127.96	125.67	2.30
8	0.8	200	5	37.5	60.19	60.03	0.15
9	0.6	150	6	30.0	46.76	42.09	4.67
10	0.4	200	5	37.5	92.02	88.89	3.13
11	0.6	150	6	35.0	53.38	66.85	-13.46
12	0.2	150	6	35.0	86.81	85.49	1.31
13	0.4	100	5	37.5	25.86	37.87	-12.01
14	0.6	250	6	35.0	56.85	58.38	-1.52
15	0.8	200	7	32.5	35.24	27.96	7.27
16	0.6	50	6	35.0	15.90	9.03	6.87
17	0.4	100	7	37.5	88.72	84.12	4.60
18	1.0	150	6	35.0	39.44	35.41	4.03
19	0.8	100	7	32.5	25.91	29.64	-3.73
20	0.8	100	5	37.5	44.41	37.33	7.09
21	0.4	200	5	32.5	50.70	48.22	2.48
22	0.6	150	8	35.0	71.13	66.75	4.37
23	0.8	200	5	32.5	28.22	33.43	-5.21
24	0.6	150	6	35.0	72.37	66.85	5.53
25	0.4	100	7	32.5	45.98	50.87	-4.89
26	0.4	200	7	32.5	69.81	77.51	-7.70
27	0.8	100	7	37.5	41.61	48.83	-7.22
28	0.6	150	6	40.0	102.62	101.95	0.67
29	0.6	150	6	35.0	66.54	66.85	-0.31
30	0.6	150	6	35.0	64.94	66.85	-1.91

Table 5.4 ANOVA for the RSM model of acetaminophen adsorption onto RGM.

Source	**Sum of squares**	**Mean square**	***F*- value**	***p*-value Prob > *F***	**Remark**
Model	20431.82	1459.42	23.43	< 0.0001	Significant
A	3762.71	3762.71	60.41	< 0.0001	Significant
B	3652.59	3652.59	58.64	< 0.0001	Significant
C	2495.82	2495.82	40.07	< 0.0001	Significant
D	5374.78	5374.78	86.29	< 0.0001	Significant
AB	801.80	801.80	12.87	0.0027	Significant
AC	1207.85	1207.85	19.39	0.0005	Significant
AD	197.89	197.89	3.18	0.0949	Insignificant
BC	89.83	89.83	1.44	0.2484	Insignificant
BD	222.27	222.27	3.57	0.0784	Insignificant
CD	56.04	56.04	0.90	0.3579	Insignificant
A^2	70.13	70.13	1.13	0.3054	Insignificant
B^2	1883.26	1883.26	30.24	< 0.0001	Significant
C^2	719.61	719.61	11.55	0.0040	Significant
D^2	45.89	45.89	0.74	0.4042	Insignificant
Residual	934.27	62.28			
Lack of Fit	664.63	66.46	1.23	0.4326	Insignificant
Pure Error	269.65	53.93			
Std. dev.	7.89		R^2	0.9563	
Mean	55.88		R^2_{adj}	0.9155	
			R^2_{pred}	0.8027	
			Adequate precision	20.901	

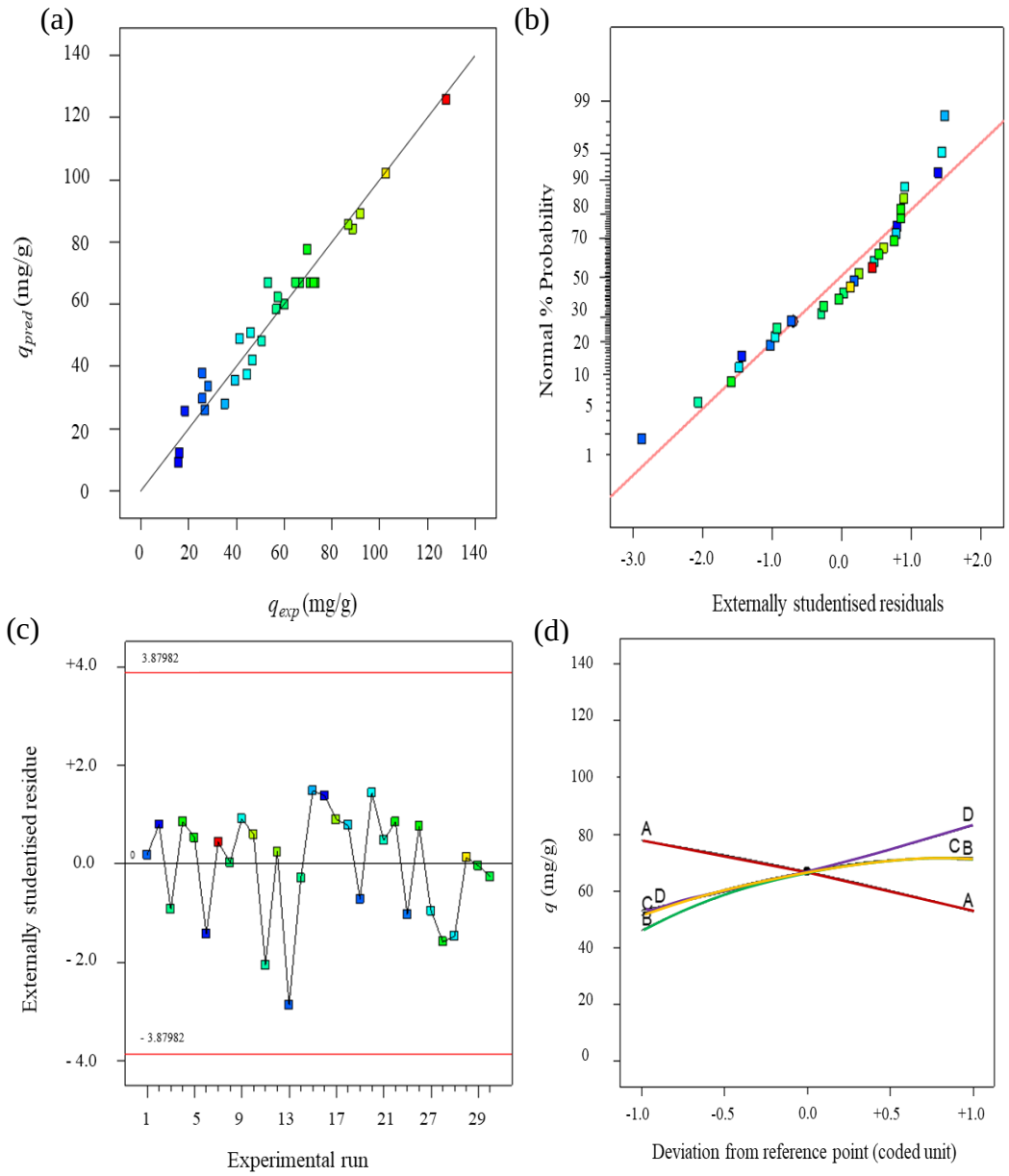

Fig. 5.3: Diagnostic plots: (a) predicted versus actual plot, (b) normal residuals distribution plot, (c) externally studentised residuals versus experimental run plot and (d) perturbation plot.

5.3.2 Perturbation study

The degree of influence of each independent variable on the process response (q) was examined by using the mathematical expression derived according to the CCD design matrix in coded unit (Eq. (5.4)).

$$q = +66.85 - 12.52\,A + 12.34\,B + 10.20\,C + 14.96\,D - 7.08\,AB - 8.69\,AC - 3.52\,AD - 2.37\,BC + 3.73\,BD + 1.87\,CD - 1.60\,A^2 - 8.29\,B^2 - 5.12\,C^2 + 1.29\,D^2 \quad (5.4)$$

Parameters such as initial acetaminophen concentration (*B*), pH (*C*) and temperature (*D*) have synergistic effects on the response as shown by the positive vector in Eq. (5.4), while the dosage (*A*) with negative vector had an antagonistic effect on the response. Additionally, the relative impacts of *A* and *D* were more influential than other terms as evident by the higher numerical magnitude in Eq. (5.4). The sensitivity of the process parameters is reflected by the curvature of the perturbation plots shown in Fig. 5.3(d). As observed, the curvatures for *A* and *D* were steeper than *B* and *C*, thus confirming the adsorption of acetaminophen onto RGM was highly affected by temperature (*D*), followed by dosage (*A*), initial concentration (*B*) and pH (*C*).

5.3.3 3D response surface analysis and process optimisation

The interactive relationship of two factors and the process response (q) is represented by 3D response surface plot (Fig. 5.4). Furthermore, the 3D response surfaces were studied to deduce the optimal range to maximise q in optimisation study. In this study, the simultaneous interactions between dosage (*A*: W = 0.1 – 0.5 g/L), initial acetaminophen concentration (*B*: C_o = 50 – 250 mg/L), pH (*C*: pH = 4 – 8) and temperature (*D*: T = 30 – 40 °C) onto q are illustrated in Fig. 5.4(a) – (f).

The interactive influence of *A* with *B*, *C* and *D* are displayed in Fig. 5.4(a), (b) and (c), respectively. Overall, the effect of *A* demonstrated a linear trend with negative gradient as the dosage was increased. Furthermore, the *q* value also decreased as the dosage was increased. This could be due to the extension of diffusional pathway for the acetaminophen molecules arising from particle agglomeration at higher dosage (Abd-Elhamid et al., 2019). In view of the contour plots for Fig. 5.4(a), (b) and (c), the highest possible *q* was achieved (q > 70 mg/g) when $A < 0.63$ g/L, $B > 160$ mg/L, $C > 6.12$ and $D > 35.8$ °C.

The response surface plots for the interactions of *B*-*A*, *B*-*C* and *B*-*D* are illustrated in Fig. 5.4(a), (d) and (e), respectively. As shown, the influence of *B* has reflected a concave surface when interacted with other parameters, and the *q* value increased with an increased in *B*. The increase in *B* provided a higher mass transfer gradient to overcome the mass transfer resistance on the solid-liquid interface during the adsorption process (Liu et al., 2019a). The zone which exhibited high adsorption capacity (q > 70 mg/g) was estimated to occur at $A < 0.59$ g/L, $B > 149$ mg/L, $C > 5.87$ and $D > 35.6$ °C based on the respective contour plot.

Fig. 5.4(b), (d) and (e) portray the simultaneous interaction of *C* with other parameters (*A*, *B* and *D*). A concave curvature can be seen from the response plots under the influence of C and it displayed a positive effect onto the process response. According to the canonical analysis, the maximum adsorption capacity was achieved within the estimated range of $A < 0.57$ g/L, $B > 180$ mg/L, $C > 5.79$ and $D > 35.9$ °C.

Influences of temperature (*D*) with *A*, *B* and *C* are shown by the response surface plots depicted in Fig. 5.4(c), (e) and (f), respectively. The temperature (*D*: *T*, °C) demonstrated a dominant synergistic effect on the acetaminophen adsorption and this

trend is represented by a steep linear line with positive gradient in the response surface plots. At higher temperature, the mass transfer rate of acetaminophen molecules to the RGM surface was accelerated, hence resulted in a higher q value (El Essawy et al., 2017). Moreover, the contour plots revealed that under the conditions of $A < 0.63$ g/L, $B > 149$ mg/L, $C > 5.78$ and $D > 35.9$ °C, a maximum q could potentially be achieved.

The optimum conditions to maximise the adsorption capacity was deduced based on the response surface analysis. Under the optimised parameters of $A = 0.47$ g/L, $B = 250$ mg/L, $C = 6.52$ and $D = 40$ °C, the adsorption capacity was predicted to be 138.77 mg/g. The predicted data was verified by conducting the adsorption experiment under the optimised conditions in triplication. The experimental adsorption capacity determined at the optimised conditions was found to be 129.35 mg/g, showing 6.79 % error deviation from the predicted data.

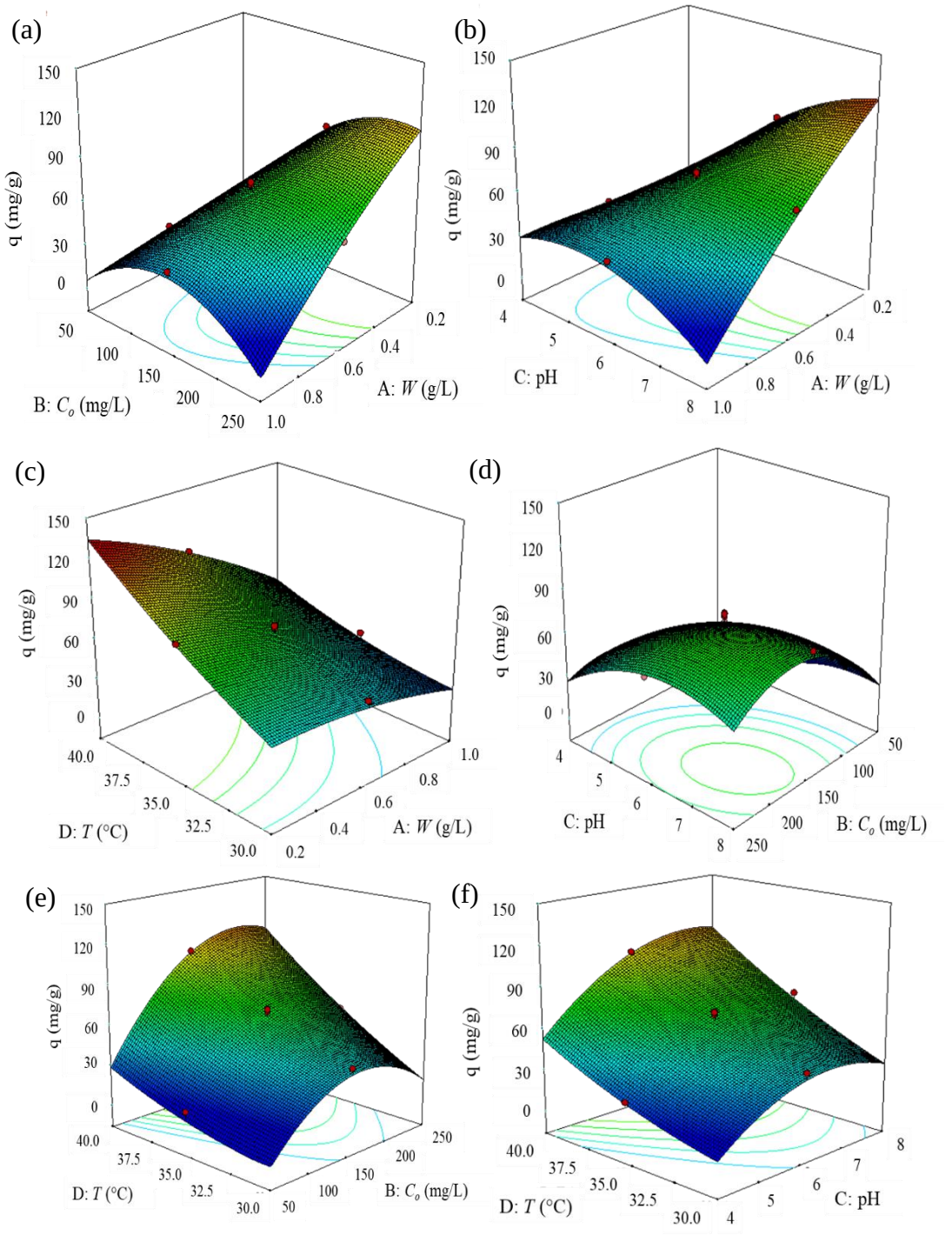

Fig. 5.4. Response surface plots for the interactions of (a) dosage and initial concentration, (b) dosage and pH, (c) dosage and temperature, (d) initial concentration and pH, (e) initial concentration and temperature and (f) pH and temperature.

5.4 RSM study on Cu^{2+} and Ni^{2+} adsorption onto ZrGA

5.4.1 Diagnostic and statistical validation

The simultaneous interactions between ZrGA dosage, pH, initial concentration and temperature on the adsorption of Cu^{2+} and Ni^{2+} are described by Eqs. (5.5) and (5.6), respectively.

$$q_{Cu} = 94.61 + 34.65\,A + 36.41\,B - 0.24\,C - 9.63\,D - 64.21\,AB - 0.41\,AC + 2.39\,AD - 0.02\,BC - 1.08\,BD + 0.042\,CD + 143.12\,A^2 + 8.86\,B^2 - 5.13 \times 10^{-4}\,C^2 + 0.08\,D^2 \quad (5.5)$$

$$q_{Ni} = -170.82 + 57.18\,A + 17.37\,B + 0.10\,C + 6.08\,D - 2.61\,AB + 0.11\,AC + 1.29\,AD - 0.03\,BC - 0.14\,BC - 1.50 \times 10^{-3}CD - 29.65A^2 - 0.03B^2 - 3.48 \times 10^{-4}\,C^2 - 0.12\,D^2 \quad (5.6)$$

The corresponding predicted data calculated using Eqs. (5.5) and (5.6) are tabulated in Tables 5.5 and 5.6, respectively. The developed models showed close approximation to the experimental data with relatively low residues varying from 0.02 to 2.923 mg/g for Cu^{2+} and 0.009 to 2.119 mg/g for Ni^{2+}. Figs. 5.5(a) and 5.6(a) exhibited close correlation between the predicted model and actual data, resulting in the high R^2 (Cu^{2+}: 0.9806; Ni^{2+}: 0.9524) for the developed model. This implied that the equation developed can accurately describe the change in response with varying process parameters. In addition, the difference between predicted R^2 (R^2_{pred}) and adjusted R^2 (R^2_{adj}) for Cu^{2+} (R^2_{pred} =0.9612; R^2_{adj} =0.9012) and Ni^{2+} (R^2_{pred} =0.9048; R^2_{adj} =0.7390) were less than 0.2, indicating that significant model coefficients were included in the developed model. The statistically significant model terms were identified based on p-value < 0.05 (95 % confidence level). As shown, *A*, *B*, *C*, *D*, *AB*, *AC*, *BD*, *CD*, A^2 and B^2 were the significant terms for Cu^{2+} adsorption, whereas *A*, *B*, *C*, *D*, *AC*, *AD*, *BC*, A^2 and D^2 were the significant terms for Ni^{2+} adsorption. Other statistical parameters such

as Fischer value (F-value) and adequate precision ($AP > 4$) validated the predictability of the empirical model for Cu^{2+} (F-value= 50.60; $AP = 32.17$) and Ni^{2+} (F-value= 20.02; $AP = 16.45$). Moreover, the p-value of lack of fit error for Cu^{2+} (0.2422) and Ni^{2+} (0.0535) uptake were more than 0.05, suggesting this error is insignificant and negligible with respect to pure error.

Apart from predicted vs. actual plot, the normal residual plots for Cu^{2+} and Ni^{2+} adsorption capacity (Figs. 5.5(b) and 5.6(b)) can be used to justify the validity of the generated equations. The normal residual plots for both models exhibited a linear profile, suggesting high degree of fitness of predicted data and the errors associated were normally distributed. Overall, Eqs. (5.5) and (5.6) provided satisfactory prediction on the adsorption system based on the randomly scattered trend in residual vs. experimental run plot (Figs. 5.5(c) and 5.6(c)).

Table 5.5 RSM-BBD design matrix with experimental and predicted response for Cu^{2+} adsorption onto ZrGA.

Independent variables			**Level**				
			-1	**0**	**+1**		
A: ZrGA dosage (g/L)			0.8	1.2	1.6		
B: pH			5	6	7		
C: Initial concentration (mg/L)			200	250	300		
D: Temperature (°C)			30	35	40		
Run	***A***	***B***	***C***	***D***	q_{exp} **(mg/g)**	q_{pred} **(mg/g)**	**Residue**
1	1.2	7	300	35	79.65	77.58	2.07
2	1.2	5	200	35	26.82	25.49	1.33
3	1.2	6	300	30	52.13	58.31	-6.18
4	1.6	6	250	40	51.59	49.97	1.62
5	1.2	7	200	35	71.54	69.73	1.81
6	1.2	7	250	40	51.27	56.57	-5.30
7	1.6	7	250	35	56.84	59.46	-2.62
8	0.8	6	250	30	96.63	94.86	1.77
9	1.2	6	250	35	40.64	42.79	-2.16
10	1.2	7	250	30	93.40	92.06	1.34
11	1.6	6	250	30	65.90	65.05	0.85
12	1.2	6	200	40	25.01	23.01	2.00
13	1.2	5	250	40	25.44	25.99	-0.55
14	1.2	6	250	35	39.33	42.79	-3.47
15	0.8	5	250	35	36.72	38.29	-1.57
16	1.2	6	250	35	47.90	42.79	5.10
17	1.2	6	250	35	41.41	42.79	-1.38
18	1.2	6	300	40	44.08	44.40	-0.32
19	0.8	6	250	40	63.22	60.67	2.55
20	1.6	6	300	35	58.58	54.04	4.55
21	0.8	6	200	35	59.88	63.63	-3.75
22	1.6	5	250	35	62.51	69.40	-6.89
23	1.6	6	200	35	62.15	59.66	2.49
24	1.2	5	300	35	40.55	38.97	1.58
25	0.8	6	300	35	88.89	90.58	-1.70
26	1.2	6	200	30	54.51	58.37	-3.87
27	0.8	7	250	35	133.78	131.08	2.70
28	1.2	6	250	35	44.70	42.79	1.91
29	1.2	5	250	30	45.88	39.78	6.09

Table 5.6 RSM-BBD design matrix with experimental and predicted response for Ni^{2+} adsorption onto ZrGA.

Independent variables					**Level**		
					-1	**0**	**+1**
A: ZrGA dosage (g/L)					1.6	2.0	2.4
B: pH					5	6	7
C: Initial concentration (mg/L)					200	250	300
D: Temperature (°C)					30	35	40
Run	***A***	***B***	***C***	***D***	q_{exp} **(mg/g)**	q_{pred} **(mg/g)**	**Residue**
1	1.6	6	300	35	43.77	41.99	1.79
2	2.4	7	250	35	38.50	38.38	0.12
3	1.6	6	250	40	35.95	37.12	-1.16
4	2.4	6	250	40	37.74	38.26	-0.52
5	2.0	6	250	35	47.38	46.98	0.40
6	2.0	6	300	30	44.37	44.99	-0.62
7	2.0	5	200	35	44.03	44.57	-0.54
8	1.6	7	250	35	43.65	44.49	-0.84
9	2.4	5	250	35	43.30	42.01	1.29
10	2.4	6	200	35	35.51	36.43	-0.92
11	2.0	5	300	35	47.88	49.12	-1.24
12	2.0	5	250	40	43.52	43.89	-0.37
13	2.0	6	250	35	47.10	46.98	0.12
14	2.0	7	250	40	41.25	40.92	0.33
15	2.0	7	250	30	46.62	45.39	1.23
16	2.0	6	250	35	47.10	46.98	0.12
17	2.0	6	200	30	43.99	44.20	-0.21
18	1.6	6	200	35	45.43	44.75	0.68
19	2.0	6	250	35	46.06	46.98	-0.92
20	2.0	6	200	40	41.49	40.42	1.07
21	2.0	6	300	40	43.37	42.71	0.66
22	1.6	6	250	30	44.53	45.31	-0.79
23	2.0	7	200	35	45.98	46.05	-0.070
24	2.0	7	300	35	43.80	44.57	-0.77
25	2.4	6	300	35	42.45	42.27	0.19
26	1.6	5	250	35	44.26	43.94	0.33
27	2.4	6	250	30	35.98	36.13	-0.15
28	2.0	5	250	30	46.02	45.49	0.54
29	2.0	6	250	35	47.24	46.98	0.27

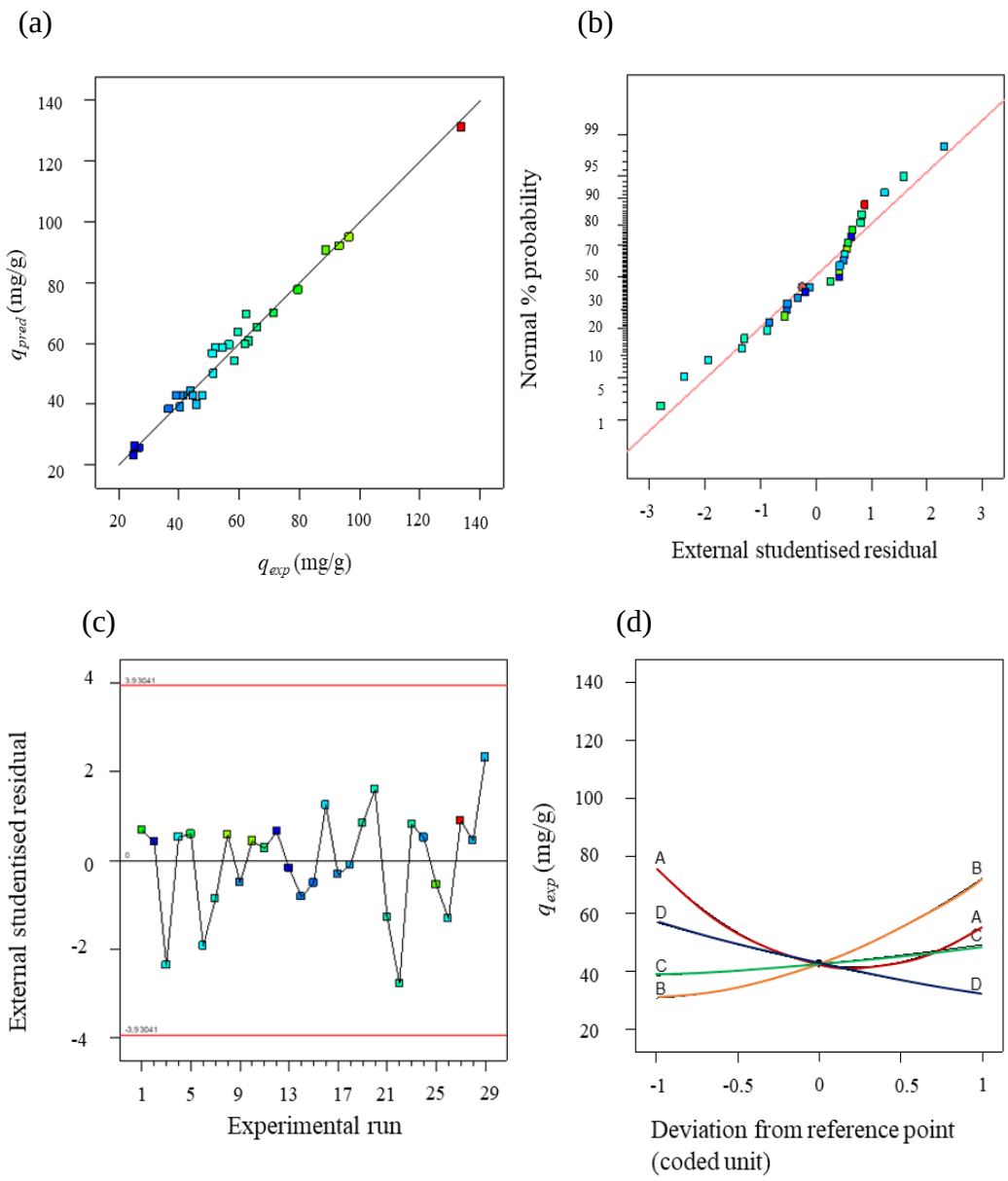

Fig. 5.5: Diagnostic plot for Cu^{2+} adsorption onto ZrGA – (a) predicted vs. actual plot, (b) normal probability plot, (c) external studentised residual vs. experimental run plot and (d) perturbation plot.

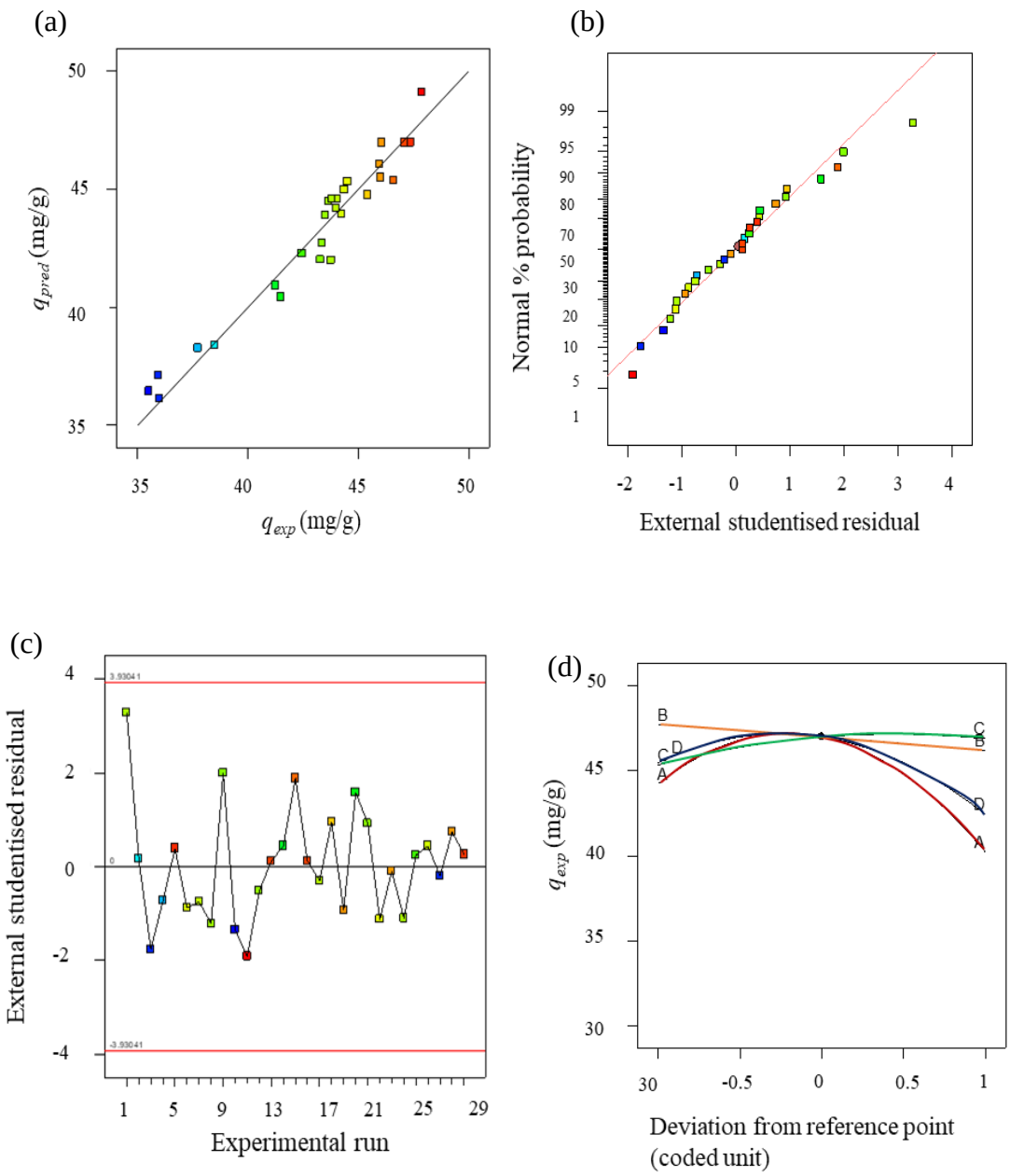

Fig. 5.6: Diagnostic plot for Ni^{2+} adsorption onto ZrGA – (a) predicted vs. actual plot, (b) normal probability plot, (c) external studentised residual vs. experimental run plot and (d) perturbation plot.

Table 5.7: ANOVA for the RSM models of Cu^{2+} and Ni^{2+} adsorption onto ZrGA.

Cu^{2+} adsorption						***Ni^{2+} adsorption***					
Source	**Sum of squares**	**Mean square**	***F*- value**	***p*-value Prob > *F***	**Remark**	**Source**	**Sum of squares**	**Mean square**	***F*- value**	***p*-value Prob > *F***	**Remark**
Model	15462.20	1104.44	50.60	< 0.0001	Significant	Model	338.28	24.16	20.02	< 0.0001	Significant
A	1231.09	1231.09	56.41	< 0.0001	Significant	*A*	48.45	48.45	40.14	< 0.0001	Significant
B	5148.74	5148.74	235.90	< 0.0001	Significant	*B*	7.10	7.10	5.88	0.0295	Significant
C	341.12	341.12	15.63	0.0014	Significant	*C*	7.07	7.07	5.86	0.0297	Significant
D	1820.75	1820.75	83.42	< 0.0001	Significant	*D*	27.54	27.54	22.82	0.0003	Significant
AB	2638.59	2638.59	120.89	< 0.0001	Significant	*AB*	4.37	4.37	3.62	0.0779	
AC	265.38	265.38	12.16	0.0036	Significant	*AC*	18.49	18.49	15.32	0.0016	Significant
AD	91.32	91.32	4.18	0.0601		*AD*	26.69	26.69	22.12	0.0003	Significant
BC	7.92	7.92	0.36	0.5566		*BC*	9.10	9.10	7.54	0.0158	Significant
BD	117.66	117.66	5.39	0.0358	Significant	*BD*	2.07	2.07	1.72	0.2112	
CD	115.12	115.12	5.27	0.0376	Significant	*CD*	0.56	0.56	0.46	0.5069	
A^2	3401.19	3401.19	155.83	< 0.0001	Significant	A^2	146.01	146.01	120.97	< 0.0001	Significant
B^2	509.49	509.49	23.34	0.0003	Significant	B^2	5.209E-003	5.209E-003	4.316E-003	0.9485	
C^2	10.71	10.71	0.49	0.4951		C^2	4.92	4.92	4.08	0.0631	
D^2	24.51	24.51	1.12	0.3072		D^2	59.38	59.38	49.20	< 0.0001	Significant
Residual	305.56	21.83				Residual	16.90	1.21			
Lack of Fit	257.31	25.73	2.13	0.2422	Insignificant	*Lack of Fit*	15.80	1.58	5.73	0.0535	Insignificant
Pure Error	48.25	12.06				*Pure Error*	1.10	0.28			
Std. dev.	4.67		R^2	0.9806		Std. dev.	1.10		R^2	0.9524	
Mean	57.27		R^2_{adj}	0.9612		Mean	43.39		R^2_{adj}	0.9048	
			R^2_{pred}	0.9012					R^2_{pred}	0.7390	
			Adequate precision	32.165					Adequate precision	16.445	

5.4.2 Perturbation analysis

The sensitivity of each factor on the adsorption capacity is expressed in mathematical forms for Cu^{2+} and Ni^{2+} adsorption by Eqs. (5.7) and (5.8):

$$q_{Cu} = 42.79 - 10.13\,A + 20.71\,B + 5.33\,C - 12.32\,D - 25.68\,AB - 8.15\,AC + 4.78\,AD \pm 1.41\,BC - 5.42\,BD + 5.36\,CD + 22.90\,A^2 + 8.86\,B^2 + 1.28C^2 + 1.94\,D^2 \quad (5.7)$$

$$q_{Ni} = 46.98 - 2.01\,A - 0.77\,B + 0.77\,C - 1.52\,D - 1.05\,AB + 2.15\,AC + 2.58\,AD - 1.51BC - 0.72\,BD - 0.37\,CD - 4.74\,A^2 - 0.03\,B^2 - 0.87\,C^2 - 3.03\,D^2 \quad (5.8)$$

The sign of Eqs. (5.7) and (5.8) represented the associated effect on the process response while the numerical value indicated the degree of influence of the factor. Generally, the increase in parameters such as ZrGA dosage (*A*) and temperature (*D*) would have antagonistic effect on the adsorption capacity as indicated by the negative sign on the model coefficient. The solution pH (*B*) and initial concentration (*C*) would have positive impact on Cu^{2+} and Ni^{2+} adsorption. By gauging the numerical value of the model coefficient, it can be assumed that the sequence on the most influential parameters on Cu^{2+} and Ni^{2+} adsorption onto ZrGA were $B > D > A > C$ and $A > D > B > C$, respectively.

5.4.3 Response surface plots and process optimisation

The simultaneous interactions of each investigated parameters onto Cu^{2+} and Ni^{2+} adsorption capacity by ZrGA were studied through response surface plots as illustrated in Figs. 5.7 and 5.8. ZrGA dosage exhibited a negatively effect on the response and this is reflected on the response surface plots (Fig. 5.7(a) –(c) and Fig. 5.8(a) – (c)). The decreasing trend was due to reduction of total surface area for pollutant uptake from particle agglomeration at greater ZrGA dosage. In order to achieve the highest possible adsorption capacity, the ZrGA dosage should be kept at $A < 1.2$ g/L for Cu^{2+} and $1.8 < A < 2.2$ g/L for Ni^{2+}.

The effect of pH (B) showed favourable potential in achieving highest sorption capacity at pH > 6 as indicated by Figs. 5.7 – 5.8 (a), (d) and (f). The ZrGA surface was negatively charged above pH 6 (PZC = 4.8) and this facilitated in the adsorption of positively charged Cu^{2+} and Ni^{2+} through electrostatic attraction. However, electrostatic repulsion occurred when the like-charged adsorbates co-existed with ZrGA at pH < 6. Similarly, the initial metal concentration (C) demonstrated a positive trend with adsorption capacity. According to Figs. 5.7 – 5.8 (b), (d) and (e), the adsorption capacity increased when $C > 240$ mg/L and this was possibly due to the enhancement in concentration driving force to overcome the mass transfer resistance at the solid-liquid phase, thus improve the diffusion of the heavy metals onto ZrGA surface and increased the adsorption capacity. The adsorption capacity of Cu^{2+} and Ni^{2+} was decreased with as temperature increased, as illustrated in Fig. 5.7 – 5.8 (c), (e) and (f). This could be attributed to the breakdown of weak sorption forces such as Van der Waals and hydrogen bonding at higher temperature, which in turn led to the release of adsorbed heavy metals from the ZrGA surfaces. Therefore, temperature (D) should be maintained below 34 °C for Cu^{2+} adsorption and $34 < D < 38$ °C for Ni^{2+}.

Based on the response surface plots, the optimum conditions to achieve the highest adsorption capacity for Cu^{2+} (58.31 mg/g) and Ni^{2+} (44.57 mg/g) were *A* = 1.2 g/L, *B* = 6, *C* = 300 mg/L and *D* = 30 °C, and *A* = 2 g/L, *B* = 7, *C* = 300 mg/L and *D* = 35 °C, respectively. Experiments were carried out based on the optimum conditions and the results obtained for Cu^{2+} adsorption capacity = 53.14 mg/g (error = 8.87 %) and Ni^{2+} adsorption capacity = 41.64 mg/g (error = 6.57 %). The experimentally obtained data showed close approximation to the predicted data, signifying the accuracy of the model.

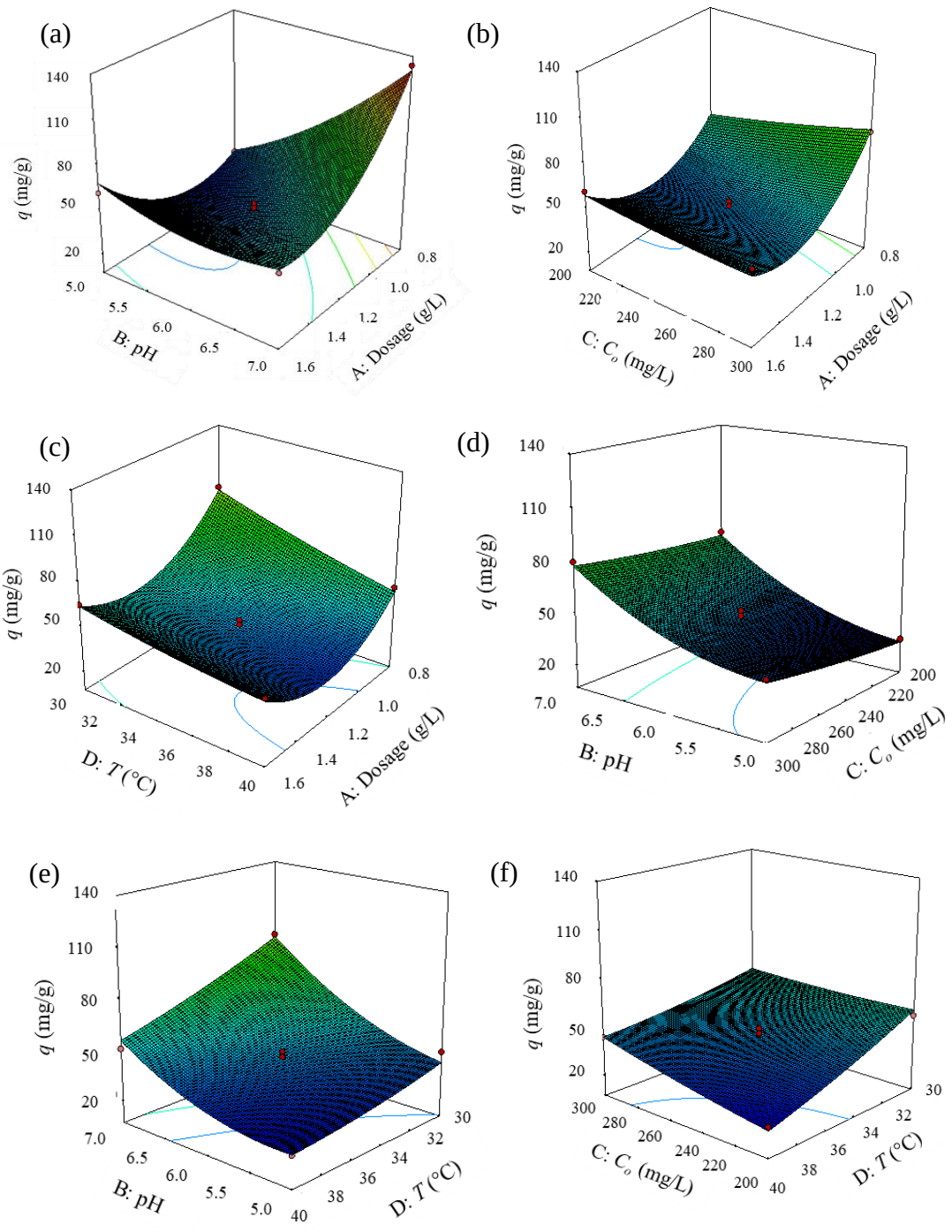

Fig. 5.7: Effects of (a) dosage and pH, (b) dosage and initial concentration, (c) dosage and temperature, (d) pH and initial concentration (e) temperature and pH, and (f) temperature and initial concentration on *q*.

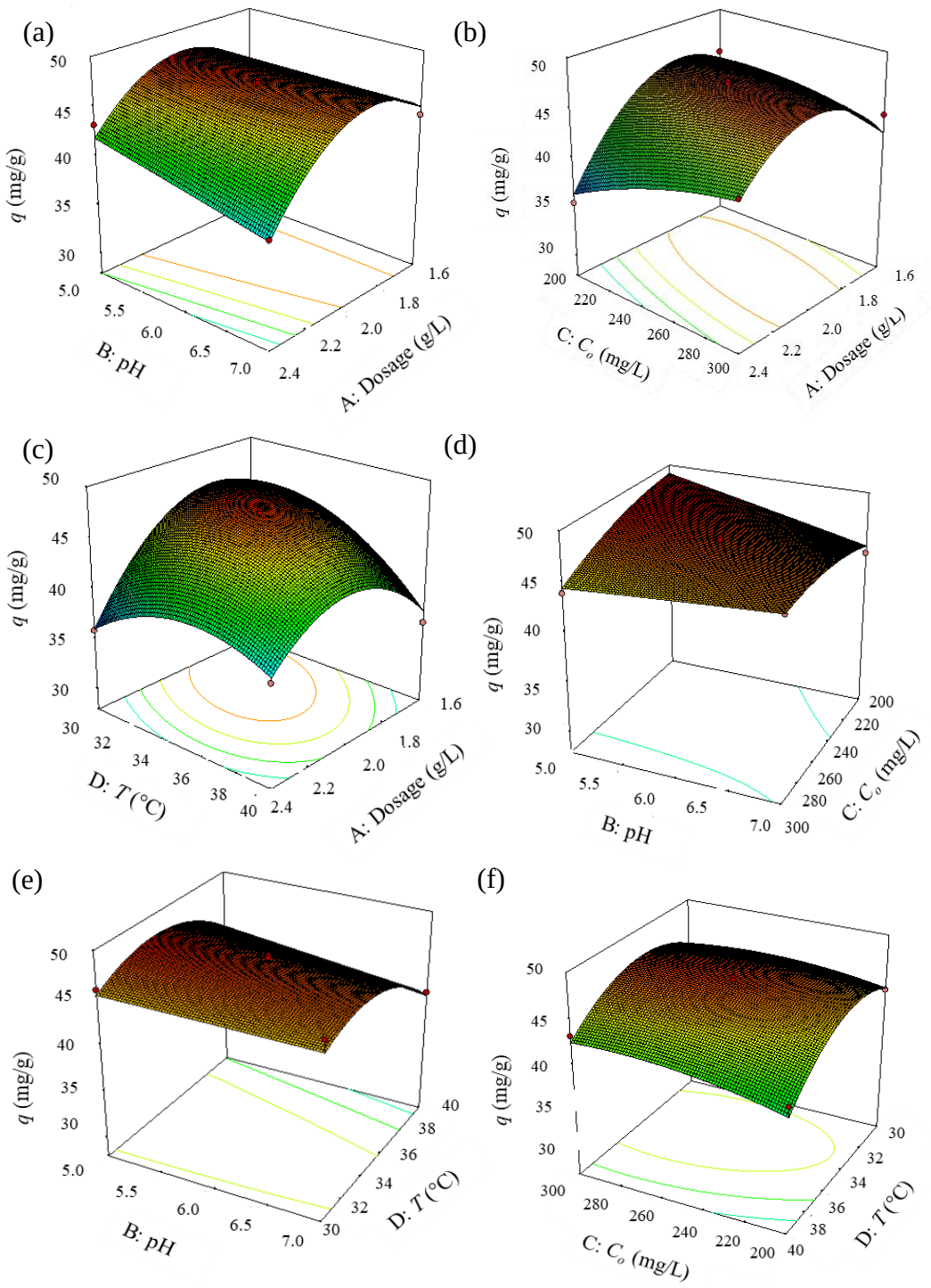

Fig. 5.8: Effects of (a) dosage and pH, (b) dosage and initial concentration, (c) dosage and temperature, (d) pH and initial concentration (e) temperature and pH, and (f) temperature and initial concentration on *q*.

5.5 Conclusions

Mathematical model for the adsorption of diclofenac onto rGOA was developed by RSM. The developed model was statistically significant at 95 % confidence level. Simultaneous interactions among four independent variables, namely dosage, shaking speed, initial concentration and temperature, were evaluated and the dominant parameters affecting the process were found to be dosage and initial concentration. The perturbation study showed that shaking speed, initial concentration and temperature have synergistic impacts on diclofenac adsorption capacity, while rGOA dosage has antagonistic effect on the pharmaceutical uptake. The optimum adsorption capacity of 596.71 mg/g was achieved at the following conditions: 0.25 g/L dosage, 200 rpm shaking speed, 325 mg/L initial concentration and 30 °C.

The RSM model for estimation of the adsorption capacity of RGM towards acetaminophen was verified to be statistically significant. The simultaneous interactions of adsorption parameters such as RGM dosage, initial concentration, pH and temperature, were investigated by RSM. The influences of dosage and temperature were found to be dominant towards the process response. The highest adsorption capacity was achieved (129.35 mg/g) under the optimised conditions of 0.47 g/L dosage, 250 mg/L initial concentration, pH 6.52 and 40 °C temperature.

The single component adsorption of Cu^{2+} and Ni^{2+} onto ZrGA was studied by varying several parameters such as ZrGA adsorbent dosage, pH, initial concentration and temperature, simultaneously using RSM. The mathematical expressions for predicting the Cu^{2+} and Ni^{2+} adsorption capacities were developed, and the models were statistically significant based on analysis of variance (ANOVA) evaluation. The most influential parameters for Cu^{2+} adsorption was initial Cu^{2+} concentration, followed by temperature, ZrGA dosage and pH, while the order decreased from ZrGA dosage >

temperature > initial Ni^{2+} adsorption > pH for Ni^{2+} adsorption. The highest Cu^{2+} adsorption capacity (53.14 mg/g, error = 8.87 %) was achieved under the optimised condition of ZrGA dosage = 1.2 g/L, pH = 6, initial Cu^{2+} concentration = 300 mg/L and temperature = 30 °C. The highest Ni^{2+} adsorption capacity (41.64 mg/g, error = 6.57 %) was obtained under the optimised condition of ZrGA dosage = 2.0 g/L, pH = 7, initial Ni^{2+} concentration = 300 mg/L and temperature = 35 °C.

In this study, four independent process parameters were determined to exhibit quadratic relationships which affected the adsorption capacities of the 3D graphene structures. Furthermore, RSM was successfully applied to examine the type of interactions and to develop statistically significant models to describe the batch adsorption systems. The adsorption capacities were optimised based on the 3D response surface plots. The batch adsorption studies demonstrated that the developed 3D graphene structures had high removal efficiency for the pharmaceutical and heavy metal contaminants, hence the next chapter presents the application of the adsorbents in continuous adsorption mode.

Chapter 6: Packed Bed Adsorption of Pharmaceuticals and Heavy Metals onto 3D Graphene Aerogels

6.1 Introduction

Three-dimensional (3D) graphene-based structures such as hydrogel (Ma et al., 2020), aerogel (Han et al., 2017), beads (Li et al., 2020b) and fibre (Tang et al., 2020) are potential adsorbents for wastewater treatment. The use of 3D graphene-based aerogels in wastewater remediation has become an important research field as they have advantages such as ultralight weight, high porosity and relatively easy to modify. The 3D structures could be formed by introducing chemical additives, acting as binder or structural support, into the graphene precursor prior to freeze drying. The performance of graphene aerogel in removing heavy metals has been documented in the literature recently. A novel GO/carboxymethyl chitosan aerogel which was synthesised via vacuum assisted self-assembly method, exhibited 95.37 mg/g of adsorption capacity towards Cu^{2+} (Luo et al., 2019). A polyethyleneimine functionalised rGO/molybdenum disulphide composite aerogel was reported to achieve 184.53 mg/g in uranium adsorption (Guo et al., 2020).

To date, most graphene adsorption studies on pharmaceuticals and heavy metals removal have been conducted in batch mode which has limited application in industrial wastewater treatment. In general, a fixed bed adsorption column contains fixed mass of adsorbent in which the polluted water flows through at a constant flowrate. The column set-up which is relatively straightforward and low cost, can treat comparatively large volume of wastewater with varying pollutant loads (Du et al., 2018; Sausen et al., 2018). Hence, fixed bed adsorption is more practical for large scale wastewater treatment. Although conventional adsorbents such as granular activated carbon (Ang et al., 2020), clay composite (Soleymani et al., 2019) and biochar (Jung et al., 2017) have been

widely applied in fixed bed adsorption for removal of various pollutants, there are very limited data on 3D graphene aerogel fixed bed adsorption. Therefore, this study aimed to establish the dynamic adsorption behaviour of the synthesised 3D graphene structures (rGOA, RGM and ZrGA) described previously in Chapter 4. The column adsorption performance of the aerogels was evaluated for diclofenac, acetaminophen, Cu^{2+} and Ni^{2+} removal. The experimental breakthrough curves were by fitted to the Thomas, BDST, Yoon-Nelson and Adams-Bohart models to obtain further column design data.

6.2 Packed bed adsorption of diclofenac onto rGOA

6.2.1 Effect of bed height

Bed height is a crucial column adsorption parameter to determine the efficiency of the fixed bed operation. The total uptake of adsorbate is highly affected by the amount of adsorbent packed in the column as it contributes to the total number of sorption sites available for the pollutant attachment. The effect of bed height was investigated by varying the bed height from 10 to 15 cm while keeping the flowrate at 2 mL/min and influent concentration of diclofenac at 50 mg/L. Fig. 6.1 shows the breakthrough curves as a function of bed height for this study. It can be seen that the curves show unsymmetrical S-shaped pattern and the gradient of the curves became less steep as the bed height was increased from 10 to 15 cm.

Table 6.1: Fixed bed adsorption parameters for diclofenac-rGOA system.

Column parameters	**Bed height (*h*, cm)**		
	10	**12.5**	**15**
Influent concentration (C_o, mg/L)		50	
Flowrate (Q, mL/min)		2	
Adsorbent mass (m, g)	0.34	0.43	0.51
Breakthrough time (t_b, min)	30	75	130
Exhaustion time (t_s, min)	350	500	900
Total adsorbate adsorbed (q_{total}, mg)	12.98	22.96	38.25
Equilibrium column adsorption capacity (q_{ec}, mg/g)	38.19	53.40	74.99
Fractional bed utilisation (*FBU*)	0.2271	0.3245	0.3358
Empty bed contact time (*EBCT*, min)	8.84	11.04	13.25
Mass transfer zone (*MTZ*, cm)	9.14	10.63	12.83
Minimum time to initiate adsorption (t_f, min)	72.69	137.93	258.54
Moving rate of adsorption zone (U_z, cm/min)	0.0286	0.0250	0.0167

Column parameters	**Influent concentration (C_o, mg/L)**		
	25	**50**	**75**
Bed height (h, cm)		12.5	
Flowrate (Q, mL/min)		2	
Breakthrough time (t_b, min)	210	75	30
Exhaustion time (t_s, min)	1000	500	325
Total adsorbate adsorbed (q_{total}, mg)	17.81	22.96	7.53
Equilibrium column adsorption capacity (q_{ec}, mg/g)	41.42	53.40	17.51
Fractional bed utilisation (*FBU*)	0.2095	0.3245	0.5859
Empty bed contact time (*EBCT*, min)	11.04	11.04	11.04
Mass transfer zone (*MTZ*, cm)	9.88	10.63	11.35
Minimum time to initiate adsorption (t_f, min)	165.47	137.93	172.85
Moving rate of adsorption zone (U_z, cm/min)	0.0125	0.0250	0.0385

Column parameters	**Flowrate (Q, mL/min)**		
	1	**2**	**3**
Bed height (h, cm)		12.5	
Influent concentration (C_o, mg/L)		50	
Breakthrough time (t_b, min)	300	75	30
Exhaustion time (t_s, min)	750	500	233.33
Total adsorbate adsorbed (q_{total}, mg)	24.66	22.96	15.53
Equilibrium column adsorption capacity (q_{ec}, mg/g)	57.36	53.40	36.11
Fractional bed utilisation (*FBU*)	0.6054	0.3245	0.2880
Empty bed contact time (*EBCT*, min)	22.09	11.04	7.36
Mass transfer zone (*MTZ*, cm)	7.50	10.63	10.89
Minimum time to initiate adsorption (t_f, min)	272.41	137.93	58.57
Moving rate of adsorption zone (U_z, cm/min)	0.0167	0.0250	0.0536

As shown in Table 6.1, bed height (h) exhibited synergistic effect on both the breakthrough time (t_b) and saturation time (t_s) of the column, as proven by the increasing t_b and t_s from 30 to 130 min and 350 to 900 min, respectively, at increasing bed height from 10 to 15 cm. The empty bed contact time (EBCT) of the 15 cm bed

(13.25 min) was noticeably longer than that of the 10 cm bed (8.84 min), implying that diclofenac molecules would have longer residence time in the rGOA bed (Reynel-Avila et al., 2015). The situation hence allowed more diclofenac to be adsorbed onto the rGOA surface which led to an extended breakthrough time. Notably, the transportation of diclofenac across rGOA bed was relatively slow at larger bed height, as evident from the decreasing trend of the moving rate of adsorption zone (U_z = 0.0286 > 0.0167 cm/min). The broader breakthrough curves indicated that the mass transfer resistance was greater at larger bed height, thus reducing the U_z rate of diclofenac at larger bed heights. Hence, this enabled diclofenac to be diffused into the inner pores of rGOA and improve the operation time of the column.

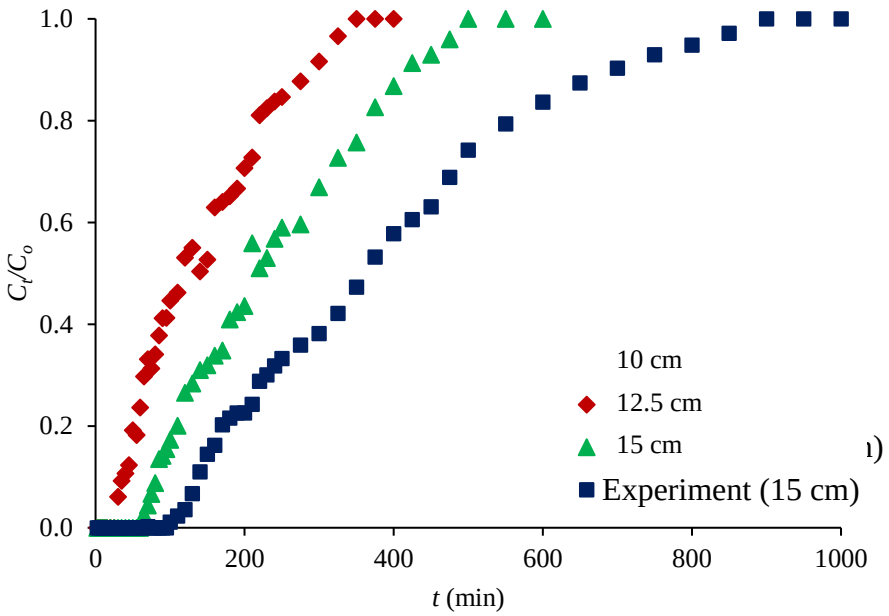

Fig. 6.1: Breakthrough curves for diclofenac adsorption onto rGOA fixed bed at different bed heights.

Furthermore, the availability of sorption sites increases with the mass or bed height of rGOA which in turn allowed more diclofenac to be adsorbed onto the bed, thus enhancing the column adsorption capacity (74.99 mg/g at 15 cm bed height).

6.2.2 Bed-depth service time model (BDST)

The bed height experimental data were fitted to the BDST model for the prediction of service time of column as a function of bed height. The graphical illustration and parameters of the BDST model are presented in Fig. 6.2 and Table 6.2, respectively.

Table 6.2: BDST model parameters for diclofenac-rGOA system.

C_t/C_o	BDST parameters				h_o (cm)
	N_o' (mg/L)	k_α (L/ min mg)	Service time equation	R^2	
0.05	1131.78	3.43E-04	$t = 20.0\ h + 171.67$	0.9967	8.58
0.1	17316.05	7.90E-05	$t = 20.0\ h + 161.67$	0.9967	8.08
0.2	18957.08	4.74E-05	$t = 22.0\ h + 161.67$	0.9973	7.35

Overall, the equation developed from BDST modelling demonstrated strong correlation between service time and bed height (R^2 > 0.99). The saturation concentration (N_o') increased from 1131.77 to 1244.94 mg/L and BDST kinetic constant (K_α) decreased from 3.43E-4 to 1.72E-4 L/min mg as the breakthrough limit increased from 5 to 20 %. Additionally, the minimum bed heights required to avoid 5, 10 and 20 % breakthrough were calculated to be 8.58, 8.08 and 7.35 cm, respectively. Hence, the BDST model could predict the breakthrough time with varying bed heights without further experimental work.

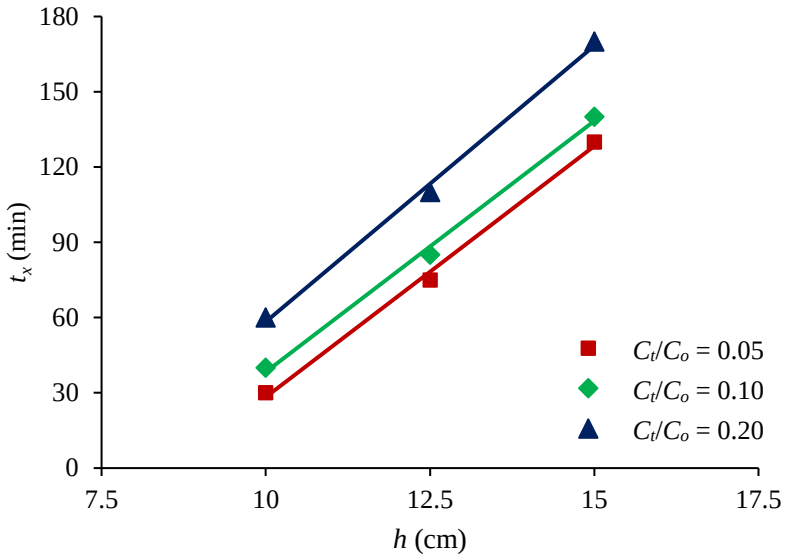

Fig. 6.2: BDST plot for diclofenac adsorption on rGOA fixed bed.

6.2.3 Effect of influent concentration

The effect of influent concentration was investigated at diclofenac concentrations of 25, 50 and 75 mg/L whereas the rGOA bed height was set at 12.5 cm and flowrate at 2 mL/min. The experimental breakthrough curves are depicted in Fig. 6.3 while the column design data are shown in Table 6.1.

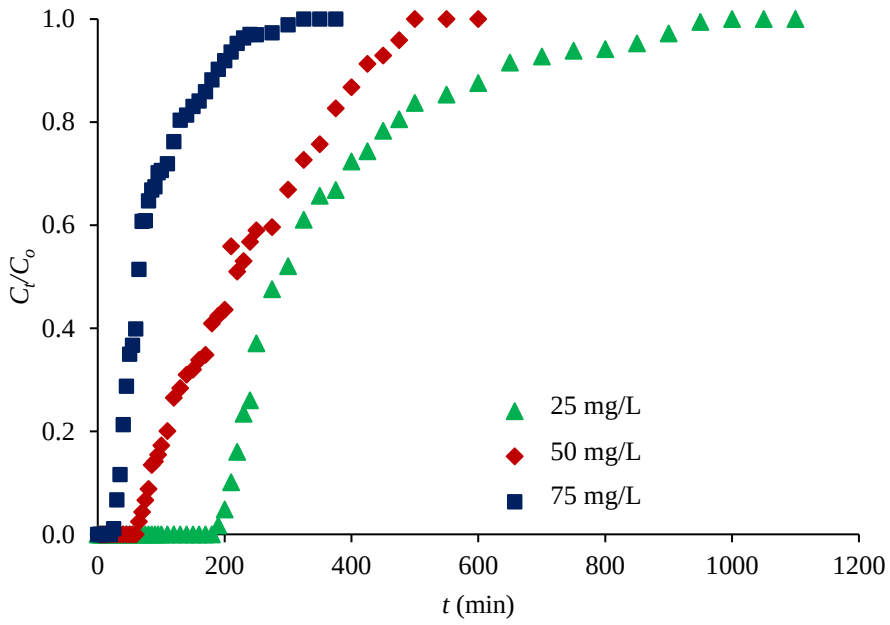

Fig. 6.3: Breakthrough curves for diclofenac adsorption onto rGOA fixed bed at different influent concentrations.

The t_b and t_s decrease from 210 to 30 min, and 1000 to 325 min, respectively, at elevating influent concentration (25 – 75 mg/L) under constant EBCT (11.04 min). This decreasing pattern was due to the enhanced concentration driving force at high concentration had accelerated the saturation rate of rGOA sorption sites, thus saturated the column more rapidly (Darweesh & Ahmed, 2017a). The adsorption capacity was expected to increase at higher influent concentration and this study showed an increasing trend as the influent concentration was increased from 25 (41.42 mg/g) to 50 mg/L (53.40 mg/g), but it dropped at 75 mg/L (17.51 mg/g). This could possibly due to the faster moving rate of diclofenac at 75 mg/L (0.0385 cm/min) than those at 50 mg/L (0.025 cm/min), which quicken the column saturation by 35 % and the sorption sites at inner pores of rGOA might not be fully occupied by diclofenac, thus reducing its adsorption capacity.

6.2.4 Effect of flowrate

The shape of breakthrough curves and column parameters for diclofenac adsorption at different flowrates (1, 2 and 3 mL/min) are shown in Fig. 6.4 and Table 6.1, respectively. Overall, the slope of breakthrough curve became steeper with increasing flowrate, indicating that the mass transfer resistance was reduced at high flowrates, leading to faster saturation of the column. Notably, the EBCT of the column decreased (22.09 > 7.36 min) significantly as the flowrate was increased to 3 mL/min, implying that the residence time for diclofenac in the column was shortened at higher flowrates (Albayati & Kalash, 2020). Therefore, diclofenac exited the column at shorter t_b (300 > 30 min) and t_s (750 > 233.33 min). Notably, the slope of 3 mL/min breakthrough curve was steeper than other breakthrough curves, implying that the mass transfer resistance in 3 mL/min column was smaller and the column saturated faster.

Additionally, the calculated U_z for 1, 2 and 3 mL/min flowrates were 0.0167, 0.0250 and 0.0536 cm/min, respectively. As diclofenac moved slowly across the rGOA bed, there was sufficient time for the pharmaceutical to diffuse through the pores of rGOA. Hence, the increase in column adsorption capacity from 36.11 to 57.36 mg/g was observed at lower flowrates (Darweesh & Ahmed, 2017b). The results obtained from this study revealed that low flowrate was favourable for adsorption of diclofenac onto rGOA column.

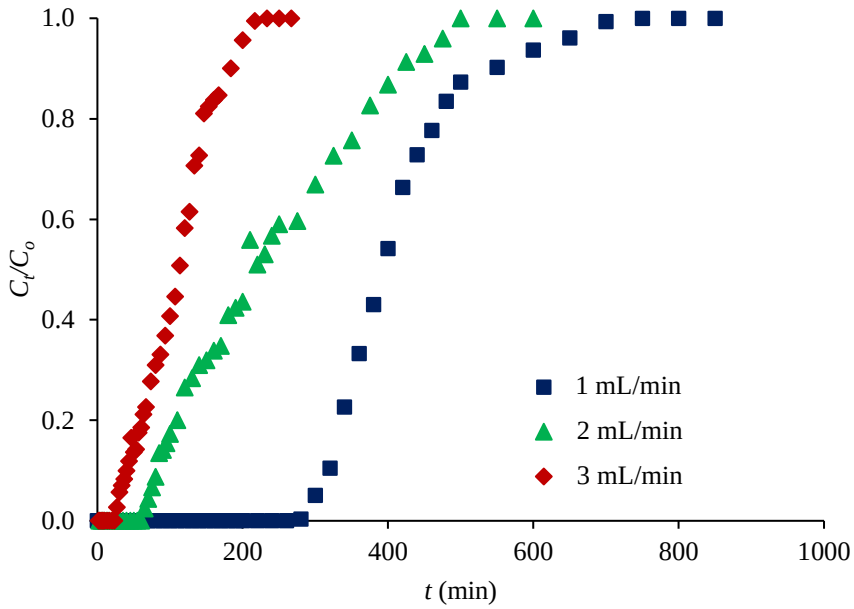

Fig. 6.4: Breakthrough curves for diclofenac adsorption onto rGOA fixed bed at different flowrates.

6.2.5 Packed bed adsorption properties

The dynamic behaviour of diclofenac adsorption onto rGOA was modelled by fitting the experimental breakthrough curves to the Thomas, Yoon-Nelson and Adams-Bohart models. Fig. 6.5 (a), (b) and (c) display the breakthrough curves predicted by the models for the effects of bed height, influent concentration and flowrate, respectively.

As the bed height was increased, the rate constants for the Thomas (K_{Th}: 0.3523 – 0.1808 L/min g), Yoon-Nelson (K_{YN}: 0.018 – 0.009 L/min g) and Adams-Bohart (K_{Th}: 0.0876 – 0.0445 L/min g) models were decreased. This trend could be attributed to the increase in mass transfer resistance at the solid-liquid interface when a longer bed was used, resulting in a lower adsorption rate constant, as supported by the decreasing *Uz* (Sheng et al., 2018). However, larger bed height offered greater availability of sorption sites for diclofenac adsorption. As a result, the maximum Thomas adsorption capacity (q_{Thm}), time required to achieve 50 % breakthrough (τ) and saturation concentration (N_o) showed synergistic effect with bed height owing to more diclofenac being adsorbed to

the rGOA bed. Hence, at 15 cm, the achieved q_{Thm}, τ and N_o were 78.19 mg/g, 367.47 min and 3261.87 mg/L, respectively.

The modelled kinetic constants for the effect of influent concentration did not show any clear trend, but τ and N_o exhibited a decreasing trend as the influent concentration was increased. The mass transfer driving force was enhanced at higher concentration, causing diclofenac molecules to move rapidly across the column and hence speed up the saturation rate of column (τ =72.7 min) but lowered the saturation concentration (N_o =1613.29 mg/L) (Bhangi & Ray, 2020).

For the effect of flowrate, q_{Thm} and τ were decreased from 84.50 to 32.08 mg/g and from 397.13 to 109.08 min, respectively as the flowrate was increased, however parameters such as K_{Th}, K_{YN} and N_o did not show any specific trends at elevated flowrates. The decrease in q_{Thm} and τ was caused by the quick saturation of column at high flowrate as the diclofenac molecules did not have sufficient time to diffuse into the inner pores of rGOA. Interestingly, the Adams-Bohart kinetic constant (K_{AB}) demonstrated an increasing trend at increasing flowrate, indicating the overall adsorption kinetic was dominated by external mass transfer (Kizito et al., 2016).

Judging by the highest R^2 in Table 6.3, the Thomas and Yoon-Nelson models could be used to model the breakthrough curves for diclofenac adsorption at different rGOA bed heights, influent concentrations and flowrates.

(a)

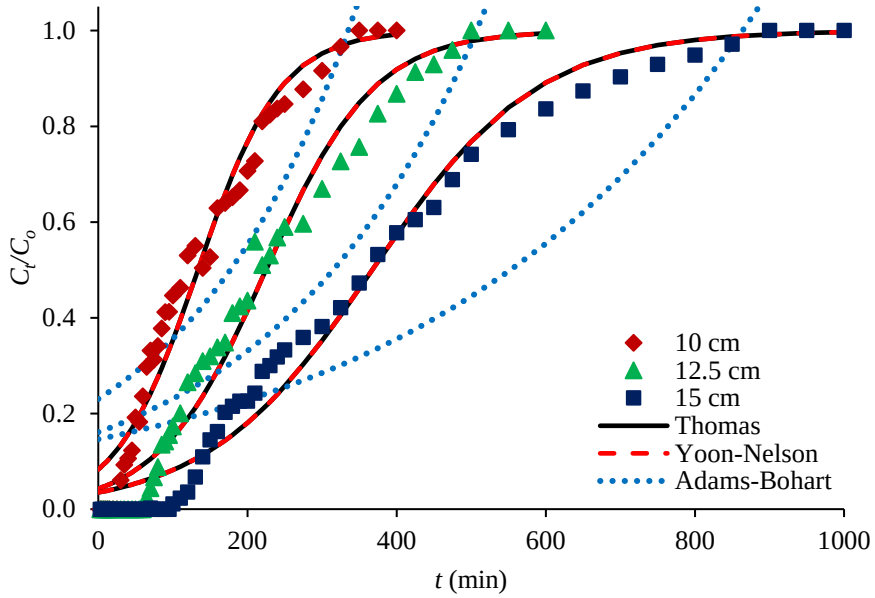
1.0
0.8
0.6
0.4
0.2
0.0
C_t/C_o
0
200
400
600
800
1000
t (min)
10 cm
12.5 cm
15 cm
Thomas
Yoon-Nelson
Adams-Bohart

(b)

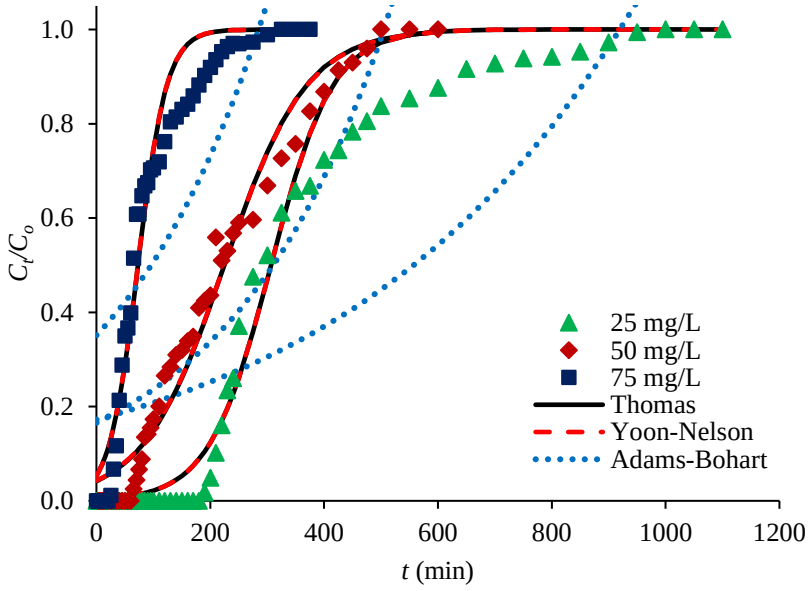
1.0
0.8
0.6
0.4
0.2
0.0
C_t/C_o
0
200
400
600
800
1000
1200
t (min)
25 mg/L
50 mg/L
75 mg/L
Thomas
Yoon-Nelson
Adams-Bohart

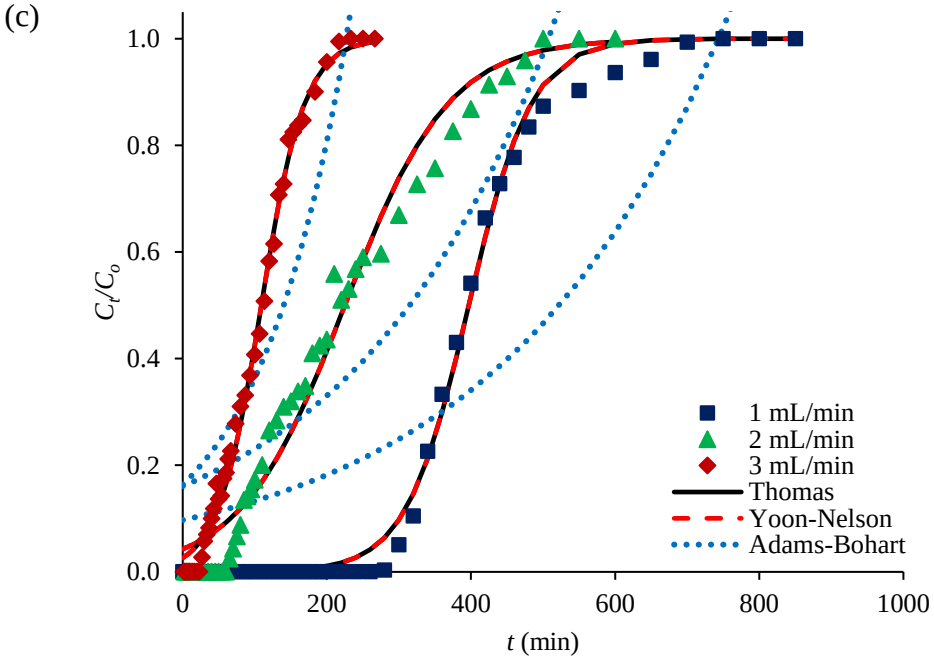

Fig. 6.5: Kinetic models fitting of breakthrough curves for the effect of (a) bed height, (b) influent concentration and (c) flowrate.

Table 6.3: Kinetic model parameters for diclofenac adsorption onto rGOA fixed bed.

Model parameters	**Bed height (*h*, cm)**		
	10	**12.5**	**15**
Thomas			
K_{Th} (mL/min mg)	0.3600	0.2766	0.1808
q_{Th} (mg/g)	39.27	52.30	78.19
R^2	0.9619	0.9775	0.9835
Yoon- Nelson			
K_{YN} (1/min)	0.0180	0.0138	0.0090
τ (min)	133.53	224.89	367.47
R^2	0.9619	0.9775	0.9835
Adam-Bohart			
K_{AB} (mL/min mg)	0.0876	0.0720	0.0445
N_o (mg/L)	1898.12	2298.44	3261.87
R^2	0.8095	0.8397	0.8434

Model parameters	**Influent concentration (C_o, mg/L)**		
	25	**50**	**75**
Thomas			
K_{Th} (mL/min mg)	0.7372	0.2766	0.5256
q_{Th} (mg/g)	45.08	52.30	23.28
R^2	0.9778	0.9775	0.9834
Yoon- Nelson			
K_{YN} (1/min)	0.0152	0.0138	0.0395
τ (min)	321.68	224.89	72.70
R^2	0.9785	0.9775	0.9611
Adam-Bohart			
K_{AB} (mL/min mg)	0.0765	0.0720	0.0490
N_o (mg/L)	2603.74	2298.44	1613.29
R^2	0.7535	0.8397	0.7136

Model parameters	**Flowrate (*Q*, mL/min)**		
	1	**2**	**3**
Thomas			
K_{Th} (mL/min mg)	0.4580	0.2766	0.6616
q_{Th} (mg/g)	84.50	52.30	32.08
R^2	0.9963	0.9775	0.9943
Yoon- Nelson			
K_{YN} (1/min)	0.0229	0.0138	0.0331
τ (min)	397.13	224.89	109.08
R^2	0.9963	0.9775	0.9943
Adam-Bohart			
K_{AB} (mL/min mg)	0.0627	0.0720	0.1597
N_o (mg/L)	1403.03	2298.44	1942.96
R^2	0.8041	0.8397	0.8273

6.2.6 Mass transfer analysis for diclofenac-rGOA system

In adsorption, the overall (global) mass transfer generally involves the migration of adsorbate from bulk phase to the adsorbent surface via film mass transfer, followed by

diffusion within the pores of adsorbent (pore diffusion). Fig. 6.6 illustrates the variation of global mass transfer coefficient with breakthrough concentration at varying bed heights, influent concentrations and flowrates.

As shown, the global mass transfer coefficient ($[K_La]_g$) exhibited an exponential depletion trend with the progressive saturation of the column. This could be interpreted as the global mass transfer rate was rapid during the initial adsorption stage and the mass transfer of diclofenac to rGOA bed was gradually slowed down as the sorption sites were occupied until they were fully saturated. Furthermore, the adsorption of diclofenac onto rGOA bed was significantly affected by influent concentration as evident by the highest $[K_La]_g$ value (0.1934 min^{-1}), followed by flowrate (0.1791 min^{-1}) and bed height (0.1432 min^{-1}). Notably, the mass transfer was fast when the column was operated at 75 mg/L influent concentration, 3 mL/min flowrate and 10 cm bed height, as shown by the high $[K_La]_g$ values. This was consistent with the findings obtained from the fixed bed experimental study. At higher influent concentration and flowrate, the transportation rate of diclofenac into rGOA was rapid due to higher driving force of mass transfer. Meanwhile, at lower bed height, undesired flow patterns such as axial dispersion and channelling occurring during adsorption had caused insufficient contact time between diclofenac and rGOA sorption sites, thus allowing more unbound diclofenac to pass through the column.

The fixation of adsorbate to the adsorption sites was considered fast and thus, has no significant impact on the overall mass transfer of adsorbate to the adsorbent. Hence, the overall mass transfer resistance of the system was mainly due to film mass transfer or pore diffusion, or both. The change in the individual mass transfer coefficient for film diffusion ($[K_La]_f$) and pore diffusion ($[K_La]_p$) with breakthrough concentration is

depicted in Fig. 6.7 (a), (b) and (c) in accordance to the effects of bed height, influent concentration and flowrate, respectively.

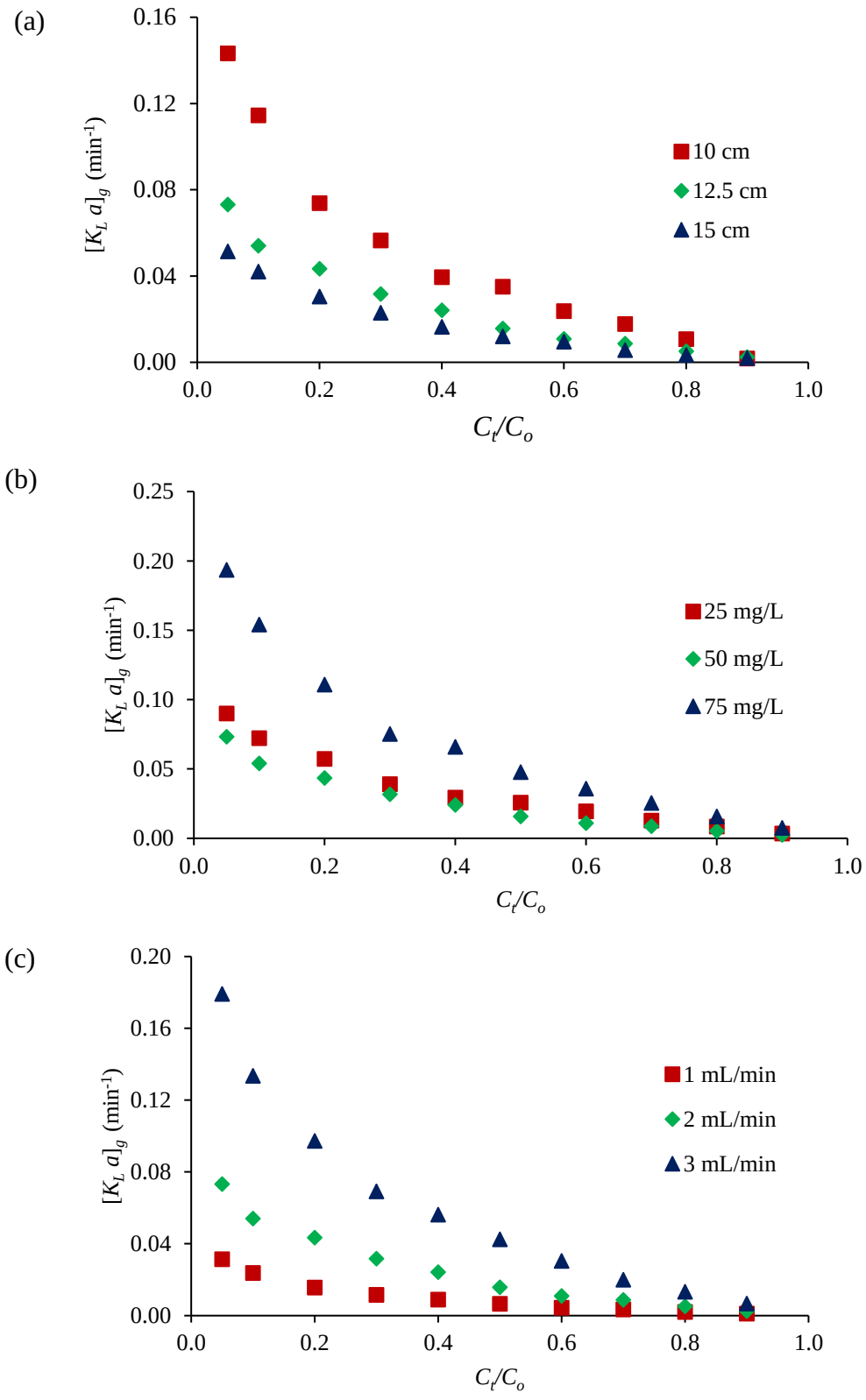

Fig. 6.6: Global mass transfer coefficient versus with breakthrough concentration at varying (a) bed heights, (b) influent concentrations and (c) flowrates.

(a)

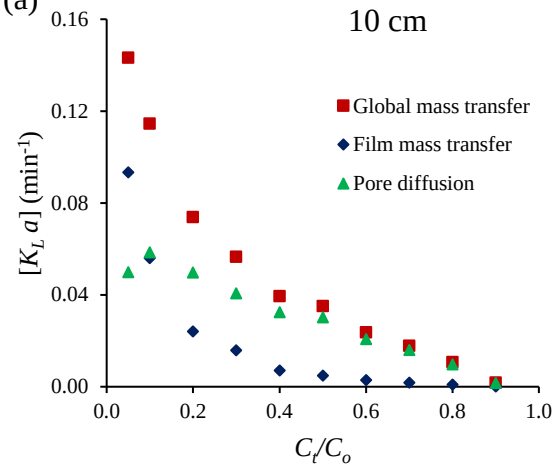
10 cm
Global mass transfer
Film mass transfer
Pore diffusion
$[K_L a]$ (min^{-1})
C_t/C_o
0.00
0.04
0.08
0.12
0.16
0.0
0.2
0.4
0.6
0.8
1.0

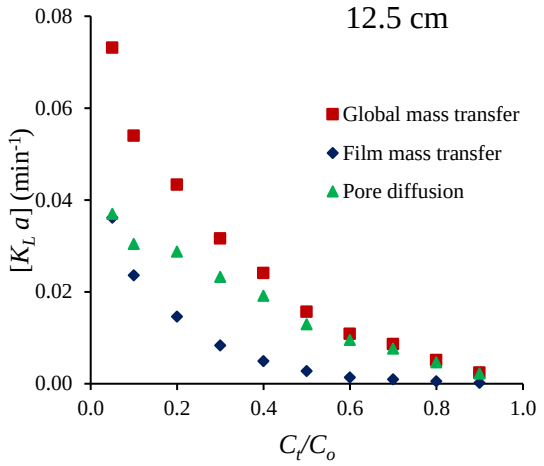
12.5 cm
Global mass transfer
Film mass transfer
Pore diffusion
$[K_L a]$ (min^{-1})
C_t/C_o
0.00
0.02
0.04
0.06
0.08
0.0
0.2
0.4
0.6
0.8
1.0

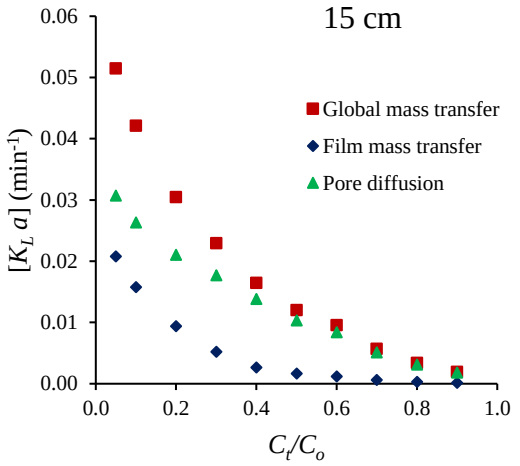
15 cm
Global mass transfer
Film mass transfer
Pore diffusion
$[K_L a]$ (min^{-1})
C_t/C_o
0.00
0.01
0.02
0.03
0.04
0.05
0.06
0.0
0.2
0.4
0.6
0.8
1.0

(b)

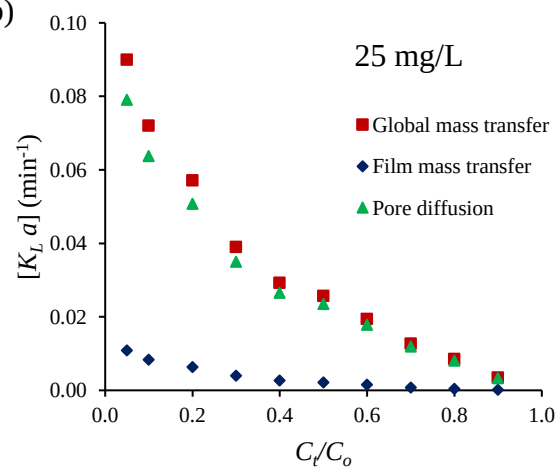
25 mg/L
Global mass transfer
Film mass transfer
Pore diffusion
$[K_L a]$ (min^{-1})
C_t/C_o
0.00
0.02
0.04
0.06
0.08
0.10
0.0
0.2
0.4
0.6
0.8
1.0

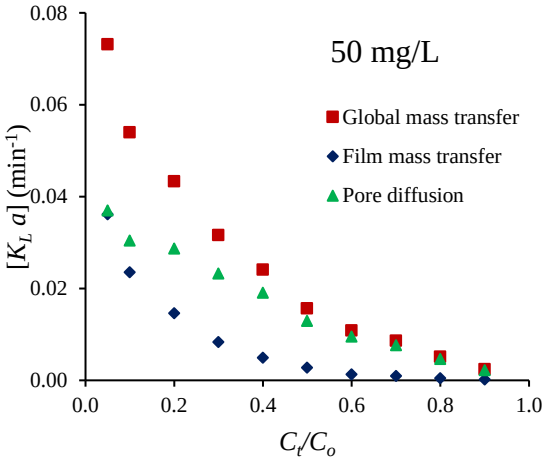
50 mg/L
Global mass transfer
Film mass transfer
Pore diffusion
$[K_L a]$ (min^{-1})
C_t/C_o
0.00
0.02
0.04
0.06
0.08
0.0
0.2
0.4
0.6
0.8
1.0

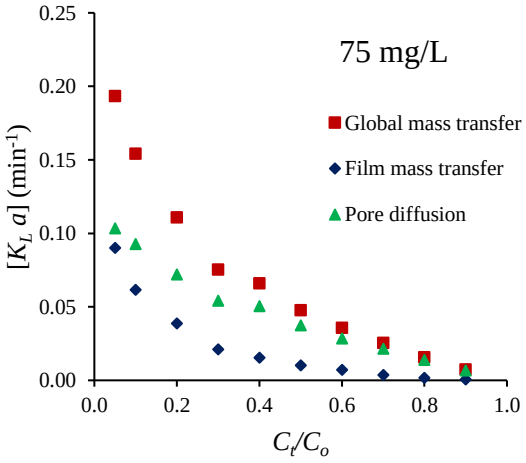
75 mg/L
Global mass transfer
Film mass transfer
Pore diffusion
$[K_L a]$ (min^{-1})
C_t/C_o
0.00
0.05
0.10
0.15
0.20
0.25
0.0
0.2
0.4
0.6
0.8
1.0

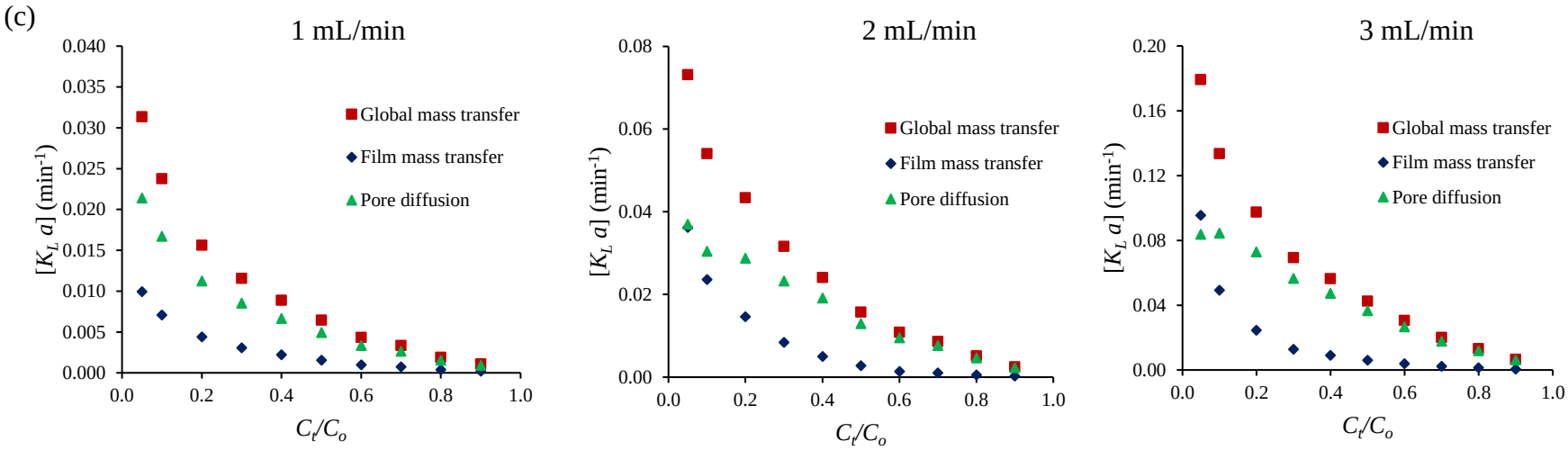

Fig. 6.7: Individual mass transfer coefficients versus breakthrough concentration at varying (a) bed heights, (b) influent concentrations and (c) flowrates.

Fig. 6.7 (a) shows that the global mass transfer coefficient was decreased as the bed height increased from 10 cm (0.1432 min^{-1}) to 15 cm (0.0515 min^{-1}). This implied that the mass transfer resistance in longer beds was larger which slowed down the transportation of diclofenac to the rGOA surface. Interestingly, the film diffusion mass transfer coefficient ($[K_La]_f$, 0.0934 min^{-1}) was noticeably to be higher than pore diffusion mass transfer coefficient ($K_La]_p$, 0.0498 min^{-1}) at 5 % column saturation in the 10 cm bed. This indicates that the overall mass transfer resistance in the 10 cm bed was limited by pore diffusion during the column operation up to 5 % saturation. For the remaining column operation, film diffusion occurred as the main controlling step for mass transfer. As bed height increased, the pore diffusion mass transfer coefficients were greater than film diffusion mass transfer coefficients. This finding indicated that film diffusion became the dominant controlling step in longer beds.

The influent concentration plays a vital role in providing the mass transfer gradient for adsorption process. At initial adsorption stage (5 % breakthrough), the film mass transfer coefficient, $[K_La]_f$, was the highest for 75 mg/L (0.09 min^{-1}), followed by 50 mg/L (0.0362 min^{-1}) and lastly 25 mg/L (0.0099 min^{-1}). This indicated that the transport of diclofenac through the boundary film zone was fast when the column was treating the high concentration of diclofenac. It was noticeable in Fig. 6.7(b) that $[K_La]_p$ were significantly higher than $[K_L\ a]_f$ in the case of 25 mg/L. This suggested that the overall mass transfer resistance for diclofenac adsorption onto rGOA bed at 25 mg/L concentration was dependent mainly on the external mass transfer of the adsorbate from the bulk phase to the solid surface i.e. film mass transfer controlling.

The effect of flowrate is associated to the moving rate of diclofenac across the rGOA bed. Generally, high flowrate results in higher mass transfer rate as more adsorbates move rapidly acorss the adsorbent bed. This is reflected by the high global

mass transfer coefficient at 3 mL/min operation (0.1791 min^{-1}) > 2 mL/min (0.0731 min^{-1}) > 1 mL/min (0.0313 min^{-1}), as shown in Fig. 6.7(c). At 3 mL/min, the overall mass transfer resistance was controlled by pore mass transfer when the column operates up to 5 % breakthrough, thereafter film diffusion took control of the mass transfer until column saturation (10 – 90 %). However, film diffusion was the primary mass transfer limiting factor as evident by $[K_La]_f < [K_La]_p$ in both 2 mL/min and 1 mL/min columns. At higher flowrates, the mass transfer boundary layer around the adsorbent was reduced, resulting in the decrease on external mass transfer resistance, hence increasing the mass transfer coefficient at film zone (Yaumi et al., 2018).

The mass transfer factor analysis revealed that the rate limiting step for fixed bed adsorption of diclofenac onto rGOA was mostly controlled by external or film mass transfer resistance, whereas cases such as the 10 cm bed and 3 mL/min flowrate, were limited by internal mass transfer (pore diffusion) resistance up to 5 % breakthrough before being replaced by external mass transfer controlling until total column saturation.

6.3 Fixed bed adsorption of acetaminophen onto RGM

The as-synthesised RGM adsorbent was found to be more effective for application in batch mode than in fixed bed operation. A number of trial runs have been carried out to utilise RGM in fixed bed adsorption of acetaminophen. However, the results showed that the graphene aerogel has low column removal efficiency for acetaminophen. An example result of this study is illustrated in Fig. 6.8.

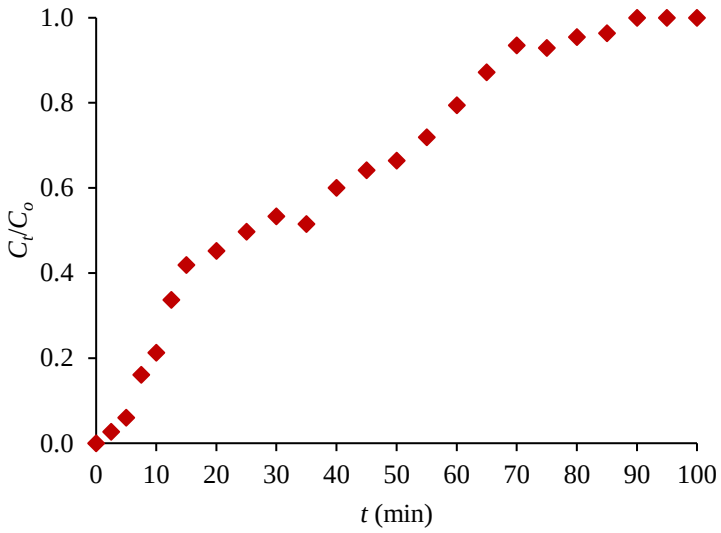

Fig. 6.8: Continuous adsorption of acetaminophen onto RGM fixed bed.

Fig. 6.8 shows the breakthrough curve obtained for the column adsorption of acetaminophen at a ZrGA bed height of 4 cm, influent concentration of 50 mg/L and flowrate of 2 mL/min. The breakthrough time (t_b) and exhaustion time (t_{ex}) of the column were 5 and 90 min, respectively. The total amount of acetaminophen adsorbed (q_{total}) was 1.19 mg/g and the column equilibrium adsorption capacity (q_{ec}) was 2.37 mg/g. Furthermore, the adsorption column exhibited a q_b = 0.39 mg/g and q_s = 2.35 mg/g. The FBU was calculated to be 0.1660. The mass transfer zone (MTZ) was approximated to be 5 cm and the time required for adsorption zone to travel its own height distance (t_z) was 4.42 min, while the *EBCT* = 5.30 min. It was observed that the MTZ was greater than bed height, implying the adsorption system was highly

inefficient. This could be due to agglomeration of RGM particles during acetaminophen adsorption in the fixed bed.

6.4 Packed bed adsorption of Cu^{2+} and Ni^{2+} onto ZrGA

6.4.1 Effect of bed height

From batch study, adsorbent dosage plays a significant role in Cu^{2+} and Ni^{2+} removal. In fixed bed adsorption, the bed height is linked to the amount of adsorbent used in the column. Hence, the effect of bed height is one of the most influential parameters affecting the column performance. The effect of bed heights on the breakthrough curves for Cu^{2+} and Ni^{2+} adsorption onto ZrGA are portrayed in Fig. 6.9 (a) and (b), respectively.

In general, the breakthrough curves for Cu^{2+} and Ni^{2+} adsorption demonstrated that the column operation time was extended at larger bed heights. According to Table 6.4, the breakthrough time (t_b) and saturation time (t_s) for the heavy metals increased proportionally with the bed height. The t_b (15 – 80 min) and t_s (110 – 220 min) for Cu^{2+} adsorption were longer than those for Ni^{2+} adsorption (t_b =12.5 – 70 min; t_s =75 – 180 min). The increase in column operation time at larger bed height was due to the higher availability of sorption sites at longer bed. This in turn extended the residence time for heavy metals to be contacted with ZrGA bed, thus providing sufficient time for the heavy metals to be adsorbed (Nithya et al., 2020). This observation was further supported by the calculated EBCT for the 5 cm bed (4.42 min) which was greater than that for the 3 cm column (2.65 min) indicating that the heavy metals had longer contact time with the 5 cm bed than the 3 cm bed.

Additionally, the column adsorption capacity (q_c) for Cu^{2+} (32.73 – 40.99 mg/g) and Ni^{2+} (26.26 – 28.53 mg/g) was increased as the bed height increased. At smaller

bed height, the *MTZ* was shorter and the moving rate of heavy metals in the *MTZ* was faster than that at larger bed height. This led to the occurrence of axial dispersion, therefore saturation of the 3 cm bed was quicker than the 5 cm bed (Singh et al., 2017). This finding was consistent with the calculated fractional bed utilisation (*FBU*) whereby *FBU* of Cu^{2+} and Ni^{2+} adsorption columns were increased from 0.3148 to 0.6458, and 0.3078 to 0.8100, respectively, as the bed height increased from 3 to 5 cm.

Table 6.4: Fixed bed adsorption parameters for Cu^{2+}- and Ni^{2+}-ZrGA systems.

Pollutant	**Cu^{2+}**			**Ni^{2+}**		
	Bed height (*h*, cm)					
Column parameters	**3**	**4**	**5**	**3**	**4**	**5**
Influent concentration (C_o, mg/L)		50			50	
Flowrate (Q, mL/min)		2			2	
Adsorbent mass (m, g)	0.143	0.195	0.3	0.143	0.195	0.3
Breakthrough time (t_b, min)	15	40	80	12.5	25	70
Exhaustion time (t_s, min)	110	160	220	75	120	180
Total adsorbate adsorbed (q_{total}, mg)	4.68	6.98	12.30	3.76	5.54	8.56
Equilibrium column adsorption capacity (q_{ec}, mg/g)	32.73	35.80	40.99	26.26	28.40	28.53
Fractional bed utilisation (*FBU*)	0.4582	0.5560	0.6458	0.3078	0.4414	0.8100
Empty bed contact time (*EBCT*, min)	2.65	3.53	4.42	2.65	3.53	4.42
Mass transfer zone (*MTZ*, cm)	2.59	3.00	3.18	2.50	3.17	3.06
Minimum time to initiate adsorption (t_f, min)	29.91	66.72	90.41	19.24	41.94	89.10
Moving rate of adsorption zone (U_z, cm/min)	0.0273	0.0250	0.0227	0.0400	0.0333	0.0278
	Influent concentration (C_o, mg/L)					
Column parameters	**25**	**50**	**75**	**25**	**50**	**75**
Bed height (h, cm)		4			4	
Flowrate (Q, mL/min)		2			2	
Breakthrough time (t_b, min)	65	40	20	65	25	20
Exhaustion time (t_s, min)	300	160	80	170	120	55
Total adsorbate adsorbed (q_{total}, mg)	7.34	6.98	6.90	4.76	5.54	4.33
Equilibrium column adsorption capacity (q_{ec}, mg/g)	37.66	35.80	35.39	24.42	28.40	22.21
Fractional bed utilisation (*FBU*)	0.4358	0.5560	0.4225	0.6777	0.4414	0.4051
Empty bed contact time (*EBCT*, min)	3.53	3.53	3.53	3.53	3.53	3.53
Mass transfer zone (*MTZ*, cm)	3.13	3.00	3.00	2.47	3.17	2.55
Minimum time to initiate adsorption (t_f, min)	102.42	66.72	25.35	71.16	41.94	14.18
Moving rate of adsorption zone (U_z, cm/min)	0.0133	0.0250	0.0500	0.0235	0.0333	0.0727

	Flowrate (Q, mL/min)					
Column parameters	**1**	**2**	**3**	**1**	**2**	**3**
Bed height (h, cm)		4			4	
Influent concentration (C_o, mg/L)		50			50	
Breakthrough time (t_b, min)	80	40	10	50	25	5
Exhaustion time (t_s, min)	280	160	120	200	120	93.33
Total adsorbate adsorbed (q_{total}, mg)	7.28	6.98	6.61	5.77	5.54	4.98
Equilibrium column adsorption capacity (q_{ec}, mg/g)	37.31	35.80	33.89	29.57	28.40	25.56
Fractional bed utilisation (*FBU*)	0.5330	0.5560	0.2203	0.5274	0.4414	0.0929
Empty bed contact time (*EBCT*, min)	7.07	3.53	2.36	7.07	3.53	2.36
Mass transfer zone (*MTZ*, cm)	2.86	3.00	3.67	3.00	3.17	3.79
Minimum time to initiate adsorption (t_f, min)	106.60	66.72	24.23	79.11	41.94	8.20
Moving rate of adsorption zone (U_z, cm/min)	0.0143	0.0250	0.0333	0.0200	0.0333	0.0429

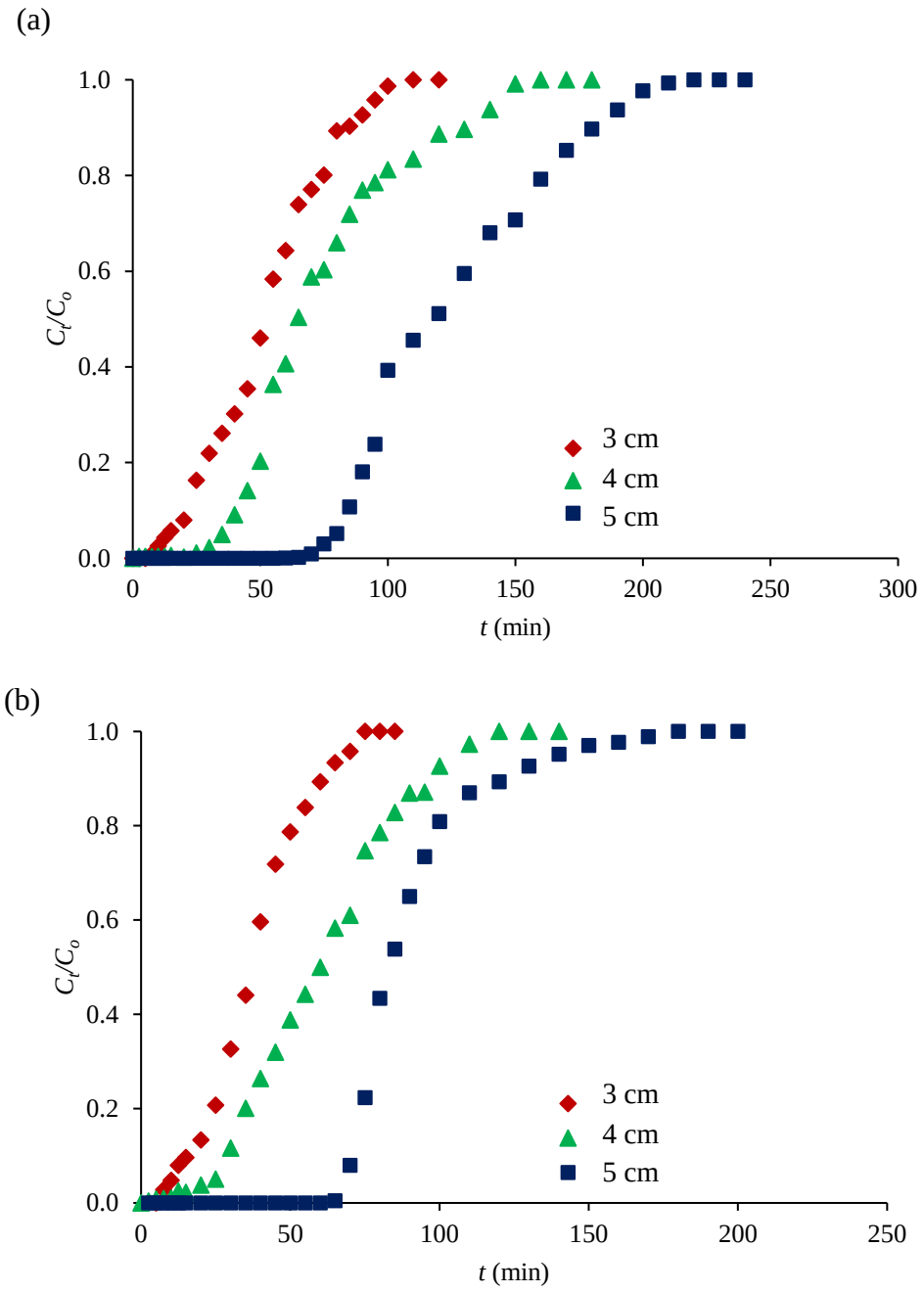

Fig. 6.9: Breakthrough curves for (a) Cu^{2+} and (b) Ni^{2+} adsorption onto ZrGA at different bed heights.

6.4.2 Bed-depth service time (BDST) analysis

The BDST model was commonly used to describe the relationship between the service times of column as a function of bed height. This study aimed to derive a predictive equation based on experimental breakthrough curve for use in process scale-up without having to carry out further experiments.

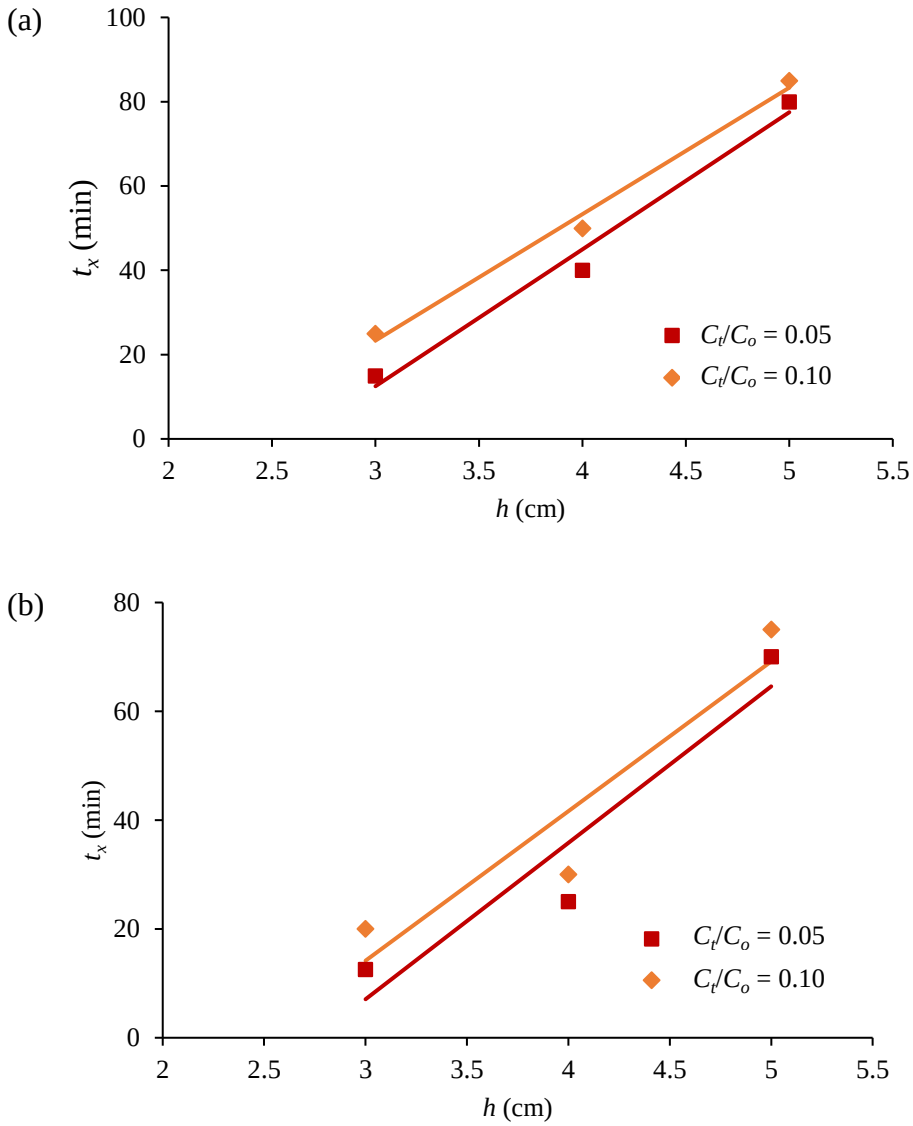

Fig. 6.10: BDST plot for (a) Cu^{2+} and (b) Ni^{2+} adsorption onto ZrGA fixed bed.

The assumptions made for this model are the bed height (h) and service time (t_x) presented a linear relationship under 50 % breakthrough, the moving rate in adsorption

zone is constant across the column and the surface adsorption is the rate controlling step (Hutchins, 1973). The k_α and N_o' values can be evaluated from the intercept and slope of t_x vs. h plot, respectively, and subsequently be used to calculate the minimum bed height required to prevent breakthrough (h_o).

Table 6.5: BDST model parameters for Cu^{2+}- and Ni^{2+}-ZrGA systems.

BDST – Cu^{2+} adsorption column				
C_t/C_o	**BDST parameters**		**Service time equation**	R^2
	$K\alpha$ **(L/min mg)**	No' **(mg/L)**		
0.05	6.93E-04	1839.12	$t = 32.5\,h + 85$	0.9829
0.10	6.59E-04	1697.65	$t = 30\,h + 66.67$	0.9909
BDST – Ni^{2+} adsorption column				
C_t/C_o	**BDST parameters**		**Service time equation**	R^2
	$K\alpha$ **(L/min mg)**	No' **(mg/L)**		
0.05	7.44E-04	1626.92	$t = 28.75\,h + 79.17$	0.9122
0.10	6.43E-04	1556.18	$t = 27.50\,h + 68.33$	0.8937

The BDST model parameters, predictive models and h_o for Cu^{2+} and Ni^{2+} adsorption are shown in Table 6.5 while the BDST plots are depicted in Fig. 6.10. Overall, N_o' was increased while k_α was decreased as the breakthrough limit increased from 5 to 10 % and the equations derived showed satisfactory linearity based on the high R^2. The respective minimum bed height required to prevent 5 % breakthrough for Cu^{2+} and Ni^{2+} were 2.62 and 2.75 cm, respectively, whereas to prevent 10 % breakthrough were 2.22 and 2.48 cm, respectively.

6.4.3 Effect of influent concentration

The mass transfer gradient across ZrGA bed was provided by the influent concentration. The effect of influent concentration on the breakthrough curves for Cu^{2+} and Ni^{2+} adsorption on ZrGA fixed bed is illustrated in Fig. 6.11. The slope of breakthrough curve became steeper as the influent concentration was increased from 25 to 75 mg/L. This trend indicated that higher influent concentration provided greater mass transfer driving force to overcome the mass transfer resistance. In Cu^{2+} adsorption, the moving rate of Cu^{2+} increased from 0.0133 to 0.05 cm/min as the influent concentration

increased (25 – 75 mg/L), signifying higher mass transfer gradient at high influent concentration and this led to the fast saturation of column (Zhang et al., 2019b). Notably, the moving rate of Ni^{2+} (0.0235 – 0.0727 cm/min) was higher than that of Cu^{2+}, implying that the operation time (t_b and t_s) was shorter than Cu^{2+} adsorption column. This was further supported by the longer operational time (t_s) for Cu^{2+} (80 – 300 min) adsorption than for Ni^{2+} adsorption (t_s = 55 – 170 min).

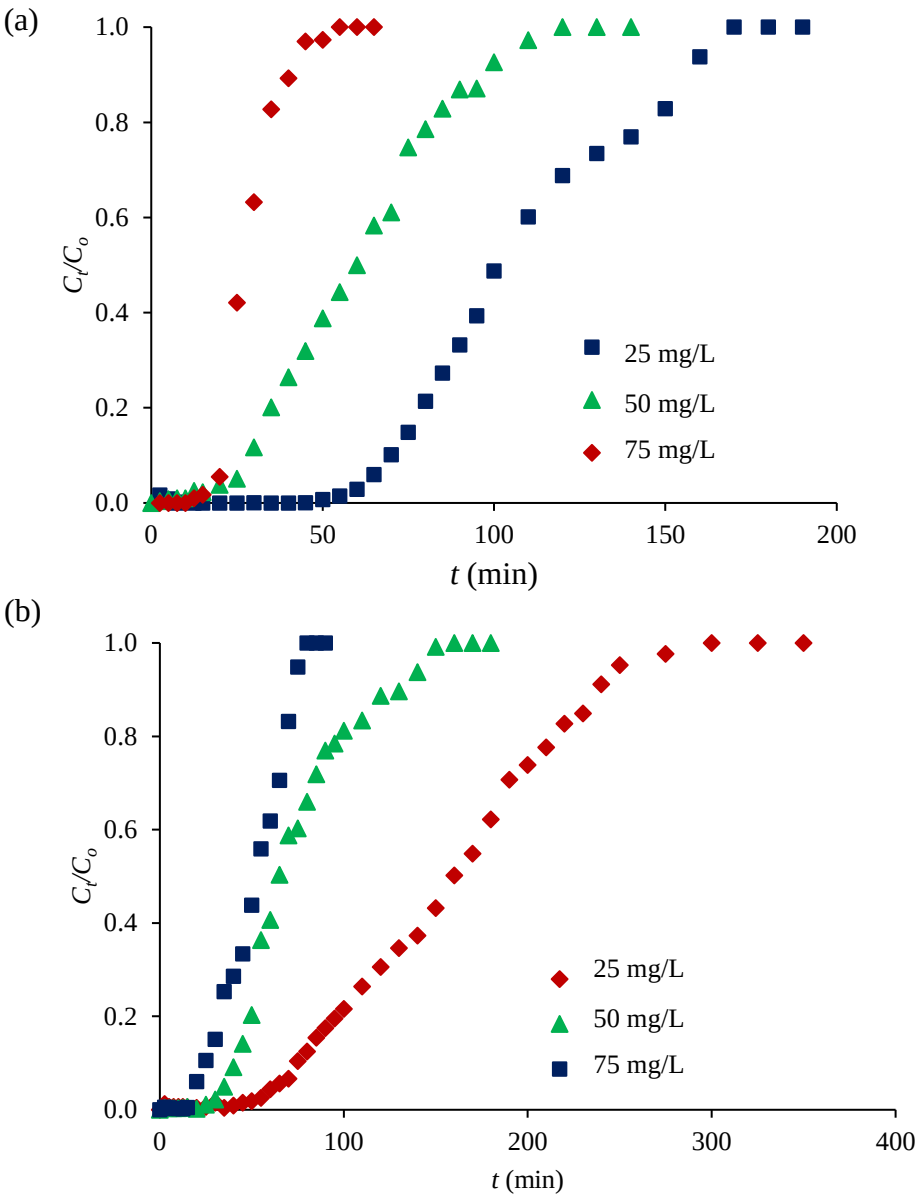

Fig. 6.11: Breakthrough curves for (a) Cu^{2+} and (b) Ni^{2+} adsorption onto ZrGA fixed bed at different influent concentrations.

Apart from shortening of operational time, the q_c for Cu^{2+} and Ni^{2+} adsorption was also decreased as the influent concentration increased. This was due to insufficient time for the heavy metals to fully diffuse into the inner pore of ZrGA thus decreasing the adsorption capacity (Du et al., 2018).

6.4.4 Effect of flowrate

Flowrate is another important process parameter for fixed bed adsorption of heavy metals as it governs the residence time of adsorbate in the column (Marin et al., 2019).

From Fig. 6.12, the breakthrough time for Cu^{2+} (80 > 10 min) and Ni^{2+} (50 > 5 min) and saturation time (Cu^{2+}: 280 > 120 min; Ni^{2+}: 200 > 93.33 min) were decreased as the flowrate increased from 1 to 3 mL/min. Furthermore, the slope of the breakthrough curve at higher flowrate was steeper than that at lower flowrate, indicating lower mass transfer resistance at higher flowrate, allowing the heavy metal to move quicker along the adsorbent bed. This phenomenon was attributed to the higher Reynold's number at high flowrate, creating high transportation rate of heavy metals (Cu^{2+} = 0.0333 mL/min; Ni^{2+} = 0.0429 mL/min) across ZrGA bed (Lin et al., 2017). The depletion in EBCT (7.07 min > 2.66 min) at high flowrate has caused insufficient residence time for diffusion of Cu^{2+} and Ni^{2+} into ZrGA, thus the heavy metals exited the column quicker at higher flowrate and decreased the adsorption capacity (Yusuf et al., 2020). Another possible reason could be related to the degree of turbulence and mixing at high flowrate, causing undesired flow pattern such as axial dispersion and channelling in the column.

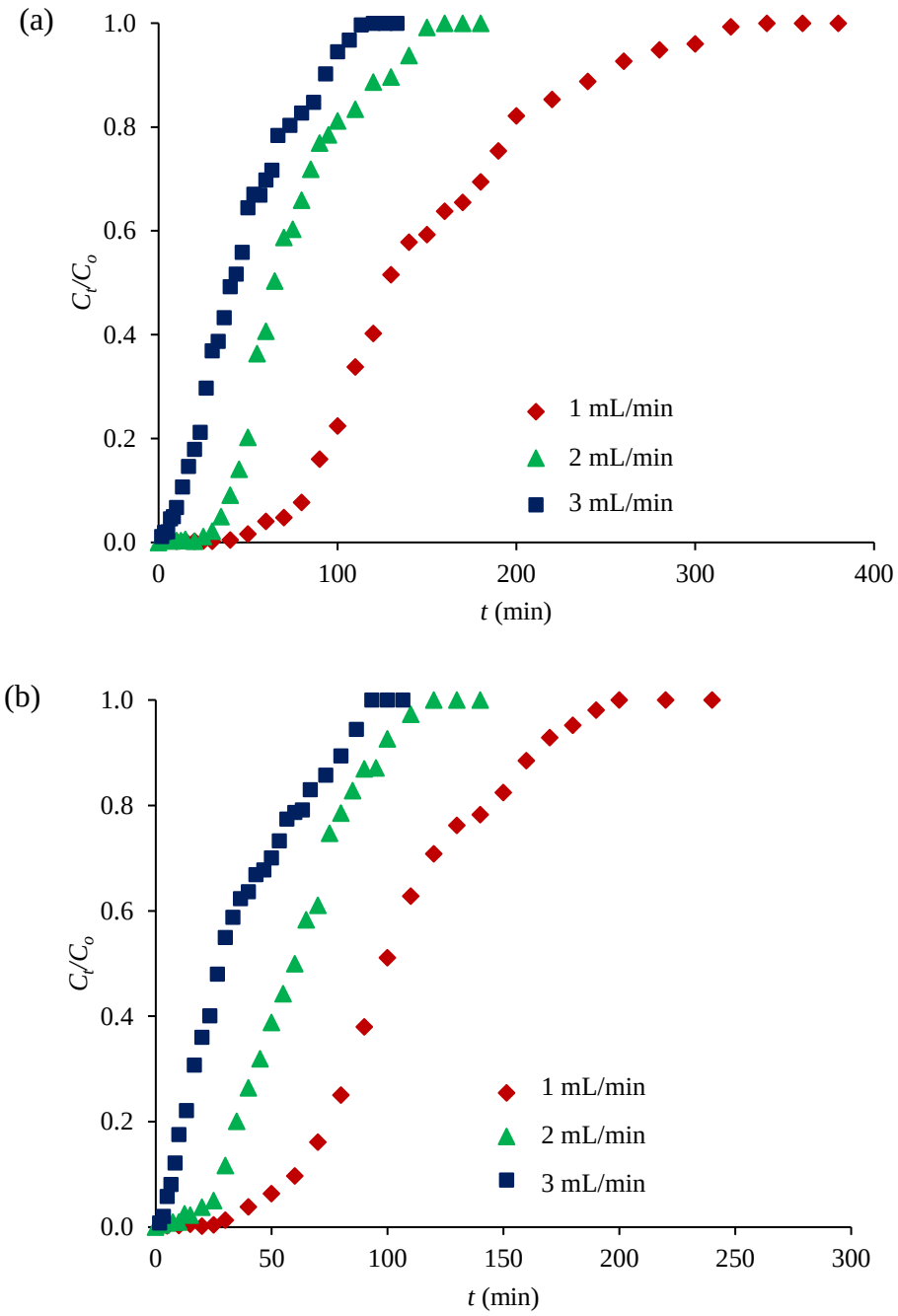

Fig. 6.12: Breakthrough curves for (a) Cu^{2+} and (b) Ni^{2+} adsorption onto ZrGA fixed bed at different flowrates.

6.4.5 Packed bed adsorption properties

The dynamic adsorption behaviour of Cu^{2+} and Ni^{2+} onto ZrGA was assessed through non-linear model fitting of experimentally acquired breakthrough curves to kinetic models such as the Thomas, Yoon-Nelson and Adams-Bohart models at different column parameters (bed height, influent concentration and flowrate). The modelled breakthrough curves at different operating conditions are depicted in Fig. 6.13 while the dynamic kinetic constants and their corresponded R^2 values are shown in Table 6.6.

The Thomas rate constant (K_{Th}) was decreased and the maximum Thomas adsorption capacity (q_{Th}) was increased as the bed height increased from 3 to 5 cm. At greater bed height, the mass transfer resistance across the adsorbent bed was higher causing the slower moving rate (U_z, Table 6.4) of heavy metals, thus decreasing the K_{Th} (Chang et al., 2018). The increase in q_{Th} at greater bed height could be due to the greater availability of sorption sites at larger ZrGA bed height. Furthermore, the K_{Th} increased and q_{Th} decreased proportionally with the increased in flowrate and influent concentration. This was due to the enhancement of concentration gradient at higher influent concentration and flowrate, causing insufficient contact time between the heavy metals and ZrGA bed.

Similarly, the Yoon-Nelson rate constant (K_{YN}) exhibited same trend as K_{Th}, where K_{YN} decreases with increasing bed height, but it increases with increasing influent concentration and flowrate. However, the value of τ has synergistic effect with bed height (Cu^{2+}: 51.71 – 122.69 min; Ni^{2+}: 37.16 – 85.28 min) and antagonistic effect with influent concentration (Cu^{2+}: 158.09 – 51.91 min; Ni^{2+}: 105.76 – 27.73 min) and flowrate (Cu^{2+}: 141.21 – 43.85 min; Ni^{2+}: 103.07 – 33.08 min). This was because at higher K_{YN} values, the adsorption was rapid and the column saturation was fast, thus leading to shorter breakthrough time, whereas at lower K_{YN} values, there was sufficient

residence time for the heavy metals to be adsorbed onto ZrGA, hence resulting in the extended breakthrough time (Du et al., 2018).

As shown in Table 6.6, the high sorption vacancy at larger bed height would decrease the Adams-Bohart rate constant (K_{AB}) and increase the saturation concentration (N_o), providing enough time for the heavy metals to diffuse into the inner structure of ZrGA bed and increased the heavy metals uptake. Contrary to bed height, the influent concentration would accelerate the K_{AB} from higher mass transfer gradient and reduce the overall N_o as the column saturate rapidly from the fast moving rate of heavy metals across the ZrGA bed. Interestingly, the flowrate has synergistic effects on both K_{AB} and N_o which could be related to the high flowrate favoured the surface adsorption of Cu^{2+} and Ni^{2+} onto the ZrGA.

Table 6.6: Kinetic model parameters for adsorption of Cu^{2+} and Ni^{2+} onto ZrGA fixed bed.

Pollutant	**Cu^{2+}**			**Ni^{2+}**		
	Bed height (*h*, cm)					
Thomas	**3**	**4**	**5**	**3**	**4**	**5**
K_{Th} (mL/min mg)	1.4211	1.2199	0.9177	2.113	1.2776	2.3262
q_{Th} (mg/g)	36.16	35.53	40.90	25.99	30.52	28.43
R^2	0.9967	0.9870	0.9883	0.9982	0.9954	0.9925
Yoon-Nelson						
K_{YN} (1/min)	0.0711	0.0610	0.0459	0.1057	0.0639	0.1163
τ (min)	51.71	69.28	122.69	37.16	59.51	85.28
R^2	0.9987	0.9870	0.9883	0.9982	0.9954	0.9925
Adams-Bohart						
K_{AB} (mL/min mg)	0.2902	0.2137	0.229	0.4681	0.2849	0.2265
N_o (mg/L)	2058.18	2178.88	2433.90	1412.70	1694.26	1952.90
R^2	0.8253	0.8009	0.8586	0.8566	0.8342	0.7822
	Influent concentration (C_o, mg/L)					
Thomas	**25**	**50**	**75**	**25**	**50**	**75**
K_{Th} (mL/min mg)	1.0496	1.2199	1.1796	2.1030	1.2776	3.1525
q_{Th} (mg/g)	40.53	35.53	39.93	27.12	30.52	21.33
R^2	0.9957	0.9870	0.9906	0.9906	0.9954	0.9945
Yoon-Nelson						
K_{YN} (1/min)	0.02624	0.0610	0.0885	0.0526	0.0639	0.2364
τ (min)	158.09	69.28	51.91	105.76	59.51	27.73
R^2	0.9957	0.9870	0.9906	0.9906	0.9954	0.9945

Adams-Bohart						
K_{AB} (mL/min mg)	0.2660	0.2137	0.3862	0.5954	0.2849	0.4255
N_o (mg/L)	2116.43	2178.88	1756.61	1227.16	1694.26	1202.17
R^2	0.8382	0.8009	0.9254	0.8845	0.8342	0.8040
	Flowrate (*Q*, mL/min)					
Thomas	**1**	**2**	**3**	**1**	**2**	**3**
K_{Th} (mL/min mg)	0.5703	1.2199	1.2058	0.8869	1.2776	1.2579
q_{Th} (mg/g)	36.21	35.53	33.72	26.43	30.52	25.45
R^2	0.9881	0.9870	0.9853	0.9951	0.9954	0.9640
Yoon-Nelson						
K_{YN} (1/min)	0.0285	0.0610	0.060	0.0443	0.0639	0.0629
τ (min)	141.21	69.28	43.85	103.07	59.51	33.09
R^2	0.9881	0.9870	0.9853	0.9951	0.9954	0.9640
Adams-Bohart						
K_{AB} (mL/min mg)	0.0987	0.2137	0.2428	0.1722	0.2849	0.2767
N_o (mg/L)	2284.91	2178.88	2403.10	1440.56	1694.26	1925.77
R^2	0.7993	0.8009	0.8177	0.8270	0.8342	0.8130

(a)

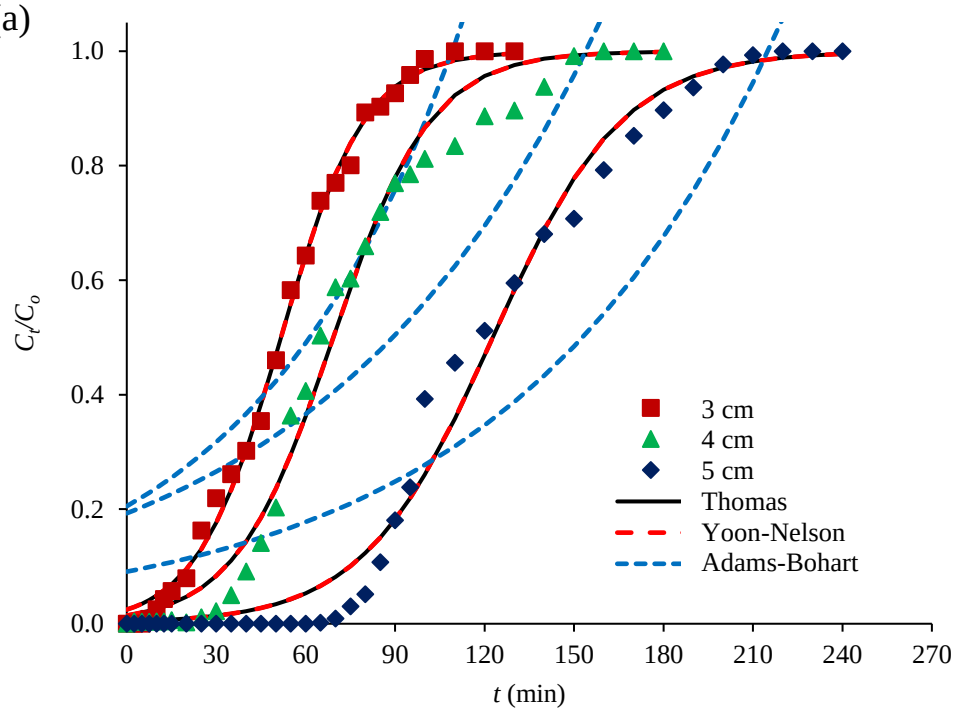
1.0
0.8
0.6
0.4
0.2
0.0
C_t/C_o
0
30
60
90
120
150
180
210
240
270
t (min)
3 cm
4 cm
5 cm
Thomas
Yoon-Nelson
Adams-Bohart

(b)

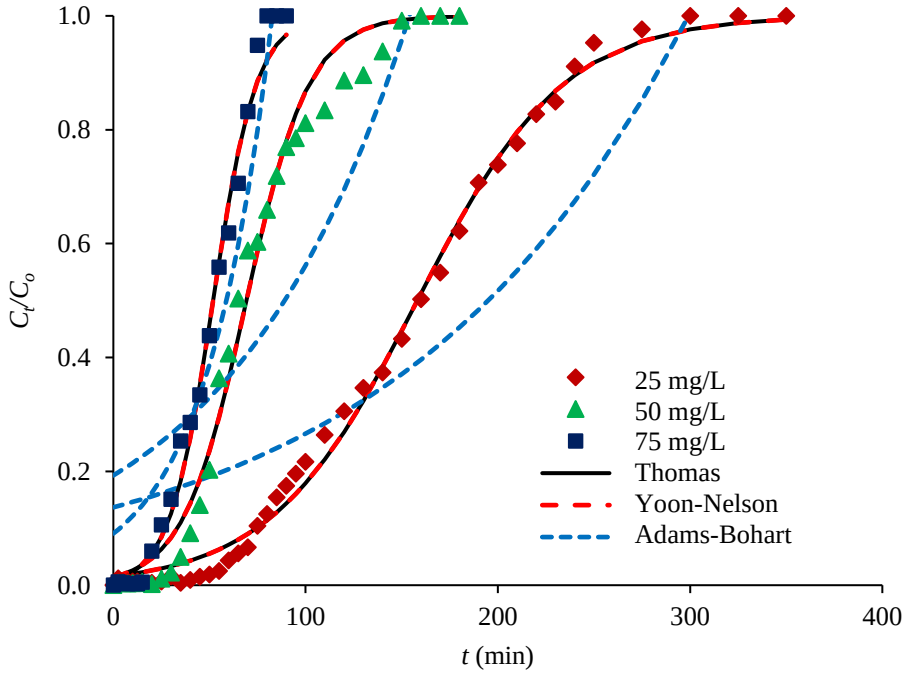
1.0
0.8
0.6
0.4
0.2
0.0
C_t/C_o
0
100
200
300
400
t (min)
25 mg/L
50 mg/L
75 mg/L
Thomas
Yoon-Nelson
Adams-Bohart

(c)

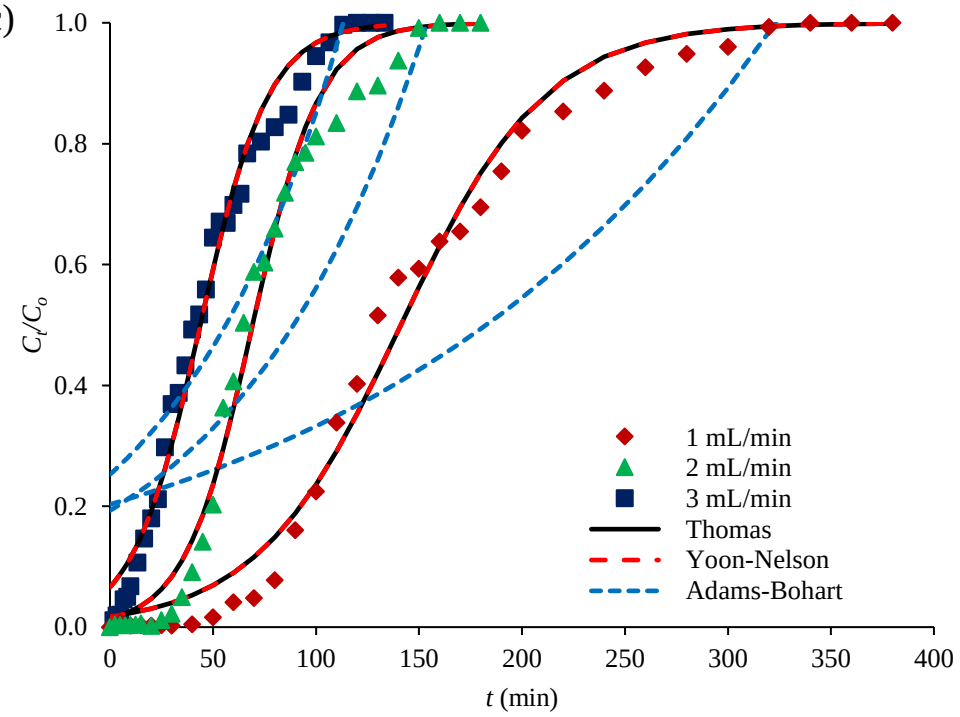
1.0
0.8
0.6
0.4
0.2
0.0
C_t/C_o
0
50
100
150
200
250
300
350
400
t (min)
1 mL/min
2 mL/min
3 mL/min
Thomas
Yoon-Nelson
Adams-Bohart

(d)

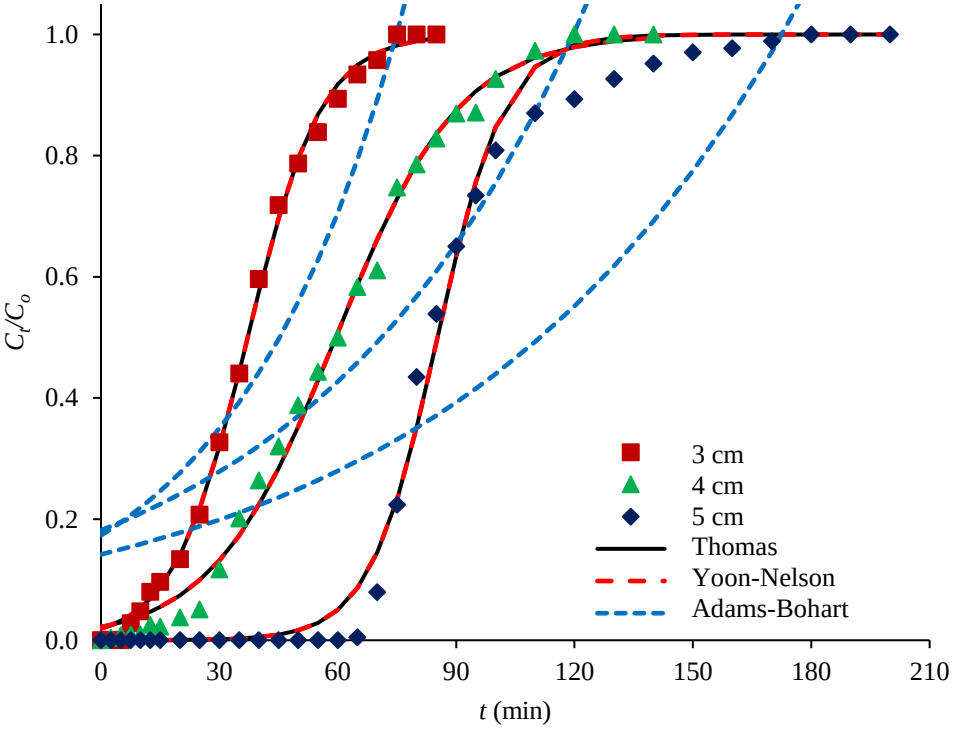
1.0
0.8
0.6
0.4
0.2
0.0
C_t/C_o
0
30
60
90
120
150
180
210
t (min)
3 cm
4 cm
5 cm
Thomas
Yoon-Nelson
Adams-Bohart

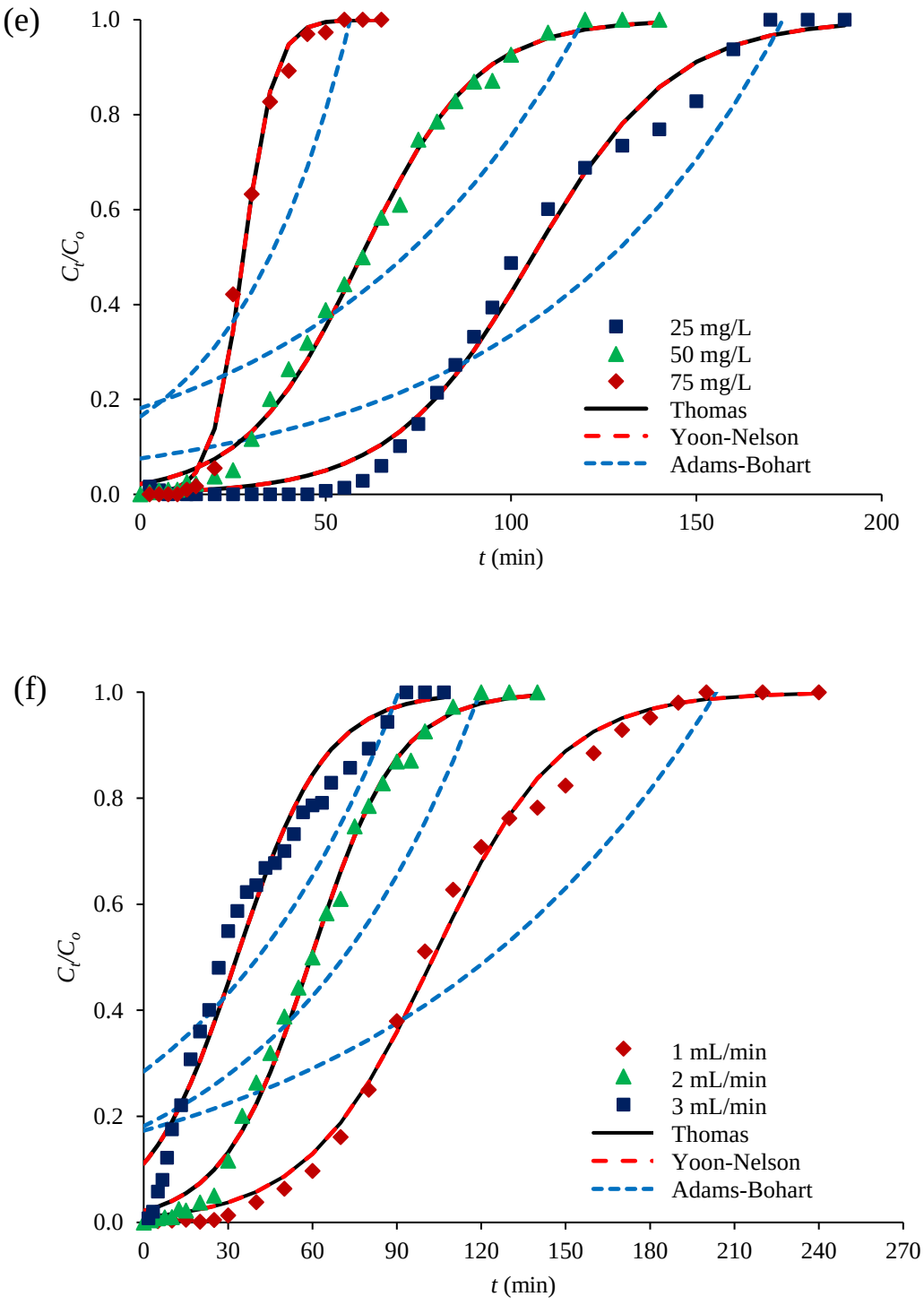

Fig. 6.13: Breakthrough curves for Cu^{2+} column adsorption for the effect of (a) bed height, (b) influent concentration and (c) flowrate; for Ni^{2+} column adsorption for effects of (d) bed height, (e) influent concentration and (f) flowrate

Overall, the Thomas and Yoon-Nelson models demonstrated good correlation with both Cu^{2+} and Ni^{2+} breakthrough curves obtained at the investigated parameters, as shown by the high R^2 values: effect of bed height (Cu^{2+}: $0.9870 < R^2 < 0.9967$; Ni^{2+}: $0.9925 < R^2 < 0.9982$), effect of influent concentration (Cu^{2+}: $0.9870 < R^2 < 0.9957$; Ni^{2+}: $0.9906 < R^2 < 0.9954$) and effect of flowrate (Cu^{2+}: $0.9853 < R^2 < 0.9881$; Ni^{2+}: $0.9040 < R^2 < 0.9954$). This implied that the continuous adsorption equilibrium of the heavy metals behaved according to the Langmuir model and the adsorption kinetic obeyed the pseudo-second-order model (Thomas, 1944), whereas the time required to achieve 50 % breakthrough was determined by the τ values of Yoon-Nelson model (Yoon & Nelson, 1984). The Adams-Bohart model was applied to describe the adsorption kinetic up to 50 % breakthrough, but significant deviation was observed between the experimental and predicted data which resulted in the low R^2 (< 0.90).

6.4.6 Mass transfer analysis for Cu^{2+}- and Ni^{2+}-ZrGA systems

Based on the experimental breakthrough curves, mathematical modelling was employed to evaluate the mass transfer phenomena of the heavy metals adsorption through global, external (film diffusion) and internal (pore diffusion) mass transfer coefficients. Fig. 6.14 depicts the individual mass transfer coefficient for Cu^{2+} and Ni^{2+} adsorption onto ZrGA fixed bed under the influences of bed height, influent concentration and flowrate.

The global mass transfer ($[K_L a]_g$) describes the global average of local mass transfers (external and internal mass transfer) at the solid-liquid interface for the whole adsorption process. Fig. 6.14 shows that $[K_L a]_g$ decreases exponentially with increasing percentage of breakthough concentration (C_t/C_o) as the column operation progresses. The high numerical values of $[K_L a]_g$ indicated rapid mass transfer rate of the heavy metals along the ZrGA bed and the mass transfer rate for Cu^{2+} adsorption was heavily influenced by flowrate (0.4452 min^{-1}) > bed height (0.3826 min^{-1}) > influent concentration (0.3126 min^{-1}), while for Ni^{2+} adsorption it was affected by flowrate (0.6779 min^{-1}) > influent concentration (0.4870 min^{-1}) > bed height (0.4759 min^{-1}). It is worth mentioning that the $[K_L\ a]_g$ of Ni^{2+} adsorption was noticeably higher than Cu^{2+} adsorption, implying the mass transfer rate of Ni^{2+} was faster than that of Cu^{2+} along the ZrGA bed and the saturation of column was faster. This was reflected by the breakthrough curves of Ni^{2+} adsorption where the adsorption column showed early breakthrough and saturation times.

(a) (i) h = 3 cm

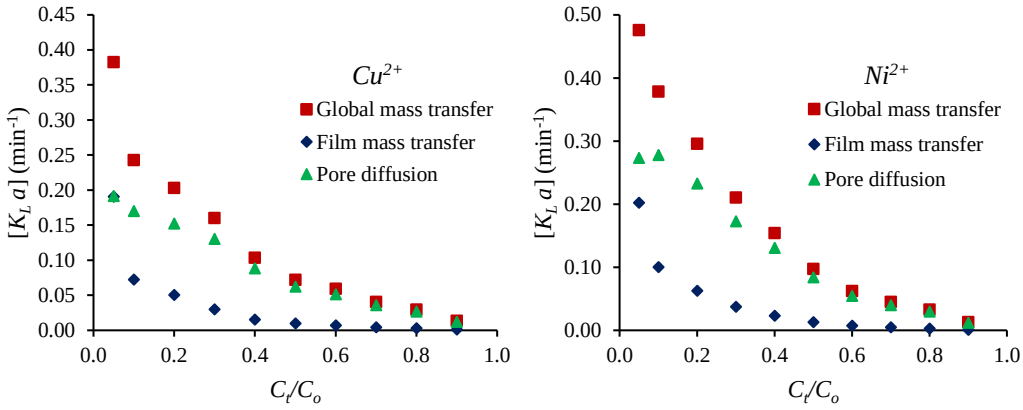

(ii) h = 4 cm

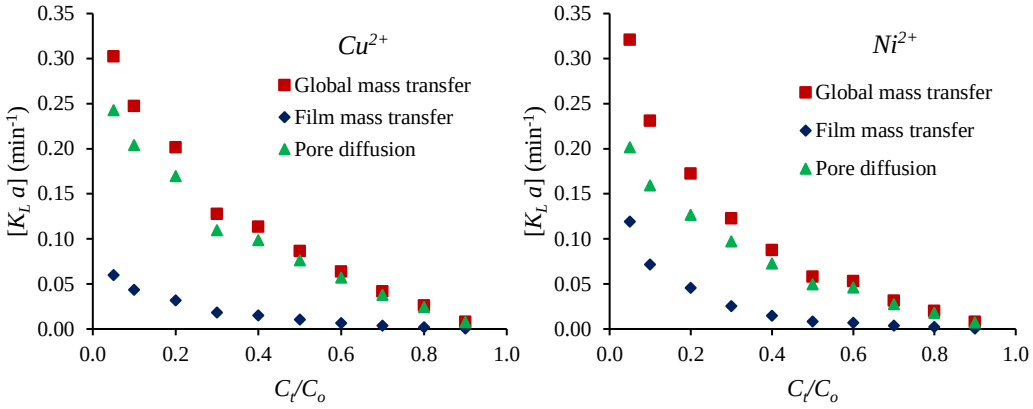

(iii) h = 5 cm

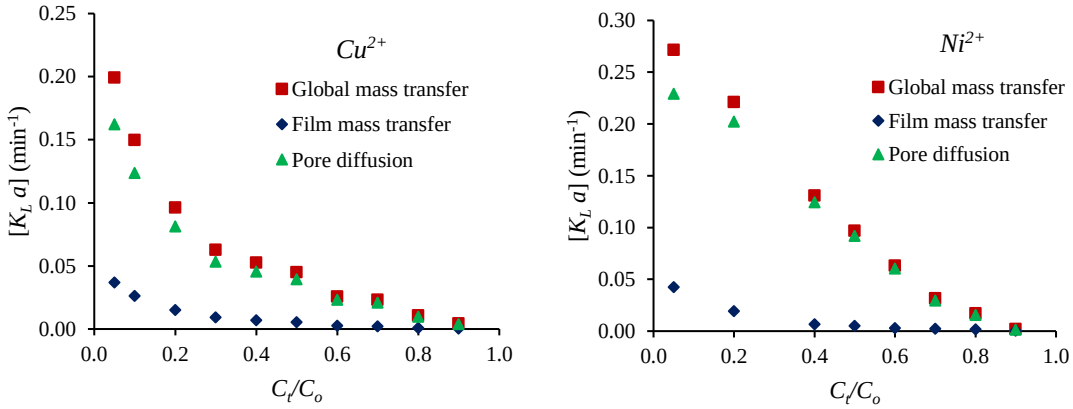

(b) (i) C_o = 25 mg/L

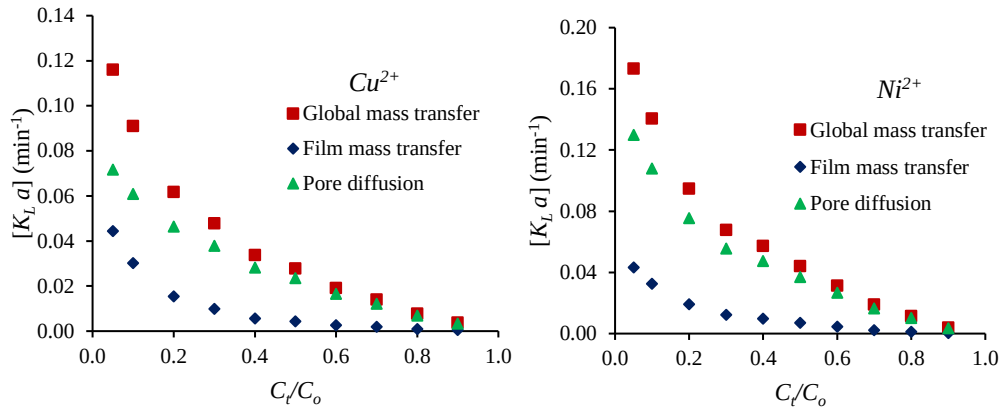

(ii) C_o = 50 mg/L

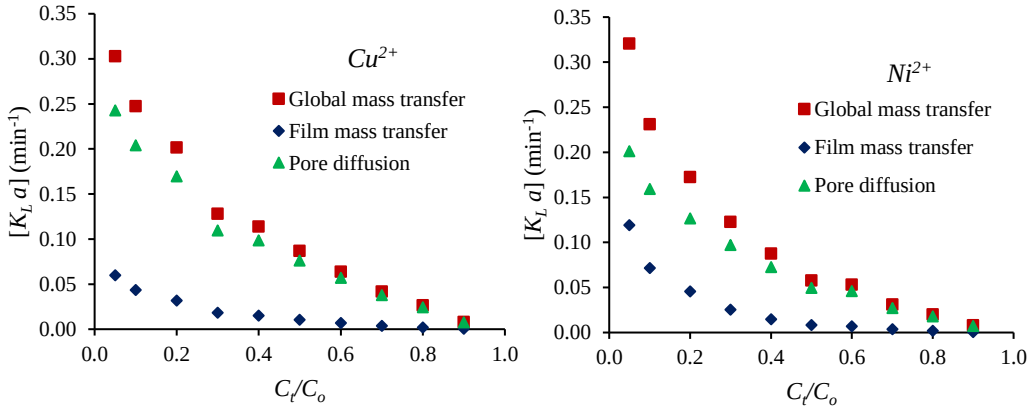

(iii) C_o = 75 mg/L

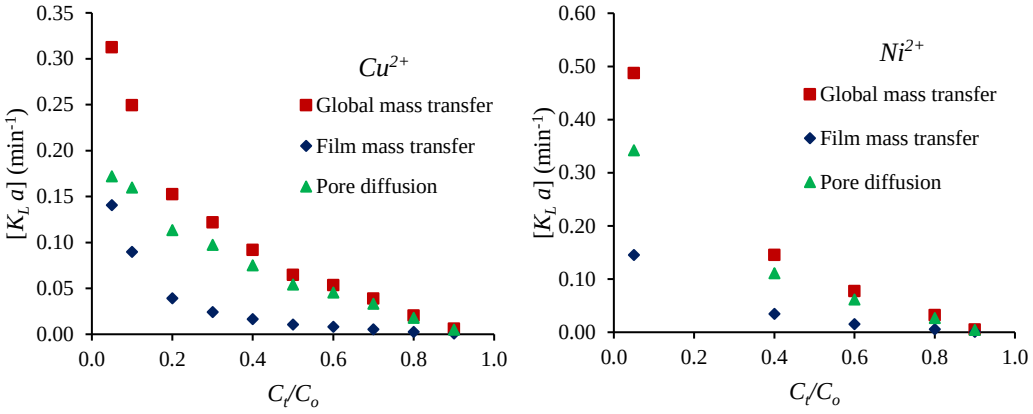

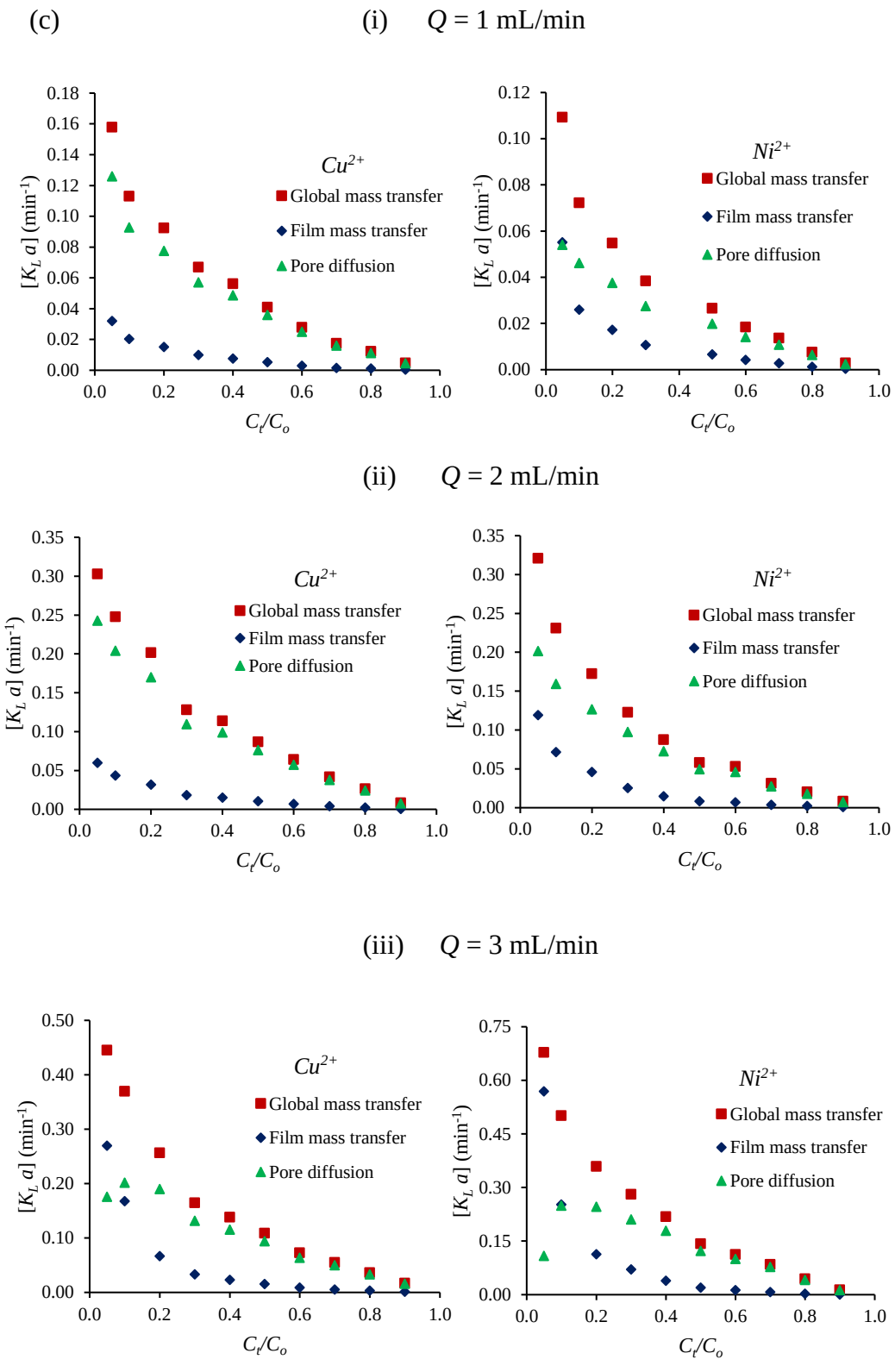

Fig. 6.14: Global and individual mass transfer coefficients variation with breakthrough concentration on the effect of (a) bed height, (b) influent concentration and (c) flowrate.

$[K_La]_f$ indicates the magnitude of external mass transfer rate during the heavy metals adsorption onto ZrGA fixed bed. It can be observed in Fig. 6.14 (a) – (c), $[K_La]_f$ exhibited similar pattern to the variation in $[K_La]_g$ as the column was progressively saturated. In general, the external mass transfer rate at film zone was fast during the initial stage of adsorption (C_t/C_o = 0.05) and rapidly decreased until C_t/C_o = 0.20 and beyond that it showed minimum change until the column was saturated. Additionally, $[K_La]_f$ was increased when the influent concentration and flowrate were increased, and bed height was decreased. The highest $[K_La]_f$ occurred at 5 % breakthrough when the column was operated at a flowrate of 3 mL/min (Cu^{2+}: 0.2694 min^{-1}; Ni^{2+}: 0.5690 min^{-1}). This could be due to the enhancement in mass transfer driving forces at higher influent concentration and flowrate, hence speed up the external mass transfer rate for transporting the heavy metals from the bulk phase to the adsorbent surface.

The internal mass transfer or pores diffusion which was represented by $[K_La]_p$, exhibited a descending order as the column saturation was increased. The decreasing trend could be explained by accumulation of the heavy metals in the pores of ZrGA adsorbent. As the exterior part of pores was occupied, the free metal ions slowly transported to the inner part of pores. Even though the moving rate of heavy metals through the external film zone was rapid, diffusion through the pores of adsorbent was slow. Notably, the internal mass transfer rate of Ni^{2+} adsorption was mostly higher than that of Cu^{2+} adsorption as evident by the higher $[K_La]_p$ of Ni^{2+} than Cu^{2+}. This could be due to the molecular weight of Ni^{2+} (237.69 g/mol) which is smaller than that of Cu^{2+} (249.69 g/mol) which enabled Ni^{2+} to travel faster through the pores of ZrGA (Ezechi et al., 2020).

Overall, this study showed that the mass transfer resistance in Cu^{2+} and Ni^{2+} adsorption onto ZrGA fixed bed was dependent on both pore diffusion and film mass

transfer as indicated by the simultaneous decrease in $[K_L\ a]_f$ and $[K_L\ a]_p$ in accordance to $[K_L\ a]_g$. The maximum mass transfer rate occurs at 5 % breakthrough concentration and thereafter it depleted sharply up till 20 % breakthrough before gradually decreased until column saturation. This implied that at 5 % breakthrough, the mass transfer rate was rapid due to large availability of sorption sites and fast-moving rate of adsorbate from the bulk liquid phase to the adsorbent surface. The mass transfer rate slowed down in proportion to the column saturation and finally stopped when the column was totally exhausted. According to the mass transfer factor analysis, the mass transfer rate exhibited synergistic relationship with influent concentration and flowrate while antagonistic relationship with bed height.

6.5 Conclusions

Fixed bed adsorption study is essential for the evaluation of the potential application of 3D graphene-based adsorbents in treating relatively large volume of wastewater. Column parameters such as bed height, influent concentration and flowrate were investigated to obtain the breakthrough curves which were used to calculate the column design data. The obtained breakthrough curves were fitted to fixed bed kinetic model such as the Thomas, Yoon-Nelson and Adams-Bohart models. The mass transfer properties of the fixed bed systems were determined by the mass transfer factor model.

The adsorption of diclofenac onto rGOA fixed bed was investigated with respect to variation in bed height (10 – 15 cm), influent concentration (25 – 75 mg/L) and flowrate (1 – 3 mL/min). The study revealed that breakthrough time (t_b) increased with increasing bed height and decreasing influent concentration and flowrate. The relationship between bed height and column service time exhibited a linear trend and the equation developed using the BDST model demonstrated high R^2. As judged by the high R^2, the breakthrough curves were well correlated to the Thomas and Yoon-Nelson

models. The rate-limiting steps of diclofenac adsorption onto rGOA was controlled by both film mass transfer and pore diffusion.

However, the RGM adsorbent showed poor performance in fixed bed adsorption due to structural instability when subjected to operation pressure of the fixed bed column. Although RGM was not investigated further using the fixed bed mode, it was highly suitable for use in batch adsorption.

Heavy metal (Cu^{2+} and Ni^{2+}) adsorption was conducted in fixed bed operation using ZrGA as the packing material. The effects of bed height (3 – 5 cm), influent concentration (25 – 75 mg/L) and flowrate (1 – 3 mL/min) were investigated and the respective breakthrough curves were determined. The t_b showed positive synergy with higher bed height but negative synergy with high influent concentration and flowrate. Furthermore, the t_b of Cu^{2+} fixed bed adsorption was longer than Ni^{2+} fixed bed adsorption. This could possibly due to the slower moving rate of adsorption zone for Cu^{2+} compared to Ni^{2+}, thus allowing longer time for Cu^{2+} to diffuse through the pores of ZrGA. The column service time varied linearly with bed height. The BDST model parameters were obtained and subsequently used for generating the mathematical model to describe the column service time as a function of bed height. The obtained mathematical models showed high R^2. The breakthrough curves were best described by the Thomas and Yoon-Nelson model as evident from the high R^2 (> 0.98). According to mass transfer factor analysis, the film mass transfer and pore diffusion were found to be the main controlling steps.

Chapter 7: Conclusions and Future Work

7.1 Conclusions

This thesis offers significant insights contributing to the advancement of nanotechnology in wastewater treatment following successful synthesis of the 3D graphene-based adsorbents for fixed bed adsorption of wastewater. GO was initially synthesised by the modified Hummers method and the 3D graphene structures (rGOA, RGM and ZrGA) were fabricated by solution-based method using GO precursor. The synthesis of rGOA involved chemical reduction of GO with L-ascorbic acid and freeze drying. Meanwhile, RGM and ZrGA were synthesised using the ice-templating method with carboxymethyl cellulose as the chemical binder, and Mn and Zr as the functionalising agents for RGM and ZrGA, respectively.

With the successful fabrication of 3D graphene-based adsorbents, this research further explored their adsorption performance towards pharmaceutical and heavy metal residues using batch mode. From preliminary study, rGOA and RGM showed highest removal efficiencies for diclofenac and acetaminophen, respectively, whereas ZrGA showed the highest efficiency for Cu^{2+} and Ni^{2+}. The adsorption equilibrium, kinetic and thermodynamic parameters were determined by fitting the experimental data to theoretical adsorption models. Additionally, the suitable eluents for desorption of the heavy metals and pharmaceuticals were identified and the regenerability of the 3D graphene adsorbents was investigated. The possible adsorption mechanisms involved in the heavy metals and pharmaceuticals adsorption onto the 3D graphene adsorbents were also identified.

RSM was applied to study the simultaneous interaction of different independent parameters on the adsorption capacity. Mathematical models were developed to

describe the batch adsorption study and model predictability was gauged by analysis of variance. This study provides valuable information on the relative impact of each studied parameters towards adsorption capacity as well as interactive effects from 3D response surface plots. Moreover, this information enables the identification of sensible regions and parameters to achieve highest possible adsorption capacity. Hence, this approach enables the complex interactions of different parameters in adsorption process to be established, as well as for process optimisation.

The 3D graphene adsorbents were investigated by fixed bed adsorption mode. This study offers valuable data for process scale up and process design such as the breakthrough curves and column design parameters (mass transfer zone, fractional bed utilisation, breakthrough time, saturation time, etc). The breakthrough curve modelling was performed by fitting the experimental data to dynamic adsorption kinetic models. The rate limiting steps for the fixed bed adsorption were identified using the experimental breakthrough curves and mass transfer factor model. The mathematical expression to predict column service time as a function of bed height was developed and the model can be used to scale up the process without additional experimental work.

Overall, this thesis presents a comprehensive study to support the utilisation of 3D graphene structures in adsorption of heavy metal and pharmaceutical contaminants via batch and fixed bed adsorption systems.

7.2 Future work

This thesis describes the application of 3D graphene-based structures for pharmaceuticals and heavy metals adsorption in batch and fixed bed modes. In view of potential commercialisation of the 3D graphene adsorbents for wastewater treatment,

several opportunities have been identified for further exploration. The proposed future work are as follows:

7.2.1 Improvement on mechanical strength

Despite demonstrating good adsorption performance, the developed 3D graphene-based adsorbent was observed to experience structural changes after adsorption, particularly during fixed bed operation. Moreover, the ultralight attribute of 3D graphene structures made the adsorbent stayed afloat in aqueous media which is undesirable. Therefore, the selection of appropriate chemical binders that can act as structural support such as long chain polymers, metal organic framework and cross-linker may improve the overall mechanical strength of adsorbent, especially with the aid of GO. Furthermore, the shape of adsorbent should also be investigated as it could potentially affect the expose surface for adsorption and structural stability.

7.2.2 Pilot scale experimentation

The fixed bed adsorption study was conducted in laboratory scale which does not provide complete representation of industrial adsorption system. For improvement of the fixed bed adsorption study, auxiliary equipment such as pump should be installed for better control on flowrate, and the adsorption column arrangement (series or parallel) should be studied. Furthermore, the effect of flow direction (up flow or down flow) on the column performance should be investigated to determine the best operation mode for the column. The current work was conducted using synthetic wastewater containing single component contaminant. However, real industrial effluent generally consists of complex water composition with multiple contaminants, high salinity and chemical/biological oxygen demand. Hence, it is recommended to perform future work using real wastewater from the industry for testing the adsorption performance of the 3D graphene adsorbents.

References

Abarrategi, A., Gutiérrez, M.C., Moreno-Vicente, C., Hortigüela, M.J., Ramos, V., López-Lacomba, J.L., Ferrer, M.L., del Monte, F. 2008. Multiwall carbon nanotube scaffolds for tissue engineering purposes. Biomaterials, 29(1), 94-102.

Abd-Elhamid, A.I., Kamoun, E.A., El-Shanshory, A.A., Soliman, H.M.A., Aly, H.F. 2019. Evaluation of graphene oxide-activated carbon as effective composite adsorbent toward the removal of cationic dyes: Composite preparation, characterization and adsorption parameters. Journal of Molecular Liquids, 279, 530-539.

Abdolhosseinzadeh, S., Asgharzadeh, H., Seop Kim, H. 2015. Fast and fully-scalable synthesis of reduced graphene oxide. Scientific Reports, 5(1), 10160.

Abdullah, N., Yusof, N., Lau, W.J., Jaafar, J., Ismail, A.F. 2019. Recent trends of heavy metal removal from water/wastewater by membrane technologies. Journal of Industrial and Engineering Chemistry, 76, 17-38.

Abo El Naga, A.O., El Saied, M., Shaban, S.A., El Kady, F.Y. 2019. Fast removal of diclofenac sodium from aqueous solution using sugar cane bagasse-derived activated carbon. Journal of Molecular Liquids, 285, 9-19.

Acosta, R., Fierro, V., Martinez de Yuso, A., Nabarlatz, D., Celzard, A. 2016. Tetracycline adsorption onto activated carbons produced by KOH activation of tyre pyrolysis char. Chemosphere, 149, 168-176.

Acuña, V., Ginebreda, A., Mor, J.R., Petrovic, M., Sabater, S., Sumpter, J., Barceló, D. 2015. Balancing the health benefits and environmental risks of pharmaceuticals: Diclofenac as an example. Environment International, 85, 327-333.

Adhikari, B., Biswas, A., Banerjee, A. 2012. Graphene Oxide-Based Hydrogels to Make Metal Nanoparticle-Containing Reduced Graphene Oxide-Based Functional Hybrid Hydrogels. ACS Applied Materials & Interfaces, 4(10), 5472-5482.

Ahmed, M.J., Hameed, B.H. 2019. Insights into the isotherm and kinetic models for the coadsorption of pharmaceuticals in the absence and presence of metal ions: A review. Journal of Environmental Management, 252, 109617.

Ahmed, M.J., Hameed, B.H. 2018. Removal of emerging pharmaceutical contaminants by adsorption in a fixed-bed column: A review. Ecotoxicology and Environmental Safety, 149, 257-266.

Akhtar, J., Amin, N.S., Aris, A. 2011. Combined adsorption and catalytic ozonation for removal of sulfamethoxazole using Fe_2O_3/CeO_2 loaded activated carbon. Chemical Engineering Journal, 170(1), 136-144.

Akpotu, S.O., Moodley, B. 2018a. Application of as-synthesised MCM-41 and MCM-41 wrapped with reduced graphene oxide/graphene oxide in the remediation of acetaminophen and aspirin from aqueous system. Journal of Environmental Management, 209, 205-215.

Akpotu, S.O., Moodley, B. 2018b. MCM-48 encapsulated with reduced graphene oxide/graphene oxide and as-synthesised MCM-48 application in remediation of pharmaceuticals from aqueous system. Journal of Molecular Liquids, 261, 540-549.

Al-Ghouti, M.A., Al-Degs, Y.S., Khraisheh, M.A.M., Ahmad, M.N., Allen, S.J. 2009. Mechanisms and chemistry of dye adsorption on manganese oxides-modified diatomite. Journal of Environmental Management, 90(11), 3520-3527.

Al-Khateeb, L.A., Almotiry, S., Salam, M.A. 2014. Adsorption of pharmaceutical pollutants onto graphene nanoplatelets. Chemical Engineering Journal, 248, 191-199.

Al-Khateeb, L.A., Hakami, W., Salam, M.A. 2017. Removal of non-steroidal anti-inflammatory drugs from water using high surface area nanographene: Kinetic and thermodynamic studies. Journal of Molecular Liquids, 241, 733-741.

Al-Qaim, F.F., Abdullah, M.P., Othman, M.R., Latip, J., Zakaria, Z. 2014. Multi-residue analytical methodology-based liquid chromatography-time-of-flight-mass spectrometry for the analysis of pharmaceutical residues in surface water and effluents from sewage treatment plants and hospitals. J Chromatogr A, 1345, 139-53.

Albayati, T.M., Kalash, K.R. 2020. Polycyclic aromatic hydrocarbons adsorption from wastewater using different types of prepared mesoporous materials MCM-41in batch and fixed bed column. Process Safety and Environmental Protection, 133, 124-136.

Aleksandrzak, M., Kukulka, W., Mijowska, E. 2017. Graphitic carbon nitride/graphene oxide/reduced graphene oxide nanocomposites for photoluminescence and photocatalysis. Applied Surface Science, 398, 56-62.

Álvarez-Torrellas, S., Peres, J.A., Gil-Álvarez, V., Ovejero, G., García, J. 2017. Effective adsorption of non-biodegradable pharmaceuticals from hospital wastewater with different carbon materials. Chemical Engineering Journal, 320, 319-329.

Amalraj Appavoo, I., Hu, J., Huang, Y., Li, S.F., Ong, S.L. 2014. Response surface modeling of Carbamazepine (CBZ) removal by Graphene-P25 nanocomposites/UVA process using central composite design. Water Res, 57, 270-9.

Ang, T.N., Young, B.R., Taylor, M., Burrell, R., Aroua, M.K., Baroutian, S. 2020. Breakthrough analysis of continuous fixed-bed adsorption of sevoflurane using activated carbons. Chemosphere, 239, 124839.

Antunes, M., Esteves, V.I., Guégan, R., Crespo, J.S., Fernandes, A.N., Giovanela, M. 2012. Removal of diclofenac sodium from aqueous solution by Isabel grape bagasse. Chemical Engineering Journal, 192, 114-121.

Arfin, T., Tarannum, A. 2019. Rapid determination of lead ions using polyaniline-zirconium (IV) iodate -based ion selective electrode. Journal of Environmental Chemical Engineering, 7(1), 102811.

Awad, A.M., Jalab, R., Benamor, A., Nasser, M.S., Ba-Abbad, M.M., El-Naas, M., Mohammad, A.W. 2020. Adsorption of organic pollutants by nanomaterial-based adsorbents: An overview. Journal of Molecular Liquids, 301, 112335.

Aydın, C. 2019. Synthesis of SnO_2:rGO nanocomposites by the microwave-assisted hydrothermal method and change of the morphology, structural, optical and electrical properties. Journal of Alloys and Compounds, 771, 964-972.

Bai, H., Li, C., Wang, X., Shi, G. 2010. A pH-sensitive graphene oxide composite hydrogel. Chemical Communications, 46(14), 2376-2378.

Bai, H., Sheng, K., Zhang, P., Li, C., Shi, G. 2011. Graphene oxide/conducting polymer composite hydrogels. Journal of Materials Chemistry, 21(46), 18653-18658.

Bai, X., Qin, C., Feng, R., Ye, Z. 2017. Binary adsorption of 17β-estradiol and bisphenol A on superparamagnetic amino-functionalized graphene oxide nanocomposites. Materials Chemistry and Physics, 189, 96-104.

Banerjee, P., Das, P., Zaman, A., Das, P. 2016. Application of graphene oxide nanoplatelets for adsorption of Ibuprofen from aqueous solutions: Evaluation of process kinetics and thermodynamics. Process Safety and Environmental Protection, 101(Supplement C), 45-53.

Bao, C., Bi, S., Zhang, H., Zhao, J., Wang, P., Yue, C.Y., Yang, J. 2016. Graphene oxide beads for fast clean-up of hazardous chemicals. Journal of Materials Chemistry A, 4(24), 9437-9446.

Baruah, B., Kumar, A. 2018. PEDOT:PSS/MnO_2/rGO ternary nanocomposite based anode catalyst for enhanced electrocatalytic activity of methanol oxidation for direct methanol fuel cell. Synthetic Metals, 245, 74-86.

Bhadra, B.N., Seo, P.W., Jhung, S.H. 2016. Adsorption of diclofenac sodium from water using oxidized activated carbon. Chemical Engineering Journal, 301, 27-34.

Bhangi, B.K., Ray, S.K. 2020. Nano silver chloride and alginate incorporated composite copolymer adsorbent for adsorption of a synthetic dye from water in a fixed bed column and its photocatalytic reduction. International Journal of Biological Macromolecules, 144, 801-812.

Bhargava, S., Makowiec, M.E., Blanchet, T.A. 2020. Wear reduction mechanisms within highly wear-resistant graphene- and other carbon-filled PTFE nanocomposites. Wear, 444-445, 203163.

Bian, Y., Bian, Z.-Y., Zhang, J.-X., Ding, A.-Z., Liu, S.-L., Wang, H. 2015. Effect of the oxygen-containing functional group of graphene oxide on the aqueous cadmium ions removal. Applied Surface Science, 329, 269-275.

Bianco, A., Cheng, H.-M., Enoki, T., Gogotsi, Y., Hurt, R.H., Koratkar, N., Kyotani, T., Monthioux, M., Park, C.R., Tascon, J.M.D., Zhang, J. 2013. All in the graphene family – A recommended nomenclature for two-dimensional carbon materials. Carbon, 65, 1-6.

Blair, H.A., Plosker, G.L. 2015. Diclofenac Sodium Injection (Akis®, Dicloin®): A Review of Its Use in the Management of Pain. Clinical Drug Investigation, 35(6), 397-404.

Bo, Z., Shuai, X., Mao, S., Yang, H., Qian, J., Chen, J., Yan, J., Cen, K. 2014. Green preparation of reduced graphene oxide for sensing and energy storage applications. Scientific Reports, 4(1), 4684.

Bohart, G.S., Adams, E.Q. 1920. Some aspects of the behaviour of charcoal with respect to chlorine.1. Journal of the American Chemical Society, 42(3), 523-544.

Boudrahem, N., Delpeux-Ouldriane, S., Khenniche, L., Boudrahem, F., Aissani-Benissad, F., Gineys, M. 2017. Single and mixture adsorption of clofibric acid, tetracycline and paracetamol onto Activated carbon developed from cotton cloth residue. Process Safety and Environmental Protection, 111, 544-559.

Box, G.E.P., Behnken, D.W. 1960. Some New Three Level Designs for the Study of Quantitative Variables. Technometrics, 2(4), 455-475.

Branca, C., Crupi, C., D'Angelo, G., Khouzami, K., Rifici, S., Visco, A., Wanderlingh, U. 2015. Effect of montmorillonite on the rheological properties of dually crosslinked guar gum-based hydrogels. Journal of Applied Polymer Science, 132(5), n/a-n/a.

Brodie, B.C. 1859. XIII. On the atomic weight of graphite. Philosophical Transactions of the Royal Society of London(149), 249-259.

Cai, D., Song, M. 2007. Preparation of fully exfoliated graphite oxide nanoplatelets in organic solvents. Journal of Materials Chemistry, 17(35), 3678-3680.

Cai, N., Larese-Casanova, P. 2014. Sorption of carbamazepine by commercial graphene oxides: A comparative study with granular activated carbon and multiwalled carbon nanotubes. Journal of Colloid and Interface Science, 426, 152-161.

Carolin, C.F., Kumar, P.S., Saravanan, A., Joshiba, G.J., Naushad, M. 2017. Efficient techniques for the removal of toxic heavy metals from aquatic environment: A review. Journal of Environmental Chemical Engineering, 5(3), 2782-2799.

Chang, S., Fu, H., Wu, X., Liu, C., Li, Z., Dai, Y., Zhang, H. 2018. Batch and fixed-bed column studies for selective removal of cesium ions by compressible Prussian blue/polyurethane sponge. RSC Advances, 8(64), 36459-36467.

Chen, H., Gao, B., Li, H. 2014a. Functionalization, pH, and ionic strength influenced sorption of sulfamethoxazole on graphene. Journal of Environmental Chemical Engineering, 2(1), 310-315.

Chen, H., Gao, B., Li, H. 2014b. Removal of sulfamethoxazole and ciprofloxacin from aqueous solutions by graphene oxide. J Hazard Mater.

Chen, H., Xing, X., Tan, H., Jia, Y., Zhou, T., Chen, Y., Ling, Z., Hu, X. 2017a. Covalently antibacterial alginate-chitosan hydrogel dressing integrated gelatin microspheres containing tetracycline hydrochloride for wound healing. Materials Science and Engineering: C, 70, 287-295.

Chen, L., Li, Y., Du, Q., Wang, Z., Xia, Y., Yedinak, E., Lou, J., Ci, L. 2017b. High performance agar/graphene oxide composite aerogel for methylene blue removal. Carbohydrate Polymers, 155, 345-353.

Chen, S., Hong, J., Yang, H., Yang, J. 2013a. Adsorption of uranium (VI) from aqueous solution using a novel graphene oxide-activated carbon felt composite. Journal of Environmental Radioactivity, 126, 253-258.

Chen, Y., Chen, L., Bai, H., Li, L. 2013b. Graphene oxide–chitosan composite hydrogels as broad-spectrum adsorbents for water purification. Journal of Materials Chemistry A, 1(6), 1992-2001.

Cheng, Y., Zhou, S., Hu, P., Zhao, G., Li, Y., Zhang, X., Han, W. 2017. Enhanced mechanical, thermal, and electric properties of graphene aerogels via supercritical ethanol drying and high-temperature thermal reduction. Scientific Reports, 7(1), 1439.

Chu, H.-J., Lee, C.-Y., Tai, N.-H. 2014. Green reduction of graphene oxide by Hibiscus sabdariffa L. to fabricate flexible graphene electrode. Carbon, 80, 725-733.

Chu, Y., Khan, M.A., Xia, M., Lei, W., Wang, F., Zhu, S., Yan, X. 2020. Synthesis and micro-mechanistic studies of histidine modified montmorillonite for lead(II) and copper(II) adsorption from wastewater. Chemical Engineering Research and Design, 157, 142-152.

Chua, C.K., Pumera, M. 2014. Chemical reduction of graphene oxide: a synthetic chemistry viewpoint. Chemical Society Reviews, 43(1), 291-312.

Cristine de Sousa Santos, T., Monte Almeida, A.C., Pinheiro, D.d.R., Leal Costa, C.M., Estumano, D.C., Fernando da Paixão Ribeiro, N. 2020. Synthesis and characterization of colourful aluminates based on nickel and zinc. Journal of Alloys and Compounds, 815, 152477.

Czech, B., Tyszczuk-Rotko, K. 2018. Visible-light-driven photocatalytic removal of acetaminophen from water using a novel MWCNT-TiO_2-SiO_2 photocatalysts. Separation and Purification Technology, 206, 343-355.

Da'na, E., Awad, A. 2017. Regeneration of spent activated carbon obtained from home filtration system and applying it for heavy metals adsorption. Journal of Environmental Chemical Engineering, 5(4), 3091-3099.

Dai, C.-m., Geissen, S.-U., Zhang, Y.-l., Zhang, Y.-j., Zhou, X.-f. 2011. Selective removal of diclofenac from contaminated water using molecularly imprinted polymer microspheres. Environmental Pollution, 159(6), 1660-1666.

Dai, H., Huang, H. 2017. Enhanced Swelling and Responsive Properties of Pineapple Peel Carboxymethyl Cellulose-g-poly(acrylic acid-co-acrylamide) Superabsorbent Hydrogel by the Introduction of Carclazyte. Journal of Agricultural and Food Chemistry, 65(3), 565-574.

Dai, J., Huang, T., Tian, S.-q., Xiao, Y.-j., Yang, J.-h., Zhang, N., Wang, Y., Zhou, Z.-w. 2016. High structure stability and outstanding adsorption performance of graphene oxide aerogel supported by polyvinyl alcohol for waste water treatment. Materials & Design, 107, 187-197.

Darvishi, S., Souissi, M., Kharaziha, M., Karimzadeh, F., Sahara, R., Ahadian, S. 2018. Gelatin methacryloyl hydrogel for glucose biosensing using Ni nanoparticles-reduced graphene oxide: An experimental and modeling study. Electrochimica Acta, 261, 275-283.

Darweesh, T.M., Ahmed, M.J. 2017a. Adsorption of ciprofloxacin and norfloxacin from aqueous solution onto granular activated carbon in fixed bed column. Ecotoxicology and Environmental Safety, 138, 139-145.

Darweesh, T.M., Ahmed, M.J. 2017b. Batch and fixed bed adsorption of levofloxacin on granular activated carbon from date (Phoenix dactylifera L.) stones by KOH chemical activation. Environmental Toxicology and Pharmacology, 50, 159-166.

Das, N. 2010. Recovery of precious metals through biosorption — A review. Hydrometallurgy, 103(1), 180-189.

Dastgheib, S.A., Rockstraw, D.A. 2002. A model for the adsorption of single metal ion solutes in aqueous solution onto activated carbon produced from pecan shells. Carbon, 40(11), 1843-1851.

Daughton, C.G., Ternes, T.A. 1999. Pharmaceuticals and personal care products in the environment: agents of subtle change? Environmental Health Perspectives, 107(Suppl 6), 907-938.

De Silva, K.K.H., Huang, H.H., Joshi, R.K., Yoshimura, M. 2017. Chemical reduction of graphene oxide using green reductants. Carbon, 119, 190-199.

Dean, J. 1990. Lange's handbook of chemistry. Material and manufacturing process, 5(4), 687-688.

DOE. 1979. Environmental Quality (Sewage and Industrial Effluents) Regulations 1979, (Ed.) M.o.N.R. Environment. Malaysia.

Dong, S., Sun, Y., Wu, J., Wu, B., Creamer, A.E., Gao, B. 2016. Graphene oxide as filter media to remove levofloxacin and lead from aqueous solution. Chemosphere, 150, 759-764.

Drake, P.L., Hazelwood, K.J. 2005. Exposure-Related Health Effects of Silver and Silver Compounds: A Review. The Annals of Occupational Hygiene, 49(7), 575-585.

Du, M., Sun, J., Chang, J., Yang, F., Shi, L., Gao, L. 2014. Synthesis of nitrogen-doped reduced graphene oxide directly from nitrogen-doped graphene oxide as a high-performance lithium ion battery anode. RSC Advances, 4(80), 42412-42417.

Du, Z., Zheng, T., Wang, P. 2018. Experimental and modelling studies on fixed bed adsorption for Cu(II) removal from aqueous solution by carboxyl modified jute fiber. Powder Technology, 338, 952-959.

Dubin, S., Gilje, S., Wang, K., Tung, V.C., Cha, K., Hall, A.S., Farrar, J., Varshneya, R., Yang, Y., Kaner, R.B. 2010. A One-Step, Solvothermal Reduction Method for Producing Reduced Graphene Oxide Dispersions in Organic Solvents. ACS Nano, 4(7), 3845-3852.

Dubinin, M. 1947. The equation of the characteristic curve of activated charcoal. Dokl. Akad. Nauk. SSSR. pp. 327-329.

Durán-Álvarez, J.C., Prado, B., Ferroud, A., Juayerk, N., Jiménez-Cisneros, B. 2014. Sorption, desorption and displacement of ibuprofen, estrone, and 17beta estradiol in wastewater irrigated and rainfed agricultural soils. Sci Total Environ, 473-474, 189-98.

Ehtesabi, H., Bagheri, Z., Yaghoubi-Avini, M. 2019. Application of three-dimensional graphene hydrogels for removal of ofloxacin from aqueous solutions. Environmental Nanotechnology, Monitoring & Management, 12, 100274.

El Essawy, N.A., Ali, S.M., Farag, H.A., Konsowa, A.H., Elnouby, M., Hamad, H.A. 2017. Green synthesis of graphene from recycled PET bottle wastes for use in the adsorption of dyes in aqueous solution. Ecotoxicology and Environmental Safety, 145, 57-68.

Elanchezhiyan, S.S., Sivasurian, N., Meenakshi, S. 2016. Enhancement of oil recovery using zirconium-chitosan hybrid composite by adsorptive method. Carbohydrate Polymers, 145, 103-113.

Elessawy, N.A., El-Sayed, E.M., Ali, S., Elkady, M.F., Elnouby, M., Hamad, H.A. 2020. One-pot green synthesis of magnetic fullerene nanocomposite for adsorption characteristics. Journal of Water Process Engineering, 34, 101047.

Eloussaief, M., Sdiri, A., Benzina, M. 2013. Modelling the adsorption of mercury onto natural and aluminium pillared clays. Environmental Science and Pollution Research, 20(1), 469-479.

Ericson, H., Thorsén, G., Kumblad, L. 2010. Physiological effects of diclofenac, ibuprofen and propranolol on Baltic Sea blue mussels. Aquatic Toxicology, 99(2), 223-231.

Evgenidou, E.N., Konstantinou, I.K., Lambropoulou, D.A. 2015. Occurrence and removal of transformation products of PPCPs and illicit drugs in wastewaters: A review. Science of The Total Environment, 505, 905-926.

Ezechi, E.H., Isa, M.H., Muda, K., Kutty, S.R.M. 2020. A comparative evaluation of two electrode systems on continuous electrocoagulation of boron from produced water and mass transfer resistance. Journal of Water Process Engineering, 34, 101133.

Fan, L., Yang, H., Yang, J., Peng, M., Hu, J. 2016. Preparation and characterization of chitosan/gelatin/PVA hydrogel for wound dressings. Carbohydrate Polymers, 146, 427-434.

Fan, X., Peng, W., Li, Y., Li, X., Wang, S., Zhang, G., Zhang, F. 2008. Deoxygenation of Exfoliated Graphite Oxide under Alkaline Conditions: A Green Route to Graphene Preparation. Advanced Materials, 20(23), 4490-4493.

Fang, Q., Chen, B., Lin, Y., Guan, Y. 2014. Aromatic and Hydrophobic Surfaces of Wood-derived Biochar Enhance Perchlorate Adsorption via Hydrogen Bonding to Oxygen-containing Organic Groups. Environmental Science & Technology, 48(1), 279-288.

Fei, Y., Li, Y., Han, S., Ma, J. 2016. Adsorptive removal of ciprofloxacin by sodium alginate/graphene oxide composite beads from aqueous solution. Journal of Colloid and Interface Science, 484, 196-204.

Feng, L., van Hullebusch, E.D., Rodrigo, M.A., Esposito, G., Oturan, M.A. 2013. Removal of residual anti-inflammatory and analgesic pharmaceuticals from aqueous systems by electrochemical advanced oxidation processes. A review. Chemical Engineering Journal, 228, 944-964.

Feng, Z., Odelius, K., Rajarao, G.K., Hakkarainen, M. 2018. Microwave carbonized cellulose for trace pharmaceutical adsorption. Chemical Engineering Journal, 346, 557-566.

Fent, K., Weston, A.A., Caminada, D. 2006. Ecotoxicology of human pharmaceuticals. Aquatic Toxicology, 76(2), 122-59.

Fernández-Merino, M.J., Guardia, L., Paredes, J.I., Villar-Rodil, S., Solís-Fernández, P., Martínez-Alonso, A., Tascón, J.M.D. 2010. Vitamin C Is an Ideal Substitute for Hydrazine in the Reduction of Graphene Oxide Suspensions. The Journal of Physical Chemistry C, 114(14), 6426-6432.

Firdhouse, M.J., Lalitha, P. 2014. Phyto-reduction of graphene oxide using the aqueous extract of Eichhornia crassipes (Mart.) Solms. International Nano Letters, 4(4), 103-108.

Freundlich, H. 1906. Over the adsorption in solution. The Journal of Physical Chemistry, 57(385471), 1100-1107.

Fu, X., Zhan, Y., Meng, Y., Li, Y., Liao, C., Lu, Z. 2017. Graphene oxide/poly(vinyl alcohol) hydrogels with good tensile properties and reusable adsorption properties. Plastics, Rubber and Composites, 46(2), 53-59.

Fulazzaky, M.A. 2011. Determining the resistance of mass transfer for adsorption of the surfactants onto granular activated carbons from hydrodynamic column. Chemical Engineering Journal, 166(3), 832-840.

Gao, X., Jang, J., Nagase, S. 2010. Hydrazine and Thermal Reduction of Graphene Oxide: Reaction Mechanisms, Product Structures, and Reaction Design. The Journal of Physical Chemistry C, 114(2), 832-842.

Gao, Y., Li, Y., Zhang, L., Huang, H., Hu, J., Shah, S.M., Su, X. 2012. Adsorption and removal of tetracycline antibiotics from aqueous solution by graphene oxide. Journal of Colloid and Interface Science, 368(1), 540-546.

Ge, X., Shan, Y., Wu, L., Mu, X., Peng, H., Jiang, Y. 2018. High-strength and morphology-controlled aerogel based on carboxymethyl cellulose and graphene oxide. Carbohydrate Polymers, 197, 277-283.

Ghosh, D., Das, C.K. 2015. Hydrothermal Growth of Hierarchical Ni_3S_2 and Co_3S_4 on a Reduced Graphene Oxide Hydrogel@Ni Foam: A High-Energy-Density Aqueous Asymmetric Supercapacitor. ACS Applied Materials & Interfaces, 7(2), 1122-1131.

Gómez-Navarro, C., Burghard, M., Kern, K. 2008. Elastic Properties of Chemically Derived Single Graphene Sheets. Nano Letters, 8(7), 2045-2049.

Gómez-Navarro, C., Meyer, J.C., Sundaram, R.S., Chuvilin, A., Kurasch, S., Burghard, M., Kern, K., Kaiser, U. 2010. Atomic Structure of Reduced Graphene Oxide. Nano Letters, 10(4), 1144-1148.

Gracia-Lor, E., Sancho, J.V., Serrano, R., Hernández, F. 2012. Occurrence and removal of pharmaceuticals in wastewater treatment plants at the Spanish Mediterranean area of Valencia. Chemosphere, 87(5), 453-462.

Gu, D., Fein, J.B. 2015. Adsorption of metals onto graphene oxide: Surface complexation modeling and linear free energy relationships. Colloids and Surfaces A: Physicochemical and Engineering Aspects, 481, 319-327.

Guo, D., Song, X., Zhang, L., Chen, W., Chu, D., Tan, L. 2020. Recovery of uranium (VI) from aqueous solutions by the polyethyleneimine-functionalized reduced graphene oxide/molybdenum disulfide composition aerogels. Journal of the Taiwan Institute of Chemical Engineers, 106, 198-205.

Gupta, A., Garg, A. 2019. Adsorption and oxidation of ciprofloxacin in a fixed bed column using activated sludge derived activated carbon. Journal of Environmental Management, 250, 109474.

Hadi, A., Zahirifar, J., Karimi-Sabet, J., Dastbaz, A. 2018. Graphene nanosheets preparation using magnetic nanoparticle assisted liquid phase exfoliation of graphite: The coupled effect of ultrasound and wedging nanoparticles. Ultrasonics Sonochemistry, 44, 204-214.

Hall, K.R., Eagleton, L.C., Acrivos, A., Vermeulen, T. 1966. Pore- and Solid-Diffusion Kinetics in Fixed-Bed Adsorption under Constant-Pattern Conditions. Industrial & Engineering Chemistry Fundamentals, 5(2), 212-223.

Han, D., Yan, L., Chen, W., Li, W. 2011. Preparation of chitosan/graphene oxide composite film with enhanced mechanical strength in the wet state. Carbohydrate Polymers, 83(2), 653-658.

Han, Q., Yang, L., Liang, Q., Ding, M. 2017. Three-dimensional hierarchical porous graphene aerogel for efficient adsorption and preconcentration of chemical warfare agents. Carbon, 122, 556-563.

Haynes, W., Handbook, C. 2010. Chemistry and Physics, CRC Press.

He, Y., Li, J., Luo, K., Li, L., Chen, J., Li, J. 2016. Engineering Reduced Graphene Oxide Aerogel Produced by Effective γ-ray Radiation-Induced Self-Assembly and Its Application for Continuous Oil–Water Separation. Industrial & Engineering Chemistry Research, 55(13), 3775-3781.

He, Y., Liu, Y., Wu, T., Ma, J., Wang, X., Gong, Q., Kong, W., Xing, F., Liu, Y., Gao, J. 2013a. An environmentally friendly method for the fabrication of reduced graphene oxide foam with a super oil absorption capacity. Journal of Hazardous Materials, 260, 796-805.

He, Y., Zhang, N., Wu, F., Xu, F., Liu, Y., Gao, J. 2013b. Graphene oxide foams and their excellent adsorption ability for acetone gas. Materials Research Bulletin, 48(9), 3553-3558.

He, Y.Q., Zhang, N.N., Wang, X.D. 2011. Adsorption of graphene oxide/chitosan porous materials for metal ions. Chinese Chemical Letters, 22(7), 859-862.

Henriques, B., Gonçalves, G., Emami, N., Pereira, E., Vila, M., Marques, P.A.A.P. 2016. Optimized graphene oxide foam with enhanced performance and high selectivity for mercury removal from water. Journal of Hazardous Materials, 301, 453-461.

Hernando, M.D., Mezcua, M., Fernandez-Alba, A.R., Barcelo, D. 2006. Environmental risk assessment of pharmaceutical residues in wastewater effluents, surface waters and sediments. Talanta, 69(2), 334-42.

Ho, Y.S., McKay, G. 1998. Sorption of dye from aqueous solution by peat. Chemical Engineering Journal, 70(2), 115-124.

Hoan, V., Thi, N., Thu, A., Thi, N., Duc, H.V., Cuong, N.D., Quang Khieu, D., Vo, V. 2016. Fe3O4/reduced graphene oxide nanocomposite: synthesis and its application for toxic metal ion removal. Journal of Chemistry, 2016.

Hofmann, U., König, E. 1937. Untersuchungen über graphitoxyd. Zeitschrift für anorganische und allgemeine Chemie, 234(4), 311-336.

Hong, J.-Y., Sohn, E.-H., Park, S., Park, H.S. 2015. Highly-efficient and recyclable oil absorbing performance of functionalized graphene aerogel. Chemical Engineering Journal, 269, 229-235.

Hossein Beyki, M., Mohammadirad, M., Shemirani, F., Saboury, A.A. 2017. Magnetic cellulose ionomer/layered double hydroxide: An efficient anion exchange platform with enhanced diclofenac adsorption property. Carbohydrate Polymers, 157, 438-446.

Huang, M., Li, F., Dong, F., Zhang, Y.X., Zhang, L.L. 2015a. MnO_2-based nanostructures for high-performance supercapacitors. Journal of Materials Chemistry A, 3(43), 21380-21423.

Huang, T., Zhang, L., Chen, H., Gao, C. 2015b. A cross-linking graphene oxide–polyethyleneimine hybrid film containing ciprofloxacin: one-step preparation, controlled drug release and antibacterial performance. Journal of Materials Chemistry B, 3(8), 1605-1611.

Huang, X., Qian, K., Yang, J., Zhang, J., Li, L., Yu, C., Zhao, D. 2012. Functional Nanoporous Graphene Foams with Controlled Pore Sizes. Advanced Materials, 24(32), 4419-4423.

Huang, Y., Wang, M., Li, Z., Gong, Y., Zeng, E.Y. 2019. In situ remediation of mercury-contaminated soil using thiol-functionalized graphene oxide/Fe-Mn composite. Journal of Hazardous Materials, 373, 783-790.

Huang, Y., Zhang, M., Ruan, W. 2014. High-water-content graphene oxide/polyvinyl alcohol hydrogel with excellent mechanical properties. Journal of Materials Chemistry A, 2(27), 10508-10515.

Hummers, W.S., Offeman, R.E. 1958. Preparation of Graphitic Oxide. Journal of the American Chemical Society, 80(6), 1339-1339.

Hutchins, R. 1973. New Method Simplifies Design of Activated Carbon Systems. Chem. Eng., 80, 133-138.

Jang, J., Lee, D.S. 2016. Enhanced adsorption of cesium on PVA-alginate encapsulated Prussian blue-graphene oxide hydrogel beads in a fixed-bed column system. Bioresource Technology, 218, 294-300.

Jang, J., Lee, D.S. 2018. Three-dimensional barium-sulfate-impregnated reduced graphene oxide aerogel for removal of strontium from aqueous solutions. Journal of Nuclear Materials, 504, 206-214.

Jaria, G., Lourenço, M.A.O., Silva, C.P., Ferreira, P., Otero, M., Calisto, V., Esteves, V.I. 2020. Effect of the surface functionalization of a waste-derived activated carbon on pharmaceuticals' adsorption from water. Journal of Molecular Liquids, 299, 112098.

Järup, L. 2003. Hazards of heavy metal contamination. British Medical Bulletin, 68(1), 167-182.

Jauris, I.M., Matos, C.F., Saucier, C., Lima, E.C., Zarbin, A.J.G., Fagan, S.B., Machado, F.M., Zanella, I. 2016. Adsorption of sodium diclofenac on graphene: a combined experimental and theoretical study. Physical Chemistry Chemical Physics, 18(3), 1526-1536.

Jayanthi, S., KrishnaRao Eswar, N., Singh, S.A., Chatterjee, K., Madras, G., Sood, A.K. 2016. Macroporous three-dimensional graphene oxide foams for dye adsorption and antibacterial applications. RSC Advances, 6(2), 1231-1242.

Ji, J., Cooper, W.C. 1996. Nickel speciation in aqueous chloride solutions. Electrochimica Acta, 41(9), 1549-1560.

Jiang, L.-h., Liu, Y.-g., Zeng, G.-m., Xiao, F.-y., Hu, X.-j., Hu, X., Wang, H., Li, T.-t., Zhou, L., Tan, X.-f. 2016. Removal of 17β-estradiol by few-layered graphene oxide nanosheets from aqueous solutions: External influence and adsorption mechanism. Chemical Engineering Journal, 284, 93-102.

Jiang, L., Liu, Y., Liu, S., Hu, X., Zeng, G., Hu, X., Liu, S., Liu, S., Huang, B., Li, M. 2017. Fabrication of β-cyclodextrin/poly (l-glutamic acid) supported magnetic graphene oxide and its adsorption behavior for 17β-estradiol. Chemical Engineering Journal, 308, 597-605.

Jiang, S., Yu, T., Xia, R., Wang, X., Gao, M. 2019. Realization of super high adsorption capability of 2D δ-MnO_2 /GO through intra-particle diffusion. Materials Chemistry and Physics, 232, 374-381.

Jiryaei Sharahi, F., Shahbazi, A. 2017. Melamine-based dendrimer amine-modified magnetic nanoparticles as an efficient Pb(II) adsorbent for wastewater treatment: Adsorption optimization by response surface methodology. Chemosphere, 189, 291-300.

Joncour, R., Duguet, N., Métay, E., Ferreira, A., Lemaire, M. 2014. Amidation of phenol derivatives: a direct synthesis of paracetamol (acetaminophen) from hydroquinone. Green Chemistry, 16(6), 2997-3002.

Jun, B.-M., Kim, S., Kim, Y., Her, N., Heo, J., Han, J., Jang, M., Park, C.M., Yoon, Y. 2019. Comprehensive evaluation on removal of lead by graphene oxide and metal organic framework. Chemosphere, 231, 82-92.

Jung, K.-W., Jeong, T.-U., Choi, J.-W., Ahn, K.-H., Lee, S.-H. 2017. Adsorption of phosphate from aqueous solution using electrochemically modified biochar calcium-alginate beads: Batch and fixed-bed column performance. Bioresource Technology, 244, 23-32.

Kabiri, S., Tran, D.N.H., Azari, S., Losic, D. 2015. Graphene-Diatom Silica Aerogels for Efficient Removal of Mercury Ions from Water. ACS Applied Materials & Interfaces, 7(22), 11815-11823.

Karami, A., Sabouni, R., Ghommem, M. 2020. Experimental investigation of competitive co-adsorption of naproxen and diclofenac from water by an aluminum-based metal-organic framework. Journal of Molecular Liquids, 305, 112808.

Karimifard, S., Alavi Moghaddam, M.R. 2018. Application of response surface methodology in physicochemical removal of dyes from wastewater: A critical review. Science of The Total Environment, 640-641, 772-797.

Karri, R.R., Sahu, J.N. 2018. Process optimization and adsorption modeling using activated carbon derived from palm oil kernel shell for Zn (II) disposal from the aqueous environment using differential evolution embedded neural network. Journal of Molecular Liquids, 265, 592-602.

Kasprzak, K.S., Sunderman, F.W., Salnikow, K. 2003. Nickel carcinogenesis. Mutation Research/Fundamental and Molecular Mechanisms of Mutagenesis, 533(1), 67-97.

Kaur, N., Kaur, M., Singh, D. 2019. Fabrication of mesoporous nanocomposite of graphene oxide with magnesium ferrite for efficient sequestration of Ni (II) and Pb (II) ions: Adsorption, thermodynamic and kinetic studies. Environmental Pollution, 253, 111-119.

Khan, A., Wang, J., Li, J., Wang, X., Chen, Z., Alsaedi, A., Hayat, T., Chen, Y., Wang, X. 2017. The role of graphene oxide and graphene oxide-based nanomaterials in the removal of pharmaceuticals from aqueous media: a review. Environmental Science and Pollution Research, 24(9), 7938-7958.

Khazaei, M., Nasseri, S., Ganjali, M.R., Khoobi, M., Nabizadeh, R., Gholibegloo, E., Nazmara, S. 2018. Selective removal of mercury(II) from water using a 2,2-dithiodisalicylic acid-functionalized graphene oxide nanocomposite: Kinetic, thermodynamic, and reusability studies. Journal of Molecular Liquids, 265, 189-198.

Khodaverdi, E., Tekie, F.S.M., Hadizadeh, F., Esmaeel, H., Mohajeri, S.A., Tabassi, S.A.S., Zohuri, G. 2014. Hydrogels Composed of Cyclodextrin Inclusion Complexes

with PLGA-PEG-PLGA Triblock Copolymers as Drug Delivery Systems. AAPS PharmSciTech, 15(1), 177-188.

Kizito, S., Wu, S., Wandera, S.M., Guo, L., Dong, R. 2016. Evaluation of ammonium adsorption in biochar-fixed beds for treatment of anaerobically digested swine slurry: Experimental optimization and modeling. Science of The Total Environment, 563-564, 1095-1104.

Kong, Q., Preis, S., Li, L., Luo, P., Hu, Y., Wei, C. 2020a. Graphene oxide-terminated hyperbranched amino polymer-carboxymethyl cellulose ternary nanocomposite for efficient removal of heavy metals from aqueous solutions. International Journal of Biological Macromolecules, 149, 581-592.

Kong, Y., Zhuang, Y., Han, K., Shi, B. 2020b. Enhanced tetracycline adsorption using alginate-graphene-ZIF67 aerogel. Colloids and Surfaces A: Physicochemical and Engineering Aspects, 588, 124360.

Kuila, T., Bose, S., Mishra, A.K., Khanra, P., Kim, N.H., Lee, J.H. 2012. Chemical functionalization of graphene and its applications. Progress in Materials Science, 57(7), 1061-1105.

Kumar, A., Jena, H.M. 2017. Adsorption of Cr(VI) from aqueous solution by prepared high surface area activated carbon from Fox nutshell by chemical activation with H_3PO_4. Journal of Environmental Chemical Engineering, 5(2), 2032-2041.

Kuśmierek, K., Świątkowski, A. 2015. The influence of different agitation techniques on the adsorption kinetics of 4-chlorophenol on granular activated carbon. Reaction Kinetics, Mechanisms and Catalysis, 116(1), 261-271.

Kyzas, G.Z., Bikiaris, D.N., Seredych, M., Bandosz, T.J., Deliyanni, E.A. 2014. Removal of dorzolamide from biomedical wastewaters with adsorption onto graphite oxide/poly(acrylic acid) grafted chitosan nanocomposite. Bioresource Technology, 152, 399-406.

Kyzas, G.Z., Fu, J., Lazaridis, N.K., Bikiaris, D.N., Matis, K.A. 2015a. New approaches on the removal of pharmaceuticals from wastewaters with adsorbent materials. Journal of Molecular Liquids, 209, 87-93.

Kyzas, G.Z., Koltsakidou, A., Nanaki, S.G., Bikiaris, D.N., Lambropoulou, D.A. 2015b. Removal of beta-blockers from aqueous media by adsorption onto graphene oxide. Science of The Total Environment, 537, 411-420.

Lagergren, S. 1898. Handlingar. Band, 24(4), 1-39.

Lai, K.C., Lee, L.Y., Hiew, B.Y.Z., Thangalazhy-Gopakumar, S., Gan, S. 2019. Environmental application of three-dimensional graphene materials as adsorbents for dyes and heavy metals: Review on ice-templating method and adsorption mechanisms. Journal of Environmental Sciences, 79, 174-199.

Langmuir, I. 1918. The adsorption of gases on plane surfaces of glass mica and platinum. Journal of the American Chemical Society, 40(9), 1361-1403.

Lata, S., Singh, P.K., Samadder, S.R. 2015. Regeneration of adsorbents and recovery of heavy metals: a review. International Journal of Environmental Science and Technology, 12(4), 1461-1478.

Lee, C., Wei, X., Kysar, J.W., Hone, J. 2008. Measurement of the Elastic Properties and Intrinsic Strength of Monolayer Graphene. Science, 321(5887), 385.

Lee, G., Kim, B.S. 2014. Biological reduction of graphene oxide using plant leaf extracts. Biotechnology Progress, 30(2), 463-469.

Lemus, J., Moya, C., Gilarranz, M.A., Rodriguez, J.J., Palomar, J. 2017. Fixed-bed adsorption of ionic liquids onto activated carbon from aqueous phase. Journal of Environmental Chemical Engineering, 5(6), 5347-5351.

Leone, V.O., Pereira, M.C., Aquino, S.F., Oliveira, L.C.A., Correa, S., Ramalho, T.C., Gurgel, L.V.A., Silva, A.C. 2018. Adsorption of diclofenac on a magnetic adsorbent based on maghemite: experimental and theoretical studies. New Journal of Chemistry, 42(1), 437-449.

Li, C., She, M., She, X., Dai, J., Kong, L. 2014a. Functionalization of polyvinyl alcohol hydrogels with graphene oxide for potential dye removal. Journal of Applied Polymer Science, 131(3).

Li, L., Fan, L., Sun, M., Qiu, H., Li, X., Duan, H., Luo, C. 2013a. Adsorbent for chromium removal based on graphene oxide functionalized with magnetic cyclodextrin–chitosan. Colloids and Surfaces B: Biointerfaces, 107, 76-83.

Li, L., Wang, Z., Ma, P., Bai, H., Dong, W., Chen, M. 2015. Preparation of polyvinyl alcohol/chitosan hydrogel compounded with graphene oxide to enhance the adsorption properties for Cu(II) in aqueous solution. Journal of Polymer Research, 22(8), 150.

Li, L., Wei, Z., Liu, X., Yang, Y., Deng, C., Yu, Z., Guo, Z., Shi, J., Zhu, C., Guo, W., Sun, Z. 2019. Biomaterials cross-linked graphene oxide composite aerogel with a macro–nanoporous network structure for efficient Cr (VI) removal. International Journal of Biological Macromolecules, 156, 1337 – 1346.

Li, R.-X., Ren, X.-T., Tang, M.-Y., Chen, M.-X., Huang, G.-B., Fang, C.-H., Liu, T., Feng, Z.-H., Yin, Y.-B., Guo, Y.-M., Mei, S.-K., Yan, J. 2018. Fabrication of covalently linked graphene-mediated [FeFe]-hydrogenases biomimetic photocatalytic hydrogen evolution system in aqueous solution. Applied Catalysis B: Environmental, 224, 772-782.

Li, R., Chen, C., Li, J., Xu, L., Xiao, G., Yan, D. 2014b. A facile approach to superhydrophobic and superoleophilic graphene/polymer aerogels. Journal of Materials Chemistry A, 2(9), 3057-3064.

Li, W., Wang, J., Ren, J., Qu, X. 2013b. 3D Graphene Oxide–Polymer Hydrogel: Near-Infrared Light-Triggered Active Scaffold for Reversible Cell Capture and On-Demand Release. Advanced Materials, 25(46), 6737-6743.

Li, Y., Liu, S., Wang, C., Ying, Z., Huo, M., Yang, W. 2020a. Effective column adsorption of triclosan from pure water and wastewater treatment plant effluent by using magnetic porous reduced graphene oxide. Journal of Hazardous Materials, 386, 121942.

Li, Z., Chen, F., Yuan, L., Liu, Y., Zhao, Y., Chai, Z., Shi, W. 2012. Uranium(VI) adsorption on graphene oxide nanosheets from aqueous solutions. Chemical Engineering Journal, 210, 539-546.

Li, Z., Huang, X., Wu, K., Jiao, Y., Zhou, C. 2020b. Fabrication of regular macro-mesoporous reduced graphene aerogel beads with ultra-high mechanical property for efficient bilirubin adsorption. Materials Science and Engineering: C, 106, 110282.

Liang, Q., Luo, H., Geng, J., Chen, J. 2018. Facile one-pot preparation of nitrogen-doped ultra-light graphene oxide aerogel and its prominent adsorption performance of Cr(VI). Chemical Engineering Journal, 338, 62-71.

Liang, Y., Liu, J., Wang, L., Wan, Y., Shen, J., Bai, Q. 2019. Metal affinity-carboxymethyl cellulose functionalized magnetic graphene composite for highly selective isolation of histidine-rich proteins. Talanta, 195, 381-389.

Lin, J.-S., Ma, W.-T., Shih, C.-M., Yu, B.-C., Teng, L.-W., Wang, Y.-C., Cheng, K.-W., Chiu, F.-C., Lue, S.J. 2016. Reorientation of Magnetic Graphene Oxide Nanosheets in Crosslinked Quaternized Polyvinyl Alcohol as Effective Solid Electrolyte. Energies, 9(12).

Lin, X., Huang, Q., Qi, G., Shi, S., Xiong, L., Huang, C., Chen, X., Li, H., Chen, X. 2017. Estimation of fixed-bed column parameters and mathematical modeling of breakthrough behaviors for adsorption of levulinic acid from aqueous solution using SY-01 resin. Separation and Purification Technology, 174, 222-231.

Lin, Y., Xu, S., Li, J. 2013. Fast and highly efficient tetracyclines removal from environmental waters by graphene oxide functionalized magnetic particles. Chemical Engineering Journal, 225, 679-685.

Liu, C., Hao, F., Zhao, X., Zhao, Q., Luo, S., Lin, H. 2014a. Low temperature reduction of free-standing graphene oxide papers with metal iodides for ultrahigh bulk conductivity. Scientific Reports, 4, 3965.

Liu, C., Liu, H., Xu, A., Tang, K., Huang, Y., Lu, C. 2017a. In situ reduced and assembled three-dimensional graphene aerogel for efficient dye removal. Journal of Alloys and Compounds, 714, 522-529.

Liu, F.-f., Zhao, J., Wang, S., Du, P., Xing, B. 2014b. Effects of Solution Chemistry on Adsorption of Selected Pharmaceuticals and Personal Care Products (PPCPs) by Graphenes and Carbon Nanotubes. Environmental Science & Technology, 48(22), 13197-13206.

Liu, F.-F., Zhao, J., Wang, S., Xing, B. 2016a. Adsorption of sulfonamides on reduced graphene oxides as affected by pH and dissolved organic matter. Environmental Pollution, 210, 85-93.

Liu, F., Chung, S., Oh, G., Seo, T.S. 2012. Three-Dimensional Graphene Oxide Nanostructure for Fast and Efficient Water-Soluble Dye Removal. ACS Applied Materials & Interfaces, 4(2), 922-927.

Liu, J., Chu, H., Wei, H., Zhu, H., Wang, G., Zhu, J., He, J. 2016b. Facile fabrication of carboxymethyl cellulose sodium/graphene oxide hydrogel microparticles for water purification. RSC Advances, 6(55), 50061-50069.

Liu, J., Ge, X., Ye, X., Wang, G., Zhang, H., Zhou, H., Zhang, Y., Zhao, H. 2016c. 3D graphene/δ-MnO_2 aerogels for highly efficient and reversible removal of heavy metal ions. Journal of Materials Chemistry A, 4(5), 1970-1979.

Liu, L., Ding, L., Wu, X., Deng, F., Kang, R., Luo, X. 2016d. Enhancing the Hg(II) Removal Efficiency from Real Wastewater by Novel Thymine-Grafted Reduced Graphene Oxide Complexes. Industrial & Engineering Chemistry Research, 55(24), 6845-6853.

Liu, S., Yao, F., Oderinde, O., Zhang, Z., Fu, G. 2017b. Green synthesis of oriented xanthan gum–graphene oxide hybrid aerogels for water purification. Carbohydrate Polymers, 174, 392-399.

Liu, T., Wu, W., Liao, K.-N., Sun, Q., Gong, X., Roy, V.A.L., Yu, Z.-Z., Li, R.K.Y. 2019a. Fabrication of carboxymethyl cellulose and graphene oxide bio-nanocomposites for flexible nonvolatile resistive switching memory devices. Carbohydrate Polymers, 214, 213-220.

Liu, X.-w., Shen, L.-y., Hu, Y.-h. 2016e. Preparation of TiO_2-Graphene Composite by a Two-Step Solvothermal Method and its Adsorption-Photocatalysis Property. Water, Air, & Soil Pollution, 227(5), 141.

Liu, Y., Liu, R., Li, M., Yu, F., He, C. 2019b. Removal of pharmaceuticals by novel magnetic genipin-crosslinked chitosan/graphene oxide-SO3H composite. Carbohydrate Polymers, 220, 141-148.

Lonappan, L., Brar, S.K., Das, R.K., Verma, M., Surampalli, R.Y. 2016. Diclofenac and its transformation products: Environmental occurrence and toxicity - A review. Environment International, 96, 127-138.

Lonappan, L., Rouissi, T., Kaur Brar, S., Verma, M., Surampalli, R.Y. 2018. An insight into the adsorption of diclofenac on different biochars: Mechanisms, surface chemistry, and thermodynamics. Bioresource Technology, 249, 386-394.

Low, M.J.D. 1960. Kinetics of Chemisorption of Gases on Solids. Chemical Reviews, 60(3), 267-312.

Luan, V.H., Chung, J.S., Hur, S.H. 2015. Preparation of a reduced graphene oxide hydrogel by Ni ions and its use in a supercapacitor electrode. RSC Advances, 5(29), 22753-22758.

Luo, J., Fan, C., Xiao, Z., Sun, T., Zhou, X. 2019. Novel graphene oxide/carboxymethyl chitosan aerogels via vacuum-assisted self-assembly for heavy metal adsorption capacity. Colloids and Surfaces A: Physicochemical and Engineering Aspects, 578, 123584.

Ma, J., Jiang, Z., Cao, J., Yu, F. 2020. Enhanced adsorption for the removal of antibiotics by carbon nanotubes/graphene oxide/sodium alginate triple-network nanocomposite hydrogels in aqueous solutions. Chemosphere, 242, 125188.

Ma, Z., Liu, D., Zhu, Y., Li, Z., Li, Z., Tian, H., Liu, H. 2016. Graphene oxide/chitin nanofibril composite foams as column adsorbents for aqueous pollutants. Carbohydrate Polymers, 144, 230-237.

Madadrang, C.J., Kim, H.Y., Gao, G., Wang, N., Zhu, J., Feng, H., Gorring, M., Kasner, M.L., Hou, S. 2012. Adsorption Behavior of EDTA-Graphene Oxide for Pb (II) Removal. ACS Applied Materials & Interfaces, 4(3), 1186-1193.

Mahdi, Z., Yu, Q.J., El Hanandeh, A. 2018. Investigation of the kinetics and mechanisms of nickel and copper ions adsorption from aqueous solutions by date seed derived biochar. Journal of Environmental Chemical Engineering, 6(1), 1171-1181.

Mahmoud, M.E., Osman, M.M., Abdel-Aal, H., Nabil, G.M. 2020. Microwave-assisted adsorption of Cr(VI), Cd(II) and Pb(II) in presence of magnetic graphene oxide-covalently functionalized-tryptophan nanocomposite. Journal of Alloys and Compounds, 823, 153855.

Mallaiah, M., Reddy, G.V. 2016. Optimization studies on a continuous catalytic reactive distillation column for methyl acetate production with response surface methodology. Journal of the Taiwan Institute of Chemical Engineers, 69, 25-40.

Marin, P., Bergamasco, R., Módenes, A.N., Paraiso, P.R., Hamoudi, S. 2019. Synthesis and characterization of graphene oxide functionalized with $MnFe_2O_4$ and supported on activated carbon for glyphosate adsorption in fixed bed column. Process Safety and Environmental Protection, 123, 59-71.

MEP. 1998. Integrated wastewater discharge standard, (Ed.) Ministry of the Environment Protection the People's Republic of China.

Michel, C., Barré, Y., Ben Guiza, M., de Dieuleveult, C., De Windt, L., Grandjean, A. 2018. Breakthrough studies of the adsorption of Cs from freshwater using a mesoporous silica material containing ferrocyanide. Chemical Engineering Journal, 339, 288-295.

Mohammed, A.A., Kareem, S.L. 2019. Adsorption of tetracycline from wastewater by using Pistachio shell coated with ZnO nanoparticles: Equilibrium, kinetic and isotherm studies. Alexandria Engineering Journal, 58(3), 917-928.

Mohan, S., Singh, D.K., Kumar, V., Hasan, S.H. 2017. Modelling of fixed bed column containing graphene oxide decorated by MgO nanocubes as adsorbent for Lead(II) removal from water. Journal of Water Process Engineering, 17, 216-228.

Mousavi, S.J., Parvini, M., Ghorbani, M. 2018. Adsorption of heavy metals (Cu^{2+} and Zn^{2+}) on novel bifunctional ordered mesoporous silica: Optimization by response surface methodology. Journal of the Taiwan Institute of Chemical Engineers, 84, 123-141.

Moussa, M., Zhao, Z., El-Kady, M.F., Liu, H., Michelmore, A., Kawashima, N., Majewski, P., Ma, J. 2015. Free-standing composite hydrogel films for superior volumetric capacitance. Journal of Materials Chemistry A, 3(30), 15668-15674.

Najafi, F., Moradi, O., Rajabi, M., Asif, M., Tyagi, I., Agarwal, S., Gupta, V.K. 2015. Thermodynamics of the adsorption of nickel ions from aqueous phase using graphene oxide and glycine functionalized graphene oxide. Journal of Molecular Liquids, 208, 106-113.

Nam, S.-W., Jung, C., Li, H., Yu, M., Flora, J.R.V., Boateng, L.K., Her, N., Zoh, K.-D., Yoon, Y. 2015. Adsorption characteristics of diclofenac and sulfamethoxazole to graphene oxide in aqueous solution. Chemosphere, 136, 20-26.

Nasiri, R., Arsalani, N., Panahian, Y. 2018. One-pot synthesis of novel magnetic three-dimensional graphene/chitosan/nickel ferrite nanocomposite for lead ions removal from aqueous solution: RSM modelling design. Journal of Cleaner Production, 201, 507-515.

Nithya, K., Sathish, A., Kumar, P.S. 2020. Packed bed column optimization and modeling studies for removal of chromium ions using chemically modified Lantana camara adsorbent. Journal of Water Process Engineering, 33, 101069.

Nourmoradi, H., Moghadam, K.F., Jafari, A., Kamarehie, B. 2018. Removal of acetaminophen and ibuprofen from aqueous solutions by activated carbon derived from Quercus Brantii (Oak) acorn as a low-cost biosorbent. Journal of Environmental Chemical Engineering, 6(6), 6807-6815.

Ocsoy, I., Temiz, M., Celik, C., Altinsoy, B., Yilmaz, V., Duman, F. 2017. A green approach for formation of silver nanoparticles on magnetic graphene oxide and highly effective antimicrobial activity and reusability. Journal of Molecular Liquids, 227, 147-152.

Oh, W.-D., Lee, M.G.H., Chanaka Udayanga, W.D., Veksha, A., Bao, Y., Giannis, A., Lim, J.-W., Lisak, G. 2019. Insights into the single and binary adsorption of copper(II) and nickel(II) on hexagonal boron nitride: Performance and mechanistic studies. Journal of Environmental Chemical Engineering, 7(1), 102872.

Oh, Y.J., Yoo, J.J., Kim, Y.I., Yoon, J.K., Yoon, H.N., Kim, J.-H., Park, S.B. 2014. Oxygen functional groups and electrochemical capacitive behavior of incompletely

reduced graphene oxides as a thin-film electrode of supercapacitor. Electrochimica Acta, 116, 118-128.

Ooi, J., Lee, L.Y., Hiew, B.Y.Z., Thangalazhy-Gopakumar, S., Lim, S.S., Gan, S. 2017. Assessment of fish scales waste as a low cost and eco-friendly adsorbent for removal of an azo dye: Equilibrium, kinetic and thermodynamic studies. Bioresource Technology, 245, 656-664.

Ouyang, A., Wang, C., Wu, S., Shi, E., Zhao, W., Cao, A., Wu, D. 2015. Highly Porous Core–Shell Structured Graphene-Chitosan Beads. ACS Applied Materials & Interfaces, 7(26), 14439-14445.

Park, S., An, J., Potts, J.R., Velamakanni, A., Murali, S., Ruoff, R.S. 2011. Hydrazine-reduction of graphite- and graphene oxide. Carbon, 49(9), 3019-3023.

Park, S., Lee, K.-S., Bozoklu, G., Cai, W., Nguyen, S.T., Ruoff, R.S. 2008. Graphene Oxide Papers Modified by Divalent Ions—Enhancing Mechanical Properties via Chemical Cross-Linking. ACS Nano, 2(3), 572-578.

Park, S., Ruoff, R.S. 2009. Chemical methods for the production of graphenes. Nature Nano, 4(4), 217-224.

Patiño, Y., Díaz, E., Ordóñez, S., Gallegos-Suarez, E., Guerrero-Ruiz, A., Rodríguez-Ramos, I. 2015. Adsorption of emerging pollutants on functionalized multiwall carbon nanotubes. Chemosphere, 136, 174-180.

Patrolecco, L., Ademollo, N., Grenni, P., Tolomei, A., Barra Caracciolo, A., Capri, S. 2013. Simultaneous determination of human pharmaceuticals in water samples by solid phase extraction and HPLC with UV-fluorescence detection. Microchemical Journal, 107, 165-171.

Pazani, F., Aroujalian, A. 2020. Enhanced CO_2-selective behavior of Pebax-1657: A comparative study between the influence of graphene-based fillers. Polymer Testing, 81, 106264.

Pei, S., Cheng, H.-M. 2012. The reduction of graphene oxide. Carbon, 50(9), 3210-3228.

Peng, A., Huang, M., Chen, Z., Gu, C. 2017a. Oxidative coupling of acetaminophen mediated by Fe3+-saturated montmorillonite. Science of The Total Environment, 595, 673-680.

Peng, W., Li, H., Hu, Y., Liu, Y., Song, S. 2016a. Does silicate mineral impurities in natural graphite affect the characteristics of synthesized graphene? Materials Research Bulletin, 74, 333-339.

Peng, W., Li, H., Liu, Y., Song, S. 2016b. Comparison of Pb(II) adsorption onto graphene oxide prepared from natural graphites: Diagramming the Pb(II) adsorption sites. Applied Surface Science, 364, 620-627.

Peng, W., Li, H., Liu, Y., Song, S. 2017b. A review on heavy metal ions adsorption from water by graphene oxide and its composites. Journal of Molecular Liquids, 230, 496-504.

Pinalli, R., Dalcanale, E., Misztal, K., Lucentini, R., Ugozzoli, F., Massera, C. 2018. Metal ion complexation by tetraphosphonate cavitands: The influence of the ionic radius. Inorganica Chimica Acta, 470, 250-253.

Platero, E., Fernandez, M.E., Bonelli, P.R., Cukierman, A.L. 2017. Graphene oxide/alginate beads as adsorbents: Influence of the load and the drying method on their

physicochemical-mechanical properties and adsorptive performance. Journal of Colloid and Interface Science, 491, 1-12.

Portinho, R., Zanella, O., Féris, L.A. 2017. Grape stalk application for caffeine removal through adsorption. Journal of Environmental Management, 202, 178-187.

Pourbeyram, S. 2016. Effective Removal of Heavy Metals from Aqueous Solutions by Graphene Oxide–Zirconium Phosphate (GO–Zr-P) Nanocomposite. Industrial & Engineering Chemistry Research, 55(19), 5608-5617.

Puangjan, A., Chaiyasith, S. 2016. An efficient ZrO_2/Co_3O_4/reduced graphene oxide nanocomposite electrochemical sensor for simultaneous determination of gallic acid, caffeic acid and protocatechuic acid natural antioxidants. Electrochimica Acta, 211, 273-288.

Qiao, L., Li, S., Li, Y., Liu, Y., Du, K. 2020. Fabrication of superporous cellulose beads via enhanced inner cross-linked linkages for high efficient adsorption of heavy metal ions. Journal of Cleaner Production, 253, 120017.

Quesada, H.B., Baptista, A.T.A., Cusioli, L.F., Seibert, D., de Oliveira Bezerra, C., Bergamasco, R. 2019. Surface water pollution by pharmaceuticals and an alternative of removal by low-cost adsorbents: A review. Chemosphere, 222, 766-780.

Rahman, M.F., Yanful, E.K., Jasim, S.Y. 2009. Occurrences of endocrine disrupting compounds and pharmaceuticals in the aquatic environment and their removal from drinking water: Challenges in the context of the developing world. Desalination, 248(1-3), 578-585.

Rahmani, Z., Rashidi, A.M., kazemi, A., Samadi, M.T., Rahmani, A.R. 2018. N-doped reduced graphene oxide aerogel for the selective adsorption of oil pollutants from water:

Isotherm and kinetic study. Journal of Industrial and Engineering Chemistry, 61, 416-426.

Rao, Z., Ge, H., Liu, L., Zhu, C., Min, L., Liu, M., Fan, L., Li, D. 2018. Carboxymethyl cellulose modified graphene oxide as pH-sensitive drug delivery system. International Journal of Biological Macromolecules, 107, 1184-1192.

Rashidi Nodeh, H., Sereshti, H. 2016. Synthesis of magnetic graphene oxide doped with strontium titanium trioxide nanoparticles as a nanocomposite for the removal of antibiotics from aqueous media. RSC Advances, 6(92), 89953-89965.

Rasoulzadeh, M., Namazi, H. 2017. Carboxymethyl cellulose/graphene oxide bio-nanocomposite hydrogel beads as anticancer drug carrier agent. Carbohydrate Polymers, 168, 320-326.

Reynel-Avila, H.E., Mendoza-Castillo, D.I., Bonilla-Petriciolet, A., Silvestre-Albero, J. 2015. Assessment of naproxen adsorption on bone char in aqueous solutions using batch and fixed-bed processes. Journal of Molecular Liquids, 209, 187-195.

Rivera-Utrilla, J., Sanchez-Polo, M., Ferro-Garcia, M.A., Prados-Joya, G., Ocampo-Perez, R. 2013. Pharmaceuticals as emerging contaminants and their removal from water. A review. Chemosphere, 93(7), 1268-87.

Rostamian, R., Behnejad, H. 2016. A comparative adsorption study of sulfamethoxazole onto graphene and graphene oxide nanosheets through equilibrium, kinetic and thermodynamic modeling. Process Safety and Environmental Protection, 102, 20-29.

Ruthven, D.M. 1984. Principles of adsorption and adsorption processes. John Wiley & Sons.

Sadhukhan, B., Mondal, N.K., Chattoraj, S. 2016. Optimisation using central composite design (CCD) and the desirability function for sorption of methylene blue from aqueous solution onto Lemna major. Karbala International Journal of Modern Science, 2(3), 145-155.

Saharan, P., Sharma, A.K., Kumar, V., Kaushal, I. 2019. Multifunctional CNT supported metal doped MnO2 composite for adsorptive removal of anionic dye and thiourea sensing. Materials Chemistry and Physics, 221, 239-249.

Sahraei, R., Ghaemy, M. 2017. Synthesis of modified gum tragacanth/graphene oxide composite hydrogel for heavy metal ions removal and preparation of silver nanocomposite for antibacterial activity. Carbohydrate Polymers, 157, 823-833.

Sahraei, R., Sekhavat Pour, Z., Ghaemy, M. 2017. Novel magnetic bio-sorbent hydrogel beads based on modified gum tragacanth/graphene oxide: Removal of heavy metals and dyes from water. Journal of Cleaner Production, 142, 2973-2984.

Saleem, H., Haneef, M., Abbasi, H.Y. 2018. Synthesis route of reduced graphene oxide via thermal reduction of chemically exfoliated graphene oxide. Materials Chemistry and Physics, 204, 1-7.

Samah, N.A., Sánchez-Martín, M.-J., Sebastián, R.M., Valiente, M., López-Mesas, M. 2018. Molecularly imprinted polymer for the removal of diclofenac from water: Synthesis and characterization. Science of The Total Environment, 631-632, 1534-1543.

Santos, J.L., Aparicio, I., Alonso, E. 2007. Occurrence and risk assessment of pharmaceutically active compounds in wastewater treatment plants. A case study: Seville city (Spain). Environment International, 33(4), 596-601.

Sapkota, A., Sapkota, A.R., Kucharski, M., Burke, J., McKenzie, S., Walker, P., Lawrence, R. 2008. Aquaculture practices and potential human health risks: current knowledge and future priorities. Environ Int, 34(8), 1215-26.

Sathishkumar, P., Meena, R.A.A., Palanisami, T., Ashokkumar, V., Palvannan, T., Gu, F.L. 2020. Occurrence, interactive effects and ecological risk of diclofenac in environmental compartments and biota - a review. Science of The Total Environment, 698, 134057.

Saucier, C., Adebayo, M.A., Lima, E.C., Cataluña, R., Thue, P.S., Prola, L.D.T., Puchana-Rosero, M.J., Machado, F.M., Pavan, F.A., Dotto, G.L. 2015. Microwave-assisted activated carbon from cocoa shell as adsorbent for removal of sodium diclofenac and nimesulide from aqueous effluents. Journal of Hazardous Materials, 289, 18-27.

Sausen, M.G., Scheufele, F.B., Alves, H.J., Vieira, M.G.A., da Silva, M.G.C., Borba, F.H., Borba, C.E. 2018. Efficiency maximization of fixed-bed adsorption by applying hybrid statistical-phenomenological modeling. Separation and Purification Technology, 207, 477-488.

Schafer, A.I., Akanyeti, I., Semiao, A.J. 2011. Micropollutant sorption to membrane polymers: a review of mechanisms for estrogens. Adv Colloid Interface Sci, 164(1-2), 100-17.

Shakoor, M.B., Niazi, N.K., Bibi, I., Shahid, M., Sharif, F., Bashir, S., Shaheen, S.M., Wang, H., Tsang, D.C.W., Ok, Y.S., Rinklebe, J. 2018. Arsenic removal by natural and chemically modified water melon rind in aqueous solutions and groundwater. Science of The Total Environment, 645, 1444-1455.

Shan, D., Deng, S., Li, J., Wang, H., He, C., Cagnetta, G., Wang, B., Wang, Y., Huang, J., Yu, G. 2017. Preparation of porous graphene oxide by chemically intercalating a rigid molecule for enhanced removal of typical pharmaceuticals. Carbon, 119, 101-109.

Shan, H., Li, X., Cui, Y., Xiong, D., Yan, B., Li, D., Lushington, A., Sun, X. 2016. Sulfur/Nitrogen Dual-doped Porous Graphene Aerogels Enhancing Anode Performance of Lithium Ion Batteries. Electrochimica Acta, 205, 188-197.

Shao, L., Chang, X., Zhang, Y., Huang, Y., Yao, Y., Guo, Z. 2013. Graphene oxide cross-linked chitosan nanocomposite membrane. Applied Surface Science, 280, 989-992.

Sharifi, H., Zabihzadeh, S.M., Ghorbani, M. 2018. The application of response surface methodology on the synthesis of conductive polyaniline/cellulosic fiber nanocomposites. Carbohydrate Polymers, 194, 384-394.

Shehzad, K., Xu, Y., Gao, C., Duan, X. 2016. Three-dimensional macro-structures of two-dimensional nanomaterials. Chemical Society Reviews, 45(20), 5541-5588.

Sheikhmohammadi, A., Mohseni, S.M., khodadadi, R., Sardar, M., Abtahi, M., Mahdavi, S., Keramati, H., Dahaghin, Z., Rezaei, S., Almasian, M., Sarkhosh, M., Faraji, M., Nazari, S. 2017. Application of graphene oxide modified with 8-hydroxyquinoline for the adsorption of Cr (VI) from wastewater: Optimization, kinetic, thermodynamic and equilibrium studies. Journal of Molecular Liquids, 233, 75-88.

Sheng, L., Zhang, Y., Tang, F., Liu, S. 2018. Mesoporous/microporous silica materials: Preparation from natural sands and highly efficient fixed-bed adsorption of methylene blue in wastewater. Microporous and Mesoporous Materials, 257, 9-18.

Singh, D.K., Kumar, V., Mohan, S., Bano, D., Hasan, S.H. 2017. Breakthrough curve modeling of graphene oxide aerogel packed fixed bed column for the removal of Cr(VI) from water. Journal of Water Process Engineering, 18, 150-158.

Singh, R.K., Kumar, R., Singh, D.P. 2016. Graphene oxide: strategies for synthesis, reduction and frontier applications. RSC Advances, 6(69), 64993-65011.

Sires, I., Brillas, E. 2012. Remediation of water pollution caused by pharmaceutical residues based on electrochemical separation and degradation technologies: a review. Environment International, 40, 212-29.

Sitko, R., Musielak, M., Zawisza, B., Talik, E., Gagor, A. 2016. Graphene oxide/cellulose membranes in adsorption of divalent metal ions. RSC Advances, 6(99), 96595-96605.

Sitko, R., Turek, E., Zawisza, B., Malicka, E., Talik, E., Heimann, J., Gagor, A., Feist, B., Wrzalik, R. 2013. Adsorption of divalent metal ions from aqueous solutions using graphene oxide. Dalton Transactions, 42(16), 5682-5689.

Soleymani, A.R., Mahdiei, M., Haerifar, M. 2019. Nano-titania/light expanded clay aggregate fixed bed as an effective adsorbent for removal of organic pollutant from water: Equilibrium and kinetic studies. Journal of Cleaner Production, 211, 1328-1338.

Song, C., Guo, B.-B., Sun, X.-F., Wang, S.-G., Li, Y.-T. 2019a. Enrichment and degradation of tetracycline using three-dimensional graphene/MnO2 composites. Chemical Engineering Journal, 358, 1139-1146.

Song, N., Wu, Y., Wang, W., Xiao, D., Tan, H., Zhao, Y. 2019b. Layer-by-layer in situ growth flexible polyaniline/graphene paper wrapped by MnO_2 nanoflowers for all-solid-state supercapacitor. Materials Research Bulletin, 111, 267-276.

Song, Q., Wang, H., Yang, B., Wang, F., Sun, X. 2016a. A novel adsorbent of Ag-FMWCNTs for the removal of SMX from aqueous solution. RSC Advances, 6(79), 75855-75861.

Song, S.-T., Hau, Y.-F., Saman, N., Johari, K., Cheu, S.-C., Kong, H., Mat, H. 2016b. Process analysis of mercury adsorption onto chemically modified rice straw in a fixed-bed adsorber. Journal of Environmental Chemical Engineering, 4(2), 1685-1697.

Song, Z., Ma, Y.-L., Li, C.-E. 2019c. The residual tetracycline in pharmaceutical wastewater was effectively removed by using MnO_2/graphene nanocomposite. Science of The Total Environment, 651, 580-590.

Speyer, L., Fontana, S., Ploneis, S., Hérold, C. 2017. Influence of the precursor alcohol on the adsorptive properties of graphene foams elaborated by a solvothermal-based process. Microporous and Mesoporous Materials, 243, 254-262.

Sreeprasad, T.S., Berry, V. 2013. How Do the Electrical Properties of Graphene Change with its Functionalization? Small, 9(3), 341-350.

Staudenmaier, L. 1898. Verfahren zur darstellung der graphitsäure. Berichte der deutschen chemischen Gesellschaft, 31(2), 1481-1487.

Su, H., Ye, Z., Hmidi, N. 2017. High-performance iron oxide–graphene oxide nanocomposite adsorbents for arsenic removal. Colloids and Surfaces A: Physicochemical and Engineering Aspects, 522, 161-172.

Sui, Z.-Y., Cui, Y., Zhu, J.-H., Han, B.-H. 2013. Preparation of Three-Dimensional Graphene Oxide–Polyethylenimine Porous Materials as Dye and Gas Adsorbents. ACS Applied Materials & Interfaces, 5(18), 9172-9179.

Suk, J.W., Piner, R.D., An, J., Ruoff, R.S. 2010. Mechanical Properties of Monolayer Graphene Oxide. ACS Nano, 4(11), 6557-6564.

Sumalinog, D.A.G., Capareda, S.C., de Luna, M.D.G. 2018. Evaluation of the effectiveness and mechanisms of acetaminophen and methylene blue dye adsorption on activated biochar derived from municipal solid wastes. Journal of Environmental Management, 210, 255-262.

Sun, G., Zhang, X., Bao, Z., Lang, X., Zhou, Z., Li, Y., Feng, C., Chen, X. 2018a. Reinforcement of thermoplastic chitosan hydrogel using chitin whiskers optimized with response surface methodology. Carbohydrate Polymers, 189, 280-288.

Sun, J., Luo, Q., Wang, D., Wang, Z. 2015. Occurrences of pharmaceuticals in drinking water sources of major river watersheds, China. Ecotoxicology and Environmental Safety, 117, 132-140.

Sun, K., Dong, S., Sun, Y., Gao, B., Du, W., Xu, H., Wu, J. 2018b. Graphene oxide-facilitated transport of levofloxacin and ciprofloxacin in saturated and unsaturated porous media. Journal of Hazardous Materials, 348, 92-99.

Sun, Y., Yang, Y., Yang, M., Yu, F., Ma, J. 2019. Response surface methodological evaluation and optimization for adsorption removal of ciprofloxacin onto graphene hydrogel. Journal of Molecular Liquids, 284, 124-130.

Suresh, D., Nethravathi, P.C., Udayabhanu, Nagabhushana, H., Sharma, S.C. 2015. Spinach assisted green reduction of graphene oxide and its antioxidant and dye absorption properties. Ceramics International, 41(3, Part B), 4810-4813.

Tan, L., Xu, J., Xue, X., Lou, Z., Zhu, J., Baig, S.A., Xu, X. 2014. Multifunctional nanocomposite Fe_3O_4@SiO_2–mPD/SP for selective removal of Pb(ii) and Cr(vi) from aqueous solutions. RSC Advances, 4(86), 45920-45929.

Tan, P., Wen, J., Hu, Y., Tan, X. 2016. Adsorption of Cu2+ and Cd2+ from aqueous solution by novel electrospun poly(vinyl alcohol)/graphene oxide nanofibers. RSC Advances, 6(83), 79641-79650.

Tang, M., Wu, Y., Yang, J., Xue, Y. 2020. Hierarchical core-shell fibers of graphene fiber/radially-aligned molybdenum disulfide nanosheet arrays for highly efficient energy storage. Journal of Alloys and Compounds, 828, 153622.

Temkin, M., Pyzhev, V. 1940. Recent modifications to Langmuir isotherms.

Thomas, H.C. 1944. Heterogeneous Ion Exchange in a Flowing System. Journal of the American Chemical Society, 66(10), 1664-1666.

Tiwari, B., Sellamuthu, B., Ouarda, Y., Drogui, P., Tyagi, R.D., Buelna, G. 2017. Review on fate and mechanism of removal of pharmaceutical pollutants from wastewater using biological approach. Bioresource Technology, 224, 1-12.

Tortet, L., Ligner, E., Blanluet, W., Noguez, P., Marichal, C., Schäf, O., Paillaud, J.-L. 2017. Adsorptive elimination of paracetamol from physiological solutions: Interaction with MFI-type zeolite. Microporous and Mesoporous Materials, 252, 188-196.

Tyszczuk-Rotko, K., Jaworska, I., Jędruchniewicz, K. 2019. Application of unmodified boron-doped diamond electrode for determination of dopamine and paracetamol. Microchemical Journal, 146, 664-672.

Umbreen, N., Sohni, S., Ahmad, I., Khattak, N.U., Gul, K. 2018. Self-assembled three-dimensional reduced graphene oxide-based hydrogel for highly efficient and facile

removal of pharmaceutical compounds from aqueous solution. Journal of Colloid and Interface Science, 527, 356-367.

USEPA. 2009. National Primary Drinking Water Regulations, (Ed.) U.S.E.P. Agency. United States.

Varaprasad, K., Jayaramudu, T., Sadiku, E.R. 2017. Removal of dye by carboxymethyl cellulose, acrylamide and graphene oxide via a free radical polymerization process. Carbohydrate Polymers, 164, 186-194.

Vicente-Martínez, Y., Caravaca, M., Soto-Meca, A., De Francisco-Ortiz, O., Gimeno, F. 2020. Graphene oxide and graphene oxide functionalized with silver nanoparticles as adsorbents of phosphates in waters. A comparative study. Science of The Total Environment, 709, 136111.

Volesky, B., Holan, Z.R. 1995. Biosorption of heavy metals. Biotechnology Progress, 11(3), 235-250.

Vu, H.C., Dwivedi, A.D., Le, T.T., Seo, S.-H., Kim, E.-J., Chang, Y.-S. 2017. Magnetite graphene oxide encapsulated in alginate beads for enhanced adsorption of Cr(VI) and As(V) from aqueous solutions: Role of crosslinking metal cations in pH control. Chemical Engineering Journal, 307, 220-229.

Vunain, E., Mishra, A.K., Mamba, B.B. 2016. Dendrimers, mesoporous silicas and chitosan-based nanosorbents for the removal of heavy-metal ions: A review. International Journal of Biological Macromolecules, 86, 570-586.

Vuong Hoan, N.T., Anh Thu, N.T., Duc, H.V., Cuong, N.D., Quang Khieu, D., Vo, V. 2016. Fe3O4/Reduced Graphene Oxide Nanocomposite: Synthesis and Its Application for Toxic Metal Ion Removal. Journal of Chemistry, 2016, 10.

Wan, W., Zhang, F., Yu, S., Zhang, R., Zhou, Y. 2016. Hydrothermal formation of graphene aerogel for oil sorption: the role of reducing agent, reaction time and temperature. New Journal of Chemistry, 40(4), 3040-3046.

Wang, B., Zhang, F., He, S., Huang, F., Peng, Z. 2014. Adsorption behaviour of reduced graphene oxide for removal of heavy metal ions. Asian Journal of Chemistry, 26(15), 4901-4906.

Wang, F., Li, H., Liu, Q., Li, Z., Li, R., Zhang, H., Liu, L., Emelchenko, G.A., Wang, J. 2016. A graphene oxide/amidoxime hydrogel for enhanced uranium capture. 6, 19367.

Wang, G., Wang, B., Park, J., Yang, J., Shen, X., Yao, J. 2009. Synthesis of enhanced hydrophilic and hydrophobic graphene oxide nanosheets by a solvothermal method. Carbon, 47(1), 68-72.

Wang, J., Chen, C. 2006. Biosorption of heavy metals by Saccharomyces cerevisiae: A review. Biotechnology Advances, 24(5), 427-451.

Wang, J., Salihi, E.C., Šiller, L. 2017a. Green reduction of graphene oxide using alanine. Materials Science and Engineering: C, 72, 1-6.

Wang, J., Wang, S. 2016. Removal of pharmaceuticals and personal care products (PPCPs) from wastewater: A review. Journal of Environmental Management, 182, 620-640.

Wang, J., Yao, Q., Sheng, C., Jin, C., Sun, Q. 2017b. One-step preparation of graphene oxide/cellulose nanofibril hybrid aerogel for adsorptive removal of four kinds of antibiotics. Journal of Nanomaterials, 2017.

Wang, J., Yao, Q., Sheng, C., Jin, C., Sun, Q. 2017c. One-Step Preparation of Graphene Oxide/Cellulose Nanofibril Hybrid Aerogel for Adsorptive Removal of Four Kinds of Antibiotics. Journal of Nanomaterials, 10.

Wang, S., Sun, H., Ang, H.M., Tadé, M.O. 2013. Adsorptive remediation of environmental pollutants using novel graphene-based nanomaterials. Chemical Engineering Journal, 226, 336-347.

Wang, W., Cai, K., Wu, X., Shao, X., Yang, X. 2017d. A novel poly(m-phenylenediamine)/reduced graphene oxide/nickel ferrite magnetic adsorbent with excellent removal ability of dyes and Cr(VI). Journal of Alloys and Compounds, 722, 532-543.

Wang, X., Yin, R., Zeng, L., Zhu, M. 2019. A review of graphene-based nanomaterials for removal of antibiotics from aqueous environments. Environmental Pollution, 253, 100-110.

Wang, Y., Shi, Z., Yin, J. 2011. Facile Synthesis of Soluble Graphene via a Green Reduction of Graphene Oxide in Tea Solution and Its Biocomposites. ACS Applied Materials & Interfaces, 3(4), 1127-1133.

Weber, W.J., Morris, J.C. 1963. Kinetics of adsorption on carbon from solution. Journal of the sanitary engineering division, 89(2), 31-60.

White, R.L., White, C.M., Turgut, H., Massoud, A., Tian, Z.R. 2018. Comparative studies on copper adsorption by graphene oxide and functionalized graphene oxide nanoparticles. Journal of the Taiwan Institute of Chemical Engineers, 85, 18-28.

WHO. 2011. Guidelines for Drinking-water Quality. 4th ed, (Ed.) W.H. Organization.

Witek-Krowiak, A., Chojnacka, K., Podstawczyk, D., Dawiec, A., Pokomeda, K. 2014. Application of response surface methodology and artificial neural network methods in modelling and optimization of biosorption process. Bioresource Technology, 160, 150-160.

Wong, S., Lim, Y., Ngadi, N., Mat, R., Hassan, O., Inuwa, I.M., Mohamed, N.B., Low, J.H. 2018. Removal of acetaminophen by activated carbon synthesized from spent tea leaves: equilibrium, kinetics and thermodynamics studies. Powder Technology, 338, 878-886.

Worsley, M.A., Kucheyev, S.O., Mason, H.E., Merrill, M.D., Mayer, B.P., Lewicki, J., Valdez, C.A., Suss, M.E., Stadermann, M., Pauzauskie, P.J., Satcher, J.H., Biener, J., Baumann, T.F. 2012. Mechanically robust 3D graphene macroassembly with high surface area. Chemical Communications, 48(67), 8428-8430.

Wu, R., Yu, B., Liu, X., Li, H., Wang, W., Chen, L., Bai, Y., Ming, Z., Yang, S.-T. 2016. One-pot hydrothermal preparation of graphene sponge for the removal of oils and organic solvents. Applied Surface Science, 362, 56-62.

Wu, S., Zhang, K., Wang, X., Jia, Y., Sun, B., Luo, T., Meng, F., Jin, Z., Lin, D., Shen, W., Kong, L., Liu, J. 2015. Enhanced adsorption of cadmium ions by 3D sulfonated reduced graphene oxide. Chemical Engineering Journal, 262, 1292-1302.

Wu, S., Zhao, X., Li, Y., Zhao, C., Du, Q., Sun, J., Wang, Y., Peng, X., Xia, Y., Wang, Z., Xia, L. 2013. Adsorption of ciprofloxacin onto biocomposite fibers of graphene oxide/calcium alginate. Chemical Engineering Journal, 230, 389-395.

Wu, Y., Luo, H., Wang, H., Zhang, L., Liu, P., Feng, L. 2014. Fast adsorption of nickel ions by porous graphene oxide/sawdust composite and reuse for phenol degradation from aqueous solutions. Journal of Colloid and Interface Science, 436, 90-98.

Wu, Z.-S., Yang, S., Sun, Y., Parvez, K., Feng, X., Müllen, K. 2012. 3D nitrogen-doped graphene aerogel-supported Fe_3O_4 nanoparticles as efficient electrocatalysts for the oxygen reduction reaction. Journal of the American Chemical Society, 134(22), 9082-9085.

Wu, Z., Huang, W., Shan, X., Li, Z. 2020. Preparation of a porous graphene oxide/alkali lignin aerogel composite and its adsorption properties for methylene blue. International Journal of Biological Macromolecules, 143, 325-333.

Xiang, C., Guo, R., Lan, J., Jiang, S., Wang, C., Du, Z., Cheng, C. 2018. Self-assembling porous 3D titanium dioxide-reduced graphene oxide aerogel for the tunable absorption of oleic acid and RhodamineB dye. Journal of Alloys and Compounds, 735, 246-252.

Xie, Y., Zhan, Y. 2015. Electrochemical capacitance of porous reduced graphene oxide/nickel foam. Journal of Porous Materials, 22(2), 403-412.

Xing, H.T., Chen, J.H., Sun, X., Huang, Y.H., Su, Z.B., Hu, S.R., Weng, W., Li, S.X., Guo, H.X., Wu, W.B., He, Y.S., Li, F.M., Huang, Y. 2015. NH_2-rich polymer/graphene oxide use as a novel adsorbent for removal of Cu(II) from aqueous solution. Chemical Engineering Journal, 263, 280-289.

Xu, J., Cao, Z., Zhang, Y., Yuan, Z., Lou, Z., Xu, X., Wang, X. 2018. A review of functionalized carbon nanotubes and graphene for heavy metal adsorption from water: Preparation, application, and mechanism. Chemosphere, 195, 351-364.

Xu, L., Xiao, G., Chen, C., Li, R., Mai, Y., Sun, G., Yan, D. 2015. Superhydrophobic and superoleophilic graphene aerogel prepared by facile chemical reduction. Journal of Materials Chemistry A, 3(14), 7498-7504.

Yang, J., Yu, M., Qiu, T. 2014. Adsorption thermodynamics and kinetics of Cr(VI) on KIP210 resin. Journal of Industrial and Engineering Chemistry, 20(2), 480-486.

Yang, P., Liu, Q., Liu, J., Zhang, H., Li, Z., Li, R., Liu, L., Wang, J. 2017a. Bovine Serum Albumin-Coated Graphene Oxide for Effective Adsorption of Uranium(VI) from Aqueous Solutions. Industrial & Engineering Chemistry Research, 56(13), 3588-3598.

Yang, Y., Ok, Y.S., Kim, K.-H., Kwon, E.E., Tsang, Y.F. 2017b. Occurrences and removal of pharmaceuticals and personal care products (PPCPs) in drinking water and water/sewage treatment plants: A review. Science of The Total Environment, 596-597, 303-320.

Yang, Y., Xie, Y., Pang, L., Li, M., Song, X., Wen, J., Zhao, H. 2013. Preparation of Reduced Graphene Oxide/Poly(acrylamide) Nanocomposite and Its Adsorption of Pb(II) and Methylene Blue. Langmuir, 29(34), 10727-10736.

Yao, Q., Fan, B., Xiong, Y., Jin, C., Sun, Q., Sheng, C. 2017. 3D assembly based on 2D structure of Cellulose Nanofibril/Graphene Oxide Hybrid Aerogel for Adsorptive Removal of Antibiotics in Water. Scientific Reports, 7(1), 45914.

Yap, P.L., Auyoong, Y.L., Hassan, K., Farivar, F., Tran, D.N.H., Ma, J., Losic, D. 2020. Multithiol functionalized graphene bio-sponge via photoinitiated thiol-ene click chemistry for efficient heavy metal ions adsorption. Chemical Engineering Journal, 395, 124965.

Yaumi, A.L., Bakar, M.Z.A., Hameed, B.H. 2018. Melamine-nitrogenated mesoporous activated carbon derived from rice husk for carbon dioxide adsorption in fixed-bed. Energy, 155, 46-55.

Ye, Y., Yin, D., Wang, B., Zhang, Q. 2015. Synthesis of Three-Dimensional Fe_3O_4/Graphene Aerogels for the Removal of Arsenic Ions from Water. Journal of Nanomaterials, 2015, 6.

Yin, S., Wu, Y.-L., Hu, B., Wang, Y., Cai, P., Tan, C.K., Qi, D., Zheng, L., Leow, W.R., Tan, N.S., Wang, S., Chen, X. 2014. Three-Dimensional Graphene Composite Macroscopic Structures for Capture of Cancer Cells. Advanced Materials Interfaces, 1(1), 1300043.

Yin, Y., Zhou, T., Luo, H., Geng, J., Yu, W., Jiang, Z. 2019. Adsorption of arsenic by activated charcoal coated zirconium-manganese nanocomposite: Performance and mechanism. Colloids and Surfaces A: Physicochemical and Engineering Aspects, 575, 318-328.

Yoon, Y., Park, W.K., Hwang, T.-M., Yoon, D.H., Yang, W.S., Kang, J.-W. 2016. Comparative evaluation of magnetite–graphene oxide and magnetite-reduced graphene oxide composite for As(III) and As(V) removal. Journal of Hazardous Materials, 304, 196-204.

Yoon, Y.H., Nelson, J.H. 1984. Application of Gas Adsorption Kinetics — II. A Theoretical Model for Respirator Cartridge Service Life and Its Practical Applications. American Industrial Hygiene Association Journal, 45(8), 517-524.

You, X., He, M., Cao, X., Wang, P., Wang, J., Li, L. 2019. Molecular dynamics simulations of removal of nonylphenol pollutants by graphene oxide: Experimental study and modelling. Applied Surface Science, 475, 621-626.

Yu, B., Bai, Y., Ming, Z., Yang, H., Chen, L., Hu, X., Feng, S., Yang, S.-T. 2017. Adsorption behaviors of tetracycline on magnetic graphene oxide sponge. Materials Chemistry and Physics, 198, 283-290.

Yu, B., Xu, J., Liu, J.-H., Yang, S.-T., Luo, J., Zhou, Q., Wan, J., Liao, R., Wang, H., Liu, Y. 2013. Adsorption behavior of copper ions on graphene oxide–chitosan aerogel. Journal of Environmental Chemical Engineering, 1(4), 1044-1050.

Yu, M., Song, A., Xu, G., Xin, X., Shen, J., Zhang, H., Song, Z. 2015. 3D welan gum–graphene oxide composite hydrogels with efficient dye adsorption capacity. RSC Advances, 5(92), 75589-75599.

Yusuf, M., Song, K., Li, L. 2020. Fixed bed column and artificial neural network model to predict heavy metals adsorption dynamic on surfactant decorated graphene. Colloids and Surfaces A: Physicochemical and Engineering Aspects, 585, 124076.

Zbair, M., Ait Ahsaine, H., Anfar, Z. 2018. Porous carbon by microwave assisted pyrolysis: An effective and low-cost adsorbent for sulfamethoxazole adsorption and optimization using response surface methodology. Journal of Cleaner Production, 202, 571-581.

Zeng, T., Yu, Y., Li, Z., Zuo, J., Kuai, Z., Jin, Y., Wang, Y., Wu, A., Peng, C. 2019. 3D MnO_2 nanotubes@reduced graphene oxide hydrogel as reusable adsorbent for the removal of heavy metal ions. Materials Chemistry and Physics, 231, 105-108.

Zhan, W., Gao, L., Fu, X., Siyal, S.H., Sui, G., Yang, X. 2019. Green synthesis of amino-functionalized carbon nanotube-graphene hybrid aerogels for high performance heavy metal ions removal. Applied Surface Science, 467-468, 1122-1133.

Zhang, H., Zhai, D., He, Y. 2014a. Graphene oxide/polyacrylamide/carboxymethyl cellulose sodium nanocomposite hydrogel with enhanced mechanical strength: preparation, characterization and the swelling behavior. RSC Advances, 4(84), 44600-44609.

Zhang, J., Yang, H., Shen, G., Cheng, P., Zhang, J., Guo, S. 2010. Reduction of graphene oxide vial-ascorbic acid. Chemical Communications, 46(7), 1112-1114.

Zhang, L., Wang, Z., Xu, C., Li, Y., Gao, J., Wang, W., Liu, Y. 2011a. High strength graphene oxide/polyvinyl alcohol composite hydrogels. Journal of Materials Chemistry, 21(28), 10399-10406.

Zhang, N., Qiu, H., Si, Y., Wang, W., Gao, J. 2011b. Fabrication of highly porous biodegradable monoliths strengthened by graphene oxide and their adsorption of metal ions. Carbon, 49(3), 827-837.

Zhang, P., Xu, P., Fan, H., Sun, Z., Wen, J. 2019a. Covalently functionalized graphene towards molecular-level dispersed waterborne polyurethane nanocomposite with balanced comprehensive performance. Applied Surface Science, 471, 595-606.

Zhang, W., Chen, J., Hu, Y., Fang, Z., Cheng, J., Chen, Y. 2018. Adsorption characteristics of tetrabromobisphenol A onto sodium bisulfite reduced graphene oxide aerogels. Colloids and Surfaces A: Physicochemical and Engineering Aspects, 538, 781-788.

Zhang, X., Sui, Z., Xu, B., Yue, S., Luo, Y., Zhan, W., Liu, B. 2011c. Mechanically strong and highly conductive graphene aerogel and its use as electrodes for electrochemical power sources. Journal of Materials Chemistry, 21(18), 6494-6497.

Zhang, X., Yan, L., Li, J., Yu, H. 2020. Adsorption of heavy metals by l-cysteine intercalated layered double hydroxide: Kinetic, isothermal and mechanistic studies. Journal of Colloid and Interface Science, 562, 149-158.

Zhang, Y.-L., Liu, Y.-J., Dai, C.-M., Zhou, X.-F., Liu, S.-G. 2014b. Adsorption of Clofibric Acid from Aqueous Solution by Graphene Oxide and the Effect of Environmental Factors. Water, Air, & Soil Pollution, 225(8), 2064.

Zhang, Y., Jin, F., Shen, Z., Wang, F., Lynch, R., Al-Tabbaa, A. 2019b. Adsorption of methyl tert-butyl ether (MTBE) onto ZSM-5 zeolite: Fixed-bed column tests, breakthrough curve modelling and regeneration. Chemosphere, 220, 422-431.

Zhang, Y., Liu, Y., Wang, X., Sun, Z., Ma, J., Wu, T., Xing, F., Gao, J. 2014c. Porous graphene oxide/carboxymethyl cellulose monoliths, with high metal ion adsorption. Carbohydrate Polymers, 101, 392-400.

Zhang, Z., Dong, Z., Wang, X., Dai, Y., Cao, X., Wang, Y., Hua, R., Feng, H., Chen, J., Liu, Y., Hu, B., Wang, X. 2019c. Synthesis of ultralight phosphorylated carbon aerogel for efficient removal of U(VI): Batch and fixed-bed column studies. Chemical Engineering Journal, 370, 1376-1387.

Zhao, B., Xu, X., Zeng, F., Li, H., Chen, X. 2018. The hierarchical porous structure bio-char assessments produced by co-pyrolysis of municipal sewage sludge and hazelnut shell and Cu(II) adsorption kinetics. Environmental Science and Pollution Research, 25(20), 19423-19435.

Zhao, D., Gao, X., Wu, C., Xie, R., Feng, S., Chen, C. 2016. Facile preparation of amino functionalized graphene oxide decorated with Fe3O4 nanoparticles for the adsorption of Cr(VI). Applied Surface Science, 384, 1-9.

Zhao, H., Jiao, T., Zhang, L., Zhou, J., Zhang, Q., Peng, Q., Yan, X. 2015a. Preparation and adsorption capacity evaluation of graphene oxide-chitosan composite hydrogels. Science China Materials, 58(10), 811-818.

Zhao, L., Chen, J., Xiong, N., Bai, Y., Yilihamu, A., Ma, Q., Yang, S., Wu, D., Yang, S.-T. 2019. Carboxylation as an effective approach to improve the adsorption performance of graphene materials for Cu^{2+} removal. Science of The Total Environment, 682, 591-600.

Zhao, L., Yu, B., Xue, F., Xie, J., Zhang, X., Wu, R., Wang, R., Hu, Z., Yang, S.-T., Luo, J. 2015b. Facile hydrothermal preparation of recyclable S-doped graphene sponge for Cu^{2+} adsorption. Journal of Hazardous Materials, 286, 449-456.

Zhong, C., Zhao, H., Cao, H., Fu, J., Xie, Y., Sun, Z. 2019. Acidity induced fast transformation of acetaminophen by different MnO_2: Kinetics and pathways. Chemical Engineering Journal, 359, 518-529.

Zhou, C., Zhu, H., Wang, Q., Wang, J., Cheng, J., Guo, Y., Zhou, X., Bai, R. 2017a. Adsorption of mercury(ii) with an Fe_3O_4 magnetic polypyrrole-graphene oxide nanocomposite. RSC Advances, 7(30), 18466-18479.

Zhou, Y., Liu, X., Xiang, Y., Wang, P., Zhang, J., Zhang, F., Wei, J., Luo, L., Lei, M., Tang, L. 2017b. Modification of biochar derived from sawdust and its application in removal of tetracycline and copper from aqueous solution: Adsorption mechanism and modelling. Bioresource Technology, 245, 266-273.

Zhu, C., Liu, T., Qian, F., Han, T.Y.-J., Duoss, E.B., Kuntz, J.D., Spadaccini, C.M., Worsley, M.A., Li, Y. 2016. Supercapacitors Based on Three-Dimensional Hierarchical Graphene Aerogels with Periodic Macropores. Nano Letters, 16(6), 3448-3456.

Zhu, J., Lou, Z., Liu, Y., Fu, R., Baig, S.A., Xu, X. 2015. Adsorption behavior and removal mechanism of arsenic on graphene modified by iron-manganese binary oxide (FeMnOx/RGO) from aqueous solutions. RSC Advances, 5(83), 67951-67961.

Zhu, S., Liu, Y.-g., Liu, S.-b., Zeng, G.-m., Jiang, L.-h., Tan, X.-f., Zhou, L., Zeng, W., Li, T.-t., Yang, C.-p. 2017. Adsorption of emerging contaminant metformin using graphene oxide. Chemosphere, 179, 20-28.

Zhu, Y., Murali, S., Cai, W., Li, X., Suk, J.W., Potts, J.R., Ruoff, R.S. 2010. Graphene and Graphene Oxide: Synthesis, Properties, and Applications. Advanced Materials, 22(35), 3906-3924.

Zhuang, Y., Yu, F., Chen, H., Zheng, J., Ma, J., Chen, J. 2016. Alginate/graphene double-network nanocomposite hydrogel beads with low-swelling, enhanced mechanical properties, and enhanced adsorption capacity. Journal of Materials Chemistry A, 4(28), 10885-10892.

Zhuang, Y., Yu, F., Ma, J. 2015. Enhanced Adsorption and Removal of Ciprofloxacin on Regenerable Long TiO_2 Nanotube/Graphene Oxide Hydrogel Adsorbents. Journal of Nanomaterials, 2015, 8.